JAERI-Review
2001-046

ANNUAL REPORT OF KANSAI RESEARCH ESTABLISHMENT 2000
APRIL 1, 2000 – MARCH 31, 2001

February 2002

Kansai Research Establishment

日本原子力研究所
Japan Atomic Energy Research Institute

本レポートは，日本原子力研究所が不定期に公刊している研究報告書です。
入手の問合わせは，日本原子力研究所研究情報部研究情報課（〒319-1195　茨城県那珂郡東海村）あて，お申し越しください。なお，このほかに財団法人原子力弘済会資料センター（〒319-1195　茨城県那珂郡東海村日本原子力研究所内）で複写による実費頒布をおこなっております。

This report is issued irregularly.
Inquiries about availability of the reports should be addressed to Research Information Division, Department of Intellectual Resources, Japan Atomic Energy Research Institute, Tokai-mura, Naka-gun, Ibaraki-ken, 319-1195, Japan.

編集兼発行　　日本原子力研究所

JAERI-Review 2001-046

Annual Report of Kansai Research Establishment 2000
April 1, 2000－March 31, 2001

Kansai Research Establishment

Japan Atomic Energy Research Institute
Kizu-cho, Souraku-gun, Kyoto-fu

(Received December 7, 2001)

This report is the second issue of the annual report of Kansai Research Establishment, Japan Atomic Energy Research Institute. It covers status reports of R&D and results of experiments conducted at the Advanced Photon Research Center and the Synchrotron Radiation Research Center during the period from April 1, 2000 to March 31, 2001.

Keywords: Annual Report, Kansai Research Establishment, JAERI, R&D, Advanced Photon Research Center, Synchrotron Radiation Research Center

---

関西研究所年報 2000
2000 年 4 月 1 日－2001 年 3 月 31 日

日本原子力研究所
関西研究所

(2001 年 12 月 7 日受理)

本報告書は、日本原子力研究所関西研究所の第 2 号の年報であり、2000 年 4 月 1 日から 2001 年 3 月 31 日までの期間（平成 12 年度）に行われた光量子科学研究センター及び放射光科学研究センターの研究活動をまとめたものである。

関西研究所：〒619-0215　京都府相楽郡木津町梅美台８－１

Contents

Foreword

This Annual Report of Kansai Research Establishment 2000 contains brief accounts of scientific activities at the Advanced Photon Research Center (APRC) and the Synchrotron Radiation Research Center (SRRC) during the fiscal year 2000. These Research Centers located at the new Science Cities, APRC in Kyoto Prefecture and SRRC in Hyogo Prefecture, are focused on advancement of optical and x-ray science with the use of lasers at APRC and synchrotron radiation at SRRC. The FY 2000 has been important for both of the Research Centers as the year to move from the development-oriented phase to the research-oriented phase. Various new results have been obtained in FY 2000 using the facilities that we have developed; high peak-power lasers at APRC and high-performance beam lines for SPring-8 at SRRC.

FY 2000 is the second year for APRC since most of the staffs and experimental facilities have moved from JAERI Tokai Research Establishment to the present site in July 1999. The major focus at APRC for this FY has been to restart and newly construct the experimental facilities in the new laboratory building. We have been able not only to activate these facilities, but also to get scientific results at the new site and to make preparations for various experiments in the years to come. A part of the simulation group, which had been working at the JAERI Neyagawa branch office in Osaka Prefecture, has moved to the new site in January-February 2001. Also a new super computer system has been installed in March 2001. Therefore all the members and facilities of APRC have been integrated to the new site in Kyoto by the end of FY 2000, except for the free electron laser research group which is using the FEL facility located at Tokai.

The FY 2000 is the fourth year since the 8-GeV synchrotron radiation facility SPring-8 became available to the public users in October 1997. SRRC has been responsible for constructing three JAERI beam lines and half of the public beam lines to be operated by JASRI. Also it has been engaged in its original scientific research with main focus on material science. The activities at SRRC have been shifting from the beam-line development and construction phase to the research phase. In FY 2000, various new results have been obtained using the JAERI and public beam lines at SPring-8, together with the JAERI beam line at KEK Photon Factory.

We would like to thank all the Members of the Research Committees for advising and supporting the activities of the Kansai Research Establishment. Also we gratefully acknowledge significant contributions to our research and development by many collaborators at universities and companies under various joint research projects.

Yoshiaki Kato
Director General
Kansai Research Establishment, JAERI

1. Summary

JAERI(Japan Atomic Energy Research Institute) is the complex research institute of nuclear science and technology where research facilities such as synchrotron radiation, x-ray laser, high-intensity proton accelerator, accelerators of electron beam and ion beam, nuclear research reactors and advanced computer system can be synthetically utilized. Kansai Research Establishment was established five years ago to promote the research of laser and synchrotron radiation.

A new Long-Term Program for research, development and utilization of nuclear energy was drawn up in The Atomic Energy Commission of Japan in November 2000. The program reminds us that nuclear science and technology has achieved remarkable developments in the 20th century and brought about substantial changes in lives and lifestyles. In the 21st century, the advance of nuclear science and technology is expected not only to form the basis for development of new energy technologies but also to challenge new frontiers. High brilliant synchrotron radiation and x-ray laser contribute to the advance of life science and materials science related to nano-structure, environment and information technology.

This Annual Report summarizes the research activities at both Synchrotron Radiation Research Center and Advanced Photon Research Center in the period from April 1, 2000 until March 31, 2001. A previous Annual Report (1995～2000) was published as JAERI-Review 2001-003 in March 2001.

2. Facilities of Advanced Photon Research Center

The main research subject at the Advanced Photon Research Center (APRC) is the development and application of novel light sources; T-cube lasers and X-ray lasers. The facilities of the APRC were constructed in Kizu-town at Kyoto in 1999 as shown in Fig. 1. Main facilities consist of four laboratories as shown in Fig. 2.

T-cube lasers are compact lasers emitting coherent light with extremely high intensity in a focusing spot, comparable to that of a solar flare, in an ultra-short duration of a fifty-trillionth of a second. X-ray lasers, which emit highly coherent light of short wavelength in the X-ray region, are developed for practical use in scientific research and industrial applications.

Activities at APRC include development of a tunable wavelength free electron laser, laser particle acceleration which may lead to downsizing conventional electron accelerators by over a factor of one hundred, optics technologies indispensable for development of novel lasers, and computer simulation of various phenomena in the photon-matter interaction, which are difficult to observe experimentally in detail.

By utilizing the novel advanced light sources, APRC challenges development of new frontiers of science and innovative technologies. The ultra-short pulse duration of the T-cube lasers enables us to observe ultra-fast chemical reactions and molecular motions as if their movements are stopped. X-ray lasers allow observation of living cells with high precision. In addition, high intensity lasers can be used to create new matter by controlling nuclear states.

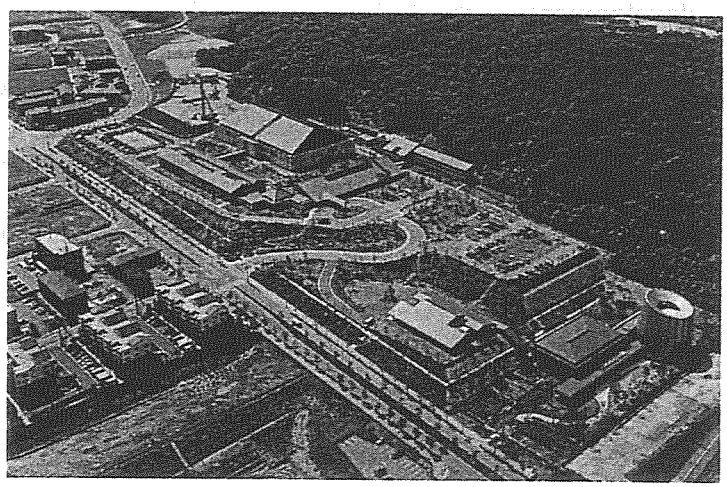

Fig. 1 Bird's eye view of the Advanced Photon Research Center

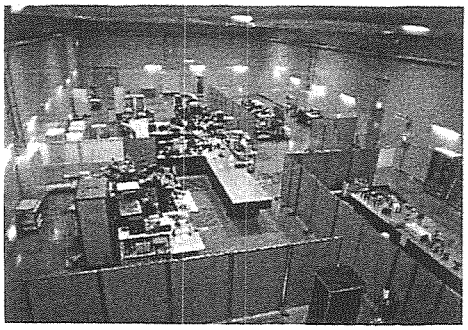

High repetition T-cube laser laboratory

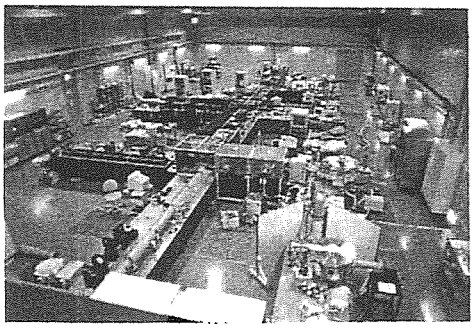

High peak power T-cube laser laboratory

Laser acceleration laboratory

X-ray laser laboratory

Fig. 2 Four main laboratories of the Advanced Photon Research Center T-cube laser beam is transmitted to the laser acceleration laboratories.

3. Facilities of Synchrotron Radiation Research Center

SPring-8 (Fig. 1) was operated in 2000 as scheduled. The JAERI beamlines of BL23SU, BL14B1 and BL11XU are operated for materials research. BL23SU is the soft x-ray beamline and has an insertion device of the double-array of variable polarization. To get lower energy to 0.3 keV with the first harmonic, the vacuum chamber was replaced to thinner one. In the BL14B1, the bender system of the monochromator crystal was upgraded to get 10 times better focusing performance. The new beamline of BL22XU is under construction for studying diffraction of condensed matter and uranium material and will be complete in March 2002.

The materials science research facility of JAERI (Fig. 2) was complete in May 2000 as a laboratory to prepare samples for experiments and process experimental data.

SPring-8 succeeded in x-ray photon beam threading 1 km vacuum duct on June 2, 2000, at BL29XU. Monochromatized x-rays were guided to the 1 km experimental station. During the summer shutdown of 2000, a lattice of the storage ring was modified to create magnet free 30 m straight sections. The 25 m long insertion device was installed at the x-ray beamline (BL19LXU).

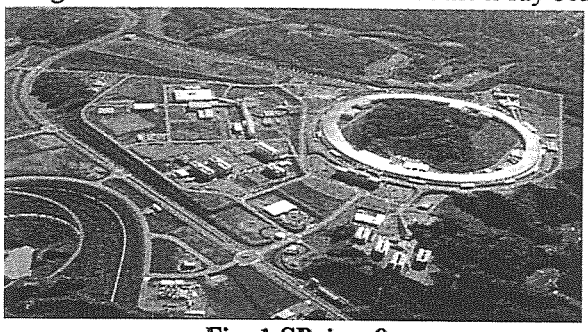

Fig. 1 SPring-8

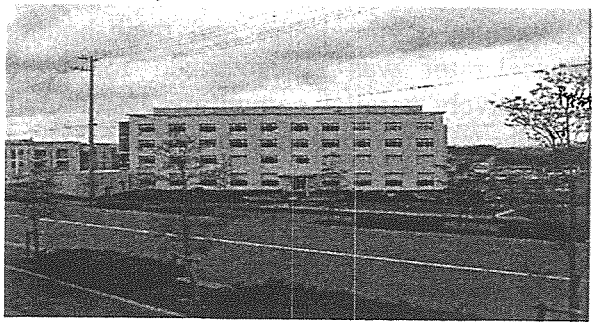

Fig. 2 Materials science research facility

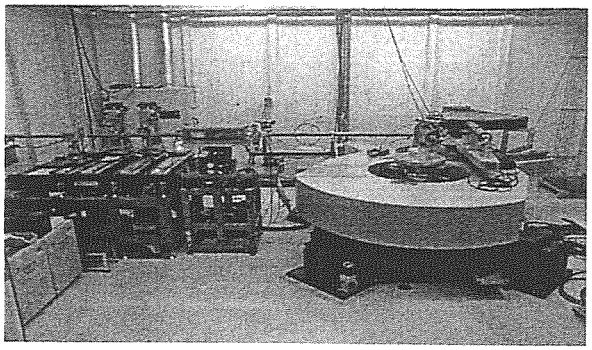

Fig. 3 Resonant inelastic x-ray scattering (RIXS) spectrometer at BL11XU

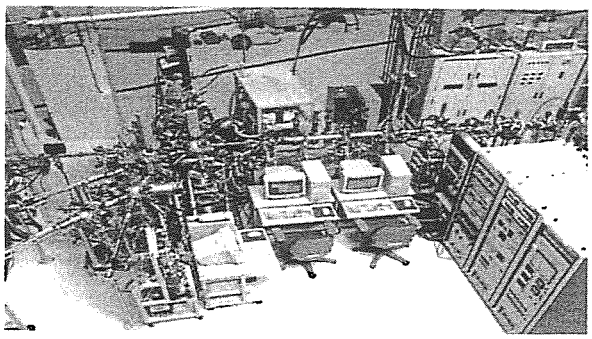

Fig. 4 Surface reaction analysis apparatus (SUREAC2000) at BL23SU

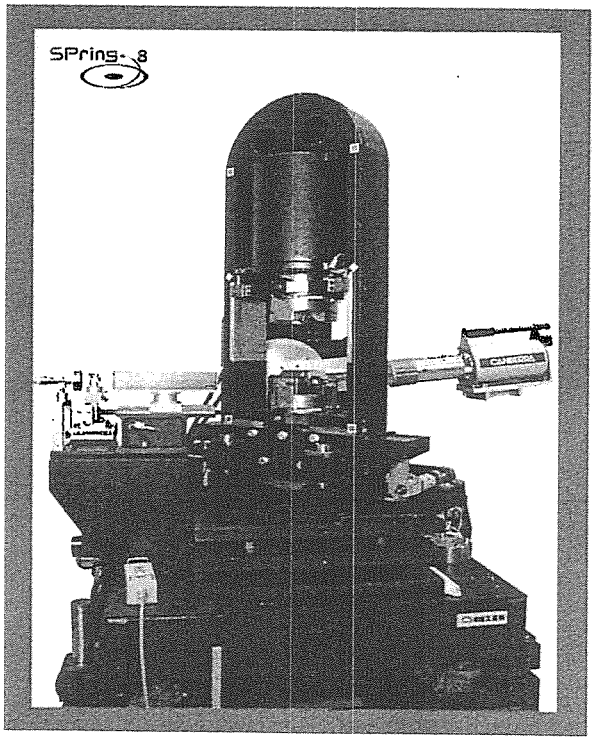

Fig. 5 Cubic-type multi-anvil apparatus (SMAP 2) at BL14B1

4. Advanced Photon Science

Takashi ARISAWA

In 2000 efforts are successively made for developing three types of advanced lasers, that is, T-cube laser, X-ray laser and superconducting free electron laser, with additional efforts to the application technology development. Some of them are summarized below.

In order to apply 100 TW laser system to the high field physics, a laser beam transport line was installed to deliver laser beam from the laser development room to the target room where the target chambers are installed for high field physics and also laser induced particle acceleration experiments. Saturated amplification was achieved in 10 nm ranges for X-ray laser. Newly developed ultra short oscillation mode with high peak power was verified in the super-conducting free electron laser.

Highly efficient multilayered X-ray optics was developed by inspecting the microscopic structure of the lasers and their boundaries. Performance of photo cathode microtron accelerator was characterized for laser induced particle acceleration experiment. A massively parallel computing system with 1.5 Tflops was installed, and some simulation codes will be tuned for this system.

4.1 High Peak Power Laser Development

Laser System Development Group

Koichi YAMAKAWA, Yutaka AKAHANE, Makoto AOYAMA, Kyoichi DEKI, Yuji FUKUDA, Norihiro INOUE, Junji KAWANAKA, Hiromitsu KIRIYAMA, Jinglong MA, Fumiaki MATSUOKA, Akihiko NISHIMURA, Akira OHZU, Hiideki UEDA, Koichi WADA, Ken-ichi YAGI, Akio YASUHARA and Kenzo MIYAZAKI

Over the past 4 years we have been working on the developments of an ultrafast, ultrahigh peak power Ti:sapphire laser system(100 TW, 20 fs, 10 Hz@800 nm) and a high repetition rate, high peak power Ti:sapphire laser system (0.01~0.5 TW, 100 Hz@800 nm) and completed the constructions of them in 1998. These laser systems are currently being applied to perform a number of applications ranging from micro machining to high field atomic and molecular physics as described in this Report. The laser pulses from the systems are also being characterized and controlled for improving performance and much reliable operation. We have installed two target chambers for optical field ionization and hard x-ray generation experiments in a high peak power laser laboratory as shown in Fig. 1. The beam switchyard can be used to switch one experiment and another easily and quickly, so that we run both type of experiments very efficiently. In order to perform laser wake field acceleration and high field physics experiments, we have constructed a beam transport system for bringing the 100 TW laser beam to the laser acceleration laboratory as shown in Fig. 2. After pulse compression in a vacuum compressor, the beam is transported through a 40 m long vacuum tube to prevent nonlinear effects in air. We are also currently upgrading the system to the petawatt power level. The construction of the petawatt amplifier chain and pulse compressor will be completed by the end of March of 2002.

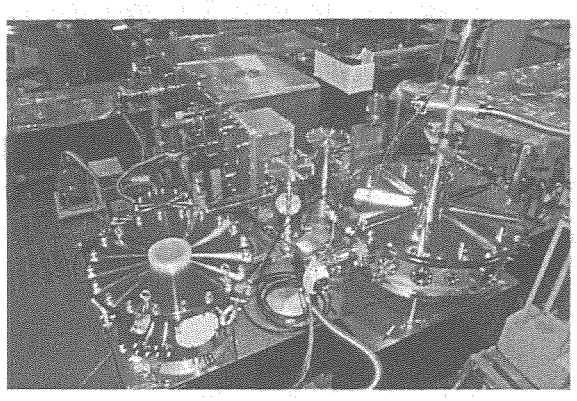

Fig. 1 Two targeting systems for high filed ionization and hard x-ray generation experiments

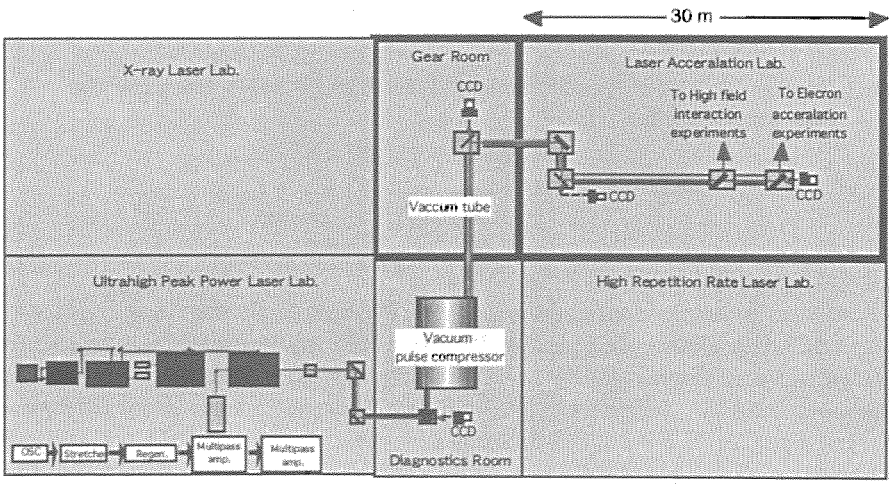

Fig. 2 Laser beam transport system

4.1.1 Current status and future developments of ultrahigh intensity lasers

Koichi YAMAKAWA, Yutaka AKAHANE, Makoto AOYAMA, Yuji FUKUDA,
Jinglong MA and Akito SAGISAKA

1. Introduction

Recent advances in femtosecond laser sources are making intensities approaching ~10^{21} W/cm^2 available for the study of nonlinear relativistic optics [1]. At such intensities the electron velocity in the laser field becomes relativistic and exhibits highly nonlinear motion, thus making it possible to investigate entirely new classes of physical effects.

The technique of chirped pulse amplification (CPA) has opened new avenues for the production of very high-energy ultrashort duration pulses without optical damage to amplifiers and optical components. The combination of CPA and ultrabroad-band solid-state laser materials has made it possible to produce terawatt and even multiterawatt femtosecond pulses with ever increasing average powers. We have developed and well characterized the 100 TW, 20 fs Ti:sapphire CPA system operating at 10 Hz repetition rate [2]. The laser system is being applied to perform high-field atomic and molecular ionization experiments at intensities of over 10^{19} W/cm^2 and also hard x-ray generation from solid targets. In order to perform laser wake field acceleration and high field physics experiments, we have constructed a beam transport system for bringing the 100 TW laser beam to the laser acceleration laboratory.

2. Characterization of the laser system

In order to fully characterize the pulse duration and phase of 20-fs laser pulses, second harmonic generation (SHG) frequency-resolved optical gating (FROG) technique was used. Figure 1 shows the pulse intensity and phase in time retrieved from the SHG FROG trace. The compressed pulse accompanied with small pre- and post-pulses resulting that the predominant phase distortion is quartic.

The contrast ratio measured by the high dynamic range cross-correlation is of the order of 10^{-6} limited by ASE mainly coming from the Ti:sapphire regenerative amplifiers.

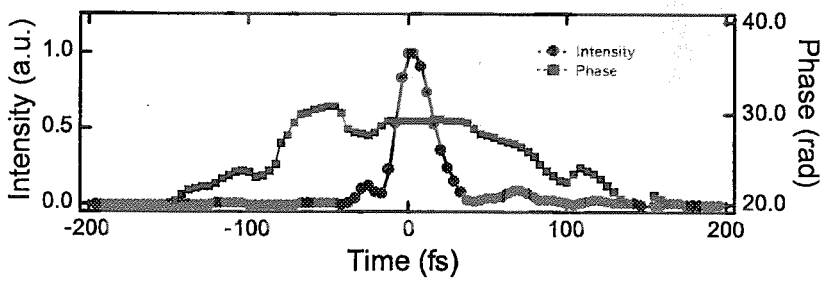

Fig. 1 Retrieved intensities and phases of the SHG FROG trace for the compressed pulse

3. High field atomic ionization

Among the numerous possible applications of 100 TW-class, ultrafast laser systems are studies of relativistic laser/mater interactions. In order to clarify the ionization mechanisms of an atom including the ionization rate at relativistic intensities, we have studied tunneling ionization of Argon using our laser system with intensities over 10^{19} W/cm^2. Using an off-axis parabolic mirror of focal length of 161 mm, we obtain the focal spot diameter of 6.8 μm at full width at half maximum (FWHM), which corresponds to the estimated peak intensity of 1.1 x 10^{19} W/cm^2. The uncertainly in the absolute value of the intensity is approximately factor of two. Argon gas is introduced into the vacuum chamber by means of a precision leak valve. The ion spectra are obtained with a 1-m time-of-flight spectrometer, which has a few hundred

volt/cm field potential. Dual micro channel plates (MCP) are used to detect the argon ions. At the highest laser intensities the first eight ion charge states (Ar^{+} to Ar^{8+}) were clearly observed and highly-charged argon ions up to Ar^{16+} were also detected. In order to clarify the ionization mechanism of L-shell states of Argon as a function of laser intensity, we used a half wave plate and polarizer to vary the intensity of the pulse. The results of the ion-yield data for Ar^{9+} and Ar^{10+} as a function of laser intensity are shown in Fig. 2. The theoretical curves calculated by the simple ADK model are also shown in this figure. It seems that the experimental data behave similar to ADK within our experimental dynamic range, but we could not conclude at the moment without more precise measurements and comparison to another models.

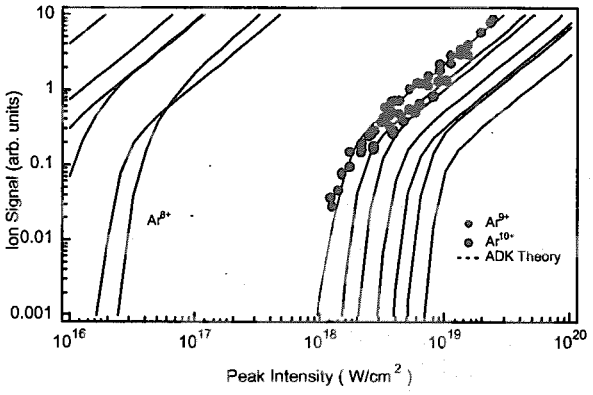

Fig. 2 Argon ion yield data compared to sequential ADK model as a function of incident laser intensity for a 20 fs 800 nm linearly polarized laser pulse

4. Conclusions

We have designed, constructed and well characterized the 100 TW, 20 fs Ti:sapphire CPA system. Since this laser system operates reliably at a 10-Hz repetition rate, it should allow the use sampling and averaging techniques even in the relativistic intensity. We have presented a systematic study of optical field ionization of Argon (n = 2) in the relativistic laser field. Ar^{16+} has been observed at laser intensity of over 1 x 10^{19} W/cm^2. Inner shell (L-shell) photoionization rate for Ar^{9+} and Ar^{10+} as a function of laser intensity has been measured over 3 orders of magnitude. The study presented here should lead to better understanding of relativistic plasmas of atoms, molecules and clusters in all of their complex interactions. We are also currently upgrading the system to the petawatt power level. Based on design studies which include the suppression of parasitic oscillation across the large-aperture Ti:sapphire amplifier disk, the optimization of the amplified pulse spectrum at the output of the amplifier and the compensation of high-order dispersion in the laser chain with a mixed grating scheme, scaling of 20-fs CPA technology to the petawatt peak power seems quite feasible.

References

1) G. Mourou, C. P. J. Barty and M. D. Perry, Phys. Today, **51**, 22-28, 1998
2) K. Yamakawa and C. P. J. Barty, IEEE J. Selected Topics in Quantum Electronics, **6**, 658-675, 2000

4.1.2 Status of high repetition rate Ti:Sapphire laser system for application research

Fumiaki MATSUOKA, Kazuyoku TEI[a)], Akira OHZU and Takashi ARISAWA
a) Department of Physics, Tokai University

1. Introduction

Laser applications such as laser processing, x-ray generation, high speed x-ray imaging and fluorescence spectroscopy, etc. are currently planned or in progress by using a high repetition rate Ti:Sapphire laser system (0.01~0.5 TW, 100 Hz@800 nm) in the APRC. Some findings of interest in the application research have been obtained so far. For those applications, the wave front correction of short pulse laser is indispensable to obtain high peak intensity at focal position with high efficiency. Therefore, a newly developed method, photorefractive phase conjugation mirror (PCM) with a $Rh:BaTiO_3$[1)] have been developed to correct the wave front distortions of laser beam in the laser system.

2. Experimental setup

The PCM was applied between a pulse stretcher and a regenerative amplifier in the laser system. A cat type configuration as illustrated in Figure 1 was used in the PCM. The laser pulses reflected by the PCM where stretched laser pulses were focused were separated with a half mirror. A plastic plate was placed as a phase distorter in front of the crystal to examine the effect of wave front correction. The wave front correction was evaluated with the beam profiles of the incident and reflected pulses.

3. Results

The beam profiles of (a) incident pulses into the PCM, (b) reflected pulses by the PCM, (c) reflected by the PCM with the distorter, and (d) reflected by an ordinary mirror with the distorter are shown in Figure 2. The fidelity of (b) 88 % and (c) 84 % against (a), which are equipped with the PCM, were >10 % higher than that 74 % of (d). This attributes to the wave front correction of the PCM. In addition, the pulse width (~110 fs) of compressed pulses was not changed when the PCM was applied. This is because the dispersion that includes higher order term of the pulses is preserved after the reflection by the PCM. This useful wave front correction is now applied to those applications in collaboration with some corporations and institutes.

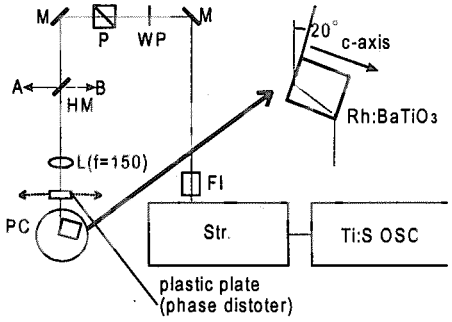

Fig. 1 Arrangement of experiment
FI : Faraday isolator
WP : $\lambda/2$ wave plate
P : polarizer
HM : half mirror
L : lens, PC : phase conjugation crystal
M : mirror

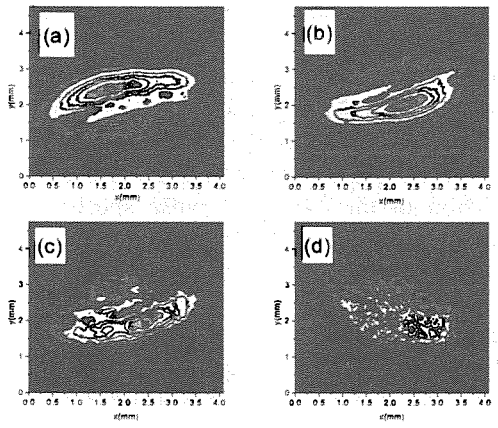

Fig. 2 Beam profiles of incident and reflected beam

Reference

1) H. Yau, P. Wang, E. Pan, J. Chen and J. Y. Chang, Opt. Comm. **135**, 331, 1997

4.1.3 Kerr-lens mode-locked oscillation with cooled Yb:YLF and Yb:glass

Junji KAWANAKA, Koichi YAMAKAWA, Hajime NISHIOKA[a)] and Ken-ichi UEDA[a)]
a) Institute for Laser Science, University of Electro-Communications (ILS/UEC)

1. Introduction

Ytterbium-doped materials are the promised laser materials of the next generation of the directly diode-pumped high-power solid-state lasers. Yb:YLF and Yb:glass have a broad spectral emission range to generate and amplify an ultrashort pulse with several ten femto seconds duration. Using such materials, a compact ultrahigh-peak-power laser system with an available output power could be developed. An efficient laser operation, however, is difficult to be achieved by using commercial laser-diodes which have rather low brightness as a pump source. Because there are much reabsorption of lower levels in a laser transition at room temperature. Cooling the materials was used for reduction of the reabsorption. Our spectroscopic research and laser oscillation at low temperature ensured that the laser gain was improved and the effective spectral gain band even in diode pumping.[1,2)]

In this report, a Kerr-lens mode-locked oscillator with Yb:YLF and Yb:glass has been demonstrated, for the first time to our knowledge, as a front-end of the diode-pumped ultrahigh-peak-power laser system. The average output power is 90 mW and 60 mW for Yb :YLF and Yb:glass, respectively, with a repetition rate of 108 MHz.

2. Experiment

Figure 1 shows an experimental apparatus of a Kerr-lens mode-locked oscillator. Yb:YLF and Yb:glass were attached to a thermally conductive copper stage of a liquid nitrogen cryostat with Brewster windows. A laser cavity was x-type configuration. The cavity length was 1.4 m. Three chirped mirrors were used to compensate dispersions of various materials in the cavity. Two 1.6-W single-emitter laser diodes (emitter size: 1 μm x 100 μm, wavelength: 940 nm) were focused on the laser materials. The maximum intensity at the focusing point was more than 50 kW/cm^2.

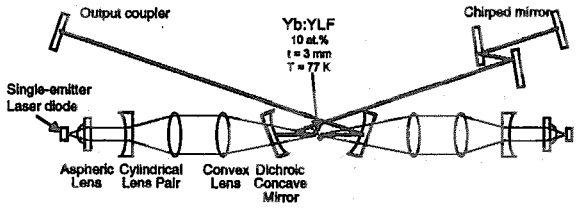

Fig. 1 Kerr-lens mode-locked oscillator with diode-pumped Yb-doped material

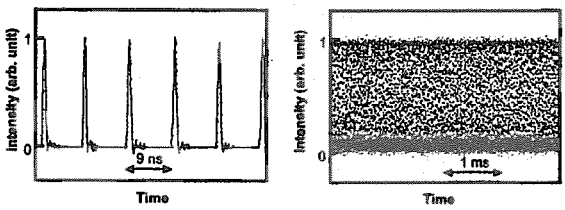

Fig. 2 Time-resolved waveforms of a mode-locked pulse train

3. Results

Kerr-lens mode-locking with Yb:YLF and Yb:glass has been demonstrated in diode-pumping. Figure 2 shows a time-resolved waveform of mode-locked pulse trains. The average output power was 90 mW and 60 mW for Yb:YLF and Yb:glass, respectively. The broad spectral width of 7 nm was observed with Yb:glass, shown in Fig. 3, which corresponded to a 150 fs pulse duration under a Fourier transform limit. The shorter pulse duration will be achieved by optimizing dispersion compensation.

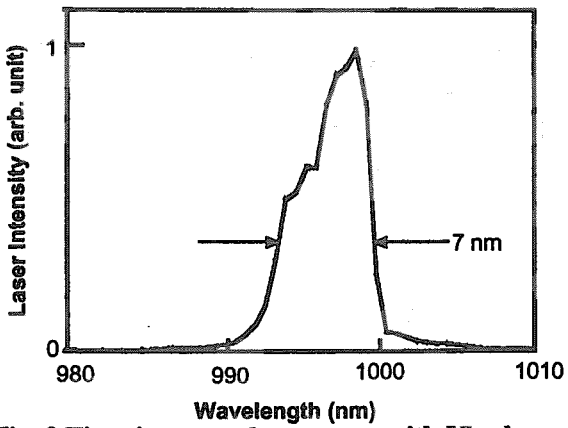

Fig. 3 Time-integrated spectrum with Yb:glass

References

1) J. Kawanaka, H. Nishioka and K. Ueda, Technical Digest of Conference on Lasers and Electro-Optics (CLEO) 2000 (OSA), 250-251, 2000
2) J. Kawanaka, H. Nishioka, N. Inoue and K. Ueda, Appl. Opt., 3542-3546, 2001

4.1.4 Conceptual design of high-average-power and high-brightness laser-diode pumped Nd:YAG phase-conjugated laser

Hiromitsu KIRIYAMA, Ken-ichi YAGI and Koichi YAMAKAWA

1. Introduction

High-average-power and high-brightness lasers with good beam quality are important for pumping high-average-power, high-repetition-rate ultrashort-pulse laser system. However, scaling the output power to the kilowatt level while simultaneously maintaining good beam quality is still challenging[1]. Laser-diode (LD) pumped solid-state lasers with phase-conjugation offer the unique combination of efficiency, reliability, and compactness. In order to achieve high-average-power, high-repetition-rate, and compactness in a ultrashort-pulse laser system, a conceptual design of a LD pumped Nd:YAG laser master-oscillator-power-amplifier (MOPA) system with an average-power in the kilowatt range have been developed.

2. Module design

For the laser gain medium, the Nd:YAG is one of candidates having the appropriate material parameters[2] for designing a high-power and high-repetition-rate laser system. The dimensions of Nd:YAG slab were determined under the several operational constraints such as thermal shock fracture, optical damage, parasitic oscillation, aspect ratio and gain. Zig-zag path slab geometry[2] greatly reduces thermal induced effects such as thermal lensing and thermal birefringence. The slab is side-pumped by a high-average-power quasi-CW LD array on each side with a total optical average-power of 3600 W at 20% duty factor. The module consists of an oscillator and two slab amplifiers. The pulse from the oscillator passes a four times per slab and is extracted by using of polarization rotation. Thermal effects are compensated by using a phase conjugation through stimulated Brillouin scattering (SBS) mirror filled with Fluorinert (FC-75) [3] and a 45 degree Faraday rotator.

Table 1 Total efficiency of the module designed

Transfer efficiency	95 %
Absorption efficiency	92 %
Quantum efficiency	95 %
Quantum defect	76 %
Storage efficiency	70 %
Extraction efficiency	59 %
Fill factor	80 %
Total efficiency	20 %

Table 2 Specifications of the module designed

Output energy	1.4 J
Repetition rate	1 kHz
Total efficiency	20 %
Beam cross-section	0.6 cm * 1.8 cm
LD	AlGaAs ; 808 nm
peak power density	571 W/cm^2
pumping time	200 μs
Stored energy density	0.1 J/cm^2
Slab	2 pieces
material	Nd:YAG
pump surface	1.8 cm * 18.7 cm

3. Results

The output performances were calculated by using the Franz-Nodvik equation[4]. The details specifications are summarized in Tables 1 and 2. The input pulse is amplified from 10 μJ to 1.4 J at the repetition rate of 1 kHz. The module has, therefore, more than 1 kW average-power and optical to optical efficiency of 20%.

References

1) T.Ishida, T.Tagawa, H.Morita, Y.Suzuki, K.Okino, H.Takenaka, K.Kubota, K.Washio and T.Yamane, Proc. SPIE **3888**, 568, 2000
2) W. Koechner, Solid-dtate laser engineering, 4th Ed. Springer-Verlag, Berlin, 1996
3) H.Yoshida, V.Kmetik, H.Fujita, M.Nakatsuka, T.Yamanaka and K.Yoshida, Appl. Opt. **36**, 3739, 1997
4) J.M.Eggleston, L.M.Franz and H.Injeyan, IEEE J. Quantum Electron. **25**, 1855, 1989

4.1.5 Pulse compressor-amplifier system by stimulated backward Raman scattering and cascaded second order nonlinear process

Kyoichi DEKI, Fumiaki MATSUOKA, Kazuyoku TEI[a)], Koichi WADA,
Takashi ARISAWA, Toshiaki MURAMATSU[b)] and Guerman PASMANIK[c)]
a) Tokai University b)Kantum Electronics Co.,LTD. c) Passat Co. LTD

1. Introduction

The ultrashort pulse laser processing has been attracting great attention recently because of its very limitted heat affected zone. In conventional ultrashort pulse laser systems a mode-locked Ti:Sapphire oscillator and a regenerative amplifier are usually used, and further Nd:YAG SHG lasers are used for pumping the gain mediums. Because of these complexties the laser system becomes expensive, large size, and needs delicate handling. These are the main reasons why the ultrashort pulse lasers have not been used in industrial applications. Because of this we have been investigating another ways for ultrashort pulse laser systems *i.e.*, inexpensive, compact, easily handling pulse compressor/amplifier systems for both industrial and scientific use. Figure 1 shows one of our answers. The numerical estimation shows that the combination of the backward Raman scattering and the cascaded second order nonlinear process (CSN) can compresses sub-nanosecond Nd:YAG laser pulses to sub-picosecond. The leading edge of the backward Raman signal is strongly amplified by the unsaturated Raman gain which is generated by the Nd:YAG pump laser. This amplifying process compresses the pulse duration from sub-nanosecond to several tens of picoseconds with the Stokes shift of the wavelength. The subsequent CSN process causes nonlinear phase shift in the fundamental beam from the SHG crystal. It is known that under the existence of large phase mismatch in the SHG process the back-conversion arises, which causes nonlinear phase shift and frequency chirp in the fundamental light beam[1-3]. As the back-conversion can be interpreted as $\chi^{(2)}(-2\omega;\omega,\omega):\chi^{(2)}(-\omega;2\omega,-\omega)$ cascade process, it is referred to as Cascaded Second order Nonlinear process. The CSN is equivalent to the well known optical Kerr effect. Assuming around 2.2 nm spectral broadening in the fundamental wavelength, less than 1 ps pulse duration is possible with prism pair or grating pair pulse compressor.

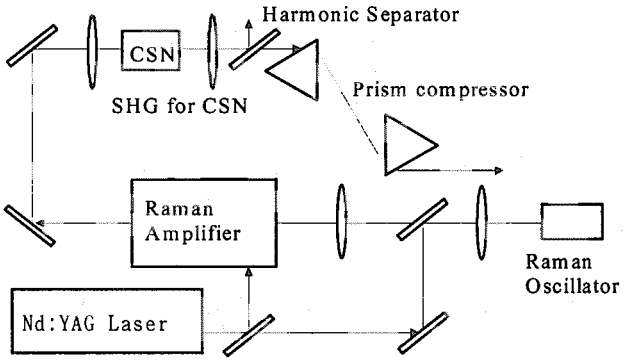

Fig. 1 A promising candidate for compact ultrashort pulse laser system

2. Experiments and discussion

For the first step, we investigated the Raman compressor/amplifier stage experimentally. Figure 2 shows the experimental setup in detail. A 61 mm length calcite crystal was used as the Raman Oscillator which also acts as the compressor. The backward Raman pulse duration t is known to be roughly proportional to Z_R/V, where Z_R is the Rayleigh range of the focused pumping beam, V is the speed of light in the Raman medium. According to this approximation the pulse duration can be much shortened as much as

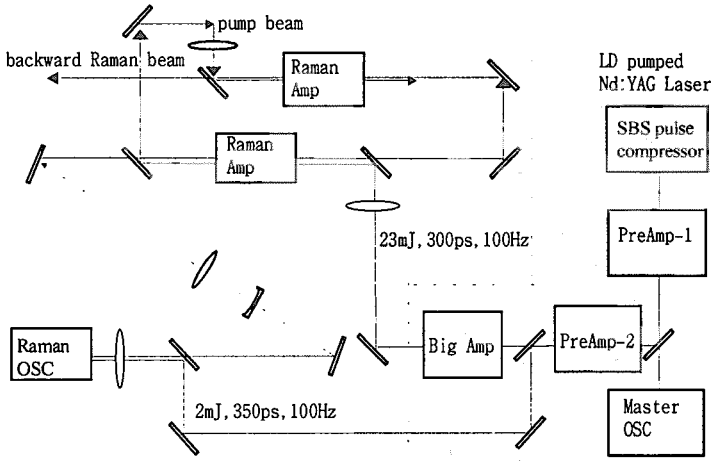

Fig. 2 The Raman compressor/amplifier system

the waist size of the pump beam in the Raman crystal can be decreased. The limitation of this pulse compression is the damage threshold and the lifetime of optical phonon of the Raman crystal. Figure 3 shows the experimental pulse duration as a function of the focal length of the Raman crystal. The pulse duration calibration at 250 mm focal length with model C5680 streak camera (Hamamatsu photonics) shows that the duration at 100 mm focal length in Fig. 3 have to be 20 ps (FWHM). From the results the pulse compression ratio can be estimated to be larger than 12. Figure 4 shows the output power and the efficiency of the Raman oscillator with f = 100 mm focal length. 20% efficiency was attained with 0.2 mJ Raman output. The beam quality of the Raman oscillator output was also evaluated by the beam propagation properties. The $M_x^2 = 1.17$ and $M_y^2 = 1.07$ were obtained. The beam profile is shown in Fig. 5. The Raman oscillator output was fed to the double stage Raman amplifier to amplify its energy. These amplifier was excited by the 23 mJ, 300 ps pump beam from the Nd:YAG Big amplifier as shown in Fig. 2. The experimental results of the amplifier stage are summarized in Table 1. The total amplifier gain can be estimated to be larger than 145 by the experimental result with the focal length of 120 mm. Table 1 also shows the SHG experimental result of the output of the Raman amplifier. High conversion efficiency (>55%) was attained with the 6 mm long type I LBO as SHG crystal.

Table 1 Summary of the experimental results in the Raman amplifier

	Output Energy
First Amp.	2.8mJ(Input 0.03mJ)
Second Amp.	4.8 mJ
SHG of the Raman	2.7mJ 56%(efficiency)

3. Conclusion

It was verified that the backward Raman pulse compressor by solid-state medium such as calcite crystal is promising for compact short pulse laser system because of its simplicity. Further Compression to the sub-picosecond region requires another method other than backward Raman scattering. In this phase of experiment we believe that the cascaded second order nonlinear process will carry out the important role.

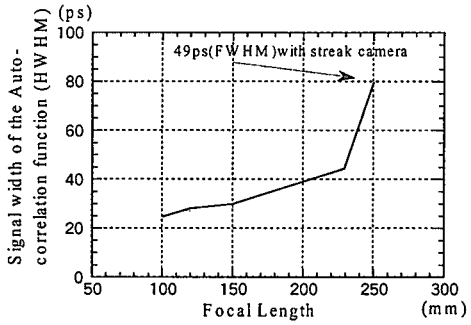

Fig. 3 The pulse width of the Raman oscillator output vs. focal length of the focusing lens

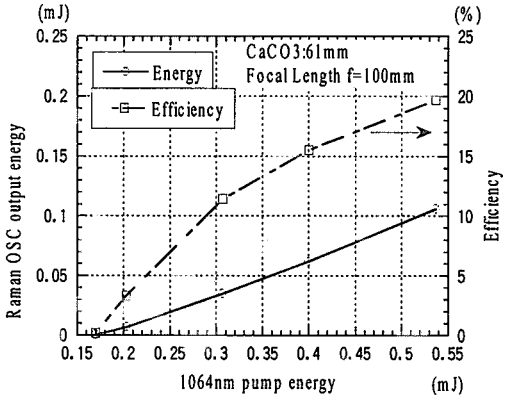

Fig. 4 The Raman oscillator output and the pumping efficiency vs. 1064 nm

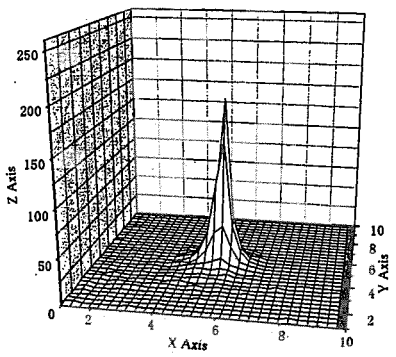

Fig. 5 The beam profile of the output of the Raman oscillator

References

1) R.C.Eckardt and A.J.Reintjes, IEEE J. Quantum.Electron. **QE-20**, 1178, 1984
2) H.J.Bakker *et al.*, Phys.Rev. A **42**, 4085, 1990
3) X.Liu *et al.*, Opt. Letters, **24**, 1777, 1999

4.1.6 Laser processing of silicon wafer and polyimide film

Kyoichi DEKI, Fumiaki MATSUOKA, Koichi WADA, Akihiko NISHIMURA, Takashi ARISAWA, Yuzo SHIMOBEPPU[a)] and Noboru HAYASAKA[a)]

a) Fujitsu Co. Ltd.

1. Introduction

Drilling and cutting of semiconductor materials by laser processing has become much more important as the high density packaging has been developed greatly by the progress of chip size package(CSP) or ball grid array (BGA) fabrication technique. Because these new devices require processing sizes too small for mechanical processes. For example, silicon device cutting less than 50 μm thickness, laser processing is required for suppressing chipping and oxide film cracking these are unavoidable by the conventional diamond wheel dicing. For the micro via-hole drillings less than 50 μm diameter, shorter wavelength laser processing, especially ultra violet laser processing are also required because of their limited sizes. On the other hand, ultrashort pulse laser processing has been attracting great attention recently because of its very limited heat affected zone and non-wavelength dependent characteristics[1)]. However because of its system complexity the ultrashort pulse lasers have not been employed in industrial micro-electronic production. In JAERI we have developed various types of laser systems which can serve the wide variety of laser pulse characteristics. For example pulse duration covering from several tens of femtoseconds to micro-seconds. Laser processing characteristics of silicon wafer, polyimide film are investigated experimentally by the use of these lasers to investigate which laser is suitable for each materials.

2. Experiment and discussion

The laser processing experiments were performed by unidirectional one time scanning of the materials normal to the optical axis with keeping focus position on to the material surfaces and keeping scanning speed constant as shown in Fig. 1, which forms a groove on them. A confocal laser microscope, Keyence VK8500 was used for the evaluation of the laser processing.

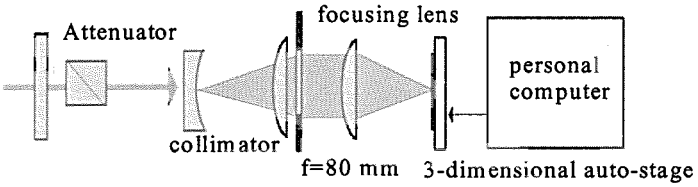

Fig. 1 Experimental setup for the laser processing

Si wafer: Figure 2 shows the shapes of the single pulse irradiation of 27 ns (Nd:YAG 1064 nm), 30 ps (602 nm Calcite Raman SHG), 67 fs (800 nm, Ti: Sapphire) laser on silicon wafer, respectively. No heavy redeposition is seen in Fig. 2(b), (c) compared with the long pulse laser irradiation (Fig. 2(a)). The cutting area processed by the Raman SHG laser is the smooth and no chipping is seen compared with dicing by diamond wheel as seen in Fig. 3. The shape of the groove edge comparison processed with the Raman SHG and Ti:Sapphire shows that the Raman SHG laser has smoother one. The scan times required for 50 μm thick silicon wafer cutting was compared by using three different types of lasers. The Raman SHG laser is the fastest as seen in Table 1.

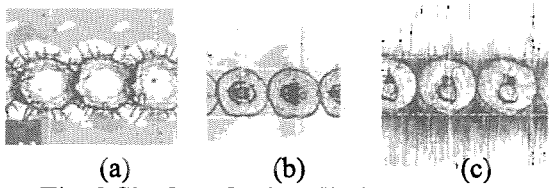

Fig. 2 Single pulse irradiations on to silicon wafers
(a) 27 ns (Nd:YAG 1064 nm)
(b) 30 ps (602 nm Raman SHG)
(c) 67 fs (800 nm, Ti: Sapphire)

On the other hand, we also tested the drilling process with a high energy laser pulse. A free running Ti:sapphire laser pulse drills a hole with some hundreds of micro seconds pulse duration. To clarify the keyhole formation of Si wafer, a pair of fast semiconductor photo detector monitored a reflected light and a penetrated flash on Si wafer

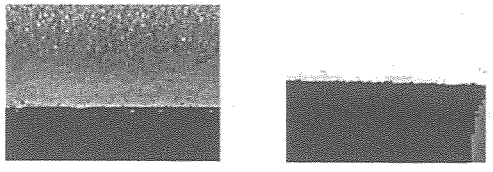

Fig. 3 Edges of the silicon cutting processed by (a) Raman SHG and (b)diamond wheel

laser processing. The laser pulse duration was long enough to reach the penetration. The minimum pulse energy of 13.3 mJ was required for ablation. Figure 4 shows that 56.5 mJ pulse energy has penetrated the 50 μm thickness Si wafer with a surface hole of 353 μm diameter. Figure 5 shows that the reflection light of Ch-1 vanished at 20 μs after and the penetration flash of Ch-2 appeared at 55 μs after. The Si vapor has been exhausted through the keyhole. At the moment a laser pulse hit a Si wafer, the flat surface of the wafer in room temperature reflects a large portion of laser pulse energy. However, the absorbed energy of several percentage of total energy rises the surface temperature. Reflectivity of Si wafer surface decreases with increasing the surface temperature. The heated thin layer on the surface also increases the absorption coefficient. This irreversible heating process should exist at the initial stage of keyhole formation.

Table 1 Results of the silicon cutting

Laser	Raman	Raman SHG	Ti:Sapphire
wavelength	1204nm	602nm	800nm
Pulse duration	30ps	30ps	67fs
Pulse energy		0.7mJ	
Scan speed		0.5mm/sec	
Scanning times untili cutting completion	15 times	5 times	8 times

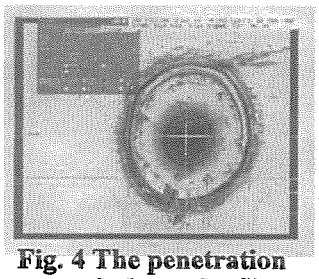

Fig. 4 The penetration hole on the Si Wafer with a Free running high energy laser pulse

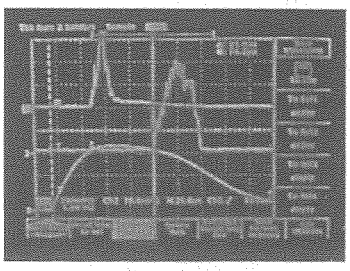

Fig. 5 Ch-1 Reflection (up) and Ch-2 Penetration (middle) signals with discharge current (down)

Polyimide film: No carbonized area is seen around the grooves when the Raman fundamental (1204 nm wave length), the Raman SHG, and the ultrashort pulse Ti:Sapphire lasers are used. Carbonized area is only seen evidently when the long pulse (>20 nsec) Nd:YAG laser is used (Fig. 6).

Figure 7 compares the removed volume processed with the three different types of lasers. The Raman SHG case is the largest as seen. We believe the reason is that the dissociation energies of C-N, C-C, C-O bonds which constitute polyimide[2] are located in less than 4.1eV, *i.e.*, the two-photon energy of the Raman SHG wavelength. In other words the wavelength effect considered to be much more important for polyimide laser processing.

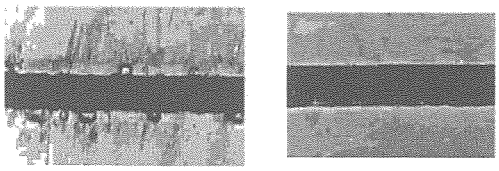

(a) (b)

Fig. 6 Grooves on polyimide film processed by (a) the long pulse (>20 nsec) Nd:YAG and (b) the Raman (30ps, 1204nm) lasers

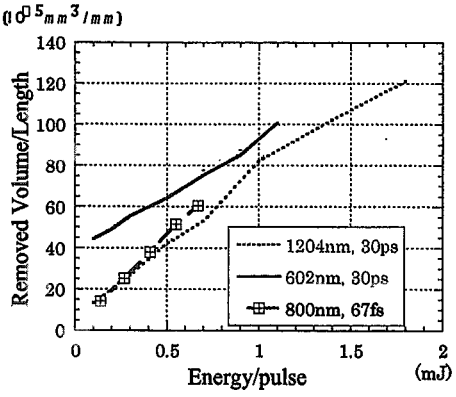

Fig. 7 Removed volume per length of polyimide vs. single shot energy

3. Conclusion

The laser processing characteristics of silicon wafer, and polyimide film were evaluated by using various types of lasers with the wide variety of laser pulse characteristics. As we stood the view point of material-cutting the performance was evaluated by the groove depth formed on the materials and the change rate of its width. Experimental results shows that processing by the Raman SHG laser, *i.e.*, 30 ps 602 nm laser is the most effective for both silicon and polyimide materials cutting. As the Raman compressor-amplifier system is very much easier to fabricate and handle and is inexpensive compared with the conventional CPA Ti:Sapphire laser system, the Raman laser system will be a powerful tool for industrial microelectronic device production.

References

1) X. Liu *et al.*, IEEE J. Quantum. Electron. **33**, 1706, 1997
2) H. Kumagai *et al.*, Appl. Phys. Lett. **65**(14), 1850, 1994

4.1.7 Second - harmonic generation of ultra-high intensity femtosecond pulses with a KDP crystal

Makoto AOYAMA, Tetsuo HARIMOTO[a)], Jinglong MA, Yutaka Akahane, Norihiro INOUE, Hideki UEDA, and Koichi YAMAKAWA

a) Faculty of Engineering, Yamanashi University, Takeda 4-3-11, Kofu, Yamanashi 400-8511, Japan

1. Introduction

In general the ultrashort laser pulses from a CPA laser system have amplified spontaneous emission (ASE) background associated with the main laser pulse and pre- and post-pulses[1)]. In a laser - matter interaction experiment, such pre-pulses and ASE would create a low density plasma in advance of the main laser pulse and thus significantly alter the physics of the laser - matter interaction. So it is significantly important for the study of the high field laser - solid target interaction experiments. Frequency conversion of femtosecond pulses can improve intensity contrast of laser pulses. Simple experimental configuration of second-harmonic generation (SHG) and improvement of intensity contrast are so attractive for some applications of intense femtosecond laser pulses. However it is well known that there are problems in frequency conversion such as SHG with sub-picosecond and femtosecond laser pulses[2-3)]. In order to solve these problems and accomplish simple experimental configuration of SHG, we investigated frequency conversion with a thin crystal and ~100 fs ultrahigh intensity laser pulses from a terawatt Ti: sapphire laser system.

2. Experimental setup

We used a part of our Ti:sapphire CPA laser system in this study[4)]. The compressed pulses have a spectral width of 14.7 nm at full-width at half maximum (FWHM) and a center wavelength of 800 nm. The output pulse duration used in this experiment was about 130 fs. The fundamental pulses were focused with a 1000 mm focal-length concave mirror on a SHG crystal. SHG was achieved in the Type I 1-mm-thick KDP crystal which has a sol-gel antireflective coating and a transmission spatial quality of λ / 7.5 @ 800 nm. The crystal was positioned 56 cm away from the focusing mirror. The generated SH and fundamental pulses were separated with a dichroic mirror. Spectral properties of the dichroic mirror were calibrated with a spectrophotometer (U-400, Hitachi Ltd.). Images of the SH and fundamental pulses were taken with charge-coupled device (CCD) cameras that were placed after the nonlinear crystal. We observed the images of a point on the nonlinear crystal.

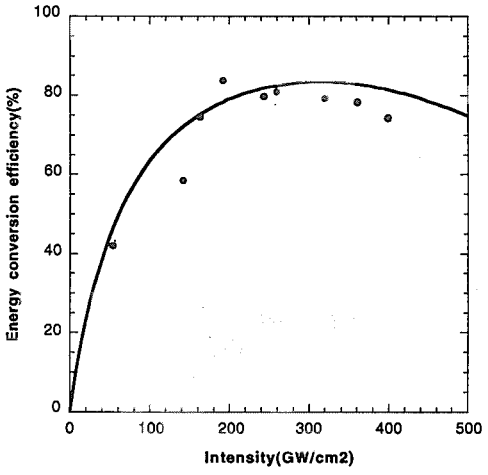

Fig. 1 Experimental and numerical energy conversion efficiencies of SHG as a function of fundamental intensity
Circles indicate experimental results. The solid curve shows the numerical result

3. Results

We have achieved an energy conversion efficiency of about 80% for a type I KDP crystal with 130 fs laser pulses for intensities as high as 192 GW/cm^2 and have found no optical fatal damage of the nonlinear crystal. SHG with intense femtosecond pulses makes experimental arrangements of frequency conversion simple. Therefore, it is feasible to apply to any kind of CPA laser system.

References

1) M. Aoyama, A. Sagisaka, S. Matsuoka, Y. Akahane, F. Nakano, and K. Yamakawa, Appl. Phys. B.**70**, S149, 2000
2) I. V. Tomov, R. Fedosejevs and A. A. Offenberger: IEEE J. Quantum Electron. **18**, 2048, 1982
3) R. C. Eckard, and J. Reintjes: IEEE J. Quantum Electron. **20**, 1178, 1984
4) K. Yamakawa, M. Aoyama, S. Matsuoka, T. Kase, Y. Akahane, and H.Takuma: Opt. Lett. **23**, 1468.1998

4.2 X-ray Laser Research

X-ray Laser Research Group

Keisuke NAGASHIMA, Tetsuya KAWACHI, Momoko TANAKA, Noboru HASEGAWA, Masataka KADO, Maki KISHIMOTO, Kouta SUKEGAWA, Shinichi NAMBA, Kenjiro TAKAHASHI, Renzhong TAI, Peixiang LU, Huajing TANG [a)], Alexander V. KILPIO [b)], Akira SASAKI, Kengo MORIBAYASHI, Masato KOIKE, Akira NAGASHIMA, Hiroyuki DAIDO and Yoshiaki KATO

a) Institute of Laser Engineering, Suita, Osaka, 575-0001, Japan

b) General Physics Institute, Russian Academy of Science, 117942, Moscow, Russia

1. Outline of x-ray laser research

The x-ray laser research at Advanced Photon Research Center has started on April 1998. The main purpose is to develop compact high performance x-ray laser system. In 1999, the experimental system, of which main device is a CPA (chirped pulse amplification) laser using Ti:sapphire and Nd:glass, has been installed in a new laboratory at the KIZU site. We achieved the first x-ray lasing at 32.6 nm (Ti target) by transient collisional excitation scheme. In 2000, we have succeeded in generating x-ray lasing at shorter wavelengths of 11.9 nm (Sn target) and 13.9 nm (Ag target). The saturated amplification was achieved by using traveling wave pumping and we examined the characteristics of the x-ray laser beam in detail.

2. Experimental apparatus

The experimental system for x-ray laser research consists of CPA laser systems and vacuum systems. The total system is shown in Fig. 1. The high energy picosecond laser is a hybrid laser system using Ti:sapphire and Nd:glass. This system is used as a pumping driver by transient collisional excitation. The pumping laser is focused with a line shape and is irradiated on solid metal targets (Ti, Ag and Sn). Further experiments will be planned using seeding light amplification for generating highly coherent x-ray lasers. The seeding light is generated from higher harmonics using wavelength variable sub-picosecond laser. This system is now under construction.

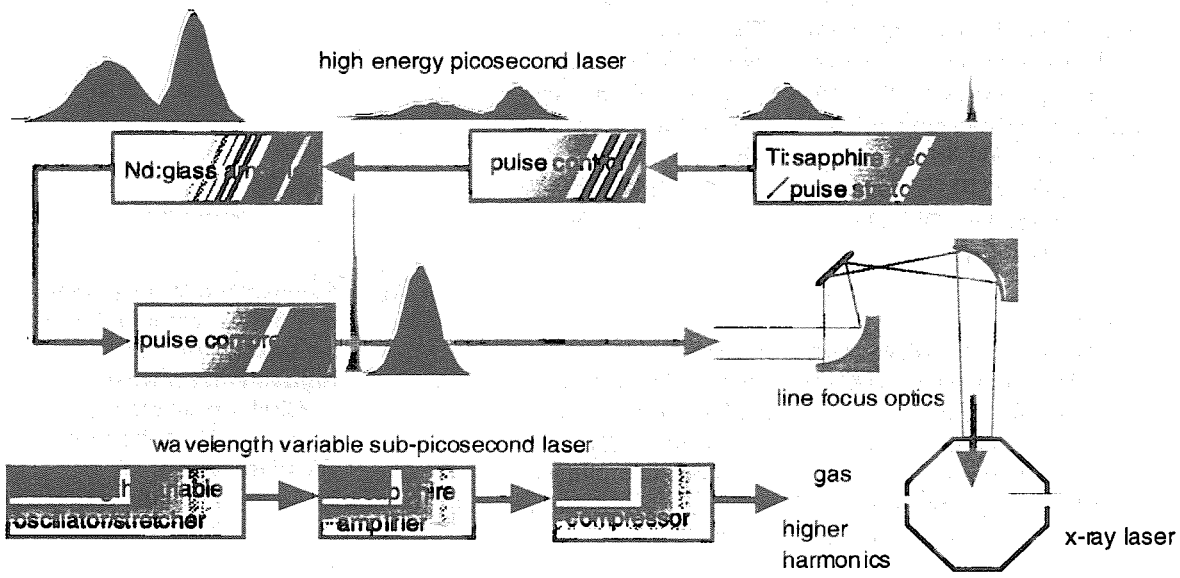

Fig. 1 Experimental system for x-ray laser

4.2.1 Gain saturation of Ni-like silver and tin x-ray lasers by use of a traveling wave pumping

Tetsuya KAWACHI, Momoko TANAKA, Noboru HASEGAWA, Masataka KADO, Alexander V. KILPIO [a], Shinichi NAMBA, Kouta SUKEGAWA, Peixiang LU, Keisuke NAGASHIMA, Kenjiro TAKAHASHI, Huajing TANG [b], Maki KISHIMOTO, Renzhong TAI, Masato KOIKE, Hiroyuki DAIDO and Yoshiaki KATO

a) General Physics Institute, Russian Academy of Science, 117942, Moscow, Russia

b) Institute of Laser Engineering, Suita, Osaka, 575-0001, Japan

1. Introduction

Since the demonstration of soft x-ray amplification, x-ray laser research has been intensively studied. Development of highly efficient and intense output in a short wavelength region has been one of the most important objects. Recently, using small size CPA Nd:glass lasers with an energy of ~15 J, strong amplifications of x-ray have been reported in the transient collisional excitation lasers for the wavelength region up to 13.9 nm [1]. In view of these progresses, employment of traveling wave pumping plays a decisive role. In this report, we describe recent our experiment in which a 6 step mirror is installed in our line-focusing system to generate a quasi-traveling wave pumping and show the result of gain-saturation of the nickel-like silver (13.9 nm) and tin (11.9 nm) x-ray lasers.

2. Experiment and result

A silver or tin slab target was irradiated by one beam of our Nd:glass CPA laser [2]. In this experiment, we installed a 6 step mirror in our line focusing system to generate a quasi-traveling wave pumping . The laser pulse consisted of two pulses (pre- and main pulses), and the pump energy was 12 J for the silver laser and 14 J for the tin laser. The irradiances of the pre-pulse and the main-pulse on target were 6.4 $\times 10^{14}$ and 4.5 $\times 10^{15}$ W/cm^2, respectively, for the silver case and 8.5 $\times$ 10^{14} and 5.3 $\times$ 10^{15} W/cm^2, respectively, for the tin case. The amplified x-ray was observed by use of a grazing incidence spectrometer with a back-illuminated CCD, in which a holographic laminar grating was used [3]. We observed amplified x-ray for various target lengths, and derived the gain coefficients. Figure 1 shows the photoelectron counts of the output of nickel-like tin x-ray laser (11.9 nm) versus the target lengths. The gain coefficient (g) and the gain length product (gl) was 30 cm^{-1} and 13.2, respectively. For the target length longer than 0.44 cm, gain-saturation behavior could be seen. The output energy and the intensity of the x-ray was 17 ± 4 μJ and 2.8 $\times$ 10^{10} W/cm^2, respectively, and this experimental intensity was consistent with theoretical prediction of gain-saturation intensity. It should be noted that the present result was the first demonstration of gain-saturation at this wavelength by use of a table-top-size pumping system.

Similar result was achieved for the silver laser at a wavelength of 13.9 nm, in which g = 35cm^{-1}, gl = 13.5, and we could observe gain-saturation behavior for target lengths longer than 0.37 cm. The output energy and the output intensity was about 25 μJ and 2.8 $\times$ 10^{10} W/cm^2, respectively.

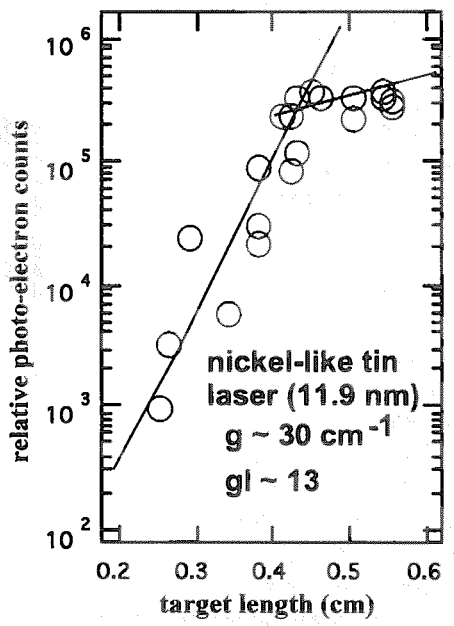

Fig. 1 Linford plot of output x-ray at 11.9 nm for various target lengths

References

1) J. Dunn, Y. Li, A.L. Osterheld, J. Nilsen, J.R. Hunter and V. N. Shlyaptsev, Phys. Rev. Lett. **84**, 4834, 2000

2) T. Kawachi *et al.*, to be published in Applied Optics.

3) M. Koike *et al.*, *SPIE vol.4146* (W.M. Kaiser and R.H. Stulen, eds.), SPIE, Washington, 163, 2000 p.163

4.2.2 Near field pattern of Ni-like Ag x-ray laser

Momoko TANAKA, Tetsuya KAWACHI, Masataka KADO, Noboru HASEGAWA,
Kouta SUKEGAWA, Keisuke NAGASHIMA, Yoshiaki KATO and Hisataka TAKENAKA[a)]

a) Optical Device Division, NTT Advanced Technology Corporation

1. Introduction

Measurement of near field pattern of x-ray gain medium is indispensable not only for various applications using x-ray lasers, but also for improving the beam quality and the peak brilliant of the x-ray laser system. Here we will report the results of near field imaging of our Ni-like Ag x-ray laser.

2. Experimental set-up

The x-ray laser was generated by use of our Nd:glass CPA laser with traveling-wave construction. The typical energy of input laser was 10 - 14 J, and the energy ratio of the pre-pulse and the pumping pulse was 1 : 5. The time separation between the pre-pulse and the pumping pulse was 1.2 ns and the pulse duration of each pulse was 4 ps. The length of the line-focusing was 6 mm and the plasma length was varied by changing the target length.

The near field imaging system was constructed with a concave mirror with curvature of 1020 mm, two planar mirrors, and a soft x-ray CCD camera. The image of the x-ray gain region was transfered at the CCD camera with magnification of 10. The mirrors were coated with molybdenum/silicon multilayers for 13.9 nm x-ray (NTT-AT). In order to eliminate visible light and attenuate the x-ray laser intensity we used 0.2 μm thick Si_3N_4 filters coated with Al or Y. Transparencies of the filters were calibrated using plasma emission of Al target.

3. Experimental results and discussion

Shown in Fig. 1 are the results of the near field imaging for the plasma lengths of (a) 1.8 mm, (b) 3.4 mm, and (c) 6.0 mm. The target surface is on the right hand side of each image and the pumping laser comes from the left hand side. As seen in the image for the plasma length of 1.8 mm, the region of x-ray emission had a round shape and was similar to that of typical plasma emission. As seen in Fig. 1(b), (c) two intense spots appeared at 30 - 50 μm distant from the target surface. Since the x-ray intensity of these areas apparently increased with increasing the plasma length, these areas correspond to the x-ray laser gain regions. The two spots were separated by 50 μm in the vertical direction at the end of plasma. The size of each spot was approximately 20 μm at FWHM and the x-ray photon densities of the two spots were almost same. The energy of the x-ray laser was estimated to be 25 μJ at the end of the plasma using Fig. 1 (c).

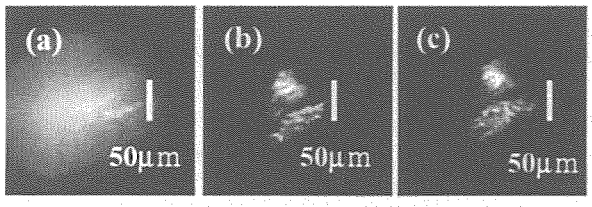

Fig. 1 Near field image of the Ni-like Ag x-ray laser with traveling-wave pumping
The length of the plasma was (a) 1.8mm, (b) 3.4mm, and (c) 6.0mm.

The present near field pattern suggests two candidates. Firstly, the propagating x-ray laser light was divided into two parts by the vertical density gradient. Secondly, the gain region consists of two parts. From Fig. 1 (b) and (c), the deflection angle in the vertical direction is less then 2 mrad. This means that the experimental results cannot be explained only by the vertical density gradient, so the gain region consists of two parts in our case.

4.2.3 High order harmonics generation for the high spatial coherent x-ray laser

Noboru HASEGAWA, Keisuke NAGASHIMA, Tetsuya KAWACHI, Shinichi NAMBA,
Kouta SUKEGAWA, Hiroyuki DAIDO and Yoshiaki KATO

1. Introduction

The transient collisional excitation (TCE) x-ray lasers have unique characteristics, such as monochromatic, high peak irradiance and short pulse duration. However the spatial coherence is not satisfactory for the applications which is required it. We proposed a method to generate highly spatial coherent x-ray laser, in which high order harmonics was used as a seed light of a laser-produced x-ray amplifier. The high-order harmonics has a high spatial coherence[1], and it is well investigated.

In this scheme, the intensity of the output x-ray is depended on the harmonic conversion efficiency (ε_n), the spectral and spatial coupling efficiencies (ε_v, ε_s) between the harmonics and the x-ray amplifier. The output x-ray intensity is written by equation (1).

$$I_{out} = I_{in}\, \varepsilon_n\, \varepsilon_v\, \varepsilon_s\, G \quad (1)$$

I_{in} is the fundamental laser intensity ($\sim 10^{15}$ W/cm^2), G ($\sim 10^5$) is the amplitude by x-ray amplifier. For this purpose we constructed a Ti;Sapphire laser system in which the central wavelength and the spectral bandwidth are tunable, and we conducted a preliminary experiment for the generation of the seed light for the spatial coherent x-ray laser.

2. Experiment and results

The x-ray lasers have a very narrow bandwidth ($d\lambda/\lambda \sim 10^{-4}$)[2] and have a few picosecond pulse duration in the case of TCE x-ray laser. We have developed the wavelength and bandwidth tunable picosecond Ti;Sapphire laser system in order to generate a seed light it has an exactly equal wavelength and has almost equal pulse duration to the x-ray laser. The central wavelength can be selected from 780 nm through 820 nm, which covers the wavelength of several x-ray lasers, such as the Ne-like titanium (32.4 nm x 25th = 810 nm), the Ni-like silver (13.9 nm x 57th = 792.3 nm) and the Ni-like tin (11.9 nm x 67th = 797.3 nm). The bandwidth is adjusted by the slit in the stretcher with an accuracy of 10^{-3}. The Ne-like Ti x-ray laser at a wavelength of 32.4 nm was taken as an example, and harmonics at the same wavelength was generated using Ar gas target under the conditions that the central wavelength of 810 nm and the pulse duration of 1 ps, incident laser intensity was 1.0×10^{15} W/cm^2, neutral gas density was 3×10^{18} cm^{-3}, focal F-number was 53, and the spectrum was integrated over 600 shots. Figure 1 is a typical spectrum of high-order harmonics. The 25th harmonics has a wavelength equal to Ne-like Ti (32.4 nm), a narrow bandwidth (0.05 nm), small beam divergence (1.8 mrad), and conversion efficiency (2.5×10^{-8}). However the bandwidth of this harmonics is equal to the resolution of this spectrometer. The high precision measurement is required. From these results, the spectral coupling efficiency is estimated to be over 0.06 and the spatial coupling efficiency is estimated to be 0.2.

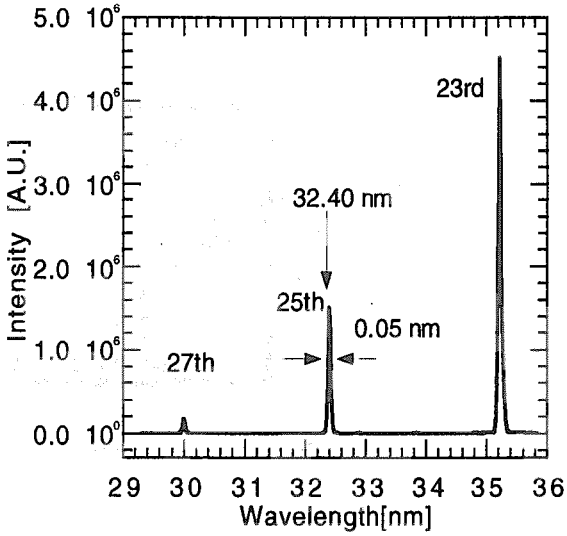

Fig. 1 A typical spectrum of high-order harmonics The 25th order harmonics was obtained and it has 32.40 nm wavelength and 0.05 nm bandwidth. The bandwidth is limited from the resolution of the spectrometer.

3. Summary

We obtained the 25th-order harmonics seed light for the Ne-like Ti x-ray laser. The characteristics of this light were investigated and it was good enough for the seed light of TCE x-ray lasers. If we use this seed light, a contrast ratio of coherent part of output x-ray to the incoherent part is calculated to be 30 and the output intensity is estimated to be 10^{11} W/cm^2, it is saturation intensity of this x-ray laser.

References

1) T. Ditmire *et al.*, Phys. Rev. Lett. 77, 4756, 1996
2) Jeffrey A. Koch *et al.*, Phy. Rev. A **50**, 1877, 1994

4.2.4 Development of frequency variable sub-picosecond laser system

Keisuke NAGASHIMA, Noboru HASEGAWA and Yoshiaki KATO

1. Introduction

Spatial coherence is an essential parameter for coherent applications of x-ray lasers. The coherence have been measured for x-ray lasers from amplified spontaneous emission (ASE) [1], which have inherently low spatial and temporal coherence. The higher order harmonics exhibit a high degree of spatial coherence if they are generated under phase matching condition. However, the conversion efficiency is relatively low and the amount of photons per pulse is not enough for some applications. Therefore, in order to produce coherent and intense x-ray lasers, higher harmonic radiation is possible to be used as a seeding pulse for amplification with x-ray laser media. This idea have been studied experimentally using Nd:glass CPA laser for generating a seeding pulse [2]. Although the experimental results showed clear demonstration of amplifying the seeding pulse, it was not successful in generating x-ray lasers enough for coherent applications.

2. Development of new laser system

The frequency variable sub-picosecond laser system have been developed using Ti:sapphire laser. The laser system consists of an oscillator, a pulse stretcher, three-stage amplifiers and a pulse compressor. The configuration of the oscillator and the pulse stretcher is shown in Fig. 1. The oscillator is a standard self-mode-locked Ti:sapphire oscillator using a prism pair for dispersion compensation in a cavity. The acousto-optical modulator is installed for obtaining stable mode-locked operation optionally. The movable slit is set in a position where the laser pulse is dispersed spatially and it control the spectral range in a cavity. The cavity frequency is 80.0 MHz and the typical output power is 300 mW. The tunable range of center wavelength is 780-820 nm and the width is about 10 nm for self-mode-locked operation. The output pulse is temporally expanded by the pulse stretcher using a holographic gating with a groove number of 2000/mm. The injection angle of the grating is adjusted to the center wavelength. The absorption filer with one-dimensional spatial variation is used to control the spectral width and the shape in the pulse stretcher. The total efficiency of the pulse stretcher is 25% when the absorption filer is removed. The commercial system (BMI industries ALPHA 10 US/B) is used to amplify the chirped pulse from the pulse stretcher. The pulse is amplified from 1 nJ to 200 mJ in a regenerative amplifier and two stage multi-pass amplifiers. The pulse is compressed to the near transform limited duration in the pulse compressor using the grating pair with the groove number same as that of the stretcher. The energy of the output pulse is 100 mJ and the pulse length is 0.5-1 ps.

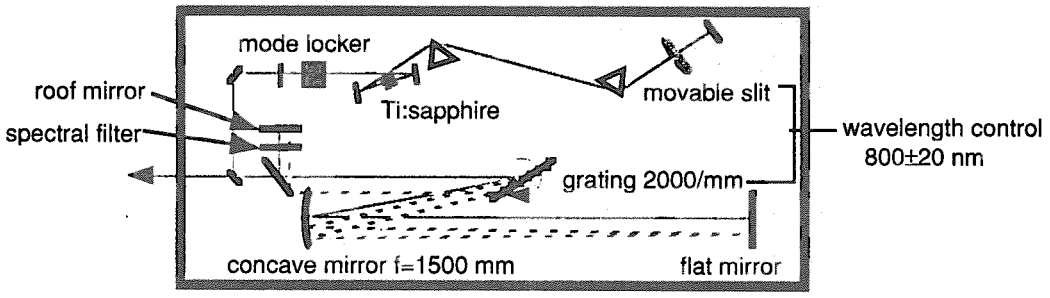

Fig. 1 Configuration of the oscillator and the pulse stretcher

References

1) J. E. Trebes *et al.*, Phys. Rev. Lett. **68**, 588, 1992
2) T. Ditmire *et al.*, Phys. Rev. A **51**, R4337, 1995

4.2.5 Charge exchange recombination x-ray laser

Shinichi NAMBA, Tetsuya KAWACHI, Keisuke NAGASHIMA, Noboru HASEGAWA,
Kouta SUKEGAWA, Momoko TANAKA, Maki KISHIMOTO and Hiroyuki DAIDO

1. Introduction

Since an electron is captured into a selected state in charge exchange recombination (CXR), this process has been considered to be one of the candidates for the realization of x-ray lasers. So far, some proposals of x-ray lasers using CXR have been made [1-4]. Chichikov *et al.* estimated theoretically a gain coefficient of x-ray laser in the high-density plasma produced by interaction of an ultrashort high-intensity pulse laser and C_{60} cluster[5]. By use of the similar method, we will attempt to demonstrate CXR x-ray laser. In particular, a CXR process between N^{7+} ions and neutral helium atoms, $N^{7+} + He \rightarrow N^{6+}(n=4) + He^{+}$, may lead to lasing actions of n=2-4 transition (9.9 nm) and n=1-4 (2.0 nm). The cross section of this process was measured to be ~1 x 10^{15} cm^2 [6]. We report the possibility of the demonstration of x-ray laser due to CXR process.

2. Calculation

A program to calculate the population densities of the excited levels of hydrogen-like ions, "COLRAD" by N.N. Ljepojevic *et al.*, was used [7]. In order to investigate the time evolution of population densities, we modified this program. The initial condition was assumed to be pure fully striped nitrogen ions.

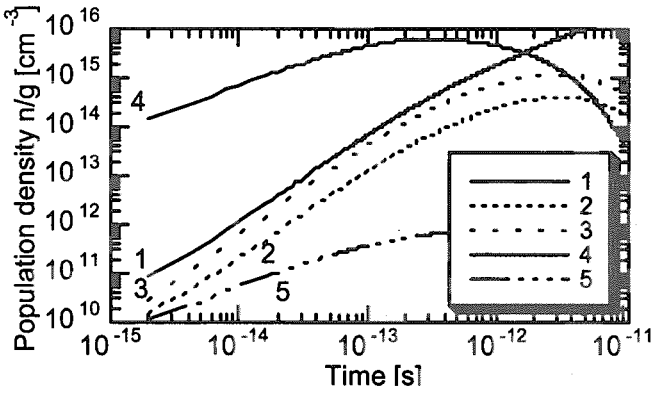

Fig. 1 Time evolution of population densities of H-like nitrogen ion

3. Results and Discussion

Figure 1 shows the time evolution of the population densities under the plasma parameters of the electron density 1 x 10^{19} cm^{-3}, temperature 40 eV, ion density 1 x 10^{19} cm^{-3}, neutral helium density 1 x 10^{18} cm^{-3}, collision velocity 1 x 10^7 cm/s. Population density of n=4 increases rapidly due to CXR process. The gain coefficient corresponding to n=1s-4p and n=2p-4d transition is shown in Fig. 2. Here, we assumed the spectral profile was Gaussian shape. Maximum gain coefficients were found to be g=6 and g=28 cm^{-1} for 1s-4p and 2p-4d, respectively. As a result of this calculation, it is likely to be able to realize the x-ray laser due to CXR process.

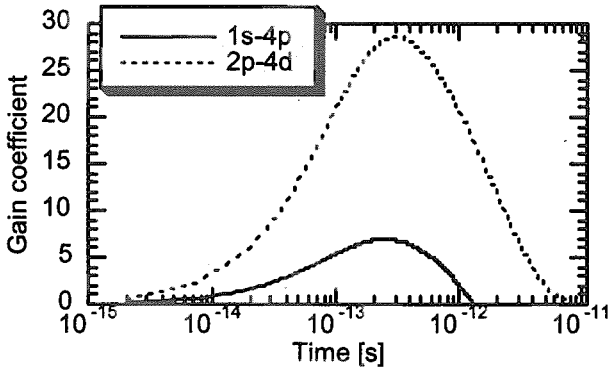

Fig. 2 Calculated gain coefficients of 1s-4p and 2p-4d transition

References

1) B. M. Smirnov, JETP Lett. **6**, 78, 1967
2) L. P. Presnyakov and V. P. Shevel'ko, JETP Lett. **13**, 203, 1971
3) M. O. Scully, W. H. Louisell and W. B. McKnight, Opt. Commun. **9**, 249, 1973
4) A. V. Vinogradov and I. I. Sobelman, Sov. Phys. JETP **36**, 1115, 1973
5) B. N. Chichikov, A. Egbert, S. Meyer, B. Wellegehausen, L. Aschke, H-J Kunze and Y. Kato, Jpn. J. Appl. Phys. **38**, 1975, 1999
6) M. Kimura, T. Iwai, Y. Kaneko, N. Kobayashi, A. Matsumoto, S. Ohtani, K. Okuno, S. Takagi and H. Tawara, J. Phys. Soc. Jpn. **53**, 2224, 1984
7) N. N. Ljepojevic, R. J. Hucheon, and J. Payne, Comput. Phys. Commun. **44**, 157, 1987

4.2.6 Absorption of ultra-short laser pulse by solid target

Kouta SUKEGAWA, Noboru HASEGAWA, Maki KISHIMOTO, Shinichi NAMBA,
Keisuke NAGASHIMA, Tetsuya KAWACHI and Hiroyuki DAIDO

1. Introduction

Absorption mechanism of ultra-short pulse laser on a material surface is important to understand the laser-matter interaction. A coupled years ago, Price *et al.* have measured incident, reflected and transmitted energies of ultra-short laser pulse on the several simple substances with an intensity from 10^{13} through 10^{18} W/cm^2. Their result showed that "universal plasma mirror" state was generated for all the materials with the intensity higher than 10^{13} W/cm^2. [1] In a viewpoint of laser-matter interaction, absorption or reflection mechanism under much lower intensity region (10^{11} ~ 10^{12} W/cm^2) has to be clarify. In the following we will report a measurement of reflectivity of aluminum in this intensity region.

2. Experiment of absorption

An experiment was performed with Ti:sapphire laser system(wavelength :800 nm, repetition ratio :10 Hz, pulse width : 55 fs). The laser pulse irradiated metal Al target. Tape-target was aluminum coated CH. Thickness is 10μm for Al, 50 μm for CH. This tape could be slid with motor in order to irradiate flesh target surface. The incident laser intensity was 10^{11}~10^{15} W/cm^2, focal spot size was 40 μm, incident angle was about 20 degree. Polarized light was S so that main process of the absorption was inverse bremsstrahlung. We measured the energy of the reflected light using a biplanar, and measured the energy of the incident light using a photodiode. Both a biplanar and a photodiode were calibrated by a calorimeter. A reflectivity was obtained from a ratio of incident and reflected light energy.

Figure 1 shows reflectivity vs. laser intensity for the experiment about aluminum. The dots show the experimental data. We used Drude model in order to analyze the experimental data. According to this model, the dielectric equation is given by

$\varepsilon/\varepsilon_0=1-\omega p^2/(\omega^2+\gamma^2)+i\gamma\omega p^2/\omega(\omega^2+\gamma^2)$,

where ωp is plasma frequency. The calculated results by this model are shown in Fig. 1. In the low intensity region, the upper line shows the calculated reflectivity change of Al film with the incident laser intensity using the reflectivity value of 90 % for the perfect surface of Al film. However the reflectivity is reduced by the oxidation of the Al film surface, so we need to consider this effect for the exact evaluation of the reflectivity. The lower line shows the reflectivity change calculated on the condition that the reflectivity of Al film used in this experiment is 65 %. From the figure, one can see the reflectivity decreases with the laser intensity in the low intensity region. On the other hand, the reflectivity increases with laser intensity in the high intensity region (above 10^{14} W/cm^2).

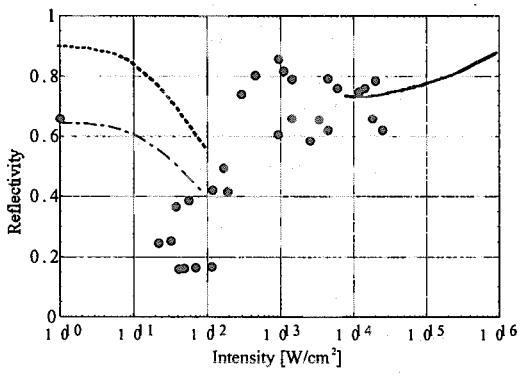

Fig. 1 Reflectivity vs. laser intensity

3. Result

We measured the reflectivity for the simple metal like Al in the middle intensity region (10^{10}~10^{12} W/cm^2). We need propose a new theoretical model for middle intensity and improve precision of experimental data. Further experiments for other materials will be carried out in the future.

Reference

1) D.F. Price *et al.*, Phys.Rev.Lett., 75(2), 252, 1995

4.3 Free-Electron Laser Development

Eisuke J. MINEHARA

1. Brief Description of FEL Group Activities

We need a powerful and efficient free-electron laser (FEL) for industrial uses, for examples, pharmacy, medical, civil engineering, shipbuilding, semiconductor industry, chemical industries, environmental sciences, space-debris orbit control, power beaming and so on[1]. In order to realize such a tunable, highly-efficient, high average power, high peak power and ultra-short pulse FEL, the JAERI FEL group have successfully demonstrated the efficient and powerful FEL driven by a compact, stand-alone and zero-boil off super-conducting rf linac without an energy-recovery geometry[2]. Because the JAERI FEL has successfully produced the world-shortest FEL pulse length of 250 fs, the highest efficiency of 6-9%, the highest peak power of 1 GW and the highest average power of >2 kW, we have first opened and originated the novel researches and applications using the femtosecond ultrashort, highly-efficient and high average power FELs[3].

Our reports and discussions on the FELs in the subsections will cover the industrial high power FELs, the JAERI compact, stand-alone and zero-boil off cryostat and operational experiences over these years[4], our discovery of the new, highly-efficient, high-power, and ultra-short pulse lasing mode, some preparatory works of the energy-recovery experiments and so on. Applications of the IRFEL and nuclear isomer studies will be included as a possible and future extension in the JAERI FEL research activities. As a typical example, we could succeed to run the system without any trouble for 355 days in 1996 Japanese fiscal year and without warming up for about 500 days from November 1999 to March 2001.

2. Strategy of Industrial FELs

Original strategy to develop the industrial FEL at JAERI and other institutions consists simply of three steps, the first of making a highly efficient and high power FEL driver using an rf superconducting technology, the second of demonstrating a powerful FEL lasing using the driver[4,5], and the third of increasing an total system efficiency using a beam-energy recovering[6]. After we recently found the new FEL lasing mode of high efficiency last year[3], I modified slightly the original, and added a new path to the old in the third step to develop and to realize the industrial FELs using the new lasing mode.

As well known in a simple theory that an FEL conversion efficiency from the beam power equals with $1/2N_w$ where N_w stands for the number of wiggler periods, it is naturally understood that the FEL efficiency will become large if N_w will become small by another novel mechanism. There have been expected to become small number of the period effectively, and efficient after the FEL saturation[7] because of some pulse-shortening mechanisms. As reported that pulse width of the new mode was measured to be a few cycle lasing of 3.4 cycle and 250 fs at 22.4 μm, the high efficiency of 6-9% is consistent with $1/2N_{cycle}$ where N_{cycle} stands for the number of cycle over the ultrashort FEL pulse width. If we can find a trick or some mechanism and succeed to realize the smaller cycle numbered lasing than the 3.4 cycle, the higher FEL efficiency from the beam power can be feasible to convert almost the whole beam power to the FEL power. For examples, a single cycle lasing of about 75 femtosecond would be expected to have 50% efficiency if the FEL efficiency could equal with $1/2N_{cycle}$. The brand-new lasing can open up new possibilities in FEL science and technology that we can drastically increase an FEL conversion efficiency, and the FEL peak and average power from the electron beam power, to realize a ultra-short and a few cycle FEL pulse, and to obtain a new knowledge in quantum optics understanding the new FEL lasing mechanism.

References

1) J. Hecht and D. Teresi, Laser, Supertool of the 1980s, Ticker & Fields, 383 Orange Street, New Heaven, Connecticut 06511, U.S.A., 1982
2) E.J.Minehara *et al.*, Nucl. Instrum. Methods Phys. Res. Sect.A**445**, 183, 2000
3) N.Nishimori *et al.*, Phys.Rev. Lett. **86**, 5707, 2001
4) E.J.Minehara *et al.*, pp159-161, in the proceedings of Particle Accelerator Conference, Dallas, 1995
5) E.J.Minehara *et al.*, Free Electron Laser Challenge 2(SPIE), **3614**, 62-71, 1999
6) G. R. Neil *et al.*, Phys. Rev. Lett. **84**, 662, 2000
7) C.A.Brau, Free-Electron Lasers, 143, Academic Press Inc., 1990

4.3.1 Demonstration of wavelength tunability of JAERI-FEL

Ryoji NAGAI, Ryoichi HAJIMA, Nobuyuki NISHIMORI, Masaru SAWAMURA,
Nobuhiro KIKUZAWA and Eisuke J. MINEHARA

1. Introduction

A free-electron laser (FEL) is a very useful light source in many applications due to its potential of high power, short pulse width and continuous wavelength tunability[1,2]. An important feature of FEL is the property of rapid and continuous tunability over a wide spectral range. The resonance wavelength of the FEL λ is given by $\lambda=\lambda_u(1+a_u2)/(2\gamma^2)$, where λ_u is the period length of the undulator field, γ is the Lorentz factor and a_u is the undulator parameter[3]. Therefore the wavelength tunability is achieved by adjustment of the electron beam energy and/or the undulator parameter.

Recently, high power, high efficiency and ultrashrot pulse generation was achieved at a superconducting rf linac based FEL in Japan Atomic Energy Research Institute (JAERI-FEL)[4,5]. In order to show the usability of JAERI-FEL for many applications, the wavelength has been varied by adjustment of the undulator parameter.

2. Experiment

Adjustment of the electron beam energy while maintaining the excellent beam quality needed for FEL oscillation is nontrivial, and involves careful adjustment of the amplitude and phase of the rf field of the linac. In contrast, the method of variation of the wavelength by adjustment of the undulator parameter dose not suffers from these limitations. This method allows rapid and continuous wavelength tunability. The undulator parameter a_u means normalized field strength of the undulator and is given by $a_u=eB_u\lambda_u/2\pi mc$, where e is the elementary electric charge, B_u is the rms magnetic field on axis, m is the rest mass of electron and c is the speed of light in vacuum[3]. The undulator is constructed from two rows of permanent magnets and magnetic poles, and the field on axis is varied by adjustment of the gap between the two rows of magnetic circuits. The movement of the undulator rows has a high mechanical accuracy in the presence of large magnetic force.

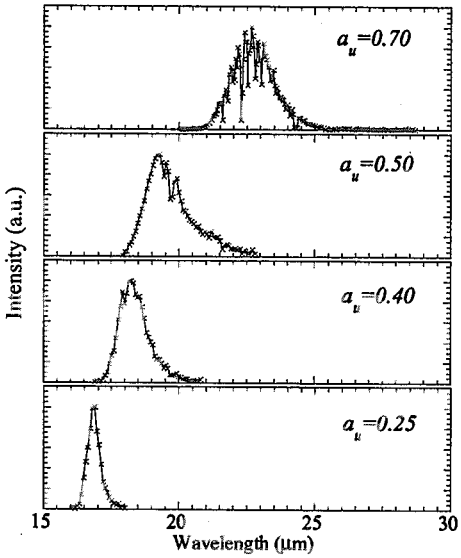

Fig. 1 The spectra of the FEL light for various undulator parameters

The variation of wavelength is demonstrated by the adjustment of the undulator parameter without any readjustment of the electron beam. The spectra of the FEL light for various undulator parameters are shown in Fig. 1. There are some dips due to the absorption in ambient water vapor. The spectral range is from 23 μm to 17 μm at the energy of 16.4 MeV. A monochromater with a HgCdTe detecter is used for the measurement of spectra of various undulator parameters. Sensitivity of the monochromater is corrected by using black-body radiation. The FEL radiation is coupled out through a 4 mm diameter center-hole in one of the mirros and extracted to the air through a KRS5 window.

3. Conclusion

The wavelength of JAERI-FEL has been rapidly and continuously varied by adjustment of the undulator parameter without any readjustment of the electron beam. The wavelength range is between 23 μm and 17 μm against the undulator parameter of between 0.70 and 0.25. The measured wavelength is in good agreement with the wavelength estimated by the undulator parameter.

References

1) E. R. Eliel *et al.*, Appl. Phys. **A60**, 113-119, 1995
2) P. C. van Son *et al.*, Nucl. Instr. and Meth. **A341**, 174-177, 1994
3) C. A. Brau, "Free-electron Lasers" Academic Press, Inc., 1990
4) E. Minehara *et al.*, Nucl. Instr. and Meth. **A445**, 183-186, 2000
5) R. Hajima *et al.*, in the Proc. of the 23rd FEL Conf.

4.3.2 Pulse width measurement of JAERI-FEL

Ryoji NAGAI, Ryoichi HAJIMA, Nobuyuki NISHIMORI, Masaru SAWAMURA,
Nobuhiro KIKUZAWA and Eisuke J. MINEHARA

1. Introduction

Extreme high efficient FEL oscillation was performed in far-infrared region at the so-called synchronism of the optical resonator by a superconducting RF linac based FEL at Japan Atomic Energy Research Institute (JAERI-FEL)[1]. At the synchronism, the round-trip time of optical pulse corresponds to the repetition of the electron beam. In usual FEL oscillation, the optical resonator length is shortened from the synchronism to compensate the laser lethargy. In short-pulse FEL, since the optical pulse width is inversely proportional to the efficiency[2], generation of ultrashort pulse is expected at JAERI-FEL. The pulse width of the FEL radiation is measured by second-order autocorrelation based on second-harmonic generation in Te crystal[3,4].

2. Experiment

The FEL radiation is coupled out through a 4 mm diameter center-hole in one of the mirros and extracted to the air through a KRS5 window. The radiation is guided via transport system in the air to the autocorrelator, which is installed near the output window in accelerator room. For minimizing distortion of the optical pulse due to absorption in ambient water vapor, the transport distance is about 3m as short as possible. Residual fundamental component after the Te crystal is blocked by ZnSe filtter. The Te crystal has a length of 2 mm. Since the Te crystal is birefringent, phase-matching is possible by fitting orientation of the crystal to phase-matching angle. Since second-harmonic conversion efficiency of the Te crystal is sufficiently high[3,4], higher harmonic signals of the FEL radiation are negligible.

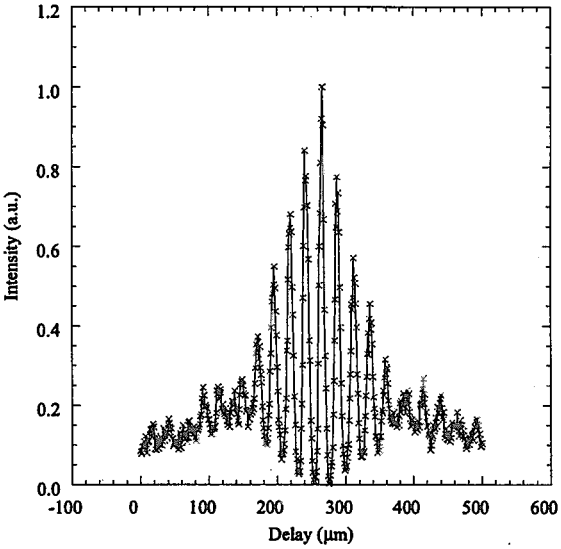

Fig. 1 Obserbed signal of the second-order autocorrelation

The observed autocorrelation signal is shown in Fig. 1. Assuming a $sech^2(t)$-pulse, the observed signal represnts an FWHM pulse width of 255 fs, which corresponds to only 3.4 optical cycles. The autocorrelation signal is averaged in the macropulse. This autocorrelation result means that a smooth single pulse is quasi-continuously generated in the macropulse. In other words, the ultrashort pulse is generated at the synchronism of the optical resonator. The FWHM of the power spectrum is estimated by the universal brightness $0.83=\eta/(\sigma\lambda/\lambda)$, where η is extraction efficiency and $\sigma\lambda/\lambda$ is rms width of the power sprectrum[5]. In this experiments, the extraction efficiency is 6 % by measurement of the electron beam energy loss. The time-bandwidth product for the estimated FWHM of the power spectrum is 0.60. The time-bandwidth product for an ideal $sech^2(t)$-pulse is 0.32 [6]. The pulse width is consistent with the extraction efficiency.

3. Conclusion

An intense ultrashort pulse has been quasi-continuously generated at the synchronism of the optical resonator in JAERI-FEL. Second-order autocorrelation measurements show that the FWHM pulse width is 255 fs, which corresponds with 3.4 optical cycles, at wavelength of 22.5 μm.

References

1) N. Nishimori *et al.*, Phys. Rev. Lett. **86**, 5707-5710, 2001
2) N. Piovella *et al.*, Phys. Rev. E **52**, 5470-5486, 1995
3) C. K. N. Patel, Phys. Rev. Lett. **15**, 1027-1030, 1965
4) G. H. Sherman and P. Coleman, IEEE J. Quantum Electron. QE-7 11971) 403-409.
5) D. A. Jaroszynski *et al.*, Phys. Rev. Lett. **78**, 1699-1702, 1997
6) K. L. Sala *et al.*, IEEE J. Quantum Electron. QE-16, 990-996, 1980

4.3.3 Linear and nonlinear harmonic generation in an FEL oscillator

Ryoichi HAJIMA, Ryoji NAGAI and Eisuke J. MINEHARA

1. Introduction

In JAERI-FEL, we have achieved high-power lasing at wavelength between 16 and 23 μm. Operation of the FEL in a broader wavelength range is preferable to use the FEL for various applications. Lasing around 7 μm is especially useful, because there is a strong absorption of human tissue applicable to laser surgery. We made experiments of harmonic generation of JAERI-FEL based on both linear and nonlinear methods.

2. Linear harmonic generation

The linear harmonic generation is lasing at a harmonic of fundamental wavelength driven by electrons micro-bunching of the same harmonic wavelength. In the linear harmonic generation, we must suppress the fundamental lasing, which has the maximum FEL gain. We prepared two type of optical cavity mirrors tuned to the 3rd harmonics, a dielectric multi-layer mirror of Zn-Se and a super-enhanced gold-coated copper mirror (SEG mirror) [1]. We obtained the 3rd harmonic lasing with the Zn-Se mirror and the 2nd and the 3rd harmonics with the SEG mirror. Figure 1 is a cavity-length detuning curve for the 3rd harmonic lasing at 7.2 μm with the Zn-Se mirror. The average power of the linear harmonic lasing was 60 W.

3. Nonlinear harmonic generation

The nonlinear harmonic generation is lasing at a harmonic driven by deeply saturated fundamental field. This type of lasing has been studied for a SASE FEL and is considered as one of the candidates realizing VUV and X-ray FEL [2]. The nonlinear harmonic generation also occurs in an FEL oscillator, if the oscillator is operated deeply saturated, superradiant or spiking-mode regime. In JAERI-FEL, we measured the 3rd harmonic component parasitically generated with the fundamental and compared with a numerical simulation based on a 1-D time dependent FEL simulation. Figure 2 shows measured and calculated fraction of the 3rd harmonic as a function of cavity-length detuning. It can be seen that the 3rd harmonic is enhanced for small-detuning regime. The fraction of the 3rd harmonic is 0.5% at zero-detuning in the experiment, which corresponds to several watts in average power.

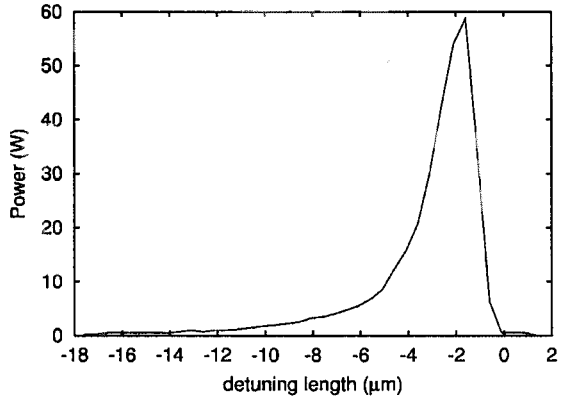

Fig. 1 Cavity-length detuning curve for linear harmonic generation at 7.2 μm

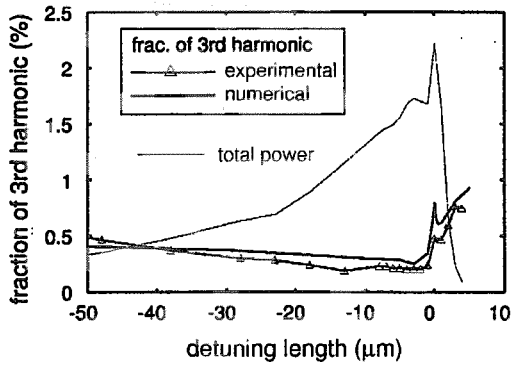

Fig. 2 Measured fraction of 3rd harmonic power and total power as a function of cavity-length detuning
A result from numerical simulation is also plotted.

References

1) R. Hajima *et al.*, Nucl. Instr. and Meth. in press.
2) Z. Huang and K-J. Kim, Phys. Rev. E62, 7295, 2000

4.3.4 Nucleosynthesis of heavy element by the photonuclear reaction

Takehito HAYAKAWA, Toshiyuki SHIZUMA, Toshihiko YAMAUCHI,
Eisuke J. MINEHARA and Takashi ARISAWA

1. Introduction

Nucleosynthesis of heavy elements is important for understanding the site mechanism in the stellar and cosmochronology [1]. The nuclei heavier than iron have been mainly synthesized by the neutron capture (n, γ) reaction, which are called to be the r- and the s-processes, in the stellar. The nuclei produced by the s-process are located at the center of stability line. It has recently been discussed the s-process in thermally pulsing stars on the asymptotic giant branch. On the other hand, the isotopes have also been produced by the β-decay after the r-process, which have been considered to be happened in the Type II supernovae explosion. In the proton rich side, many isolated even-even stable isotopes exist in the outside of the s-process path and are shielded from the β^- decay chain of post r-process. These p-nuclei have been considered to be produced by the EC/β^+ decay after the proton capture process. However, the production mechanism for p-nuclei has recently been proposed to be photodisintegration by (γ, n) reaction in the Type II supernovae [2-4]. In order to search the contribution of these processes, the analysis has been carried out.

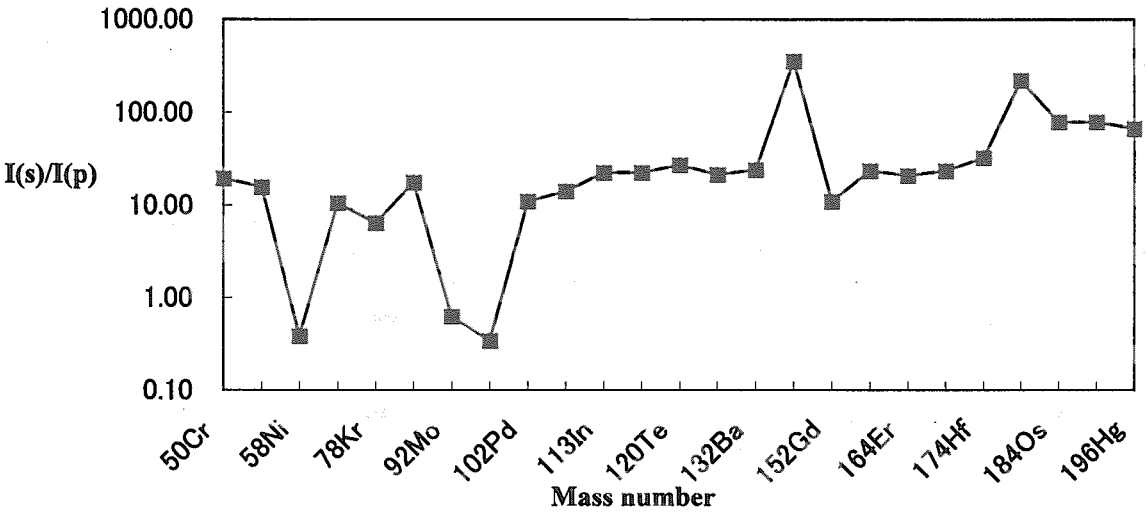

Fig. 1 The ratio between s- and p-nuclei is plotted.

2. Discussion

The ratio between s- and p-nuclei is plotted in the Fig. 1. It should be noted that the ratio of I(s)/I(p) is constant of about 22 in the region from A=50 to 180 except for some large valleys and peaks. There is some theoretical approach, and it is indicated that the Kr, Mo and Ru isotopes could not be explained by the γ-process. While, it is easy to explain for two big peaks of the Ce and W isotopes. The s-nuclei (N) is not shielded for the post r-process and combined of the β^- decay after the r-process.

3. Experimental plan

The experimental technique for the production of p-nuclei by photonuclear reaction using the photon sources has recently been developed. In order to investigate the systematics of the ratio of p- and s-process in wide mass region. The experiment using the activation technique after photon irradiation should be proposed. The stacked targets of some metals will be irradiated by the high energy γ-ray. The lightest s-process isotopes will be changed to the β unstable nuclei by the (γ, n) photonuclear reaction. After the photon irradiation, the γ-rays after the β decay of the target will be measured with one Ge detector.

References

1) M. Arnould and T. Takahashi, Rep. Prog. Phys. **61**, 395, 1999
2) W. Michael *et al.*, Astro. Jou. **373**, L5, 1991
3) P. Mohr *et al.*, Phys. Lett. B **488**, 127, 2000
4) K. Vogt *et al.*, Phys. Rev. C**63**, 055802-1, 2001

4.3.5 New candidates for nuclear isomer targets

Toshiyuki SHIZUMA, Takehito HAYAKAWA, Toshihiko YAMAUCHI,
Eisuke J. MINEHARA and Takashi ARISAWA

1. Introduction

Long-lived nuclear isomers have received much attention due to their potential usage as a storage medium of nuclear energy that may be prompt-released by irradiation of photons. One such example is the $T_{1/2}$=31-yr 16^+ state in ^{178}Hf; *the longest-lived high-spin isomer.* The decay scheme is shown in Fig. 1. The accelerated decay of this isomer by photons was first reported by Collins *et al*[1]. They used bremsstrahlung beams generated by a dental X-ray device. The endpoint energy of the bremsstrahlung photon spectrum was as low as 60 keV, peaked around 30 keV. The integrated cross section was measured as 1×10^{-21} cm^{2}keV. Recently, a similar experiment was performed by an LLNL-LANL-ANL group using synchrotron radiation derived from an undulator insertion device at the Advanced Photon Source in the Argonne National Laboratory[2]. Although they used incident beams with intensities that were over 4 orders of magnitude than those used in Ref. 1), the results show no signal to the accelerated isomeric decay.

However, one might extend the possibilities of this kind of experiment by using other long-lived isomers.

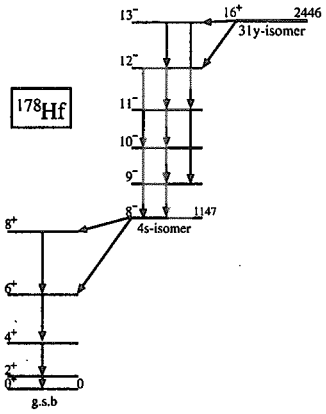

Fig. 1 A decay scheme of the 31-yr 16^+ isomer in ^{178}Hf

2. Estimation

Table 1 summarizes candidates for long-lived nuclear isomers that can be produced by neutron-capture reactions. While the isomers have half-lives of orders of year, the ground states should have much shorter half-lives. This condition is necessary to decrease the activities after appropriate time so that the irradiated materials can be safely handled. In the estimation of the production rates of isomers, we assumed neutron flux of I=1x10^{14} photons/cm^2/s and irradiation time of T^{irad}=1 year.

Table 1 Candidates of long-lived nuclear isomers and their production rates in neutron capture reaction

Nuclei		Spin/parity	$T_{1/2}$	Neutron capture cross sections (b)	Production rates[a] (%)
^{108}Ag	g.s.	1^-	142s	39	
	isomer	6^+	418y	0.33	0.1
^{166}Ho	g.s.	0^-	27h	61	
	isomer	(7^-)	1200y	3.5	1.1
^{186}Re	g.s.	1^-	91h	112	
	isomer	(8^+)	2x10^{5}y	1-0.1	0.01-0.1
^{192}Ir	g.s.	$4^{(+)}$	74d	309	
	isomer	(9)	241y	0.16	0.05
^{210}Bi	g.s.	1^-	5d	0.034	
	isomer	9^-	3x10^{6}y	0.0096	0.003

a) Ratios of isomers to the total sample.

3. Discussion

Among the candidates listed above in Table 1, the ^{186}Re isomer is most promising as an isomer target due to its very long half-life and the relatively large neutron capture cross section. Prior to the irradiation, we plan to investigate the nuclear structure of ^{186}Re for confirming its spin and parity, and measure the neutron- capture cross section of ^{185}Re(n,γ)^{186m}Re.

References

1) C.B. Collins *et al.*, Phys. Rev. Lett. **82**, 695, 1999
2) I. Ahmad *et al.*, Phys. Rev. Lett. **87**, 072503, 2001

4.3.6 Demonstration of sustained lasing in an FEL oscillator at perfect synchronism of an optical cavity

Nobuyuki NISHIMORI, Ryoichi HAJIMA, Ryoji NAGAI and Eisuke J. MINEHARA

1. Introduction

In Free Electron Laser (FEL) oscillators, optical cavity shortening from perfect synchronism is required to compensate the ``laser lethargy", which is a phenomenon that FEL optical group velocity becomes somewhat slower than speed of light in vacuum because there is no gain at the beginning of FEL interaction[1]. The perfect synchronism is the cavity length, where the cavity round-trip time for vacuum speed of light equals the injection period of electron bunches. Extraction efficiency from electron beam power to FEL radiation depends on the cavity shortening from the perfect synchronism and becomes maximum at the detuning length (δL) slightly shorter than $\delta L = 0$. At the perfect synchronism of FEL oscillators, the optical pulse centroid is retarded on successive passes and the optical pulses finally dissipate. Only a transient state therefore exists at the perfect synchronism. This transient evolution of the optical pulses at $\delta L = 0$ is supported by numerical and analytical studies[1,2].

Recently a high extraction efficiency was demonstrated in the JAERI-FEL oscillator[3]. The efficiency detuning curve obtained was well reproduced by our numerical simulation[4], which indicates that the efficiency is maximum at the perfect synchronism and the lasing is sustained. However, no measurement has been made at FEL oscillators with enough accuracy to claim the lasing at $\delta L = 0$. For an experimental confirmation of the lasing at $\delta L = 0$, we made a simultaneous measurement of FEL power and absolute detuning length.

2. Experiments and results

The absolute detuning length was measured with a mode-locked Ti:sapphire laser (Tsunami 3960, Spectra-Physics) synchronized with the frequency of 83.30000 MHz, which is the eighth harmonic of the electron bunch repetition rate. The experimental results exhibit a clear resonance peak as shown in Fig. 1. The FEL light was also coupled out by a gold-coated scraper mirror, simultaneously. The experimental data are plotted as open-circles in Fig. 1. For the calibration from the FEL power to the efficiency, we measured average energy loss of the electron beam over an entire macropulse. As shown in Fig. 1, the peak of the FEL efficiency curve coincides with the resonance peak of the Ti:sapphire signal within the accuracy of 0.1 μm. This is the first demonstration of sustained saturation at the perfect synchronism[5]. The physical mechanism of the lasing at the perfect synchronism is under investigation.

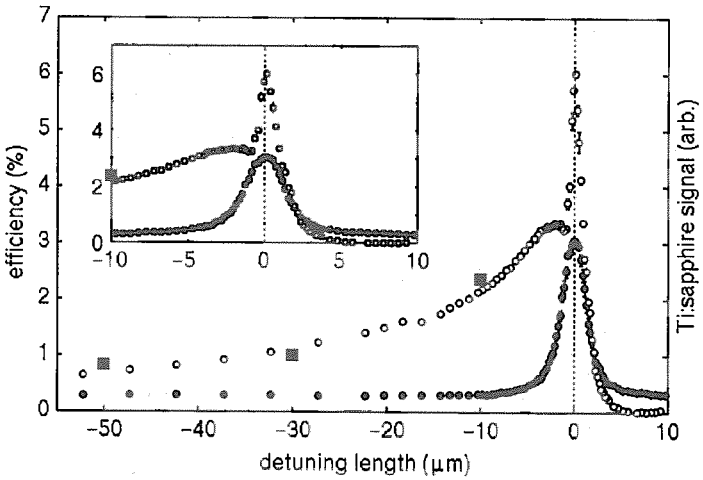

Fig. 1 FEL efficiencies (open-circles) and Ti:sapphire signals (solid-circles) as a function of detuning length

The enlargement around $\delta L = 0$ μm is also shown. The symbols without error-bars have error less than their size. The absolute vertical scale was calibrated by average energy loss of the electron beam over an entire macropulse (solid-squares) at several detuning lengths.

References

1) W.B. Colson, in Laser Handbook, edited by W.B. Colson, C. Pellegrini, and A. Renieri (North Holland, Amsterdam, 1990), **6**, 176-180
2) Nicola Piovella, Phys. Rev. E **51**, 5147, 1995
3) N. Nishimori *et al.*, in Proc. of the 22nd FEL Conf., 2000 (to be published in NIM A)
4) R. Hajima *et al.*, in Proc. of the 22nd FEL Conf., 2000 (to be published in NIM A)
5) N. Nishimori, R. Hajima, R. Nagai, and E.J. Minehara, Phys. Rev. Lett. **86**, 5707, 2001

4.4 Optics research and development

Novel Optics Research Group

Masato KOIKE, Osamu YODA, Akira SUGIYAMA, Masahiko ISHINO,
Hiroyasu FUKUYAMA, Kazuo SANO[a)] and Naoji MORIYA[b)]

a) Shimadzu Scientific Research Inc.

b) Shimadzu Corporation

1. Introduction

Development of advanced lasers such as the T-cube laser and soft X-ray laser requires novel optics including laser crystals, multi-layered mirrors, and diffraction gratings in addition to development of laser oscillation technology. The efforts of the Novel optics research group are devoted to the research and development on optical components, optical systems, and basic technologies for development and application of the advanced lasers and other soft X-ray state-of-arts sources.

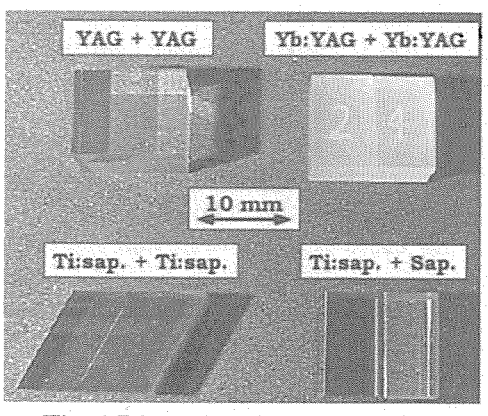

Fig. 1 Direct-bonded laser optics

2. Achievements

From the first success of our own developed direct bonding technique in Ti:sapphire laser crystals, further attempts were done in different kinds of laser crystals to realize new and admirable optical devices for high power lasers (Fig. 1). We also made optical quality measurements of the bonded crystals and revealed that the optical inferiority caused by distortion at the bonded interface is fractional and negligible.

High-resolution TEM image of Mo/Si multilayer shows that the Mo layers are polycrystalline and the Si layers are amorphous (Fig. 2). In addition, mixed-layers are formed at the interface of Mo and Si layers and the thickness of the mixed-layer at the Mo-on-Si interface is thicker than that at the Si-on-Mo interface. We have analyzed quantitatively the multilayer structure by using a four-layer model based on the TEM observations.

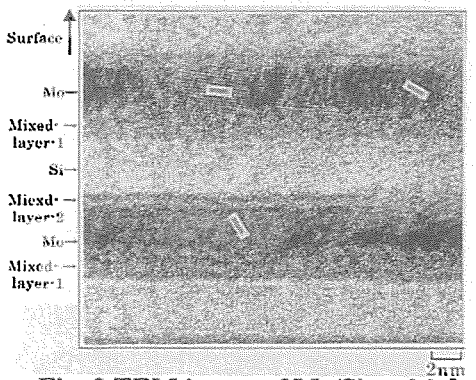

Fig. 2 TEM image of Mo/Si multiplayer optical elements

An evaluation system capable of measuring the wavelength and angler characteristics of the absolute reflectivity (or diffraction efficiency) of soft X-ray optical elements has been designed and constructed. The system was installed on a beamline (BL-11) of the AURORA, a superconducting compact storage ring, at the Synchrotron Radiation Center, Ritsumeikan University. To cover a wavelength range of 0.5 nm $< \lambda <$ 25 nm, this system incorporates conventional and surface-normal-rotation (SNR) types of Monk-Gillieson monochromators (Fig. 3). The SNR MG monochromator in this evaluation system would play a key role in bridging the gap between the grating monochromator and the crystal monochromator in the energy region of 1-2 keV.

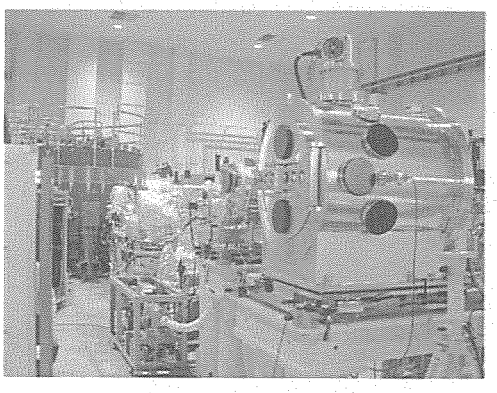

Fig. 3 New evaluation system for soft X-ray optical elements

4.4.1 Optical evaluations of direct bonded laser crystals

Akira SUGIYAMA

1. Introduction

New fabrication technique for laser crystals enlargement and enhancement of their performance has been much in demand to realize high power lasers with high repetition rate pulse generation in high efficiency. To establish the new fabrication technique, we have studied the direct bonding technique that can integrate commercially available small crystals without any adhesives. Here, we show some recent results of optical quality measurements in the evaluation for the bonded laser crystals.

2. Experimental results

Optical quality of the bonded crystal is affected by the distorted bonded interface. Therefore, we focused on the measurement of fractional signals derived from the distortion by means of two different optical methods, a transmitted wavefront measurement and a micro defect measurement.

The first measurement was carried out by a Fizeau interferometer (Zygo: GPI-XP). To devise accurate measurements with the system, the bonded crystal was located on the narrow space between transmission and reference flat mirrors to reduce the interference fringe motion by the fluctuation of airflow. Since the measured wavefront data in this system implies the roughness of the polished surfaces and distortion of the bonded region as well as inhomogeneity inside the specimen, other single crystals, having the same surface flatness of over 0.1 λ at 633 nm on both Brewster's ends and a different length of 8 mm and 18 mm, were also measured to estimate the crystal inhomogeneity. The transmitted wavefront of the bonded crystal was estimated to be 0.152 λ at 633 nm from this measurement (Fig. 1). The estimated inhomogeneity was 0.037 λ/cm at 633 nm from the measurements of the other crystals, and it was assumed that the transmitted wavefront of the single crystal having with the same length as the bonded one is 0.121 λ at 633 nm. As a result, the wavefront distortion by the bonded region was estimated to be 0.031 λ at 633 nm[1, 2].

The second measurement was done by a laser tomography system (Mitsui: MO-421). The system consists of an optical unit and a data analyzer. In the optical unit, the bonded specimen located on a 3-D translation stage was irradiated by a probe laser of the 2nd harmonic of CW Nd:YAG. The focused probe laser beam on the specimen was about 10ìm in diameter. Optical scattering signals generated from defects inside the specimen were vertically detected by a CCD camera through an optical microscope.

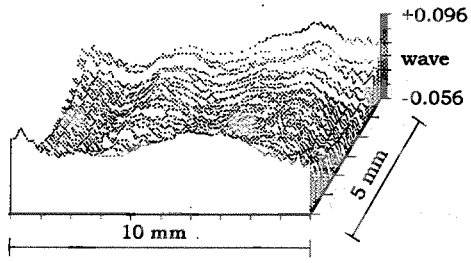

Fig. 1 Transmitted wavefront pattern

Detection of the signal was synchronized with the step motion in X-direction of the stage and each set of data was transferred to the data analyzer where the whole image of micro defects within a viewing area is framed from the stored data[3]. In Fig. 2, small spots appearing horizontally inside the oval shows the micro defects existing on the bonded surface, and the other spots spread through the whole image were intrinsic defects formed in the crystal growth. It can be seen that the number of micro defects on the bonded surface are much smaller than that of the intrinsic ones, which indicates that the optical loss at the bonded region of specimen is insignificant and the direct bonded crystal is applicable for laser oscillation[4, 5].

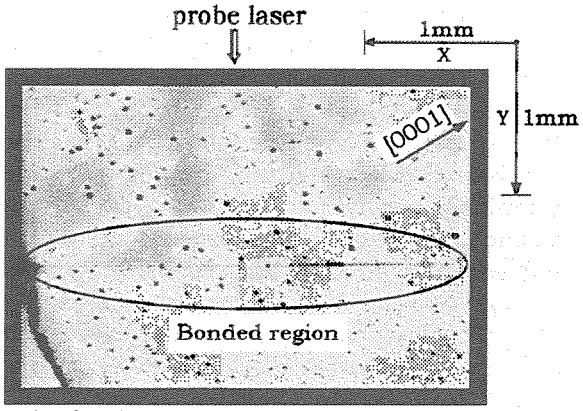

Fig. 2 Micro defects around the bonded region

References

1) A. Sugiyama, H. Fukuyama, M. Katsurayama and Y. Anzai, Proc. IEEJ, OQD-00-50, October 12, 2000
2) A. Sugiyama, H. Fukuyama, Y. Kataoka, A. Nishimura and Y. Okada, Proc. SPIE, 4231, 261, 2000
3) H. Fukuyama and A. Sugiyama, JAERI-Tech 2000-058, 1, 2000
4) A. Sugiyama, H. Fukuyama, Y. Kataoka and Y. Okada, JAERI-Conf 2001-011, 216, 2001
5) A. Sugiyama, H. Fukuyama, Y. Kataoka and Y. Okada, CLEO/PRIM2001, WH3-3, July 18, 2001

4.4.2 Evaluation of Mo/Si multilayer structures

Masahiko ISHINO and Osamu YODA

1. Introduction

The Mo/Si multilayers give a high reflectivity of soft X-rays at the wavelengths around 13nm even at the near normal incidence angles. Optical devices based on Mo/Si multilayers have been applied to Schwarzschild objectives for a soft X-ray microscope, a transmission polarizer for an X-ray ellipsometer, masks for an extreme ultraviolet lithography and so on. Optical properties of multilayer mirrors depend strongly not only on the optical constants of materials but also on the roughness of interfaces and the structure of layer boundaries. It is found that Mo layers are polycrystalline and the Mo(110) plane is textured, while Si layers are amorphous. It is known that the mixed-layers are formed at the interfaces of Mo and Si layers during multilayer fabrication. The aim of this study is to evaluate quantitatively the multilayer structure so as to fabricate the multilayer having high performance.

2. Experimental

Mo/Si multilayers were fabricated on Si wafers by means of the ion beam sputtering method[1]. X-ray scatterings including wide angle X-ray diffraction and X-ray reflectivity were measured using a high resolution X-ray diffractometer (Rigaku SLX-2000) with CuKα_1. For the evaluation of layer thickness, density and rms roughness, an X-ray reflectivity simulation/fitting program (Rigaku RGXR) was used with a four-layer model based on the TEM observations.

3. Results

Figure 1 shows the crystallite size of Mo as a function of the designed thickness of Mo layer. When the Mo layer thickness is below 8 nm, the crystallite size coincides with the Mo layer thickness. On the other hand, when the Mo layer thickness becomes larger than 8 nm, the crystallite size deviates from the layer thickness and saturates at about 10nm. Figure 2 shows the relation between the designed and calculated thickness of the Si layer. The simulated thickness of the Mo layer is equal to the designed thickness, while the thickness of Si layer is smaller than the designed one. The result of simulation is consistent with the fact that the Mo crystallite size agrees with the Mo layer thickness. In addition, this result shows that the mixed-layer is formed in the Si layer and the thickness is about 1.4nm. The simulation result reveals that densities of Mo and Si layer are slightly smaller than bulk ones and those of mixed-layers are intermediate of pure layers. The simulated rms roughness is found to be dispersed around the surface roughness of the Si substrate (= 0.3 nm).

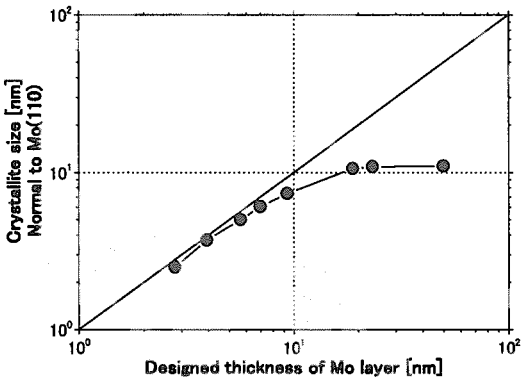

Fig. 1 Relation between the Mo(110) crystallite size and the Mo layer thickness

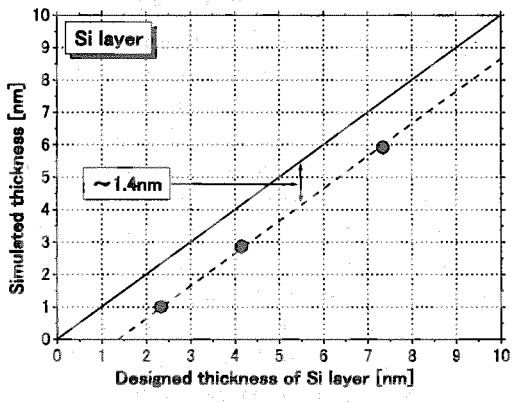

Fig. 2 Relation between the designed and the simulated thicknesses of the Si layer

Reference

1) A. Ulyanenkov, R. Matsuo, K. Omote, K. Inaba, J. Harada, M. Ishino, M. Nishii and O. Yoda, J. Appl. Phys. **87**, 7255, 2000

4.4.3 New evaluation beamline for soft X-ray optical elements

Masato KOIKE, Kazuo SANO[a)], Osamu YODA, Yoshihisa HARADA[b)], Masahiko ISHINO, Naoji MORIYA[b)], Hiroyuki SASAI[b)], Masafumi JINNO[b)], Yoshihiro UENO[b)] and Takeshi NAMIOKA[c)]

a) Shimadzu Scientific Research Inc.

b) Shimadzu Corp.

c) Tohoku University

1. Introduction

There has been a pressing need in the Japanese soft-x-ray optics community for a dedicated evaluation facility capable of characterizing state-of-the-art soft-x-ray optical elements, such as advanced gratings, soft-x-ray multilayer elements, etc. To meet the need we have designed evaluation beamline optics on the basis of a theory specifically developed for the purpose and an end station for measuring optical characteristics of soft-x-ray optical elements. We have constructed the system thus designed and installed on a beamline of the AURORA, a superconducting compact storage ring, at the Synchrotron Radiation Center of Ritsumeikan University in Kusatsu, Japan. To cover a wavelength range of 50-1000 eV, this system has two types of grazing incidence Monk-Gillieson(MG) monochromators; one is a conventional type having a varied-line-spacing(VLS) grating and two deviation angles and the other is a type having a scanning mechanism based on surface normal rotation(SNR) of the grating. The outline of the system is described together with the result of crosscheck measurements of typical samples made on the standard and calibration beamline of the Advanced Light Source (ALS) at Lawrence Berkeley National Laboratory,

2. Instrumentation

The evaluation beamline consists of three systems: (1) prefocus system, (2) monochromator system, and (3) reflectometer system (see Fig. 1). The overall length of the beamline (the source point S-to-the end station GO) is about 10.5 m.

The prefocus system comprises beam-shaping apertures, focusing mirrors, and filters. The light beam from the source point S goes through the front end and reaches to the two sets of mutually perpendicular beam-shaping apertures A. Then, the light beam is focused on the entrance slit S1 horizontally by the spherical mirror M1 and vertically by the spherical mirror M2. Tandem two filter-wheels F located in front of the entrance slit S1 hold 2 × 5 filters in total.

The monochromator system is the most unique component of the beamline and consists of two types of MG monochromators. One is a conventional MG monochromator equipped with three laminar-type VLS holographic gratings[1)] G1 (300 lines/mm), G2 (600 lines/mm), and G3 (1200 lines/mm). These gratings are used interchangeably at an included angle of either 176° or 172°,[2)] depending on a required scanning range. One particular included angle is easily selected by inserting the vertical focusing spherical mirror M3 or M5 into the beam at an angle of incidence of 88° or 86°

The other monochromator is a MG monochromator that operates in the SNR scanning mode[3)]. In this mode the vertical focusing spherical mirror M4 is inserted into the beam at an angle of incidence of 88°. The convergent beam reflected from M4 impinges on the surface of a conventional plane grating G4 (1200 llines/mm), which is used at an included angle of 176°. This SNR MG monochromator covers a wavelength range of about 0.5-2 nm. The theoretical detail of this monochromator is described in Ref. 4.

To monitor the flux stability and to aid optical alignment, an Au-mesh beam intensity monitor MN can be inserted between the gratings and the exit slit S2. The monochromatized beam emerging from S2 is focused onto a sample placed in the goniometer GO by the toroidal mirror M6. Another toroidal mirror M7 can also be used when an end station is connected the GO chamber in tandem.

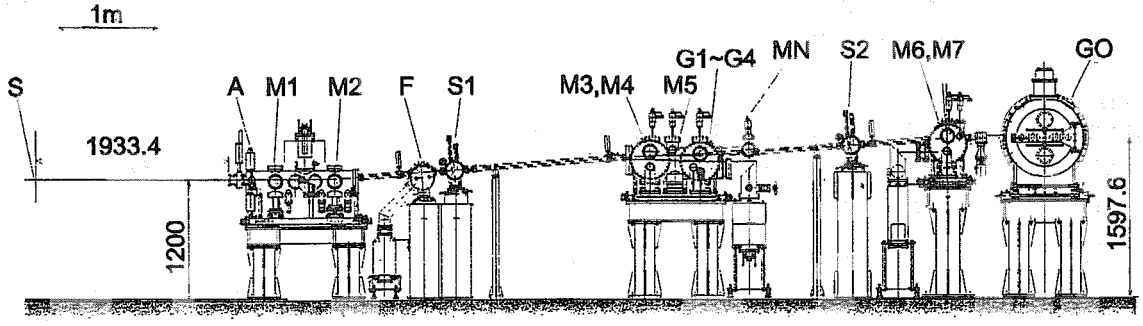

Fig. 1 Side view of the evaluation beamline

The reflectometer system consists of a modified θ-2θ reflectometer/diffractometer. The sample stage (θ-stage) of GO accommodates a sample of up to 254 mm × 254 mm, and the sample surface can be scanned by a spot of ~1 × 2 mm^2 by an *X-Y* sample translation mechanism. The reflected (or diffracted) beam from the sample is detected by a Si or GaAsP detector mounted on the 2θ-arm. The θ-stage and 2θ-arm can also be controlled independently when needed.

3. Reflectance of a Mo/Si multilayer mirror

The performance of the evaluation system for SXR optical elements has been evaluated in the course of test run. This has been done by measuring the reflectivity of a Mo/Si multilayer at around 14 nm.

The measurement on the multilayer was made in the conventional Monk Gillieson monochromator mode with G1 (300 lines/mm) and M5 (included angle of 172°). The results were compared with the data obtained at the ALS using the standard and calibration beamline (BL 6.3.2)[5] whose monochromator is of the conventional Monk-Gillieson type with a ruled master grating of 300 lines/mm at an included angle of 172°.[2]

The multilayer data thus obtained at the two facilities are compared in Fig. 2, where the solid curve and the open circles indicate the data of the ALS and Ritsumeikan, respectively. This shows the reflectivity of a Mo/Si-multilayer mirror measured at an angle of incidence of 5°. The mulitlayer used for the evaluation was deposited at NTT Advanced Technology Co. and has a period of 6.39 nm, a value of 0.4 for Mo-layer thickness/period, and 40 layer pairs. To suppress the effect of overlapping higher orders, a Si filter was used at both facilities, and a 3-mirror reflector was also used at the ALS.[5] It is clearly seen in the figure that both the data taken independently coincide with each other.

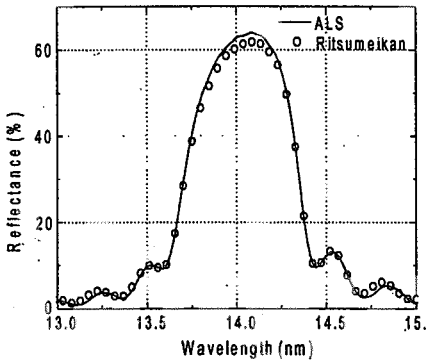

Fig. 2 Reflectance of a Mo/Si multilayer mirror at an angle of incidence of 5°

The absolute diffraction efficiencies were measured on a laminar-type master holographic grating (HG). The holographic grating was for the SXR flat-field spectrograph.[6] This grating is Au-coated and has an effective groove density of 1200 lines/mm. HG has a radius of curvature of 5409 mm and a duty ratio (ratio of the land-width to the period) of 0.32 measured at its center. The measurements were performed at a fixed angle of incidence of 87° over a range of ~4-18 nm so as to conform to the design of the flat-field spectrograph.

Figure 3 shows the absolute diffraction efficiency curves. The solid lines with the letter R indicate the data obtained at the Ritsumeikan and the dotted lines with A show those at the ALS. In the figure, *m* is the spectral order. The efficiencies of the holographic grating HG measured at the two facilities well coincide with each other.

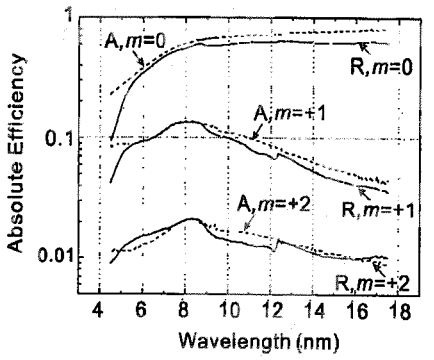

Fig. 3 Absolute diffraction efficiencies of a laminar-type master holographic grating

All the data acquired up to now support the reliability of the evaluation system installed at the BL-11 at the Synchrotron Radiation Center, Ritsumeikan University.

The authors to thank Dr. Hisataka Takenaka at Optical Device Division, NTT Advanced Technology Co. for providing a Mo/Si multilayered mirror and its data measured at the ALS necessary for the present study.

References

1) M. Koike, T. Namioka, Appl. Opt. **36**, 6308, 1997.
2) M. Koike, T. Namioka, J. Electron Spectroscopy and Related Phenomena, **80**, 303, 1996.
3) M. C. Hettrick, Appl. Opt. **31**, 7174 ,1992.
4) M. Koike, T. Namioka, to be published in Appl. Opt.
5) J.H. Underwood, E. M. Gullikson, M. Koike, P. C. Batson, Proc. SPIE **3113**, 214, 1997.
6) M. Koike, T. Namioka, E. Gullikson, Y. Haradad, S. Ishikawab, T. Imazono, S. Mrowka, N. Miyata, M. Yanagihara, J. H. Underwood, K. Sano, T. Ogiwara, O. Yoda, S. Nagai, Proc. SPIE, 4146,163, 2000.

4.5 Laser Driven Particle Acceleration Development

Laser Acceleration Research Group

Masaki KANDO, Hideyuki KOTAKI, Tomonao HOSOKAI[a)], Shuji KONDO, Shinichi MASUDA, Takashi YOKOYAMA, Shuhei KANAZAWA, Tohru MATOBA and Kazuhisa NAKAJIMA[b)]

a) Nuclear Engineering Research Laboratory, The University of Tokyo

b) JAERI Kansai and High Energy Accelerator Research Organization (KEK)

1. Introduction

The main purpose of Laser Acceleration Research Group is to perform a proof-of-principle experiment of laser wakefield acceleration (LWFA) that has a maximum energy gain of 1 GeV with improved energy spectrum. Two major problems must be overcome to accomplish the goal. One is beam matching to wakefields transversely and longitudinally. The other is extension of acceleration length that is limited to diffraction length in order to obtain high energy gain in single stage of LWFA. We have developed an photocathode radio frequency gun as an electron source and microtron accelerator as a compact energy booster as a high quality beam injector in order to achieve transverse beam matching. The combination of these two components is the first case in the world. To check the beam quality, beam characterization was performed and the details of the measurements are described in Sect. 4.5.1. As for the longitudinal beam matching, we are considering inverse free-electron laser (IFEL) technique to produce a femotosecond electron pulse. To extend the acceleration length, we are developing a plasma waveguide that is formed by a fast Z-pinch initiated by a discharge in a gas-filled capillary. We succeeded in guiding a 1TW laser pulse in a 2 cm long capillary in 1999. We are now developing 10 cm waveguide and the result is described in Sect. 4.5.2. A gas jet will be used as a gas source to generate a density of 10^{17}-10^{18} cm^{-3} plasma. We measured a gas density from the gas jet by Mach-Zehnder interferometer. This work is described in Sect. 4.5.3. We should install new components in the experimental room and the schematic of the experimental system is shown in Fig. 1. A 100 TW laser transport system has been partly installed in the experimental room (see Sect.4.1). We should extend an electron beam transport (BT) line for the LWFA experiment. We estimate radiation doses at various points at the new configuration for the permission procedure. The calculation method is briefly described in Sect.4.5.4. To control BT components remotely, additional control system is considered. The system is based on VMEbus with a high transfer rate as described in Sect.4.5.5. Other preparation is also required. With complete of these components, LWFA experiments will be started at March 2002.

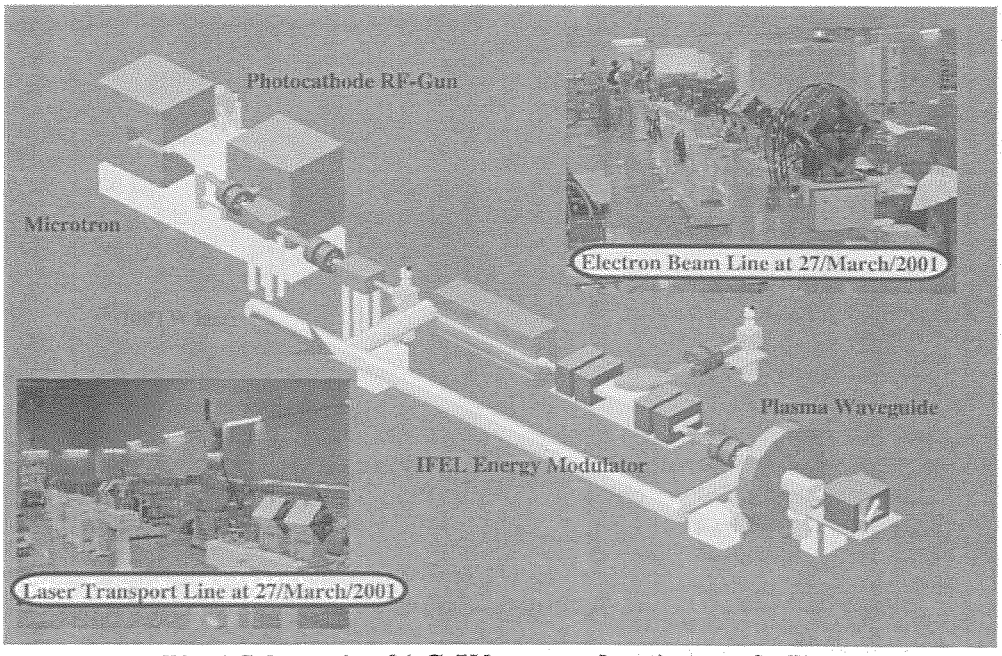

Fig. 1 Schematic of 1 GeV laser acceleration test facility

4.5.1 Performance tests of 150 MeV photocathode microtron

Masaki KANDO, Hideyuki KOTAKI, Shuji KONDO, Shinichi MASUDA, Takashi YOKOYAMA, Shuhei KANAZAWA, Tohru MATOBA and Kazuhisa NAKAJIMA[a)]

a) JAERI Kansai and High Energy Accelerator Research Organization (KEK)

1. Introduction

We are preparing the 2nd generation laser wakefield electron acceleration[1)], which will achieve an improved energy spectrum of accelerated electrons and higher energy gain such as 1 GeV over diffraction length. One of the key technologies to achieve this is high quality test electron source[2)]. We developed a photocathode RF gun based racetrack microtron accelerator (phtocathode microtron) as a candidate for the first time in the world. The photocathode microtron consists of a photocathode RF gun and a racetrack microtron (RTM) as shown in Fig. 1. The photocathode RF gun is the improved BNL-type (GUN-IV)[3)] . The drive laser is frequency quadrupled Nd:YLF laser that has a wavelength of 263 nm, a pulse length of 6 ps, and a pulse energy of 160 μJ. We have succeeded in the first commissioning of the photocathode microtron in fiscal year 1999[4)]. We performed several tests for the photocathode microtron[5,6)] and the results are presented in this report.

2. Overview of the system and beam measurement apparatus

The accelerator system can be separated to three parts: the injection section, the RTM section where the beam energy grows at each lap, and the extraction section. At the injection section, the electrons generated on the surface of copper cathode are accelerated immediately by the high RF field (100 MV/m) in the cavity. Although there exists the field emission current so called 'dark current' that has a longer pulse train about 3 μs, a total charge of ~ 50 pC, a broad energy dispersion and a bad emittance compared to the photoemission current. The beam charge is measured by a Faraday cup and an amorphous core monitor (ACM) located in the injection beam line. In the RTM section, five phosphor screens, a core monitor with an amplifier (DC – 100 MHz, 40 dB gain) are equipped. It is helpful to use a synchrotron monitor while beam handling. At the extraction beam line, there exists an ACM, an optical transition radiation (OTR) monitor, and beam dump that can read the beam current.

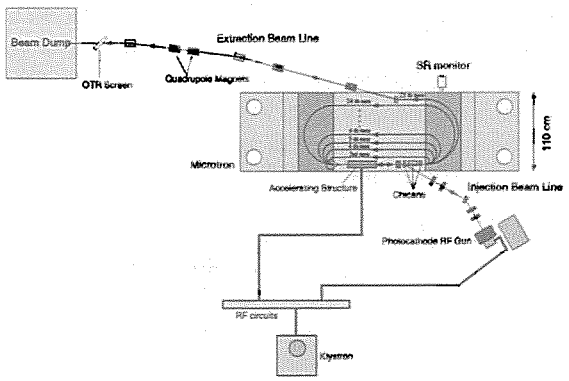

Fig. 1 Layout of the photocathode microtron

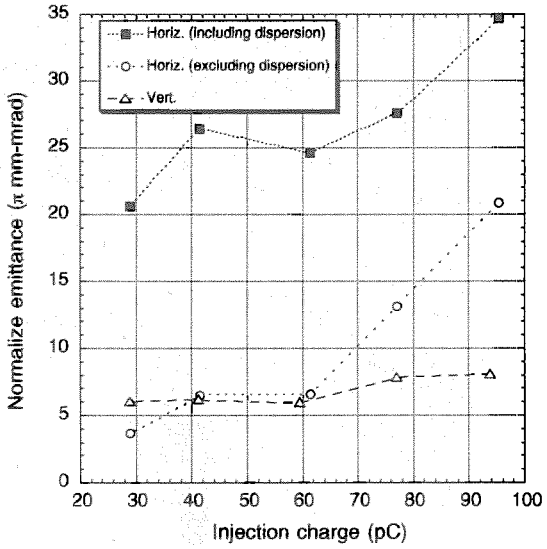

Fig. 2 Emittance versus injection charge of electrons

3. Performance tests

Beam characteristics of the photocathode microtron were tested by use of apparatus mentioned in the previous section.

Beam charge at beam dump and transmissivity from the injection point to the beam dump were measured by the CM and the Faraday cup. The maximum charge obtained was 95 pC/pulse (transmissivity was 77%) and the maximum transmissivity was 92%. In the simulation, a charge of 1

nC can be transported at a transmissivity of 26%. The charge was limited because the quantum efficiency of the copper cathode was low (2×10^{-5}) which was expected to be 1×10^{-4}. The high transmissivity was due to low charge that reduced the space-charge effect at the injection beam line. The obtained charge is high enough for the laser wakefield experiments.

Table 1 Measured beam characteristics of the 150 MeV photocathode microtron

charge	Max.	95	pC
transmissivity	Max.	92	%
emittance	Horiz.	14	π mm-mrad
	Vert.	7	
pulse duration	rms	10	ps
jitter	long term	5.5	ps
	short term	2.2	ps

Emittance was calculated by measuring beam size as a function of focal strength of a quadrupole magnet. Since the quadrupole magnet is located at dispersive section, measured horizontal emittance included the dispersion effects. The horizontal and vertical emittances were measured to be 14 and 7 π mm-mrad at a charge of 50 pC, respectively. Assuming that the energy dispersion was 0.1%, the horizontal emittance was estimated to be 7 π mm-mrad. Emittance is acceptable in focusing electron beam to tens of microns. The charge dependence of emittance was shown in Fig. 2. For the horizontal case, it is observed that emittance becomes bigger if the injected charge exceeds 60 pC. This is due to horizontal dispersion in the injection beam line caused by linear space-charge effects. There are rooms to compensate the effects by adjusting quadrupoles in the injection beam line.

The pulse length of the electron beam and timing jitter between the electron and laser beams were measured by femtosecond streak camera. For pulse length measurement, the synchrotron radiation from the circulating electron in the RTM were delivered to the streak camera. The measured pulse lengths at 21-25th laps were 10 ps (rms) and no apparent difference was observed at each lap. Timing jitter was directly measured by observing the time difference between the fundamental laser radiation (1052 nm) that irradiates the photocathode and synchrotron radiation generated from the 25th lap electron bunch in the RTM. The jitter for the long and short term were 5.5 and 2.2 ps (rms), respectively. Pulse length is rather longer than expected (1 ps), fine tuning seems to be required. Since the pulse length of the electron bunch affects acceleration efficiency rather than beam quality, acceleration experiments can be performed in these qualities.

4. Achievements

We have performed beam tests of the photocathode microtron for the first time. The measured beam characteristics are summarized in Table 1. The maximum charge and transmissivity was 92 pC. The emittance was less than 10 π mm-mrad. The pulse length was 10 ps (rms) and the timing jitter was 2.2 ps for the short term. Performance of the photocathode microtron is almost expectable and capable in performing the laser wake field experiments at JAERI Kansai.

References

1) K. Nakajima *et al.*, Proceedings of the 9th Advanced Accelerator Concepts, Santa Fe, 2000 (in print)
2) X. J. Wang *et al.*, Nuclear Instruments and Methods **A 375**, 82, 1996
3) M. Kando *et al.*, Proceedings of 1999 Particle Accelerator Conference, 3702, 2000
4) M. Kando *et al.*, Proceedings of the 25th Linear Accelerator Meeting in Japan, 9, 2000
5) M. Kando *et al.*, Proceedings of the 2nd Symposium on Advanced Photon Research (in print)
6) M. Kando *et al.*, Proceedings of the 26th Linear Accelerator Meeting in Japan, 132, 2001

4.5.2 Development of plasma waveguide using fast z-pinch capillary discharge

Shinichi MASUDA, Masaki KANDO, Hideyuki KOTAKI, Tomonao HOSOKAI[a)], Shuji KONDO, Takashi YOKOYAMA, Shuhei KANAZAWA, Tohru MATOBA and Kazuhisa NAKAJIMA[b)]

a) NERL, The University of Tokyo

b) JAERI Kansai and High Energy Accelerator Research Organization (KEK)

1. Introduction

A short laser pulse propagating in a plasma excites the electron plasma wave (laser wakefield) which accelerate an electron beam[1)]. The laser wakefield accelerator (LWFA) has high acceleration gradient, 100 to 1000 times larger than that of the traditional rf accelerators. Recent experiments[2-5)] have demonstrated the acceleration gradient of 10 GeV/m and the energy gain of 300 MeV.

Acceleration length of LWFA is limited to the diffraction length of the laser. One of the issues for GeV LWFA experiment is developing a plasma waveguide to extend acceleration length of LWFA. Several techniques have been proposed to make the acceleration length exceed the vacuum diffraction length[6-8)]. A new plasma waveguide using a fast Z-pinch discharge in a capillary is proposed and experimentally demonstrated[9)]. A high current fast Z-pinch discharge generates strong azimuthal magnetic field, which contracts the plasma radially inward down to 100 μm in diameter. The imploding current sheet drives the converging shock wave ahead of it, producing a concave electron density profile in the radial direction just before the stagnation phase. The concave electron density profile is approximately parabolic to out of radius of 50 μm, after which the density falls off. A Ti:Sapphire laser pulse λ_L = 790 nm, 90 fs, was focused to > 1 x 10^{17} W/cm^2 on the front edge of the capillary with a spot size of 40 μm in diameter. In this experiment, we succeeded in guiding a 2 TW laser over 2 cm, 12.5 times larger than the diffraction length, in the Z-pinch plasmas[9)].

We have started to develop new plasma waveguide for GeV LWFA experiment. Section 2 shows design of the 10 cm long plasma waveguide. Preliminary results of simulation study of the plasma waveguide is reported in Section 3. Section 4 summarizes this report.

2. Design of plasma waveguide

A fast rising high current generator is needed to produce the fast Z-pinch discharge. Figure 1 shows a design of the plasma waveguide using fast Z-pinch discharge. A Marx generator stores the energy up to 68 J. The maximum output is 200 kV. A laser triggered spark gap switch (LTSG) is used to minimize jitter of the Marx generator. A 10 cm long ceramic capillary is connected to the center of a water filled disk capacitor (4 nF). Four LTSGs are symmetrically located on the disk capacitor to generate axially symmetric current in the capillary. A solenoid valve is used to supply gas into the capillary. Pre-ionization by the frequency quadrupled YAG laser is adopted to produce the stable plasma waveguide.

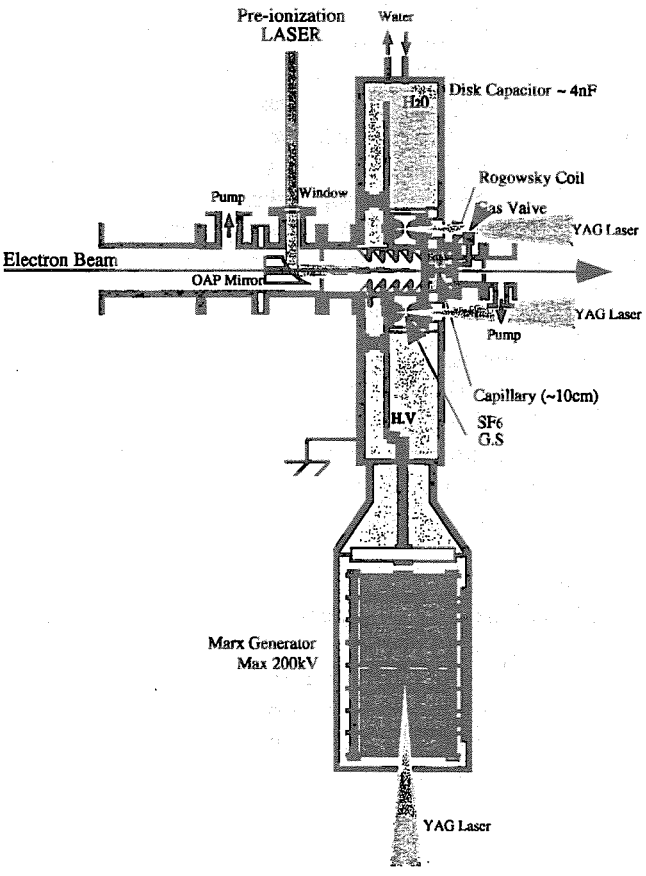

Fig. 1 Schematic drawing of plasma waveguide

3. Simulation study of plasma waveguide

We are developing particle-in-cell (PIC) codes[10)] to simulate the channel formation of the plasma waveguide, the laser propagation, the wake field excitation and the electron

acceleration. Newton-Lorentz equations,

$$m\frac{\partial \mathbf{u}}{\partial t} = q\left(\mathbf{E} + \frac{\mathbf{u}}{\gamma c} \times \mathbf{B}\right)$$
$$\frac{\partial \mathbf{r}}{\partial t} = \frac{\mathbf{u}}{\gamma}, \qquad (\mathbf{u} = \gamma \mathbf{v}), \tag{1}$$

describe the relativistic motion of the plasma particles and the electron beam in the laser wake field. The laser and the wakefield propagations are described by Maxwell equations

$$\nabla \times \mathbf{E} + \frac{1}{c}\frac{\partial \mathbf{B}}{\partial t} = 0$$
$$\nabla \times \mathbf{B} - \frac{1}{c}\frac{\partial \mathbf{E}}{\partial t} = \frac{4\pi}{c}\mathbf{j} \tag{2}$$

These differential-equations are translated to space- and time-centered finite-difference equations. **B** and **u** are updated by leap-frog method over **E** and **r**. Field quantities, **E** and **B**, are staggered in space grid. This guarantees second order accuracy and space-time reversibility. The PIC algorithm consists of two phases: In the particle push phase, the new particle position and velocities are determined according to Eq. (1). In the following field solve phase, the fields are updated, according to the particle motion. In order to push the particles, the field quantities at the particle positions are determined by linear interpolation. Current density, **j**, on each grid point is calculated from the particle position and velocity with the volume weighting scheme.

Preliminary results of 1D PIC simulations have been obtained. Figure 2 shows a typical wakefield profile excited by the short laser pulse. The laser power is 100 TW and pulse width is 20 fs. Spot size is 30 μm in the plasma. The acceleration gradient reaches 1 GeV/cm at the plasma density $n_e = 3 \times 10^{18}\text{cm}^{-3}$.

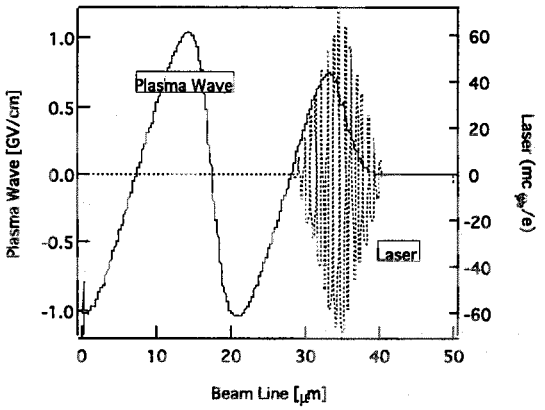

Fig. 2 Wakefield excited by the short laser pulse, P=100 TW at 20 fs, $n_e = 3 \times 10^{18}\text{cm}^{-3}$

4. Summary

We have constructed a fast rising high current generator. A short current pulse with duration of 10 ns (FWHM) is obtained for a dummy load instead of the capillary.

1D particle simulation shows the acceleration length from 1 to 10 cm is required for the 1 GeV LWFA experiment in the range of the plasma density from 10^{17} to 10^{19} cm^{-3}. Multi dimensional simulations are needed for more realistic simulation such as the laser propagation in the plasma waveguide. Next issue is development of 3D PIC code.

References

1) T. Tajima and J. M. Dawson, Phys. Rev. Lett. **43**, 267, 1979
2) K. Nakajima *et al.*, Phys. Rev. Lett. **74**, 4428, 1995
3) A. Modena *et al.*, IEEE Trans. Plasma Sci., **24**, 289, 1996
4) H. Dewa *et al.*, Nucl. Instrum. Meth. Physics Res. **A410**, 514, 1998
5) M. Kando *et al.*, Jpn. J. Appl. Phys. **38**, L967, 1999
6) K. Krushelnick *et al.*, Phys. Rev. Lett., **78** , 4047, 1997
7) C. G. Durfee III and H. M. Milchberg, Phys. Rev. Lett., **71**, 2409, 1993
8) Y. Ehrich *et al.*, Phys. Rev. Lett., **77**, 4186, 1996
9) T. Hosokai *et al.*, Optics Letters, **25**, 10, 2000
10) C. K. Birdsal and A. B. Langdon, Plasma Physics via Computer Simulation, McGrow-Hill, 1985

4.5.3 Time resolved density measurement of gas jet by interferometer

Hideyuki KOTAKI, Shinichi MASUDA, Masaki KANDO, Shuji KONDO, Shuhei KANAZAWA, Takashi YOKOYAMA, Tohru MATOBA and Kazuhisa NAKAJIMA

1. Introduction

A gas jet is an important item for laser-plasma applications such as x-ray laser[1], high harmonics generation[2], electron generation[3-5], ion production[6-8] and laser acceleration[9-13]. We have to know the distribution of the gas density to estimate a plasma density at a time to irradiate the laser at a point, the time dependence of the gas distribution and the dependence of the distance from the gas jet nozzle. It is also important for the laser plasma experiment that the length of the gas density is uniform and stable. We measured the gas density distribution to optimize the usual straight nozzle and to decide the laser focusing point. Requirement for gas densities and distributions are different with the type of experiments. It is difficult to choose the type of nozzle and the size of orifice without calculation and simulation. It is easy to use a straight type nozzle for some experiments. However, the density distribution has not been measured for straight nozzles. We measured the gas distribution of the straight nozzle to characterize it by an interferometer.

2. Experiment set up

In order to measure a gas density, we used a Mach-Zehnder interferometer shown in Fig. 1. The interferometer consisted of a He-Ne laser, two mirrors and two beam splitters. The wavelength of the laser was 632.8 nm. The vacuum chamber was interposed in the path of beam 1. The orifice of the gas jet nozzle was 0.8 mm in diameter. The laser pulse made an interferogram on the screen. The interferogram was captured by a charge-coupled-device (CCD) camera with an image intensifier of which gate time was set to be 5 μs. The CCD camera had 512 × 512 pixels whose size was 19 μm × 19 μm.

The CCD camera and the gas jet were operated by the same external trigger made from a pulse generator. We scanned the timing between the gate of the CCD camera and the gas jet opening time. The room temperature was controlled at 24 ℃.

3. Density calculation from the fringe shift

The fringe phase shift Δϕ is

$$\Delta\phi = \int (N_2 - N_1)\frac{\omega}{c}\,dL, \qquad (1)$$

where Δϕ is the phase shift in radian, N_1 is a refractive index in vacuum, N_2 is a refractive index in gas, ω is a frequency of the probe laser, c is the speed of light, and L is an interaction distance between the gas and the probe laser. The refractive index N_1 is 1 and the refractive index N_2 is $1+(n_g-1)\,p\,273/T$. The shift is re-written by

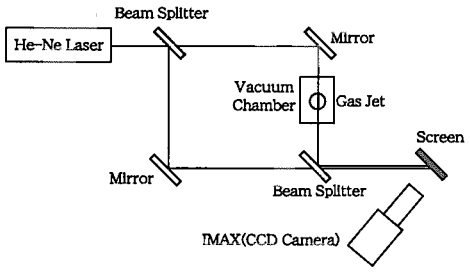

Fig. 1 Mach-Zehnder interferometer

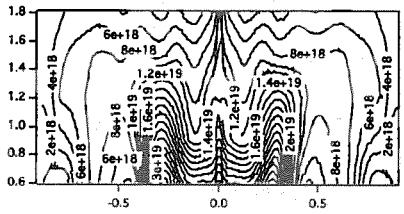

(a) 1100μs

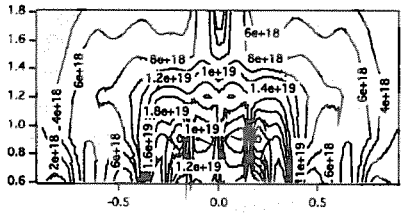

(b) 1400μs

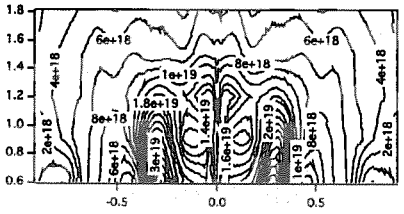

(c) 1700μs

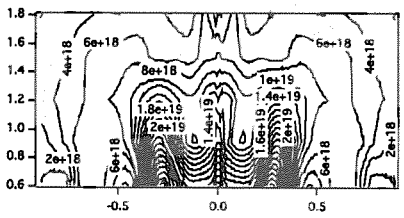

(d) 2000μs

Fig. 2 The density distribution of nitrogen depended on the time

$$\frac{\Delta\phi}{2\pi} = (n_g - 1) \cdot p \cdot \frac{273}{T} \cdot \frac{L}{\lambda}, \qquad (2)$$

where a temperature is T [K], a pressure is p [atm], and n_g is a refractive index at 0 °C and 1 atm. We assume that the gas distribution is axi-symmetry. This assumption seems valid because of its nozzle shape. Equation (2) and Abel inversion are used to calculate the distribution of the gas density.

4. Density measurement

An opening time of the gas jet was 2 ms and a gate time of the CCD camera was 5 μs. The distribution of the gas density was calculated from the fringe shift and eq. (2). We measured the gas density distributions with changing the timing between the gas jet and the CCD camera. Figure 2 shows the nitrogen density distributions as a function of the timing of the CCD camera at a back pressure of 25 atm. The abscissa shows the distance from the center of the nozzle and the ordinate shows the distance from the end of the nozzle in mm. Figure 3 shows the sliced gas densities whose position was 1.5 mm from the gas jet nozzle. The gas densities were increased with the back pressure. The gas density was 7.5×10^{18} cm^{-3} when the pressure was 25 atm. It was observed that the uniform region of 0.6 mm in radius was produced at 1.5 mm from the nozzle of which orifice was 0.8 mm.

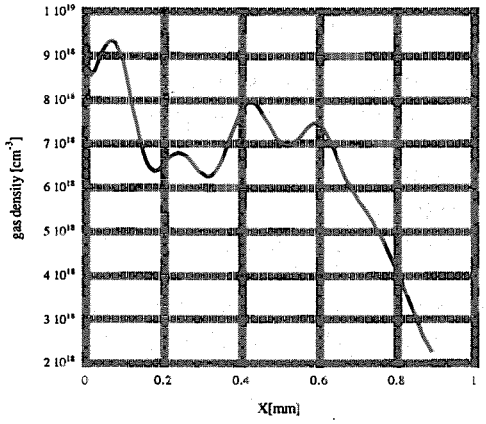

Fig. 3 Sliced gas densities

5. Conclusion

We measured the distribution of the gas density to determine the laser-plasma experiment parameters by a Mach-Zehnder interferometer. The gas distribution changes time to time in 100 μs when the opening time of the gas jet was 2 ms. The flat position of the gas density is about 1.5 mm from the nozzle with an orifice of 0.8 mm.

References

1) J. J. Rocca, V. Shlyaptsev, F. G. Tomasel, O. D. Cortázar, D. Hartshorn and J. L. A. Chilla, Phys. Rev. Lett. **73**, 2192, 1994
2) X. F. Li, A. L'Huillier, M. Ferray, L. A. Lompré and G. Mainfray, Phys. Rev. A **39**, 5751, 1989
3) T. E. Cowan, A. W. Hunt, T. W. Phillips, S. C. Wilks, M. D. Perry, C. Brown, W. Fountain, S. Hatchett, J. Johnson, M. H. Key, T. Parnell, D. M. Pennington, R. A. Snavely and Y. Takahashi, Phy. Rev. Lett **84**, 903, 2000
4) R. G. Hemker, K. –C. Tzeng, W. B. Mori, C. E. Clayton and T. Katsouleas, Phy. Rev. E **57**, 5920, 1998
5) A. J. Mackinnon, M. Borghesi, A. Iwase and O. Willl., Phys. Rev. Lett. **80**, 5349, 1998
6) E. L. Clark, K. Krushelnick, M. Zepf, F. N. Beg, M. Tatarakis, A. Machacek, M. I. K. Santala, I. Watts, P. A. Norreys and A. E. Dangor, Phys. Rev. Lett. **85**, 1654, 2000
7) F. Amiranoff, S. D. Baton, S. Hüller, V. Malka, A. Modena, Ph. Mounaix, N. Renard-Le Galloudec, C. Rousseaux and M. Salvati, Phy. Rev. E **61**, 1949, 2000
8) S. H. Glenzer, W. Rozmus, B. J. MacGowan, K. G. Estabrook, J. D. De Groot, G. B. Zimmerman, H. A. Baldis, J. A. Harte, R. W. Lee, E. A. Williams and B. G. Wilson, Phys. Rev. Lett. **82**, 97, 1999
9) T. Tajima and J. M. Dawson, Phys. Rev. Lett. **43**, 267, 1979
10) K. Nakajima, Phys. Plasmas **3**, 1, 1996
11) M. Kando, H. Ahn, H. Dewa, H. Kotaki, T. Ueda, M. Uesaka, T. Watanabe, H. Nakanishi, A. Ogata and K. Kazahisa, Jpn. J. Appl. Phys. **38**, 967, 1999
12) E. Esarey and P. Sprangle, IEEE Trans. Plasma Sci. **24**, 252, 1996
13) J. R. Marquès, F. Dorchies, F. Amiranoff, P. Audebert, J. P. Geindre, A. Antonetti, T. M. Antonsen Jr., P. Chessa and P. Mori, Phys. Plasmas **5**, 1162, 1998

4.5.4 Dose estimation of photocathode microtron

Shuji KONDO, Masaki KANDO, Hideyuki KOTAKI, Takashi YOKOYAMA,
Shuhei KANAZAWA, Tohru MATOBA and Kazuhisa NAKAJIMA[a)]

a) JAERI Kansai and High Energy Accelerator Research Organization (KEK)

1. Introduction

Laser acceleration group had constructed the photocathode microtron of which maximum beam power was 15 W as a high quality electron beam source, and it was completed in January 2000. This report covers the results of calculation, which is based on the estimation of the radiation dose generated by the loss of the accelerated electron in the microtron system.

2. Dose estimation

(1) Precondition

The radiation from the microtron is represented by the following two methods (neutrons generation by photonuclear reaction and X(γ)-ray photons caused by bremsstrahlung). We defined the following beam loss positions (S1-S4) as the radiation source points. The point S1 represents integrated beam loss in the microtron during circulation (5W loss). Points S2 and S3 are caused by beam loss at bending magnets (0.15W loss), and S4 is caused by 100% beam loss at beam dump (15 W loss). Beam losses are overestimated for radiation safety. The method to estimate doses at these points are as follows. Considering that neutron and X(γ)-ray attenuate because of the shield and the distance from the radiation source to the estimation point, we summed up the direct radiation and the streaming dose and skyshine dose. The estimation points selected from the structural condition in our facility.

(2) Direct radiation calculation

1) Direct radiation from the microtron

The radiation from the microtron is calculated based on the measurement at some representative directions (1m away from the machine surface) [1]. The direct dose rates of neutrons and X(γ)-rays are written as follows, respectively[2,3].

$$H_{dir,n}(r) = H_{dir,n}(0) \times \frac{10^{(-\sum d/\tau_n)}}{r^2}$$

$$H_{dir,\gamma}(r) = H_{dir,\gamma}(0) \times \frac{10^{(-\sum d/\tau_\gamma)}}{r^2}$$

Here, d is shield thickness [m], τ is 1/10-value layer [m], and r is distance between the source and the estimation point [m].

2) Direct radiation from other beam loss points

To estimate dose rate of X(γ)-ray, we used the following equation,

$$H_{dir,\gamma}(r) = F_1 \times F_2 \times \frac{10^{(-\sum d/\tau\gamma)}}{r^2}$$

where F_1 is a coefficient to convert air kerma (kinetic energy released in material) into effective dose [Sv/Gy](when energy is uncertain, we use maximum value 1.433), F_2 is an absorbed dose generated by beam loss (3×10^{5} E at $\theta = 0°$ or 5×10^{1} at $\theta = 90°$, θ : the angle between beam direction and estimating direction, E : photon energy [MeV]).

Differently from the X(γ)-ray, neutrons are generated isotropically by photonuclear reaction. To estimate dose rate of neutron, we used[3,4],

$$H_{dir,n}(r) = G_1 \times G_2 \times \frac{10^{(-\sum d/\tau_n)}}{4\pi r^2} \quad ,$$

where G_1 is the number of neutrons generated by photonuclear reaction ($G_1 = 282\times10^{-12}\times0.3$E , E: electron energy in GeV), G_2 is the number of lost electrons[h^{-1}].

3) Streaming calculation[6-8]

We calculated the streaming dose levels in the labyrinth separated a few sections (including service ducts) using following method.

Dose attenuation of X(γ)-ray in the first and second sections are written as

$$H_{str,\gamma}(r) = H_{dir,\gamma}(0) \times 0.22 \times (d+r)^{-3.0}$$
$$H_{str,\gamma}(r) = H_{str,\gamma}(0) \times 0.26 \times (d+r)^{-2.6}$$

where $H_{dir,\gamma}(0)$ is the X(γ)-ray dose rate at the entrance in the first [Sv/h], $H_{str,\gamma}(0)$ is the X(γ)-ray dose rate at the entrances after the second section [Sv/h], d is half of the aisle width of the labyrinth [m], r is each section length from its entrance [m].

In the case that source point of the neutron can be seen at the exit of the first section, the neutron dose rate at the calculation point r [Sv/h] can be written as

$$H_{str,n}(r) = H_{str,n}(a) \cdot \frac{2a^2}{r^2}$$

where a is the distance between neutron source and the entrance of the first section [m], r is the distance between neutron source and calculation point [m], $H_{str,n}(a)$ is neutron dose rate at the entrance of the first section [Sv/h], an factor 2 in numerator is calibrated coefficient.

In the case that source point of the neutron cannot be seen at the exit of the first section, neutron dose rate at the calculation point r [Sv/h] is

$$H_{str,n}(r) = H_{str,n}(0) \cdot fe \cdot \frac{\exp(-r/0.45) + 0.022 \cdot S^{1.3} \cdot \exp(-r/2.35)}{1 + 0.022 \cdot S^{1.3}}$$

where $H_{str,n}(r)$ is, r is the distance between the calculating point and the section's entrances [m], S is the cross section [m^2], $H_{str,n}(0)$ is neutron dose rate at the section's entrance [Sv/h], and fe is calibrated coefficient (factor 2 is used if the considering section's exit point is not seen by neutron directly, otherwise factor 1 is used).

4) Skyshine[7,8]

Skyshine dose rate is expressed as

$$H_{sky}(r) = Q(E) \frac{\exp(-r/\lambda(E))}{r^2}$$

where $Q(E)$ is the number of neutrons at the source point, $\lambda(E)$ is air effective attenuation distance [m], and r is the distance from the source point[m]. $Q(E)$ is calculated as follows. Step1: we calculate the dose rate at outside of the shielding wall. The dose rate is the sum of X(γ)-ray and neutron that are calculated by the formula to estimate direct radiation. Step2: dose rate is integrated by area of each wall. Step3: using the conversion coefficient, integrated dose rate is converted into the number of neutrons. Step4: dose rate is calculated by using 3×10^{-15} Sv·m^2/source neutron as parameter to convert the number of neutrons into skyshine dose.

3. Results

According to our calculation, the highest value was 0.34 mSv/3months. This value is much less than the regulation value (1.3 mSv/3months) at the boundary of the controlled area. We convinced that our facility has sufficient radiation safety.

4. Acknowledgements

We wish to thank Mr. T. Matsui, Dr. A. Nagashima, Mr. Y. Hayashi of JAERI for their encouragement and supports.

References

1) T. Hori, private communication
2) W. P. Swanson, Radiological Safety Aspects of the Operation of Electron Linear Accelerators, IAEA Technical Reports Series, 188,1979
3) Y. Hayashida, Shielding of Electron Synchrotron at INS and Dose of Surrounding Radiations, Genshikakukenkyu, **11**, 337, 1966 (in Japanese)
4) S. Nakamura, Shielding calculation of SOR ring and performance tests of Radiation Shielding, KEK-77-34, 30, 1978 (in Japanese)
5) K. Tesch *et al,* Attenuation of the Photon Dose in Labylinths and Ducts at Accelerators, Radiat. Prot. Dosim., **20**, 169 ,1987
6) K. Tesch, Particle Accelerator, **12**, 169, 1982
7) S.Nakamura, Radiation Physics and Accelerator Safety Engineering, Tijinsyokan, 1995 (in Japanese)
8) G.R. Stevenson, E.H. Thomas *et al.*, A Simple Procedure for the estimation of Neutron Skyshine from Proton Accelerators, Health Physics, **46**, 115, 1984

4.5.5 Design of control system for the new beam transport line with VMEbus

Takashi YOKOYAMA, Masaki KANDO, Hideyuki KOTAKI, Shuji KONDO,
Shuhei KANAZAWA, Tohru MATOBA and Kazuhisa NAKAJIMA[a)]
a) JAERI Kansai and High Energy Accelerator Research Organization (KEK)

1. Introduction

We have constructed photocathode microtron system in order to study laser-beam interactions especially for laser wakefield acceleration experiments. The control system of the present accelerator is based on GP-IB interface connected through an optical fiber[1)]. The GP-IB is easy to be programmed, however, its slow response is major problem of the present control system.

We will extend the electron beam transport (BT) line in order to perform acceleration experiments. Many apparatus, such as power supplies for magnets, vacuum gauges, and beam monitors, will be installed in BT. They should be controlled and/or monitored remotely. It is not desirable to append these controls to the existing control system because the response of the system seems to be upper limit. This report describes new control system for the BT that has quick response and high cost-performance.

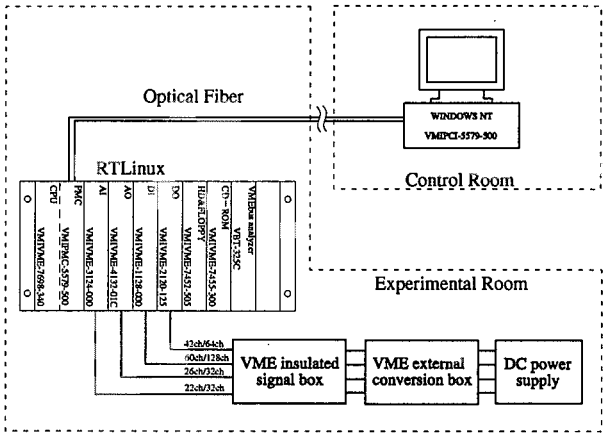

Fig. 1 Schematic of new control system

2. Overview of control system

Among various types of buses, VMEbus is widely used in industry, of course, in many accelerator facilities. Various extension boards of VME are commercially available and many components are tested for a long time. Although the trend of buses in industry shifts to CompactPCI, it seems better to use VME at this time. We append new BT control system based on VME to the accelerator independent of existing GP-IB based control system. This is because it is difficult at a point of view of throughputs to append any control components to the present system. The new BT control system is shown in Fig. 1. A single VME chassis is located in the experimental room. Four I/O boards are installed in the chassis. They are digital output (DO) of 64 channels, digital input (DI) of 128ch, analog output of 32ch, and analog input (AI) of 32ch. Analog I/O is used mainly in controlling power supplies of the magnets. In order to prevent noises, additional components, such as insulated signal box and conversion box, should be required. There are other components like a PC installed in the chassis. We select Linux as an operating system of the single board computer (Celeron 366 MHz) in the VME chassis, because Linux is open-source and freeware, and if we use RTLinux, it is easy to upgrade into real time control system. A graphical user interface (GUI) program runs on Windows2000 based PC that is stable and easy to communicate existing other PCs. The coding languages are C for low level control and Visual Basic for GUI. To communicate console computer and the computer in the VME chassis, we use reflective memory instead of usual Ethernet. The connection cable is multi-mode optical fiber. Reflective memory provides sharing memories (64 Mbyte) between remote computers. The transfer rate is 13.4Mbyte/s without redundant transfer. For a while, the system will be used only for basic components, but this system has a potential to extend to additional applications such as data acquisition of experiments and control of laser beam steering mirrors. All the components in the VME chassis are provided by the same company VMIC[2)] because of compatibility.

3. Results

We have discussed a control system of the new beam line. The system is based on VMEbus and has high transfer rate, easiness to customize, and extendibility.

References

1) Sumitomo Heavy Industries, Ltd., Document for microtron control system, 2000 (in Japanese)
2) VMIC, http://www.vmic.com

4.6 Advanced Photon Simulation Research

Simulation Group for Advanced Photon Science

Toshiki TAJIMA [a)], Toshizo SHIRAI, Mitsuru YAMAGIWA, Akira SASAKI, James KOGA, Kengo MORIBAYASHI, Yutaka UESHIMA, Takayuki UTSUMI, Takuya ARAKAWA, Keisuke NAKAGAWA, Alexei ZHIDKOV, Ichirou FUKUMOTO, Keiko SUTO, Hideo KIMURA, Hitoshi IHARA, Yasuaki KISHIMOTO, Shingo SUZUKI [b)] and Hiroo TOTSUJI [c)]

a) Univ. Texas at Austin and Lawrence Livermore National Laboratory

b) Japan Science and Technology Corporation

c) Okayama Univ.

We have developed the Progressive Parallel Plasma (P^3) 2D code and its support system tuned for the massively parallel scalar computer 'Intel Paragon XP/S 75MP834'. The scheme for parallelization was a one dimensional domain decomposition where information of particles crossing the node's boundary is communicated between 2 neighboring nodes. The performance of the calculation for plasma particle simulations is 53 nano seconds/simulation time step/particle, which corresponds to effectively 42G FLOPS. We have also completed vector-parallelization of the two-dimensional electromagnetic particle code (em2d) on the VPP5000.

We have given an explanation for the fixed blueshift observed of an intense short pulse laser propagating in a gas chamber filled with helium. The observed shift is found to be independent of the laser power and gas pressure above some critical power. The results are explained by the formation of filaments, which occur due to nonlinear gas polarization effects. The blueshift is in qualitative agreement with a one dimensional particle-in-cell simulation including ionization of the gas.

We have studied the phenomena of laser ablation via molecular dynamics simulation. We have found that the shock wave induced by laser irradiation propagates spherically from the surface to the interior and that a lot of dislocations are generated near the surface by the propagation of the shock wave.

We have done a fast atomic physics simulation of the effects of the inner-shell excitation and ionization processes by fast electron impact on the production of hollow atoms. The fast electrons are produced by high-intensity short-pulse laser irradiation on a solid. We have found that the ionization produces a more significant contribution than the excitation. We have also found that the inner-shell ionization processes play an important role in the production of highly charged ions in high density hot plasmas generated by the interaction between giant Kr clusters and high intensity lasers. We have also found that the number of X-ray photons from hollow atoms produced by collisions of multiply charged ions accelerated by a short pulse laser with a solid or foil increases with the laser energy and could reach 3×10^{11} photons for a laser energy of about 10 J.

We have calculated electron capture processes in collisions between O^{5+} ions and C^{6+} ions under a static electric field in collision energy ranges 0.25 - 4 keV/amu and field strengths below 0 - 514 MV/cm. In this calculation, increases of the cross sections by the electric field have been found. This effect becomes appreciable in the lower collision energy range.

We have critically evaluated the spectral data for nickel-like ions, Cu II through Kr IX, in relation to the research and development of x-ray lasers. These data are indispensable not only to identify observed spectrum but also to assess the reliability of the atomic energy levels and transition probabilities calculated with computer codes. To this point, wavelengths, energy levels, line classifications, and intensities have been compiled for a total of about 5000 lines.

We have developed the Hierarchical Atomic model (HIA) for the calculation of atomic processes in a high temperature plasma. The model is applied to short pulse laser pumped transient collisionally excited (TCE) x-ray lasers. The calculated gain is found to reproduce the experiments. The code will be applied not only to the optimization of x-ray lasers at shorter wavelength but to the spectroscopic studies of laboratory and space plasmas.

We have also developed an accurate numerical solver for the free and bound states of the Schrodinger and Dirac wave equations for arbitrary central fields. The main characteristics of the code are (1) the potential and radial wave functions are represented by the CIP (Constrained Interpolation Profile) method, (2) the free states at the far field are represented by the PA (Phase-Amplitude) method, (3) the ASCRK (Adaptive Step size Controlled Runge-Kuta) method is adopted as the ODE (Ordinary Differential Equation) integrator to control the integration accuracy.

4.6.1 Progressive Parallel Plasma (P^3) code support system for large data management

Yutaka UESHIMA

1. Introduction

In the interpretation of the experimentally observed acceleration of the ions, it was assumed in Ref. 1) that the ions move radially with respect to the channel under the effect of the Coulomb explosion. However, the generation of fast ions not only radially but also in forward direction was observed in 2D Particle In Cell (PIC) simulations[2]. In the case of an overdense plasma the role of the channel is taken as the hole bored by the laser pulse. In such plasmas, in addition to the plasma expansion in vacuum mentioned above and to the ion expulsion in the transverse direction due to the self-focusing channel, we also notice ion acceleration in the plasma resonance region[2] and forward ion acceleration if the laser pulse interacts with a thin foil[3]. The latter results were obtained via PIC simulations in the framework of a one dimensional planar model which is valid as long as the transverse size of the laser pulse is much larger than the acceleration length. Since in a one-dimensional planar model the electrostatic potential diverges as the width of the ion cloud increases, we must perform at least two-dimensional simulations. In addition, an ultraintense laser pulse in a near-critical density plasma and in an overdense plasma, is subject to relativistic self focusing, the description of which also requires at least two dimensional PIC simulations.

The numerical study of the interaction of an ultraintense laser with matter needs to be performed in at least two-dimensional simulations. However the computational cost of such a simulation is very high. For example, in the case of an electron density of 6.2×10^{23} cm^{-3}, *i.e.* Al^{10+}, the mesh size must be smaller than 2 nm because the skin depth is 7 nm. In a few 10's of femto seconds, ions and electrons expand to around 10 μm from the irradiation point of the matter. Therefore, a 10000 x 10000=0.1G mesh simulation is required and 1 Giga particles must be contained in a simulation box to investigate properties of the accelerated ions and electrons, *i.e.* energy and spatial distribution, etc..

2. Intel Paragon 75MP834

We have developed the P^3 2D code tuned for the massively parallel scalar computer 'Intel Paragon XP/S 75MP834'. The computer is composed of 834 nodes and every node has 1 communication and 2 calculation CPUs and 128Mbyte RAM. The Paragon has 26 I/O nodes independent of the 834 calculation nodes. Each I/O node has 64 Mbyte RAM and the effective I/O ability of 2.6 Mbyte/s. Note that every I/O node cannot accept more than 32 I/O requests. The parallel file system (pfs) is constructed with 16 I/O nodes. The computer has total performance of 100 GByte RAM and 120 GFLOPS. The scheme for parallelization is domain decomposition where information of particles crossing the node's boundary is communicated to 2 neighboring nodes.

3. P^3 Support System for large data management

In the ordinary PIC simulation, a correction of electricfield by the fast Fourier transform (FFT) was needed to satisfy the Coulomb's law in the Maxwell's equations. However, the cost of needed RAM size and communication traffic is large with the use of the FFT. In the P^3 code, a rigid local solver[4] is adopted to overcome the difficulty. As a result, the calculation speed of 53 ns/step/particle is achieved in 800 nodes and the acceleration rate as a index of parallel computing is about 800. This corresponds to 42 GFLOPS, which is 35% of the maximum hardware specification, 120 GFLOPS. By the way, the calculation speeds in NEC-SX4-16CPU and Fujitsu-VPP300-1CPU are 340 ns/step/particle and 4660 ns/step/particle, respectively.

To simulate an interaction of a real solid with a relativistic laser, ionization, collision, and radiation processes need to be calculated. In the code, ionization and collision processes were simulated by Monte-Carlo methods. Bremsstrahlung and Larmor radiation were estimated by post process.

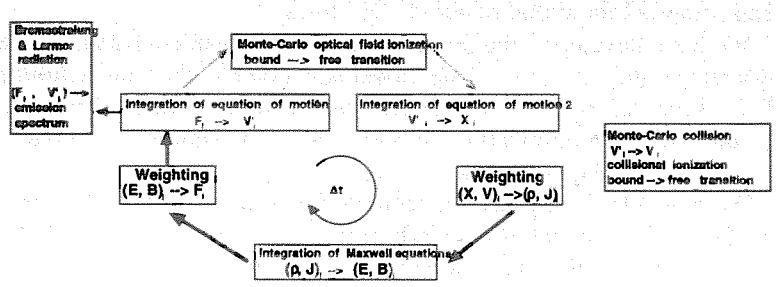

Fig. 1 The flow diagram in P^3 2D code

In the large-scale simulation, a real-time visualization and steering system is thought as a hopeful method of data analysis. This approach is valid in the fixed analysis at one time. In simulation research for an unknown problem, it is necessary that the output data can be analyzed many times because profitable analysis is difficult the first time. Consequently, output data should be filed to refer and analyze at any time. A pseudo-real-time visualization system is equipped in the P^3 code. The P^3 support system has the following automatic functions,

1) make directories in the Paragon, the file server, and graphical work station
2) transport files from the Paragon to the file server
3) create CLI or V scripts of AVS5 or AVS Express
4) execute AVS
5) convert image format and re-arrange them

In the future work, we are going to add to the P^3 support system the following functions,

1) automatic file backup and restore
2) link database server and manage data and image files

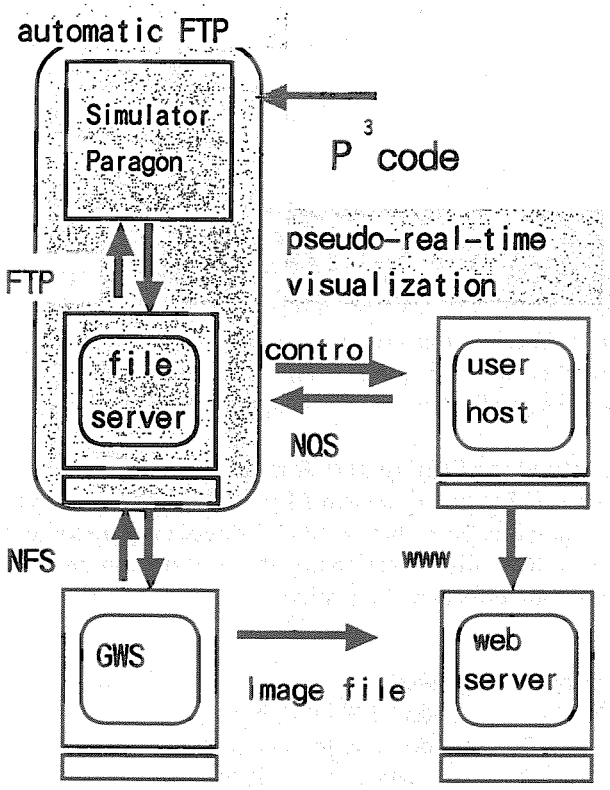

Fig. 2 Illustration of the P^3 support system

4. Results

We have developed the P^3 2D code and its support system tuned for the massively parallel scalar computer 'Intel Paragon XP/S 75MP834'. The scheme for parallelization was one dimensional domain decomposition where information of particles crossing the node's boundary is communicated between 2 neighboring nodes. The performance of the calculation for plasma particle simulations is 53 nano seconds/ simulation time step/particle, which corresponds to effectively 42GFLOPS. By using the P^3 2D code, a simulation including 1 Giga particles can be completed within a few days. In the future work, we are going to add to the P^3 support system the following functions,

1) automatic backup and restore
2) link database server and managing data and image files

With the P^3 2D code and its support system, it is found that only higher harmonics over twice as large as the plasma frequency are transmitted from the back of the foil. The higher harmonics below the plasma frequency are strongly suppressed in the transparent light. The result indicates that higher harmonics are generated in front of the foil. Separately from emissions from atomic processes induced by the intense laser, the radiation can become short-pulse and intense. The pulse length of the radiation is the same order as that of the laser.

References

1) G. S. Sarkisov, V. Yu. Bychenkov, V. N. Novikov, V. T. Tikhonchuk, A.Maksimchuk, S. Y. Chen, R. Wagner, G. Mourou and D. Umstadter, Phys. Rev. E **59**, 7042, 1999
2) S. V. Bulanov, F. Califano, G. I. Dudnikova, T. Zh. Esirkepov, F. F. Kamenets, T. V. Liseikina, N. M. Naumova, F. Pegoraro and V. A. Vshivkov, Plasma Physics Reports **25**, 701, 1999
3) S. V. Bulanov, N. M. Naumova and F. Pegoraro, Physics of Plasmas **1**, 745, 1994
4) J. Villasenor and O.Buneman. Comp. Physics. Comm. **69**, 306, 1992

4.6.2 Vector-parallelization of the two-dimensional electromagnetic particle code (em2d)

Mitsuru YAMAGIWA, Toshiyuki NEMOTO [a)], James K. KOGA, Yutaka UESHIMA and Yasuaki KISHIMOTO

a) Center for Promotion of Computational Science and Engineering (on leave from RIST)

1. Introduction

We report vector-parallelization on the VPP5000 of the two-dimensional electromagnetic particle code (em2d) developed for advanced photon simulation research. In order to treat as many particles as possible, we have divided both the spatial domain and the particles and assigned them to the processing elements (PE's). In the previous parallelization of the em2d code on the VPP500, a large working area memory was used for data transmission among PE's. Increasing this memory size leads to decreasing the number of particles to be installed. This time a method of efficient data communication with its memory size reduced as small as possible is adopted. Use has also been made of the message passing interface (MPI).

2. Partitioning of the spatial domain and particles

The em2d is two dimensional in real space (and three dimensional in momentum space). The domain partitioning has been done in the Y direction perpendicular to the laser propagation. This is because the code was basically vectorized in the X direction parallel to the laser propagation. Then, reduction of the vectorization effect can be avoided:

```
(in subroutine E_push2)
c        do 1200 j = 0, Ny
s2       do 1200 j = jsta, jend                                  ; partitoned Y loop
v2         do 1300 i = 1, Nx                                     ; keeping the long vector length
v2           Ey(i,j) = Ey(i,j) - cdlt_tox*(Bz(i,j)-Bz(i-1,j)) - dlt_t*rJy(i,j)
v2  1300   continue
s2  1200 continue
```

As for partitioning of particles, each particle is assigned to the PE corresponding to the domain to which it belongs. The data in the adjacent PE is, however, sometimes needed in the calculation. This is resolved by setting up overlap regions on both sides of the decomposed domain. The PE's adjacent each other have doubly the same data in the overlap regions. As a result, the calculation is executable without accessing the neighboring PE.

We have been able to install much more particles by this time tuning, as mentioned above. The particle number per PE also increases and hence the vector length becomes longer in the particle loop, leading to effective vectorization:

```
(in subroutine gm_P_slv)
s        do 1000 is = 1, N_sp
v          do 1100 j = l_st(is), l_ed(is)                        ; particle loop
v            P2 = P(j,1)**2 + P(j,2)**2 + P(j,3)**2
v            gamma(j) = dsqrt( 1.d0 + P2 /(p_mass(is)*c)**2 )
v  1100    continue
s  1000 continue
```

3. Other changes

We have partially avoided the increase of the execution time due to data communication by calculating and communicating at one time (non-blocking communication of MPI). We have also changed the code so that the snapshot output and the restart file I/O are excutable on each PE and tuned the graphic interface for the parallel version. The CPU time typically decreases by 1/8 (1/24) for the case of 8 PE's (32 PE's) compared to the 1 PE case. Giga-particle simulation of a solid density plasma has been possible with 32 PE's (240 GB memory) of the VPP5000.

4.6.3 Fixed blueshift of high intensity short pulse lasers propagating in gas chambers

James K. KOGA, Natalia NAUMOVA [a)], Masaki KANDO, Levan. N. TSINTSADZE [b)], Kazuhisa NAKAJIMA, Sergei V. BULANOV [a)], Hideki DEWA [c)], Hideyuki KOTAKI and Toshiki TAJIMA [d)]

a) General Physics Institute, Moscow, Russia

b) Institute of Physics, Georgian Academy of Sciences, Tbilisi, Georgia

c) Japan Synchrotron Radiation Research Institute, Hyogo, Japan

d) Department of Physics, University of Texas at Austin, Texas, USA

In this paper we have presented experimental results and physical interpretation of a high intensity short pulse laser propagating in a gas chamber containing helium, nitrogen, and argon gases. It has been found that above a certain critical power for the laser pulse a fixed blueshift of the laser pulse $\Delta\lambda/\lambda_0 \sim 6\%$ is observed where λ_0 is the initial laser wavelength. Once above the critical power the amount of blueshift is found to be independent of the density of the gas, the power of the laser, and even the type of gas. This phenomenon of the fixed blueshift is attributed to the filamentation of the beam by nonlinear self-focusing of the pulse by the background gas. Once the laser pulse filaments, the intensity of the laser light in each filament is capped by the threshold intensity for optical field ionization of the gas. Resultingly, each filament is propagating in a density gradient generated by the ionization front. It has been shown and observed experimentally that when a short pulse laser propagates in a density gradient it is blueshifted. The fact that the blueshift is fixed corresponds to the fact that the defocusing distance of each filament is inversely proportional to the plasma density. Since the blueshift is proportional to the density, the amount of shift is independent of the density. The shift can be represented by the formula $\omega = \omega_0\sqrt{1+\lambda_0/2L_0}$ where ω is the shifted frequency and L_0 is the initial laser pulse length[1)]. These results are checked by 1D PIC simulations of the propagation of the filaments in an ionizing gas. The filament propagates at the threshold intensity for ionization and is propagated until the shift is close to that of the experiment. Figure 1 shows the spectra from the simulation of the laser pulse after propagating 5mm in the gas. The pulse has shifted towards higher Kx and, therefore, shorter wavelengths. At low powers the spectra from the experiment and simulations are similar in shape. At higher powers the amount of shift is found to be the same; however, in the experiment the pulse is completely shifted whereas in the 1D simulation there is a portion of the laser pulse remaining at the original wavelength. It is expected that this component will disappear in 2D simulations where the back of the filament can refract. Two-dimensional effects are important as the initial focusing plays a vital role in the occurrence of the filament formation. If the pulse is focused too strongly then the pulse dynamics is dominated by the initial focusing. If the initial focusing is very weak then the gas self-focusing can be dominant. These factors determine the distance over which the laser pulse focuses.

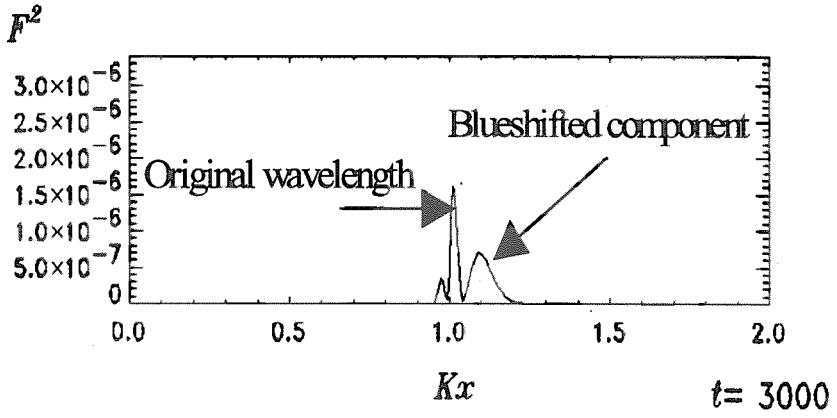

Fig. 1 PIC simulation laser spectrum

Reference

1) J. K. Koga, N. Naumova, M. Kando, L. N. Tsintsadze, K. Nakajima, S. V. Bulanov, H. Dewa, H. Kotaki, T. Tajima, Physics of Plasmas 7, 5223, 2000

4.6.4 Molecular dynamics simulation of shock phenomena due to laser irradiation

Ichirou FUKUMOTO and Etsuji OHMURA[a)]
a) Osaka University

1. Introduction

Recently, ultrashort-pulse lasers with high peak power have been developed, and their application to materials processing is expected as a tool of precision microfabrication. During the surface generation process with laser ablation, a shock wave propagates inside the material and lattice defects such as dislocations are generated beneath the surface. Lattice defects influence the quality or accuracy of materials processing, therefore it is important for laser precision microfabrication to elucidate the generation mechanism of them. In this report, laser shock phenomena of metal were analyzed using a modified molecular dynamics method [1].

2. Simulation

Monocrystalline Aluminum, which can be applied with a Morse potential[2] between two atoms, is chosen as the target of simulation. In the simulation, 400 atoms per layer and 400 layers in depth, totaling 160,000 atoms were arranged in a square configuration. Stress states of the target caused by laser irradiation of the fourth harmonics of a Nd:YAG laser with a Gaussian profile whose diameter is about 28 nm are shown in **Fig. 1**, where the average of the power density and irradiation time are 200 GW/cm^2 and 1.5 ps, respectively. Compression fields propagate from the irradiation spot to the outside as a shock wave. **Figure 2** shows the transition of the stress states in the target at every 1 ps since the start of the irradiation. The propagation velocity of the shock wave does not depend on irradiation conditions, which is equal to the elastic wave velocity of aluminum.

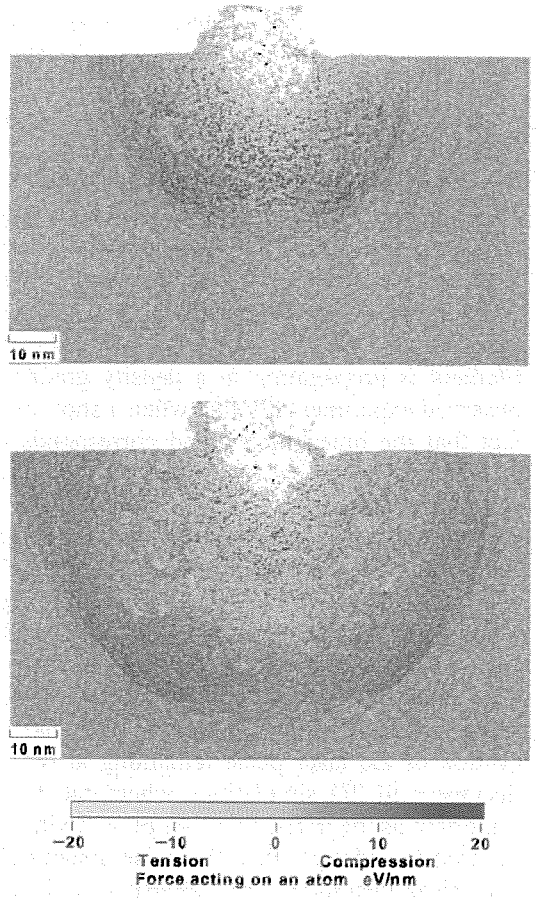

Fig. 1 Stress state of Al atoms after 200 GW/cm^2, 1.5 ps Nd:YAG (4 ω) laser irradiation, which is shown by a gray scale.

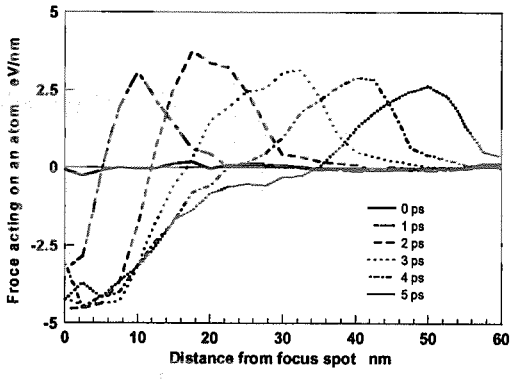

Fig. 2 Transition of the wave form at every 1 ps since the start of the irradiation Irradiation conditions are same as Fig. 1.

3. Conclusion

Laser ablation and re-solidification processes are simulated via modified molecular dynamics. Obtained results are summarized as follows:

(1) The shock wave induced by laser irradiation propagates spherically to the outside from the irradiation spot in the target.

(2) A lot of dislocations are generated from the solid-liquid interface by the propagation of the shock wave. When dislocations move with the shock wave, the velocities are near the longitudinal wave velocity. After the shock wave passes, the dislocations are slower than the traverse wave.

References

1) E. Ohmura, I. Fukumoto, Int. J. JSPE 31, 206, 1997
2) L. A. Girifalco, V. G. Weizer, Phys. Rev. 114, 687, 1959

4.6.5 Productions of hollow atoms from solids irradiated by a high intensity laser

Kengo MORIBAYASHI, Akira SASAKI and Alexei ZHIDKOV

1. Introduction

Recent progress in intense pulsed lasers gives us some new sources as high brightness x-rays, fast electrons, and multiply charged ions. These sources are efficient for the production of hollow atoms. Here we discuss the effect of the inner-shell excitation and ionization processes by fast electron impact for the production of hollow atoms. The fast electrons are generated by short-pulse high-intensity laser irradiation on a solid. Such hollow atoms have also attracted attention to the spectroscopic measurement of high density plasmas from the short pulse laser irradiation[1].

2. Atomic processes

For the calculation of the excitation and ionization cross sections, Desclaux's code[2] and BEB theory[3] are employed, respectively. The energy levels, radiative transition probabilities, and auto-ionization rates are calculated by Cowan's code[4]. We consider the 1*s*, 2*s* 2*p* bounded electrons of Mg ions, that is, the ground state, excited states, inner-shell excited states, and hollow atoms for Li-like to Ne-like ions. The initial state is the ground state of Ne-like Mg ion with the density of a solid (10^{23} cm^{-3}). The bound electrons are ionized through electron impact ionization and autoionization processes.

3. Results and discussions

For the electron impact excitation processes, we treat the excitation processes from the inner-shell 1*s* electron to the 2*s* and 2*p* in order to understand the role of these processes for the production of inner-shell excitation states and hollow atoms. Figure 1 shows the electron impact inner-shell excitation ($1s^22s \rightarrow 1s2s2p$) and ionization ($1s^22s2p \rightarrow 1s2s2p + e^-$) rates as a function of laser intensity. Both rates are almost the same at low temperature and the ionization process is a little larger at high temperature. Since the electron temperature is more than 10 keV for the high intensity laser irradiation considered here, the inner-shell ionization processes play a more important role in the production of hollow atoms. Figure 2 shows the population of hollow atoms of $2s^22p$ and $2s^22p^2$ as a function of laser intensity (I). The population increases according to about I^4 up to $I \sim 10^{18}$ W/cm^2. This comes from the fact that the electron density increases with the laser intensity.

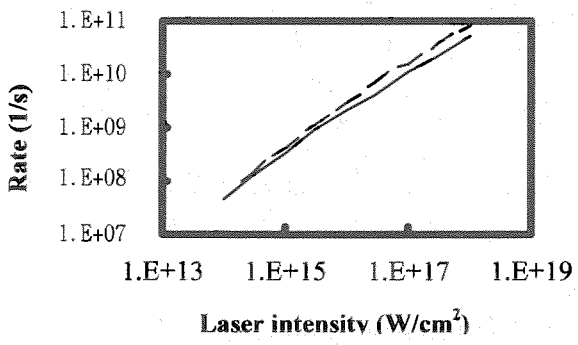

Fig. 1 Rates vs. laser intensity: excitation $1s^22s \rightarrow 1s2s2p$(solid line) and ionaization $1s^22s2p \rightarrow 1s2s2p$(dashed line)

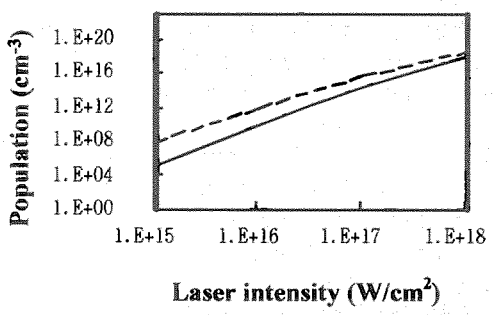

Fig. 2 Population of hollow atoms at 500 fs after laser irradiation vs. laser intensity: $2s^22p$ (solid line) and $2s^22p^2$ (dashed line)

References

1) A.Y. Faenov, J. Jr. Abdallah, R.E.H. Clark, J. Cohen, R.P. Johnson, G.A. Kyrala, A.I. Magunov, T.A. Pikuz, I.Y. Skobelev and M.D.Wilke, Proc. SPIE **3157**, 10, 1997
2) J.P. Desclaux, Comp. Phys. Comm. **9**, 31, 1975
3) Y.K. Kim and M.E. Rudd, Phys. Rev. A **50**, 3954, 1994
4) R.D. Cowan, J. Opt. Soc. Am. **58**, 808, 1968

4.6.6 Highly charged ion production by high intensity laser irradiation on Kr clusters

Kengo MORIBAYASHI, Alexei ZHIDKOV, Akira SASAKI, Keiko SUTO and Shingo SUZUKI[a)]
a) Japan Science and Technology Corporation, Kawaguchi-shi, 332-0012, Japan

1. Introduction

The interaction between giant clusters (the size of a few nm) and high-intensity short-pulse (a few 100 fs) lasers is expected to produce a high density hot plasma which continues for only about 100 fs[1)]. In the plasma, the fast electron impact forms inner-shell excited states of highly charged ions, from which short-wavelength x-rays have been emitted[2,3)]. The aim of this paper is to understand the mechanism of the production of highly charged ions with a lot of the bounded electrons in the high density hot plasma.

2. Calculation conditions

We employ the ground state of the Ni-like Kr ion as an initial state. We treat the densities of 10^{22} to 10^{24} cm^{-3} and the electron temperatures of 1 to 40 keV, respectively. We consider the electron impact ionization, electron impact excitation among the $3s$, $3p$, and $3d$ states, autoionization, and radiative transition processes.

3. Results and discussions

Figure 1 shows the population of Ne-like Kr ions as a function of time at the density of 10^{22} cm^{-3} and the electron temperature of 20 keV. We calculated the populations in cases both including and excluding inner-shell electron ($2s$, $2p$, $3s$, $3p$) ionization processes in order to understand the role of inner-shell ionization processes for the highly charged ion production. The populations including inner-shell $3s$ and $3p$ electron ionization processes and those including all the inner-shell electron ionization processes become about 10^6 and 10^8 times higher than those without inner-shell ionization processes at 100 fs, respectively. Therefore, we found that the inner-shell ionization processes play an important role in the production of highly charged ions. We will apply these atomic processes to the study of high intensity laser irradiation on giant clusters.

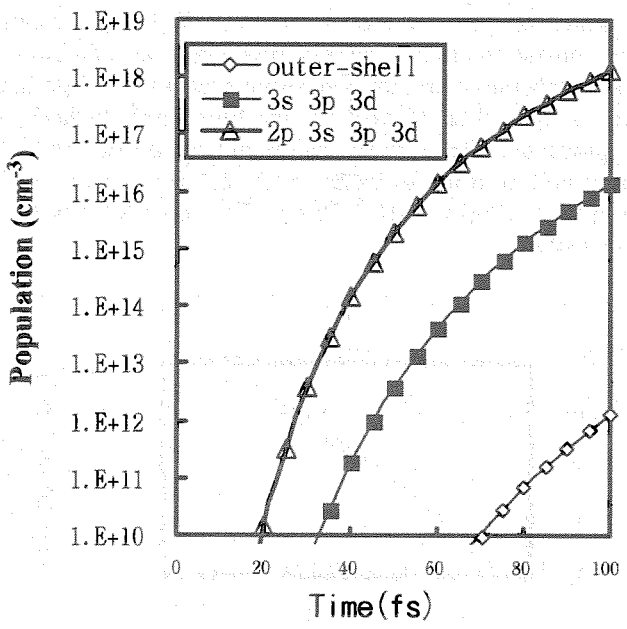

Fig. 1 Population vs. time
The states considered here to be ionized are indicated in the box.

References

1) T. Ditmire, T. Donnelly, A.M. Rubenchik, R.W. Falcone and M.D. Perry, Phys. Rev. A **53**, 3379, 1996
2) T. Ditmire, T. Donnelly, R.W. Falcone and M.D. Perry, Phys. Rev. Lett. **23**, 3122, 1995
3) A. McPherson, T.S. Luk, B.D. Thompson, A.B. Borisov, O.B. Shiryaev, X. Chen, K. Boyer and C.K. Rhodes, Phys. Rev. Lett. **72**, 1810, 1994

4.6.7 X-ray emission from hollow atoms produced by collisions of multiply charged ions with a solid

Kengo MORIBAYASHI, Keiko SUTO, Alexei ZHIDKOV, Akira SASAKI
and Takashi KAGAWA[a)]
a) Department of Physics, Nara Women's University, Nara, 630-8506, Japan

1. Introduction

Recently the production of hollow atoms has been achieved through collisions of highly charged ions with a solid[1,2], intense laser irradiation[3,4], and the interaction between high brightness x-rays and a solid[5]. Hollow atom production processes have been investigated by spectroscopy of x-rays irradiated from hollow atoms both experimentally[1] and theoretically[2]. In a laser produced plasma, atoms with relatively low atomic number such as Mg and Al can be easily ionized to hydrogen-like and fully ionized states. If a cold surface is located close to the plasma, the highly-charged ions interact with the solid surface. They capture many electrons at once to form the hollow atom state.

The aims of this study are to show (i) that the conversion efficiency to x-rays emitted from these hollow atoms is larger than the conventional $K\alpha$ x-ray source and (ii) that this x-ray emission can be used for an x-ray source.

2. Method of calculation

The x-ray emission from hollow atoms is treated with the MSCL model[2], which deals with electron capture from a solid target by the M-shell of ions, autoionization, and radiative transition processes. The average capture rate (γ^c) is assumed to be proportional to the autoionization rate (γ^a) ($\gamma^c = n\gamma^a$). Figure 1 shows the conversion efficiency to $K\alpha$ x-rays from hollow atoms (C_{hx}) generated from the collision of Ar^{17+} with a solid as a function of n. The value of C_{hx} remains almost the same at 0.04 around $n = 5$. (We also found that C_{hx} is about 0.03 for Ne^{9+} and C^{5+}+ ions.)

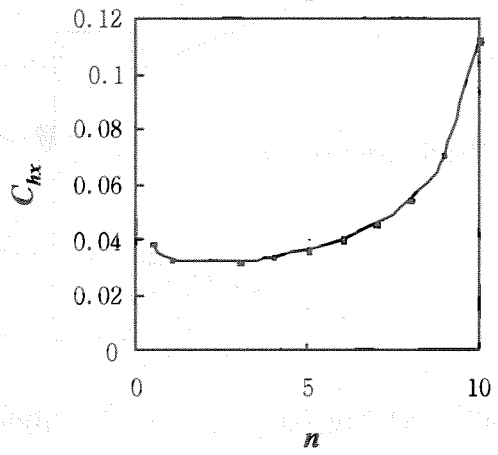

Fig. 1 Conversion efficiency to $K\alpha$ x-rays from hollow atoms for the collision of Ar^{17+} ions with a solid as a function n

The velocity distribution function of ions accelerated by hot electrons may be given by[6]

$$N(v) = N_0 \exp(-\frac{v}{C_s}), \qquad (1)$$

with the ion sound velocity $C_s = (ZkT/m_i)^{1/2}$, where Z, kT, and m_i are the charge of the ions, the hot electron temperature, and the ion mass, respectively. The total ion energy is

$$E = \frac{m_i N_0}{2C_s}\int_0^\infty v^2 \exp(-\frac{v}{C_s})dv = N_0 ZkT \sim \eta W, \qquad (2)$$

where W and η are the laser energy (in the unit of J) and conversion efficiency from the laser to the ions, respectively. Here we employ 0.1 as the typical value for η . Then the total number of ions is

$$N_{ion} = \int_0^\infty N_0 \exp(-\frac{v}{C_s})dv = N_0 \sim 10^{12} W. \qquad (3)$$

Note that N_{ion} increases with the laser energy. The conversion efficiency from laser energy to the x-ray

energy (C_{lx}) is given by

$$C_{lx} = \frac{W_{K\alpha}}{W} = \frac{\eta C_{hx} E_{K\alpha}}{ZkT} > 0.1 \times 0.03 \frac{E_{K\alpha}}{ZkT} \sim 10^{-5}, \qquad (4)$$

where $W_{K\alpha}$ and $E_{K\alpha}$ are the total x-ray energy and the energy of one x-ray photon, respectively and we take C_{hx}>0.03, $E_{K\alpha}$ ~1 keV (Z=10) and kT = 30 keV as typical values.

3. X-ray source

Figure 2 shows a concept of the hollow atom x-ray source with the use of a high intensity laser. First, a high intensity laser irradiates the foil. Then a high density plasma with highly charged ions is formed. After hollow atoms are made from the ions using a solid, high brightness x-rays are emitted. When W = 10 J, $P_{K\alpha} > 10^{13}$ x 0.03 = 3 x 10^{11} by using the total ion number of eq. (3) and C_{hx}. As the laser energy increases, the photon number becomes larger because of the larger number of fully ionized ions as mentioned before. Additionally, the pulse of the x-rays becomes shorter because of ion acceleration. (On the other hand, the photon number of the $K\alpha$ x-ray sources of the Cu target decreases as the laser intensities (I) become larger for $I > 10^{17}$ W/cm^2 [7,8].)

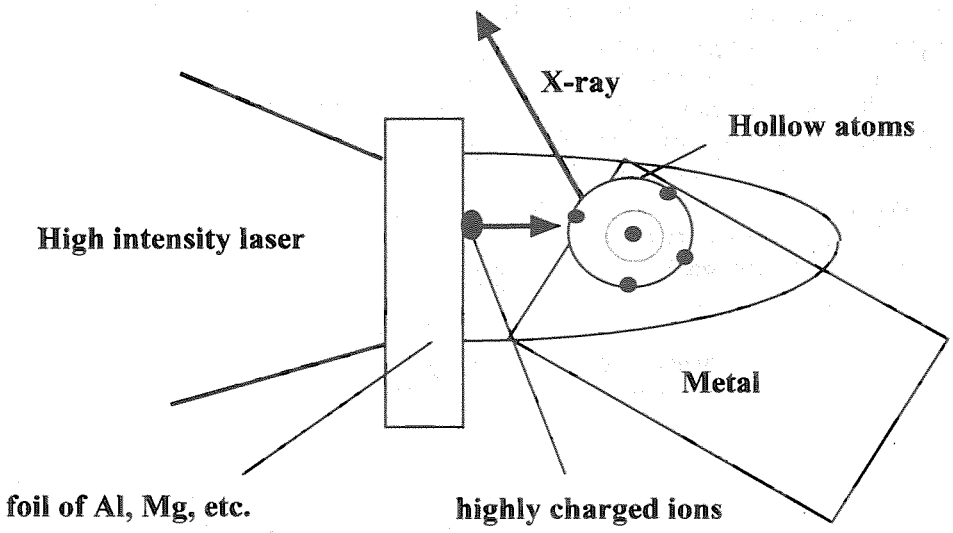

Fig. 2 Concept of a hollow atom x-ray source

References

1) J.P. Briand, G.Giardino, G. Borsoni, M. Froment, M. Eddrief, C. Sébenne, S. Bardin, D. Schneider, J. Jin, H. Khemliche and M. Prior, Phys. Rev. A **54**, 4136, 1996
2) K. Suto and T. Kagawa, Phys. Rev. A **58**, 5004, 1998
3) A.Y. Faenov, J. Jr. Abdallah, R.E.H. Clark, J. Cohen, R.P. Johnson, G.A. Kyrala, A.I. Magunov, T.A. Pikuz, I.Y. Skobelev and M.D.Wilke, Proc. SPIE **3157**, 10, 1997
4) F.B. Rosmej, A.Y. Faenov, T.A. Pikuz, A.I. Magunov, I.Y. Skobelev, T. Auguste, P. D'Oliveira, S. Hulin, P. Monot, N.E. Andreev, M.V. Chegotov and M.E. Veisman, J. Phys.B **32**, L107, 1999
5) K. Moribayashi, A. Sasaki and T. Tajima, Phys. Rev. A **58** 2007, 1998
6) A. Zhidkov, A. Sasaki and T. Tajima, Rev. Sci. Instruments **71**, 931, 2000
7) A. Zhidkov, A. Sasaki, I. Fukumoto, T. Tajima, T. Auguste, P. D' Olivera, S. Hulin, P. Monot, A.Y. Faenov, T.A. Pikuz and I.Y. Skobelev, Physics of Plasmas **8**, 3718, 2000
8) M. Yoshida, Y. Fujimoto, Y. Hironaka, K.G. Nakamura, K. Kondo, M. Ohtani and H. Tsunemi, Appl. Phys. Lett. **73**, 2393, 1998

4.6.8 Electric field effects on electron capture processes in ion-ion collisions

Shingo SUZUKI[a)], Toshizo SHIRAI, Akira SASAKI, Kengo MORIBAYASHI,
Shin-ichi NAMBA, Tetsuya KAWACHI and Noriyuki SHIMAKURA[b)]
a) Japan Science and Technology Corporation, Kawaguchi-shi, 332-0012, Japan
b) Department of Chemistry, Faculty of Science, Niigata University, Niigata-shi, 950-2181, Japan

1. Introduction

The electron capture in ion-ion collisions in high density plasmas occurs under a strong electric field by other charged particles. However, the studies on the electric field effects on the electron capture are still very limited. In the present work, electron capture cross sections in collisions between $O^{5+}(1s^22s)$ and C^{6+} ions have been calculated under a static and homogeneous electric field. The collision energy and field strength ranges studied here are 0.25-4 keV/amu and 0-514 MV/cm, respectively (The field strength of a proton at a distance of the Bohr radius is 5.14 GV/cm).

2. Calculational method

A semi-classical close-coupling method based on a molecular-orbital expansion was used in this calculation. The field effects have been included up to the first order of the field strength, *i.e.*, the energy shift by the Stark effect and the coupling brought about by the field. This means that the shifts of the potential energies and the non-adiabatic couplings by the *field-induced* polarization are neglected in this approximation. Therefore the scattering wavefunction is expanded by the molecular-orbitals with the electron translation factor (ETF) [1)]. In this treatment, a set of close-coupling equations in the electric field is as follows:

$$i\frac{dc_i}{dt} = \varepsilon_i c_i + \sum_j \left[\vec{v}\cdot(\vec{P}+\vec{A})_{ij} + \vec{E}\cdot\left\langle \phi_i^{MO}\left|\vec{r}\right|\phi_j^{MO}\right\rangle\right] c_j, \qquad (1)$$

where, $\vec{r}$ is the electron coordinate, ε_i the energy of the molecular state without the field, $\vec{v}$ the relative velocity between the target and the projectile, $(\vec{P}+\vec{A})$ the coupling term with ETF, c_i the transition amplitude of state i, and $\vec{E}$ the electric field vector. In the field-free case, this equation is just equal to the standard close-coupling equation[1)].

3. Results

The calculations are done for various field directions. The most strong variation of the transition probability is found for the field direction being parallel to the collision plane and perpendicular to $\vec{v}$, because the potential energy shifts, *i.e.*, the diagonal terms of the transition moment in the second term of the summation in the equation (1), are larger than those of the other field direction during the collision. Figure 1 shows the cross sections averaged over the field angle. In comparison of the field free case with the case of E=514 MV/cm, the electric field increases the cross sections. This field effect becomes appreciable in the lower collision energy range due to the long interaction time of the collision.

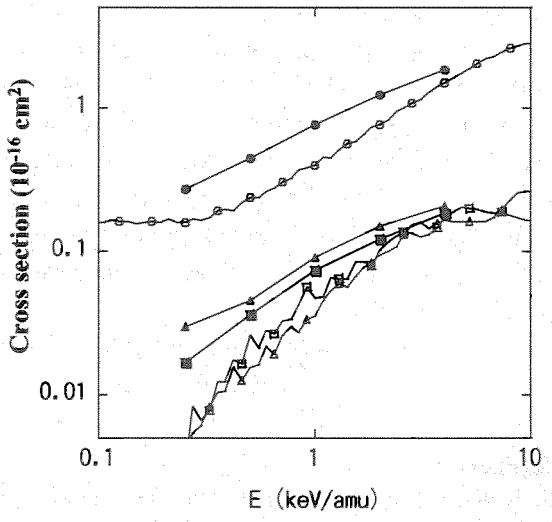

Fig. 1 Cross sections for the (O^{5+} + C^{6+}) system Circles, boxes, and triangles are the capture into C^{5+}(n=2) levels, C^{5+}(n=3) levels and excitation to O^{5+}(1s3l) levels, respectively. Open symbols are the field free case, and solid symbols are in the case of E=514 MV/cm.

Reference

1) M.Kimura *et al.*, Phys. Rev A **28**, 2085, 1983

4.6.9 Spectral data for nickel-like ions: Cu II through Kr IX

Toshizo SHIRAI and Joseph READER[a)]
a) National Institute of Standards and Technology, Gaithersburg, Maryland 20899

1. Introduction

We have undertaken critical evaluation of spectral data for nickel-like ions in relation to research and development of x-ray lasers. Critically evaluated data are indispensable not only to identify observed spectrum but also to assess reliability of the atomic energy levels and transition probabilities calculated with computer codes. We consulted two comprehensive compilations for wavelengths by Kelly[1)] and Shirai et al.[2)]. In the former, however, the literature up to 1980 was surveyed. Since then, much work on these spectra has appeared. All relevant papers on wavelengths and energy levels published through December 2000 were collected and surveyed, and the best measured data in our judgement, based on a consistency check or experimental uncertainty, have been adopted. In cases where a single measurement is available, we have adopted it as the recommended data.

We have compiled wavelengths, energy levels, line classifications, and intensities for about 5000 lines. For each spectrum we give a review of the literature from which the data are taken. This is followed by tables containing classified lines with designations of the upper and lower energy levels, and intensities. Owing to limited space, the brief review for the ions except for singly ionized copper, Cu II, and the wavelength tables are not given here.

2. Brief comments on the Cu II ion

Kaufman and Ward[3)] measured the $3d^{10}\ {}^1S_0$ - $3d^9 4p\ {}^1P_1^o$, ${}^3D_1^o$, ${}^3P_1^o$ transitions at 1358.7736A, 1367.9508A, and 1472.3946A with an estimated uncertainty of 0.0006A, by using a hollow-cathode discharge. An extensive measurement with a similar light source was performed by Ross[4)] in the wavelength range from 1979 to 11227A. Including the above three lines and the $3d^9({}^2D)4s\ {}^3D_1$ - $3d^8({}^3F)4s4p({}^3P^o)\ {}^5D_1^o$ and $3d^8 4s^2\ {}^3P_0$ - $3d^8({}^3P)4s4p({}^3P^o)\ (6)_1^o$ lines at 1147.762A and 1807.85A of Shenstone[5)], Ross identified 1822 lines as transitions between levels in the $3d^9ns$ (n=4-10), $3d^9np$ (n=4-7), $3d^9nd$ (n=4-8), $3d^9nf$ (n=4-7), $3d^9ng$ (n=5-7), $3d^8 4s^2$, and $3d^8 4s4p$ configurations. [The $3d^8({}^3P)4s4p({}^3P^o)$ level without a major component is represented by the symbol $(N)_J$, the index N increasing with energy from the lowest level (N=1) for each J.] In addition, ten weak lines in the range of 2009-2200A, observed by Shenstone[5)], were identified. These lines have also been adopted here. In Ross' analysis, a total of 351 levels were determined, of which classifications were given by Sugar and Musgrove[6)] in jj-coupling for the configuration $3d^9ns$ and in jl-coupling for $3d^9nf$ and $3d^9ng$. These level values were used to drive the wavelengths of 479 lines in the vacuum ultraviolet region by using the Ritz combination principle. These lines are in good agreement with earlier analyses by Shenstone[5)] and Kaufman and Ward[3)]. We have also adopted these results.

The uncertainty of wavelengths is estimated to be less than 0.005A for the lines longer than 2000A and 0.0005A for ones in the vacuum ultraviolet.

References

1) R. Kelly, J. Phys. Chem. Ref. Data **16**, Suppl. 2, Part II, 1987
2) T. Shirai, J. Sugar, A. Musgrove and W.L. Wiese, J. Phys. Chem. Ref. Data, Monograph 8, 2000
3) V. Kaufman and J.F. Ward, J. Opt. Soc. Am **56**, 1591, 1966
4) C. B. Ross, Wavelength and Energy Levels of Singly Ionized Copper, Cu II, Report LA-4498, Los Alamos Scientific Laboratory, 1979
5) A.G. Shenstone, Proc. Roy. Soc. (London) A**235**, 195, 1936
6) J. Sugar and A. Musgrove, J. Phys. Chem. Ref. Data **19**, 527, 1990

4.6.10 Development of the hierarchical atomic model (HIA) and its application to the transient collisionally excited x-ray lasers

Akira SASAKI

1. Introduction

In order to develop x-ray lasers in the short wavelength regime (<40Å) using a table top size pumping source, the optimization of the excitation condition is extremely important. I report the development of a sophisticated atomic model to predict ion fraction, level population, and the soft x-ray gain of the transient collisionally excited (TCE) x-ray lasers and their temporal and spatial evolution. The results of the calculation are compared with experimental gain of the Ni-like Ag lasers.

2. Model

The soft x-ray gain of the Ni-like Ag laser at λ=13.9 nm is produced from the population inversion between $3d^9 4d(5/2, 5/2)$ J=0 and $3d^9 4p(5/2, 3/2)$ J=1 level. However, the population of these levels is determined in connection to hundreds of other levels from Ni-like and other charge states. The present HIA model is designed to include states with different averaging methods, which enable me to calculate the soft x-ray gain and the ion fraction at the same time, keeping the total number of the states in the model relatively small ($\leqq$500) [1]. For the $3d^9 4l$ and other lower excited configurations of the Ni-like ion, I have calculated the energy level and rate coefficients of excitation and ionization processes in detail using the HULLAC code [2]. On the other hand, for the higher excited configurations ($3d^9 nl$, $n \geqq 6$), double- or inner-shell excited states, and states in other charge states are averaged.

3. Results and discussion

Figure 1 shows the calculated gain of the Ni-like Ag laser, pumped by two 2ps, 10^{15} W/cm^2 laser pulses. The interval of the pulses is 1.5 ns. It is found that the gain appears immediately after the heating of the preformed plasma by the second laser pulse. The calculation reveals the importance of having an appropriate pedestal level in the pumping laser to maintain the plasma temperature ($\geqq$10 eV) and the population of the Ni-like ions. Furthermore, I have investigated the formation and quenching channels of the upper and lower laser level in detail to obtain the saturation intensity as shown in Fig. 2. The HIA model can be applied to the calculation of the x-ray spectrum of the high temperature plasmas. The model will be applied to the spectroscopy of the short pulse laser produced plasmas as well as other laboratory and space plasmas.

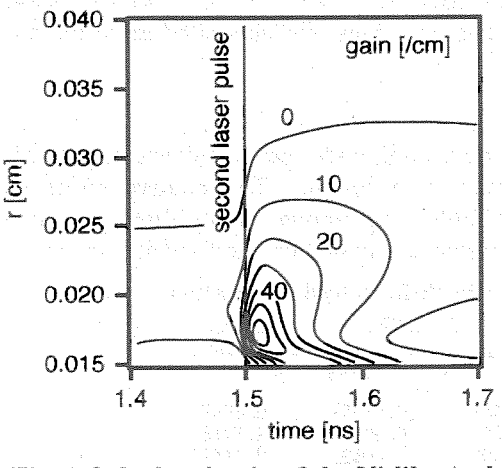

Fig. 1 Calculated gain of the Ni-like Ag laser pumped by two short laser pulses

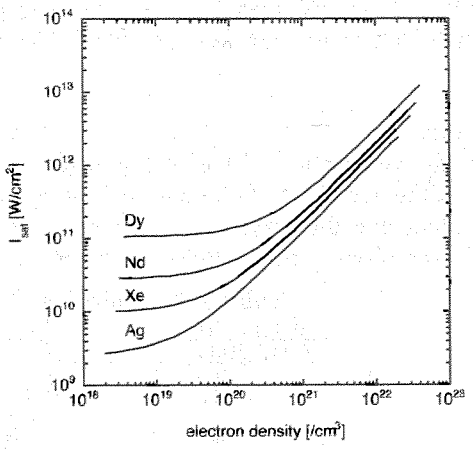

Fig. 2 The saturation intensities of the electron collisionally excited ni-like Ag, Xe, Nd, and Dy lasers

References

1) A. Sasaki, T. Utsumi, K. Moribayashi, M. Kado and T. Kawachi, Proceedings of the 12th Topical conference of atomic Processes in Plasmas, edited by R.C. Mancini and R.A. Phanef, AIP conference proceedings, **547**, 133, 2000

2) M. Klapisch and A. Bar-Shalom, J. Quant. Spectrosc. Radiat. Transf. **58**, 687, 1997

4.6.11 Accurate numerical solver for the free and bound states of the Schrödinger and Dirac equations based on the CIP method

Takayuki UTSUMI

1. Introduction

In the calculation of the atomic database necessary for simulating plasma emission and absorption spectra via a collisional radiative model, the accurate numerical solutions of the Schrödinger and Dirac wave equations for arbitrary central potential $V(r)$ are required. There are numerous numerical methods described in texts and technical papers. However, only a few computer codes could deal with arbitrary fields and energies without requiring some previous experience of the user. The main reason of the lack of a general-purpose solver is the difficulty in systematic control of the accumulation of the truncation errors. Therefore, robust solvers are continuously desired.

We have developed the solver which provides accurate numerical solutions for the free and bound states of the Schrödinger and Dirac wave equations for the central fields. The main characteristics of the code are (1) the potential and radial wave functions are represented by the CIP (Constrained Interpolation Profile) method[1] in which not only the physical values but also their derivatives are defined on the grid points, (2) the free states at the far field are represented by the PA (Phase-Amplitude) method[2] which allows the use of the logarithmic grid system, (3) the ASCRK (Adaptive Step size Controlled Runge-Kuta) method[3] is adopted as the ODE (Ordinary Differential Equation) integrator to control the integration accuracy.

2. Method of solution

The potential energy, such that $V(r) \to 0$ when $r \to \infty$ and $rV(r)$ is finite for $r = 0$, is approximated by the CIP method. With this assumption, the analytical value at the vicinity of the origin for the regular solution is obtained. Then we can integrate the wave equation outwardly with the ASCRK method requiring the relative integration error in each step should be within 10^{-12}. In the evaluation of the derivatives of the Schrödinger and Dirac equations, the potential is estimated by the CIP method which accurately interpolates values at any point. For the bound state (energy <0), the outward solution is extended up to the turning point, and the inward solution is also calculated from the far region up to the same point. Then the two solutions at the turning point are compared to find the correction value for the eigenvalue. The above procedure continues until obtaining the matched continuous wave function and the eigenvalue. For the free state (energy >0), the outward integration is carried out up to the point where the interval of the grid points is insufficient to represent the oscillation of the wave. At this point, the phase and the amplitude are calculated as the starting value for the PA method. Then the ODEs for the phase and amplitude, which are equivalent to the Schrödinger and Dirac equations, are integrated up to the far grid point.

3. Results

For the verification of the proposed algorithm and the developed code, we calculated bound and free sates in the Coulomb field and compared with the analytical solution. The relative errors of the eigenvalues and the wave function were within 10^{-8}. In Table 1 are shown the oscillator strengths for several transitions in the hydrogen atom. We can see the sum rule is satisfied with sufficient accuracy.

Table 1 The calculated oscillator strength for a hydrogen atom

Initial state	1s	2s	2p	
Final state	np	np	ns	nd
n=1			-0.13873	
2	0.41620			
3	0.07910	0.43487	0.01359	0.69578
4	0.02899	0.10276	0.00304	0.12180
5	0.01394	0.04193	0.00121	0.04437
6	0.00780	0.02163	0.00062	0.02163
7	0.00481	0.01274	0.00036	0.01233
8	0.00318	0.00818	0.00023	0.00776
n=9 to 50	0.01067	0.02608	0.00073	0.02387
Line spectrum	0.56470	0.64819	-0.11894	0.92754
Continuous Spetrum	0.43508	0.35146	0.00782	0.18326
Total	0.99978	0.99964	-0.11112	1.11080

References

1) T. Yabe and T. Aoki, Comput. Phys. Commun. **66**, 219, 1991
2) A. Bar-Shalom and M. Klapish, J. Oreg, Comput. Phys. Commun. **93**, 21, 1996
3) W.H. Press *et al.*, Numerical Recipes in Fortran 77, Cambridge Univ. Press, 1986

4.7 Applications of High Peak Power Lasers

Hiroyuki DAIDO

1. Introduction

Recently, high intensity ultra-short pulse lasers have been used in various fields such as pump probe measurement[1,2], a few MeV x-ray and ion generation[3,4]. I will describe recent activity of the application aspects of the high peak power lasers prepared at the Advanced Photon Research Center. One of the interesting applications is x-ray generation from a laser-produced plasma and its applications. The essence of the laser-produced plasma is that a laser can feed its ultra-high energy density in to the matter. Then the absorbed energy is transferred into the electrons, which excite and ionize atoms. The intense x-ray with wide range of spectrum is emitted from the excited atoms. The x-ray radiation is useful for many applications. Another important applications include ultra-short laser driven chemistry and femto-second pump-probe technique for measurement of structural changes in various materials.

2. Various kinds of laser driven x-ray sources

(1) Soft x-ray radiation from a highly ionized plasma:

Intense soft x-ray spectrum has been investigated. One of the main issues in soft x-ray applications is the production of debris. To overcome such a problem, we propose to use gas-puff target created by the pulsed injection of high-density gas through a nozzle. The result would allow for the development of an efficient and debris-less laser plasma x-ray source that would be useful for applications in various fields[5]. Very strong soft x-ray intensity from a double nozzle gas-puff target as shown schematically has been tested. The intensity is comparable to that from a solid one[6]. The pico and femto-second laser pulse has also created a high density high temperature plasma which provides kilo-electron volt intense x-ray source[7].

(2) Ultra-short x-ray sources

A femto-second laser pulse creates a high-energy electron beam through the laser-matter interaction processes. The electrons penetrate into the solid. Then they ionize inner-shell electrons efficiently[8]. The short pulse K-alpha line emission whose photon energy ranges between 1 keV to 60 keV occurs efficiently driven by the optimum shooting conditions such as intensity on target and pre-pulse level which may optimize the energetic electron energy distribution[9]. We will perform the experiments to optimize the emission property at the specific wavelengths.

(3) Ultra-high intensity laser driven laser-plasma x-ray sources

If the laser intensity on target is beyond 10^{19}W/cm^2, an electron is accelerated to the relativistic velocity during a one optical cycle. In this regime, energetic electrons from the plasma become a directional beam. As a result, ultra-short x-ray pulse is generated[10]. Hard x-ray and energetic ions are generated efficiently and they also become directional beams [11] which are useful for various applications as an intense, compact and safety radiation sources.

3. Summary

The laser-plasma sources are able to deliver x-ray which is close to or beyond the practical levels. Basic laser plasma interaction study with a practical point of view opens up the new attractive fields for basic sciences as well as industrial applications. High peak power lasers also provide a lot of useful applications such as a field of Chemistry.

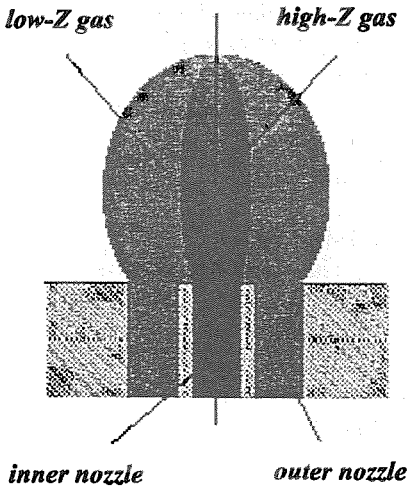

Fig. 1 Schematic diagram of the double target

References

1) C. Rischel *et al.*, Nature **390**, 490, 1997
2) C. Rose-Petruck *et al.*, Nature **398**, 310, 1999
3) S. P. Hatchett *et al.*, Phys. Plasmas **7**, 2076, 2000
4) M. Yamagiwa *et al.*, Phys. Rev. E**60**, 5987, 1999
5) H. Daido *et al.* Appl. Phys. B**72**, 385, 2001
6) H. Fiedorowicz, H. Daido *et al.*, Opt. Commun. **184**, 161, 2000
7) D. Altenbernd *et al.*, J. Phys. B: At.Mol.Opt.Phys. **30**, 3969, 1997
8) Ch. Reich *et al.*, Phys. Rev. Lett. **84**, 4846, 2000
9) A. Zhidikov *et al.*, Phys. Rev. E**62**, 7232, 2000
10) Y. Ueshima *et al.*, Laser and Particle Beams **17**, 45, 1999
11) P. A. Norreys *et al.*, Phys. Plasmas **6**, 2150, 1999

4.7.1 Development of a laser-plasma ion source at the Advanced Photon Research Center

Hiroyuki DAIDO, Koichi YAMAKAWA, Mitsuru YAMAGIWA, Yukio HAYASHI, Satoshi ORIMO, Takashi ARISAWA and Yoshiaki KATO

1. Introduction

Recently, high intensity short pulse lasers have been used in various fields such as pump probe measurement for ultra-fast phenomena in crystalline materials[1,2], a few tens of MeV x-ray for driving nuclear reactions and directional ion generation [3,4]. In this report, we will introduce the preparation of the project on the laser-driven ion generation and its applications to the medical accelerator as an ion injector performed at the Advanced Photon Research Center in collaboration with the groups listed above.

2. Design and manufacture

For the cancer treatment, desired properties of an ion source for patients is listed as; (1) 10^9 ions per second, (2) particle energy of ~100 MeV/nucleon, for a carbon ion, >1GeV is necessary. At present, a carbon ion source for cancer treatment costs too expensive to be popular in the medium size hospitals. Figure 1 shows the schematic drawing of the energetic ion production by laser shooting. The ions in the co-axial direction of the laser illumination are most useful to be fed into the next beam cooling and acceleration stages. The issues to be studied are listed below;

(1) Efficient conversion of laser energy into the energetic electrons which are created via relativistic laser-plasma interactions. We are very much interested in the high energy tail of the electron distribution functions which may be play significant role to accelerate ions.

(2) Efficient generation of energetic ions via the electrostatic potential driven by the energetic electrons. We will measure the energy distribution as well as angular distribution. The important issue for this purpose is how many ions at the specific energy with the desired energy band and desired solid angle for next stage device.

(3) Mechanism of the ion acceleration influenced by ionization time, especially for the heavy ions such as carbon ions[5]. The charge to mass ratio of the ions is very important parameter for the heavy ion accelerator. We have to investigate ionization processes by laser field.

(4) Get rid of hydrogen contamination from the surface of the laser irradiated target surface. Hydrogen atoms are easily ionized and its charge to mass ratio is high. Therefore most of the laser energy goes into the proton acceleration rather than higher atomic number ions. Removal of hydrogen contamination is very important subject for the energetic heavy ion production.

(5) Transport of the energetic ions from the laser driven ion source to the vacuum. The charge neutralization in a bunch of the energetic ions is very important for long scale propagation.

(6) Large scale particle simulation[4] contributes to make the guideline of the experiment.

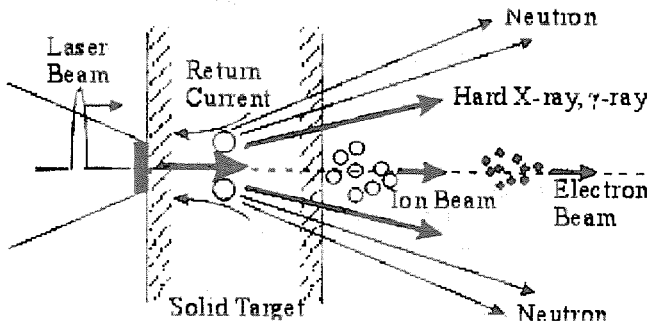

Fig. 1 The energetic ion production by laser shooting

3. Summary

The laser-plasma based energetic ion generator is able to deliver ions which are further accelerated for the cancer treatment by a small ion accelerator. Basic laser-plasma interaction study with a practical point of view opens up the new attractive fields not only the practical applications but also the new aspects of the basic sciences.

References

1) C. Rischel *et al.*, Nature **390**, 490, 1997
2) C. Rose-Petruck *et al.*, Nature **398**, 310, 1999
3) S. P. Hatchett *et al.*, Phys. Plasmas **7**, 2076, 2000
4) M. Yamagiwa *et al.*, Phys. Rev. E**60**, 5987, 1999
5) A. Zhidkov *et al.* Rev. Sci. Instrum. **71**, 931, 2000

4.7.2 Soft x-ray generation from laser irradiated gas-puff target

Masayuki SUZUKI[a)]*, Susumu YAMAGAMI[a)]*, Keiji NAGAI[a)], Takayoshi NORIMATSU[a)], Kunioki MIMA[a)], Youichi MURAKAMI[b)], Takeyoshi NAKAYAMA[b)], Wei YU[c)], Henryk FIEDOROWICZ[d)], Il Woo CHOI[a)]**, and Hiroyuki DAIDO*

a) Institute of Laser Engineering Osaka Univercity
b) School of Scence & Engineering, Kinki University
c) Shanghai Institute of Optics and Fine Mechanics
d) Institute of Optoelectronics, Warsaw, Poland
*Advanced Photon Reserch Center, JAERI
**_Present address_: Center for Optical Micro Device System, Dongshin University

1. Introduction

Soft x-ray emission from laser produced plasmas has been studied for many years. The gas-puff target[1)] can avoid debris productions from laser produced plasma. Therefore, laser produced gas-puff plasmas is applicable to proximity x-ray lithography, soft x-ray projection lithography, x-ray microscopy, solid-state and atomic physics. In order to investigate the interaction between a nano-second laser pulse and the gas puff target, we have measured the transmitted laser pulse through the gas-puff target using a bi-planar phototube and a calorimeter[2)].

2. Experimental setup

A commercial Nd: YAG laser (HOYA Continuum YG682) that delivered laser energy of 0.7 J in 8 ns at 1064 nm was used. The laser beam was focused with a plano-convex lens with a 100 mm focal length, giving the total intensity of about 10^{12} W/cm^2. A solenoid-driven pulsed valve with a 500 μm-diameter circular nozzle was used. The laser irradiated the gas-puff target perpendicularly with respect to the flow of the gas. The focused position was about 0.5 mm from the nozzle. The valve was backed with a gas having a pressure of 10 atm. We have measured the average density of argon gas at the place of 0.5 mm from the nozzle, where the laser beam was focused about 10^{19} atoms/cm^3 under the backing pressure of 10 atm. By changing the time delay t_{del}, which is between the laser pulse and the electric pulse that drives the coil, we could change the target size and the gas density at the interaction region. We have used neon (Ne Z=10), argon (Ar Z=18), krypton (Kr Z=36), and xenon (Xe Z=54) as a gas-puff target. The absorption of laser energy was measured by the laser energy transmitted through the gas-puff target with a collection lens of 87.5 mm focal length coupled with a bi-planar photo-tube (Hamamatsu R1328U-01) for the time resolved transmission measurement or with a calorimeter for accurate measurement of transmitted laser energy. The band-pass and Neutral Density (ND) filters were also placed in front of these detectors to remove the undesired visible light and to attenuate the laser energy. The calorimeter was also placed in front of the target to measure the back scattered laser light which was measured to be less than 2% of the irradiation laser energy. Soft x-ray pulses from the laser produced plasma were measured with the x-ray silicon detector (XRD AXUV-HS1) which was located at 90 degrees from the laser propagation axis and was placed at 72 mm from the gas-puff nozzle. We have also performed the time and space resolved gas-puff plasma imaging using an x-ray streak camera (Hamamatsu C5920). The temporal resolution of the streak camera was about 50 ps. The 200 μm wide slit was placed at 90 degrees from the laser axis and placed at 336 mm in front of the streak camera. A 0.35 μm-thick Zr coated 0.35 μm-thick C_8H_8 filter was placed in front of the slit. Transmitted x-ray spectrum between 5 and 20 nm wavelength region was measured.

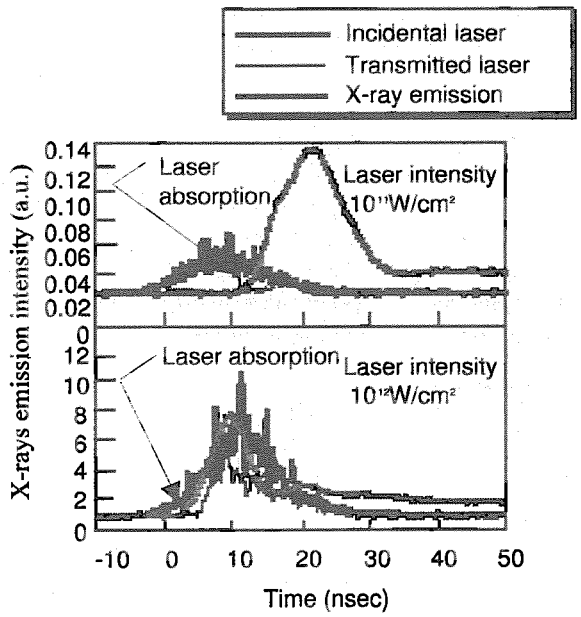

Fig. 1 The laser energy transmitted through the gas-puff target backed with 10 atm The time delay is 470 μs.

3. Experimental results and discussions

The time history of the soft x-ray radiation at 5-20 nm wavelength region from the argon gas-puff plasma is shown in Fig. 1 super-imposed with the transmitted laser pulse through the Ar gas-puff target. At the leading edge of the laser pulse, the laser pulse did not interact with a gas-puff target. The laser intensity

increased. First, the electrons were generated by the multi-photon ionization by the laser field. Then the electron avalanche took place after the electrons were accelerated by the strong laser field so-called breakdown process. Then the electrons acquired energy via the inverse bremstrahlung absorption. Through the electron-atom or ion collisions, atoms were excited and ionized. The x-ray emission occurred. During and after the laser irradiation, the laser produced plasma expanded. Finally, the gas-puff plasma was cooled down. An x-ray emission after the laser irradiation was due to the recombination process.

The slit images of the soft x-ray streak records for the krypton and xenon gas-puff plasma (white region) were shown in Fig. 2. The spectral range includes from 8 to 20 nm. The laser pulse propagates from the left to the right as shown in the top of Fig. 2. The krypton gas-puff images were shown in (a) and (b), that of the xenon was shown in (c) and (d). The delay time of the laser irradiation from the gas-puff ejection signal was 250 μs for (a) and (c), 300 μs for (b) and (d), respectively. When the delay time was 250 μs, the peak of x-ray emission is observed at about 3 ns from the leading edge of the x-ray pulse, where the incident laser pulse width was 8 ns. The gas-puff plasma expands radially outward from the center. On the other hands, the delay time was 300 μs, the place of the laser produced plasma was shifted toward the laser propagation axis and then the peak of x-ray emission is found at about 10 ns from the leading edge of x-ray pulse. Using the krypton gas-puff target after a 300 μs delay time, we found that the x-ray image was divided into two components. Especially the x-ray image in the right hand side of Fig. 2(b) moved from the left the right along the laser propagation direction when the delay time was 300 μs. On the other hand, the x-ray image in the left hand side did not move so much. Using the solid targets, the size and place of the plasmas did not change and move. We are now investigating the details of the interaction processes of these phenomena concerning the laser focusing and defocusing in the gaseous medium.

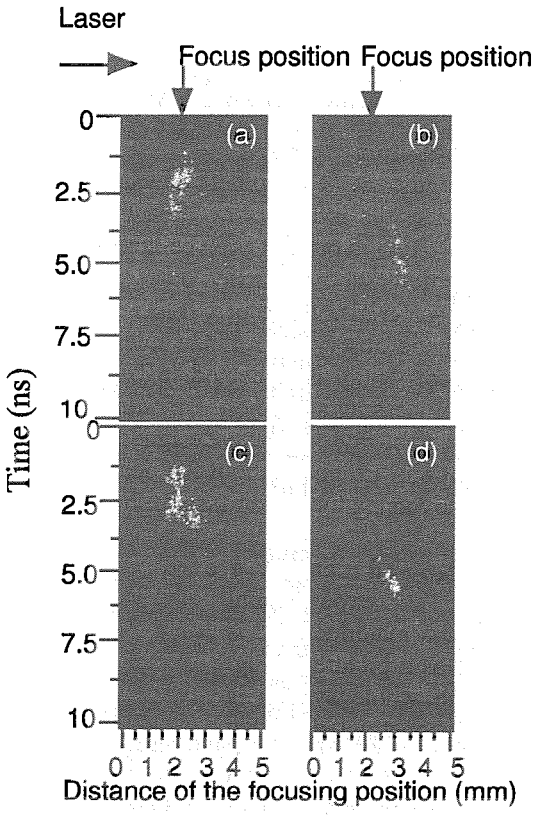

Fig. 2 Streak records of the x-ray emission images (white region) for Kr shown in (a) and (b), and Xe in (c) and (d) The backing pressures are 10atm.The laser incidents from the left. The delay time of the laser irradiation from the gas injection signal is 250 μs for (a) and (c), 300 μs for (b) and (d), respectively.

4. Conclusion

We have investigated precisely the interaction processes between a nano-second laser pulse and a gaseous medium using time and space-resolved x-ray and optical measurement techniques resulting in an efficient laser energy absorption of the gas-puff target especially for the high atomic number elements. We found that the x-ray emission started from a laser plasma after the laser absorption started. The processes of plasma formation, heating, expansion and cooling are investigated experimentally. We are now performing the same kind of experiment using a femto-second laser to obtain more general understanding the gaseous target interaction with laser pulses.

Acknowledgment

The authors are indebted the stuffs of the ILE Osaka University and Advanced Photon Research Center, JAERI. This work was partly supported by special coordination fund of Science and Technology Agency of Japanese Government.

Referance

1)H. Fiedorowicz, A. Bartnik, M. Szczurek, H. Daido, N. Sakaya, V. Kmetik, Y. Kato, M. Suzuki, M. Matsumura, J. Tajima, T. Nakayama, T. Wilhein Opt. Commun. **163** pp103-114 (1999).

2)M. Suzuki, S. Yamagami, K. Nagai, T. Norimatsu, K. Mima, Y. Murakami, T. Nakayama, W. Yu, H. Fiedorowicz , I. W. Choi, and H. Daido "Study on a High Brightness X-ray Source from a Laser Produced Plasma" *2nd International Conference on Inertial Fusion Sciences and Application (IFSA2001) Kyoto International Conference Hall, Kyoto Japan, Sept. 9-14, 2001* to be submitted and references therein.

4.7.3 Design and manufacture of an experimental apparatus for the study on the chemical reactions using soft x-ray

Yuichi SHIMIZU

1. Introduction

Recently, the development of various types of x-ray source is currently under way, so that we should be able to use the intense x-ray beams for the studies of material, life, environmental sciences in the near future. Also in our research center, an active development of x-ray laser which mainly emits lights of soft x-ray regions is being carried out. It is well known that soft x-ray beams are effectively absorbed in many kind of materials. Therefore, it is necessary to understand fundamental processes in physics and chemistry through the observation of the interaction between soft x-ray with materials. By the advances in their fields, soft x-ray is expected to be utilized in many applications such as surface physics, lithography, micro-processing and so on. For the purpose of application in chemistry field, especially chemical reaction, of the soft x-ray, we have designed the experimental apparatus and have manufactured. In this, detailed descriptions are given about the design and manufacture of the experimental apparatus. A brief discussion of a study using the apparatus will be also given.

2. Design and manufacture

An experimental apparatus manufactured is shown as a picture in Fig. 1. The whole system is mainly constructed by two parts, one a vacuum chamber part and the other an interlock system part. The former is equipped with reaction vessel for the soft x-ray irradiation and the latter is an inspection and protection system against accidental vacuum break at the chamber. Inner dimensions of the chamber are 400 mm ϕ $\times$ 375 mmH. The pressure in the whole system is maintained under 10^{-7} Torr with oil rotary pump (250 L/s) and turbo molecular pump (250 L/s). The chamber consists of a reaction vessel holder, a fluorescent screen beam monitor, Be window of 200 μm thickness and a beam intensity detector with a 5 μm thick diamond coated Si plate. The reaction vessel was composed of a Pyrex glass cylindrical vessel (volume: 0.71 ml, diameter: 3 mm, length: 100 mm) with a Si_3N_4 window (200 μm thickness) for the incidence of soft x-ray beams. This vessel was attached to the holder on a movable X-Y stage (200 $\times$ 200 mm^2) in the chamber, in where the holder is on a level with the center of the beams. Interlock system part is mainly constructed by a fast closing shutter, isolation valve and pressure sensor. In this system, the pressure change is detected in milliseconds order by the sensor against accidental vacuum break at the chamber, and the shutter is closed in the same time order to protect the beam source etc. from the brekage. One particularly exciting application of soft x-ray on the chemistry field is the environmental science such as the conversion into nontoxic substances of hormarably active agents, for example, phenols.

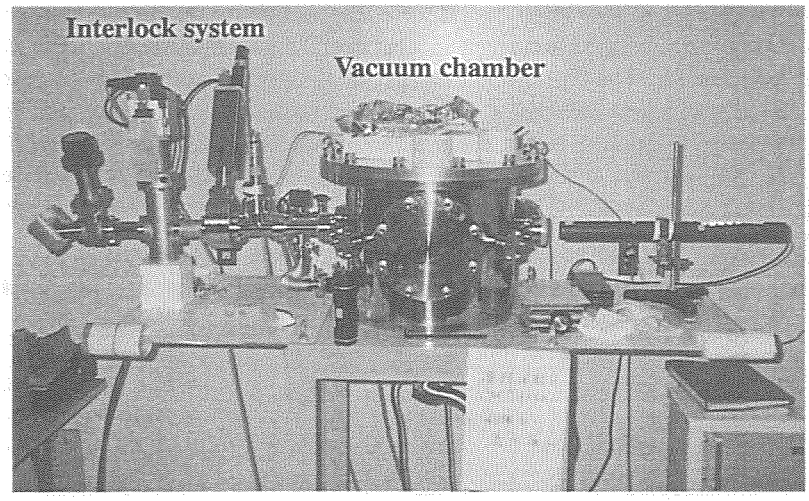

Fig. 1 An experimental apparatus manufactured

4.7.4 Global *ab initio* potential energy surfaces of the lowest three doublet states (X^2A', A^2A', and X^2A'') for the BrH_2 system

Yuzuru KUROSAKI

1. Introduction

Hydrogen abstraction and hydrogen exchange reactions of the XH_2 (X = halogen) system have been the subjects of great importance in the study of elementary chemical reactions. Many theoretical studies of both classical and quantum dynamics have been done for the BrH_2 system so far; it is surprising, however, that few ab initio calculations have been carried out for this system as compared to the FH_2 and ClH_2 systems. In this study we have carried out high-level ab initio calculations for the lowest three doublet states, X^2A', A^2A', and X^2A'', for the BrH_2 system, and present global analytical potential functions fitted to the ab initio data.

2. Methods of calculation

Potential energy surfaces for the lowest three doublet states, X^2A', A^2A', and X^2A'', for the BrH_2 system, which originate from the triply degenerate ^2P state of Br, have been calculated at the CASSCF(9,6)/aug-cc-pVTZ level of theory. Dynamical electron correlation effects were estimated using second-order multi-configuration perturbation theory (CASPT2). The calculated ab initio data were fitted to the analytical functional form which has a many-body expansion. Thermal rate constants for the ground-state potential were calculated using variational transition state theory with the tunneling correction.

3. Results and discussion

Contour plots of the ground-state potential around the TS regions for the H + HBr → H_2 + Br (abstraction) and H + H'Br → H' + HBr (exchange) reactions are depicted in Figs. 1 and 2, respectively. The potential energies are given in kcal mol^{-1} relative to the H + HBr asymptote and both the reactions are set be collinear. The barrier heights for the abstraction and exchange reactions were calculated to be 0.4 and 9.2 kcal mol^{-1}, respectively. Calculated and measured rate constants for these reactions are summarized in Table 1. The present result for abstraction is in good agreement with the previous calculation,[1] but is somewhat smaller than experiment.[2] The present rate constant for exchange is much larger than the previous calculation.[1] This is because the barrier height for exchange of our potential surface is smaller than that of the previous one.

Table 1 Calculated and experimental rate constants for the abstraction and exchange reactions around the room temperature (cm^3 $molecule^{-1}$ s^{-1})

Abstraction				Exchange			
T(K)	Theory	Expt.	Ref.	*T*(K)	Theory	Expt.	Ref.
300		6.00 (-12)	2	300	4.26 (-19)		1
	4.48 (-12)		1		2.54 (-17)		This work
	3.46 (-12)		This work				

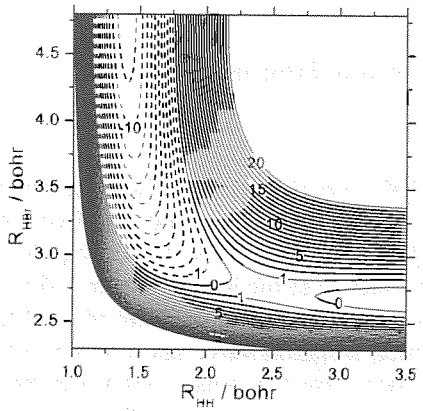

Fig. 1 Potential surface around the TS for abstraction

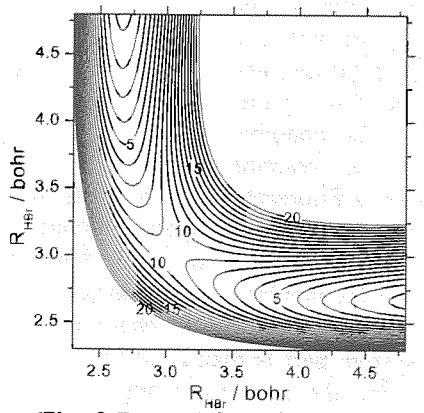

Fig. 2 Potential surface around the TS for exchange

References

1) G. C. Lynch, D. G. Truhlar, F. B. Brown and J.-G. Zhao, J. Phys. Chem. **99**, 207, 1995
2) D. Husain and N. K. H. Slater, J. Chem. Soc., Faraday Trans. 2 **76**, 276, 1980

4.7.5 Temperature dependence of ultrafast structural relaxation in complex systems

Hiroshi MURAKAMI

1. Introduction

The structural dynamics of complex systems, such as liquids, polymers and biomolecules, is currently a topic of interest. Extensive experimental studies have clarified the existence of several universal features in the structural dynamics of complex systems, while various theories for interpreting them are under lively discussion[1]. In order to study the structural dynamics of complex systems, we developed an experimental system for the femtosecond time-resolved fluorescence (FTRF) spectroscopy using an ultrashort laser pulse and measured the FTRF spectrum of a coumarin dye in glycerol at room temperature [2]. We can study the energy relaxation in the electronic excited state of a dye molecule, i.e., a probe molecule, in complex systems by the FTRF spectroscopy. The energy relaxation is due to the structural relaxation of the surroundings of the probe molecule. In the case of the coumarin dye in glycerol, it has been found that the energy relaxation occurs owing to the vibrational relaxation (~100 fs), fast β - process [3,4] (~1 ps) and α - relaxation [5,6] (~ 100 ps) of the matrix. Although we expect to study the structural dynamics on an atomic length scale by a laser-plasma X-ray pulse, it is necessary to measure other dynamic behaviors such as in the electronic and vibrational states in order to obtain the comprehensive understanding of the structural dynamics. Further, we can clarify mechanisms underlying dynamical phenomena such as reactions and biological functions through those investigations.

Most of the FTRF experiments for dye molecules in liquids have been done with a optical flow-cell system only at room temperature, because the dye molecule undergoes a breakdown due to a dense light excitation. It is effective to change experimental conditions such as temperature and pressure in order to clarify the mechanism of the structural dynamics [7]. Thus, we have developed a temperature control system in which the dye molecule is free from the breakdown due to a dense light excitation in the FTRF measurement.

2. Experimental procedure

Our experimental system for the FTRF spectroscopy is described in detail [2]. We employed a coumarin dye dissolved in a mixture of ethanol and methanol with a voluminal ratio of 4:1 as a sample. The sample was excited by the second harmonic (410 nm) of the laser pulse. A liquid nitrogen flow-type cryostat was used to control the temperature of the sample. The cryostat was moved up and down at a velocity of about 10 mm/s with a stepping-motor driven translation stage.

3. Experimental results

We measured the time profile of the fluorescence intensity of the sample at a certain delay time at 150 K over a hundred seconds to confirm whether the breakdown of the dye molecule occurs. It has been found that the fluorescence intensity is constant during the observation if the cryostat is moved, while it decays owing to the breakdown of the dye molecule with a time constant of several ten seconds if not. Further, the FTRF decay curve was measured ten times with moving the cryostat, and almost no difference was observed among the decay curves. Thus, we can say that the breakdown of the dye molecule does not occur as long as the cryostat is moved. We measured the FTRF intensity of the sample between 295 K and 130 K. The time profile of it was dependent on temperature even in the ultrashort time range below a few picoseconds. Further, the peak energy shift from the excitation energy within the temporal resolution < 200 fs in the FTRF spectrum at 295 K was larger than that at 230 K. This is the first experimental result which shows that even ultrafast energy relaxation depends on temperature, as far as we know.

References

1) See, for example, Proceedings of the International Discussion Meeting on Relaxations in Complex Systems, edited by K. L. Nagai and G. B. Wright [J. Non-Cryst. Solids 131-133, 1991]; ibid., edited by K. L. Ngai, E. Riande and G. B. Wright [J. Non-Cryst. Solids 172-174, 1994]
2) H. Murakami, J. Mol. Liq. **89**, 33, 2000
3) T. Kanaya, T. Kawaguchi and K. Kaji, J. Chem. Phys. **98**, 8262, 1993
4) R. Zorn, A. Arbe, J. Colmenero, B. Frick, D. Richter, and U. Buchenau, Phys. Rev. E**52**, 781, 1995
5) J. Colmenero, A. Alegria, J. M. Alberdi, and F. Alvarez, Phys. Rev. B**44**, 7321, 1991
6) A. Arbe, D. Richter, J. Colmenero, and B. Farago, Phys. Rev. E**54**, 3853, 1996
7) H. Murakami, T. Kushida, H. Tashiro J. Chem. Phys. **108**, 10309, 1998

4.7.6 Strong field ionization of nitrogen atoms and ions prepared by a prepulse

Junkei KOU, Akito SAGISAKA, Yuji FUKUDA, Yutaka AKAHANE, Norihiro INOUE,
Hideki UEDA, Hiroyuki DAIDO and Koichi YAMAKAWA

1. Introduction

Optical field ionization (OFI) of atoms has been extensively investigated since the invention of high intensity lasers[1,2]. In those studies, all targets were limited to noble gas atoms due to their handiness as an atomic source. The OFI of atoms other than the noble-gas elements should provide the meaningful information, interpolating or complementing the noble-gas results. Through our recent research activity, we have found that the nitrogen atoms or ions can be prepared via photodissociation of the nitrogen molecules driven by a prepulse and have demonstrated the field ionization of the nitrogen atom for the first time.

2. Experimental

A high intensity laser beam was delivered from a chirped-pulse amplification Ti:sapphire laser system which was described elsewhere[3]. In this experiment the peak intensity at the focal spot was estimated to be 1.3 x 10^{17} W/cm^2 after the calibration based on the OFI of He gas. The intensity ratio of the prepulse and the main pulse was 1:20 measured with a pin photodiode. Ions produced at the focal spot was extracted by a DC electric field (9444 V/m) toward a micro-channel-plate detector following a 1043 mm-long field free drift tube. The time of fight (TOF) spectra were averaged over 300 laser shots by a digital oscilloscope. To avoid space charge effect, the pressure of nitrogen gas was kept below 1 x 10^{-7} Torr.

3. Results

We observed non-split, single peaked signals for each N^{z+} (z=1-5) species in the TOF spectrum for a high field (10^{17}W/cm^2) experiment (Fig. 1-a), where the detection axis was perpendicular to the polarization direction. In all the OFI experiments of N_2 so far, nothing or very weak signals were observed in this perpendicular set up [4,5]. Instead, they observed split peaks for N^{z+} (z=1-3) resulting from Coulomb explosions with the detection axis parallel to the polarization direction. At a low intensity of 10^{15} W/cm^2 we also obtained the same split peaks as seen in Fig. 1-b, where the detection axis was 75° to the laser polarization. The single peaks observed in Fig. 1-a would arise from the OFI of the atomic nitrogen, N and/or N^+, since the molecular nitrogen must undergo the Coulomb explosion after the multiple ionization and thus gives the split peaks. The atomic nitrogen would be formed by an interaction with the prepulse because of the low contrast ratio (1:20) and the high peak intensity. It should be mentioned that the peak intensity applied in this study is the highest so far in the OFI experiments of N_2. We conclude that the present strong prepulse enables the observation of the OFI of the atomic nitrogen.

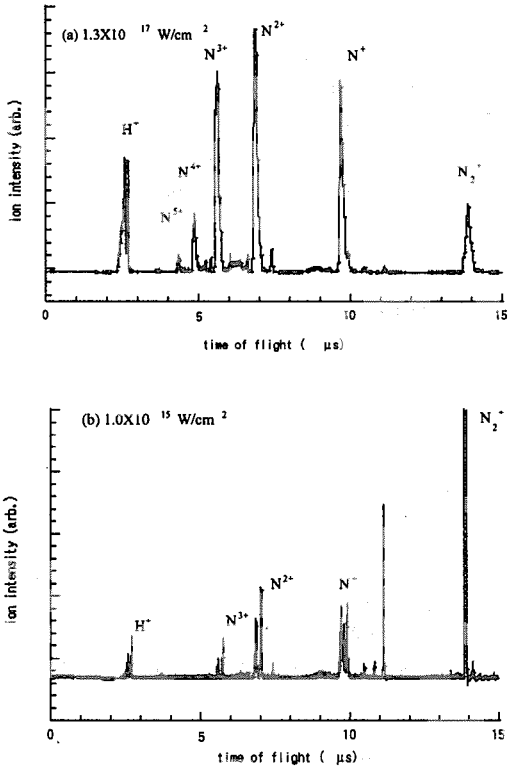

Fig. 1 TOF spectra of N_2

References

1) S. Augst, D. D. Meyerhofer, D, Strickland and S. L. Chin, J. Opt. Soc. Am. B. **4**, 858, 1991
2) E. A. Chowdhury, C. P. J. Barty and B. C. Walker, Phys. Rev. A **63**, 042712, 2000
3) K. Yamakawa, M. Aoyama, S. Matsuoka, T. Kase, Y. Akahane and H. Takuma, Opt. Lett. **23**, 1468, 1998
4) M. Schmidt, S. Dobosz, P. Meynadier, P. D'Oliveira and D. Normand, Phys. Rev. A **60**, 4706, 1999
5) Ph. Hering and C. Cornaggia, Phys. Rev. A **59**, 2836, 1999

4.7.7 Soft X-ray spectra from laser-irradiated high pressure gas puff target

Koichi OGURA

1. Introduction

When a laser beam is focused on materials (solid or gas), a hot and dense plasma is produced. The plasmas have provided a number of fruitful fundamental studies and applications. For example, the plasma is used in an X-ray source, and multicharged ion source. However, copious debris are produced in a laser-irradiated solid target. The debris give damage to X-ray optical components. It is necessary to develop the debris-free target. We have developed the high pressure gas puff target as the debris-free target and investigated the soft X-ray spectra from the gas puff target. Here, the intensity dependence of the soft X-ray emission from Ar gas puff target on the backing pressure is reported.

2. Experimental

The schematic diagram of the experimental equipment is shown in Fig. 1. The gas puff target was made by expanding gas through a nozzle. The nozzle was installed in a vacuum chamber. The throat of the nozzle was 800 μm in diameter, and the jet expansion half angle was 45°. The flow of the gas through the nozzle was initiated by a fast solenoid valve. The backing pressure of the valve was changed in the range from 0.6 to 6.3 MPa. The pressure in the vacuum chamber was maintained on the order of 10^{-5} Torr before the opening of the valve. The laser plasma was produced by focusing the laser beam (λ = 532 nm) produced with an Nd:YAG laser system. The laser beam irradiated the gas jet transversely with respect to the flow of the gas and the laser focus was placed 1.0mm above the nozzle tip. The laser pulse energy was 530mJ and the pulse duration of the laser was about 7 ns. The time delay between the laser pulse and the opening of the valve was chosen to be obtained the maximum x-ray emission. The soft X-ray spectra were measured by the monochromator. The monochromator was placed perpendicular to the laser beam and the gas flow.

3. Results

In Fig. 2 the relative peak intensity values for two selected lines belong to different charge states of Ar (Ar^{7+} 3s-4p at 158.9 Å and Ar^{9+} $2s^22p^5$-$2s2p^6$ at 165.5 Å) are shown as a function of backing pressure at fixed laser energy of 530 mJ.

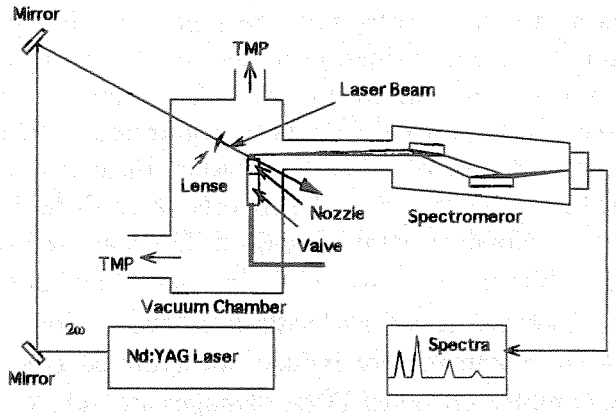

Fig. 1 Experimental apparatus to investigate soft X-ray emission from an Ar gas puff target irradiated with an Nd:YAG laser

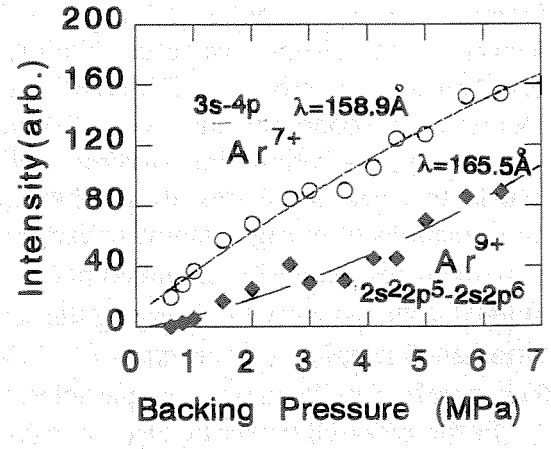

Fig. 2 Measured peak intensity of the Ar^{7+} 3s-4p line at 158.9 Å and Ar^{9+} $2s^22p^5$-$2s2p^6$ line at 165.5 Å

5. Synchrotron Radiation Science

Osamu SHIMOMURA

JAERI actively researches the following 6 fields in the synchrotron radiation sciences.

In the materials science at high pressure, liquid selenium exhibits semiconductor-to-metal transition under high pressure. The structure of liquid selenium was found to change at the boundary in the pressure-temperature phase diagram. BC_2N compounds have useful properties such as extreme hardness like a diamond. The BC_2N growth under high pressures and high temperatures was observed in situ using a multi-anvil type high-pressure apparatus. The cubic BC_2N phase is stable between 1250 and 2000℃. The phase separation into diamond phase and cubic BC_2N phase starts at temperatures above 2000℃.

In the field of the interface structure analysis of materials, the new x-ray diffractometer connected with an molecular beam epitaxy (MBE) chamber was installed in the BL11XU to get structural information on the growing surfaces of Ⅲ - Ⅴ group semiconductors. Another new x-ray spectrometer was constructed to measure the resonant inelastic x-ray scattering and to investigate electronic structure of strongly correlated transition metal oxides, including high-Tc cuprates and colossal magnetoresistance (CMR) manganites. The orbital-ordered Mott insulator $LaMnO_3$ shows $d_{3x^2-r^2}/d_{3y^2-r^2}$-type orbital-order below 780 K. Perovskite crystals including the precious catalyst metal such as palladium, $LaM_{1-x}Pd_xO_3$ (M=Fe, Co) are expected to realize a self-regeneration of the metals by reduction-oxidation fluctuation in the automotive exhaust gas without auxiliary treatment. The x-ray anomalous diffraction found that Pd occupies the B-site in the compound in the oxidation atmosphere, segregates out from the compound and forms small metallic alloy particles with Co in the reduced atmosphere, resulting in maintaining high catalytic activity.

In the research field of surface chemical reaction, the precise control of Si oxidation is important for nano-fabrication of gate insulators used in Si-based LSI. The O_2 molecules incident energy dependence of dissociative chemisorption on Si(001) surfaces was investigated by O-1s photoemission measurements in the incident energy up to 3 eV. Two incident energy thresholds (1.0 and 2.6 eV) were found to correspond to a potential energy barrier for O_2 chemisorption at Si dimer backbonds and oxidation at the second Si layer backbonds, respectively. Different crystal phases of carbon nitride (CNx) have been theoretically proposed, but most of them have not been experimentally confirmed. Near edge x-ray absorption fine structure (NEXAFS) spectra of CNx films were measured to clarify the local structures around nitrogen sites. The experiment supports three different coordinations of nitrogen atoms to carbon atoms. Yields of strand breaks of DNA as well as base damages induced in hydrated plasmid DNA film by γ -rays and α -particles have been studied systematically by changing the scavenger concentration and hydration level. For γ -irradiated samples, certain types of clustered DNA damage are induced in hydrated DNA. For samples irradiated with α -particles, more complex clustered DNA damages are induced.

In the research of heavy element materials, a new circular dichroism (CD) measurement system was installed in the BL23SU. The photon flux in the energy from 0.5 to 1.8 keV was realized to be 10^{11} photons/sec/100mA/0.02%band-width. The system provides great opportunities for the study of very weak CD signals in the soft x-ray region. X-ray absorption spectroscopy was applied to graphite, diamond, amorphous carbon films and microporous carbon to get information about the electronic structures. Spectral features of microporous carbon consist of the sum of the spectra from –COOH and >C=O groups.

In the research of the electronic and phonon properties of strongly correlated systems, the nuclear resonant scattering of ^{40}K nuclei in KCl was observed for the first time. The

electronic structures and vibrational studies on potassium in materials and biological substances are opened. Bragg angular dependence of the quantum beat in nuclear resonant scattering on $FeBO_3$ was observed in the reflections (hhh) with h = 4n +2. The Bragg angular dependence of polarization factors contributes to the quantum beat of the time spectra. The isostructural compounds $Yb_2Co_3X_9$(X=Ga, Al) show the heavy-fermion antiferromagnets for X=Al, but mixed-valence behavior for X=Ga. A difference of the electronic structures for both compounds was investigated using high-resolution photoemission spectroscopy. The origin of the change from the mixed-valent Ga-based compounds to the heavy fermion Al-based compounds is attributed to the rise of the 4f energy level and possible decrease in the 4f-ligand hybridization strength. The one-dimensional halogen bridged transition metal compounds, $[Ni(chxn)_2Br]Br_2$ to investigate the properties of the one-dimensional electronic state under the influence of strong electron-lattice interactions and electron-electron correlations. Angle-resolved photoelectron spectroscopy shows only one band having 0.5 eV energy dispersion in the first half of the Brillouin zone.

In the research and development on instrumentation and techniques of synchrotron radiation, diamond double-crystal monochromator was installed in Bragg geometry in the BL11XU. The crystals work well without significant deformation. In order to investigate the radiation fields around the insertion device beamline, photo-neutron spectra were measured outside the hutch of the BL11XU. The SAND Ⅱ code shows the neutron spectra within the factor 2 of the experimental data.

5.1 Beamline

5.1.1 A soft X-ray beamline BL23SU

Akane AGUI, Akitaka YOSHIGOE, Takeshi NAKATANI, Yoshikazu MIYAHARA[a)]
a) Japan Synchrotron Radiation Research Center

1. Introduction

BL23SU[1)] is an only soft x-ray beamline along JAERI beamlines. This has a high energy-resolution monochromator[2)]. At the beamline, soft x-ray spectroscopy studies in a wide variety of applications, such as surface chemistry, and condensed matter physics, are going.

Researches are performed not only by the JAERI beamline scientists but also by public users. During the 2000AB term, five experiments and sixty-four shifts were offered for JASRI users. They had studied gas-phase physics[3)] and biology[4)].

2. The new vacuum chamber for the ID23

An insertion device (ID23) had been installed as a light source in the storage ring at BL23IN. This is a double-array variable undulator of advanced planar polarized light emitter type (APPLE-2 type or Sasaki-type). ID23 is sitting at upper 2 m-section in the 4 m-straight section. The magnetic structure of ID23 consists of four permanent magnet rows. ID23 is of an out-vacuum type. The gap distance varies from 300 to 36 mm at present. The first harmonic (fundamental) radiation covers the energy region from 0.5 to 3 keV in the circular polarization. The gap is able to close down to 20 mm mechanically but technical requirement, during the commissioning of the SPring-8 storage ring has limited the ID gap distance at 36 mm.

To get lower energy with the first harmonic, we have replaced the vacuum chamber to a thinner chamber. Figure 1 shows the new vacuum chamber of ID23. The outer thickness of the chamber is 19 mm and inner size is 15 mm. The replacement was carried out during the winter shout-down period of the SPring-8 (2000 Dec.-2001 Jan.) by Ishikawajima-Harima heavy Industries, which is the company who made the original chamber. Using the new chamber, the ID gap distance can reach 25 mm and the lowest energy can be down to 0.3 keV. The low energy operation will start after the legal procedure for safety.

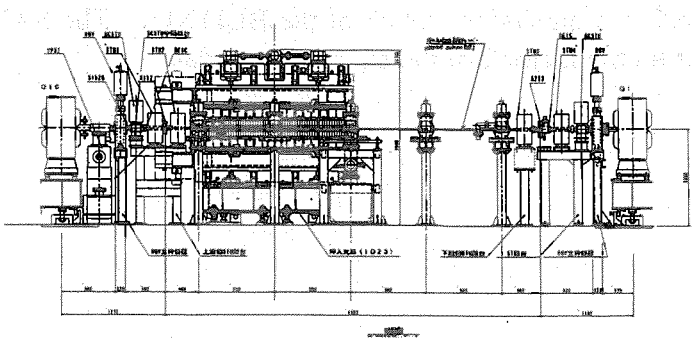

(a)

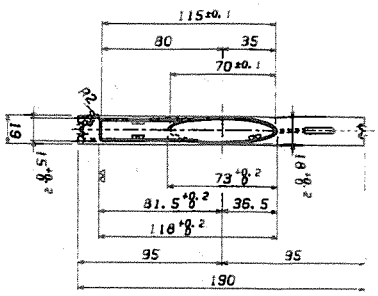

(b)

Fig. 1 (a) Side View of ID23, (b) The cross section of the new vacuum chamber

References

1) A. Agui, A. Yoshigoe, T. Nakatani, Y. Teraoka, Y. Saitoh, A. Yokoya, JAERI-Tech, 2001-043
2) Y. Saitoh, Y. Teraoka, A. Agui, A. Yoshigoe, and A. Yokoya, Nucl. Instrum. Methods (2001), to be published
3) M. Oura, H. Yamaoka, K. Kawatsura, J. Kimata, T. Hayashi, T. Takahashi, T. Koizumi, M. Terasawa, Y. Itoh, Y. Awaya, A. Yokoya, A. Agui, A. Yoshigoe, Y. Saitoh, Phys. Rev., **A63**, 14704, 2000
4) M. Tanaka, K. Nahagawa, T. Koketsu, A. Agui and A. Yokoya, J. Synchrotron Rad., **8**, 1009, 2001

5.1.2 Outline of new JAERI beamline in SPring-8

Hiroyuki KONISHI, Hideaki SHIWAKU, Kazukiyo TOZAWA and Takahisa SHOBU

The construction of a new JAERI beamline in SPring-8, a quantum structure physics beamline BL22XU, was authorized in a revised budget of FY2000. This beamline will be used mainly for following research objects.

(a) High-pressure studies by using a multi-anvil press or diamond anvil cells.
(b) Resonant X-ray scattering experiments for the observation of the magnetic structure or the orbital ordering of many kinds of interesting materials such as actinide compounds of 5f-electron system.

A high energy X-ray is useful for the purpose (a). Oppositely, a low energy X-ray is needful for the purpose (b). In addition, sufficient inspection and protection against an accidental scattering of radioactive samples both inside and outside of the evacuated beamlines must be considered in designing the system in order to handle actinide samples for the purpose (b).

An in-vacuum type undulator with a magnet period of 38 mm will be used as the light source. The design of the front-end follows the X-ray undulator beamline standard in SPring-8. However, a movable beryllium window will be adopted instead of a standard fixed-type one in order to avoid the large absorption of the low energy X-ray by the window. A differential pumping system will protect the vacuum of the front-end in the windowless state.

The basically layout of the transport channel of BL22XU is shown in Fig. 1.

BL22XU will have one optical hutch and two experimental hutches in the experimental hall of storage-ring facility, and one experimental hutch in the radioactive controlled area of RI laboratory. Exp. Hutch-1 and 3 are utilized mainly for high-pressure studies and resonant X-ray scattering, respectively.

Two double crystal monochromator, DXM1 and DXM2, will be installed in the optical hutch. DXM1 will provide the monochromatic high energy X-ray of 35 keV to 70 keV. DXM2 will be able to cover the low energy range of 3 keV to 37 keV. Si(111) plane crystals cooled by liquid nitrogen will be used as monochromator crystals.

Beryllium lens will be prepared in the optical hutch for focusing of the high energy X-rays. Focusing of low energy X-rays will be performed by a mechanical bent mirror and cylindrical mirrors installed in Exp. Hutch-2.

Several fast gate valves and acoustic delay lines will be installed in the transport channel in order to protect the vacuum of the beamline from accidental vacuum break which occur at end stations.

All apparatus and components have been ordered till the end of FY2000. The construction will be completed in the March of 2002.

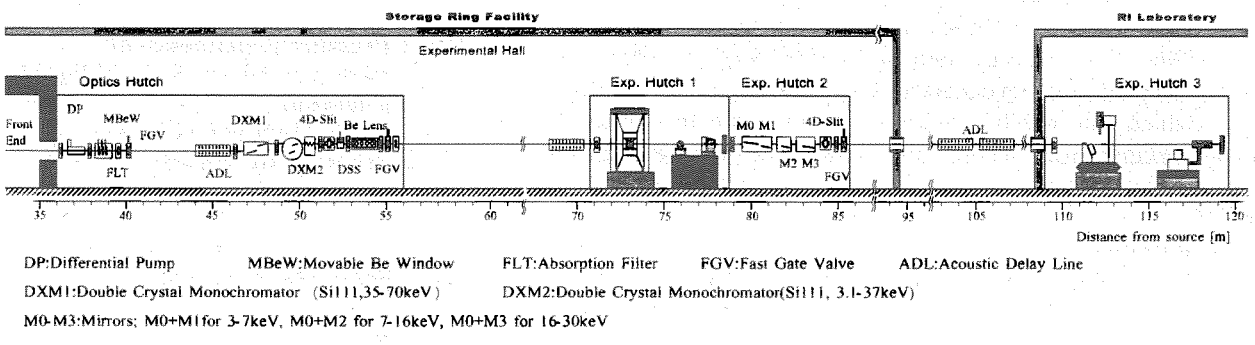

Fig. 1 Layout of BL22XU transport channel

5.2 High pressure science

5.2.1 X-ray diffraction study on structural change in liquid selenium under high pressure

Yoshinori KATAYAMA, Takeshi MIZUTANI*, Wataru UTSUMI, Osamu SHIMOMURA and Kazuhiko TSUJI[a)]

a) Department of Physics, Keio University

*Present address: SPring-8 Service Co. Ltd.

1. Introduction

At ambient pressure, liquid selenium (l-Se) is a semiconductor. It consists of long chain molecules in which each atom is covalently bonded to two neighbors. Previous X-ray diffraction studies have revealed that the structure of l-Se under pressure differs from that at atmospheric pressure: structure factor of l-Se at 8.4 GPa is similar to that of liquid tellurium (l-Te) at atmospheric pressure[1,2]. This result suggests that l-Se exhibits semiconductor-to-metal (SC-M) transition under pressure because l-Te is metallic. In fact, Brazhkin *et al.* have found that electrical conductivity of l-Se increased abruptly at a boundary in the pressure-temperature phase diagram[3]. The boundary has a negative slope ($dT/dP < 0$) and the triple equilibrium point is located at P=3.6±0.5 GPa and T=900±20 K[3]. In order to study relation between the structural change and the SC-M transition, we have measured EXAFS[4] and X-ray diffraction[5] for l-Se along a path that crossed the reported boundary.

2. Experimental

Energy dispersive X-ray diffraction experiments were carried out using a cubic-type multi-anvil apparatus (SMAP180) installed on JAERI materials science beamline I (BL14B1) at the Spring-8. Sodium Chloride sample capsule was used. Total 12 diffraction data were obtained in a pressure range from 2.2 GPa to 4.9 GPa and a temperature range from 850 K to 1210 K.

3. Results and discussion

Figure 1 shows pressure dependence of structure factor, $S(Q)$, of l-Se. The structure factor obtained just above the melting point at 2.2 GPa was very similar to that at ambient pressure reported by Waseda[6]. Above 3.5 GPa, however, the shape of the structure factor started to change: a ratio of the height of the first peak to that of the second peak increased with increasing pressure. The ratio also increased with increasing temperature at around 4 GPa. The pressure dependence of $S(Q)$ is similar to concentration dependence of $S(Q)$ for liquid Se-Te alloy[7], which also exhibits SC-M transition with increasing Te concentration. These results indicate that the SC-M transition is accompanied by a change of structure.

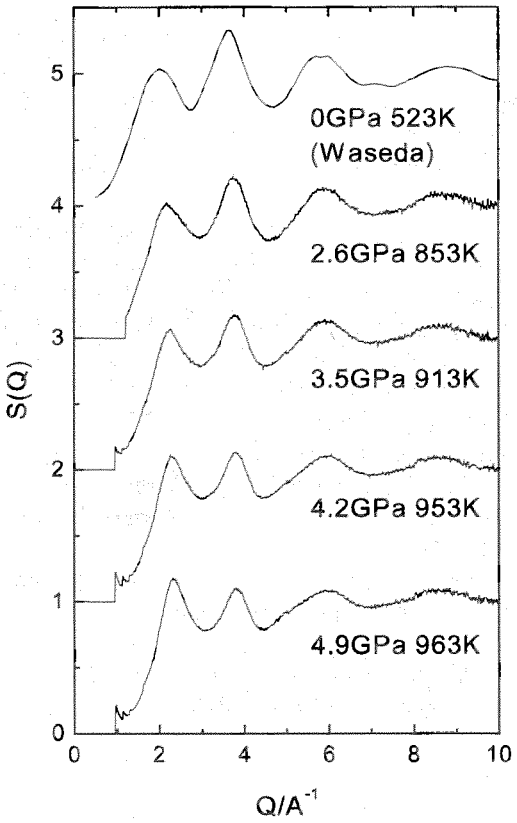

Fig. 1 Pressure dependence of structure factor, $S(Q)$, of liquid selenium
The data at 0 GPa was reported by Waseda[6].

References

1) K. Tsuji, O. Shimomura, K. Tamura, H.Endo, Z. Phys. Chem. Neue Folge **156**, 495, 1988
2) K. Tsuji, J. Non-Cryst. Solids **117&118**, 27, 1990
3) V. V. Brazhkin, R. N. Voloshin, S.V. Popova, JETP Lett. **50**,424, 1989
4) Y. Katayama, J. Synchrotron Rad. Res., **8**, 182, 2001
5) Y. Katayama, T. Mizutani, W. Utsumi, O. Shimomura, K. Tsuji, phys. stat. sol. (b) **223**, 401, 2001
6) Y. Waseda, *The Structure of Non-Crystalline Materials* (McGraw-Hill, 1980)
7) R. Bellissent, Nucl. Instrum. Methods **199**, 289, 1982

5.2.2 *In situ* x-ray observation of cubic BC_2N formation under high pressures and temperatures

Wataru UTSUMI, Taku OKADA, Ken-ichi FUNAKOSHI[a)], Osamu SHIMOMURA
a) Japan Synchrotron Radiation Research Institute

1. Introduction

Since cubic BC_2N compounds have a diamond-like structure in which some of the carbon atoms are substituted with boron and nitrogen atoms, they are expected to have useful properties, similar to diamond and cubic boron nitride, such as extreme hardness, wide band gaps, and high melting points. Several attempts to synthesize the cubic BC_2N phase have been made by the high pressure/temperature technique, but its single phase has not been obtained yet. In the present study, we have carried out an in situ x-ray experiment under HP/HT to observe the phase transitions of this material, and measured its bulk modulus by a compression at hydrostatic conditions.

2. Experimental

Experiments were carried out using a multi-anvil type high-pressure apparatus (SPEED-1500) installed on beamline BL04B1 at the SPring-8. Powdered graphite BC_2N, prepared by a vapor-phase reaction of BCl_3 and CH_3CN, was used as a starting material. A series of x-ray diffraction profiles was collected under various HP/HT by the energy dispersive method. Recovered samples were investigated by the x-ray diffraction with imaging plate and TEM observation. One of them was compressed again to obtain the pressure-volume data for the bulk modulus measurement. The sample was placed in a teflon capsule filled with methanol-ethanol together with diamond, c-BN and NaCl as references, which was compressed by a DIA type high large volume press (SMAP2) installed at BL14B1.

3. Results

Figure 1 shows the variation of the x-ray diffraction profiles with increasing temperature at 18 GPa. At room temperature, a broad peak was observed at 42 keV, which is assigned as a 002 peak of graphitic BC_2N (low-pressure phase). The low pressure phase maintained its original structure until the temperature reached 1200 ℃. When temperature was increased to 1250 ℃, intensity of the low pressure phase peaks decreased and three diffraction peaks, 111,220,311 of cubic BC_2N phase, became stronger. Although their peak widths were quite large suggesting the very small grain size, the diffraction profiles showed that the cubic BC_2N phase was dominant. When temperature was further increased, diffraction profiles showed a similar trend up to 2000 ℃, which indicates that the cubic BC_2N phase is quite stable in a wide temperature range. The phase separation into diamond and c-BN started at temperatures higher than 2000 ℃ which was confirmed by the separation of the observed diffraction peaks.

By the rapid temperature decrease before the phase separation, the cubic c phase could be quenched to the ambient conditions. The unit cell value of the quenched product was measured by the angle dispersive method with monochromatic synchrotron x-rays and an imaging plate. The obtained lattice constant is a=3.595(1) Å, which is an intermediate value between diamond and c-BN. The line-width of the diffraction peak is considerably large, suggesting the grain size of the BC_2N phase is very small (~10 nm).

The isothermal bulk modulus of the cubic BC_2N calculated from the P-V data was 350 GPa, which indicates the cubic BC_2N was more compressive even than c-BN against expectation.

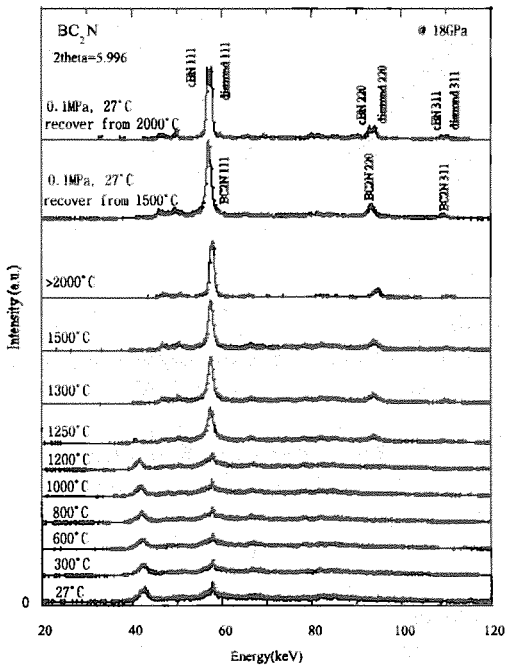

Fig. 1 A series of x-ray diffraction profiles of BCN with increasing temperature at 18 GPa

5.2.3 Structural study of icosahedral Zn-Mg-Dy quasicrystal under hydrostatic pressure up to 40 GPa

Tetsu WATANUKI, Taku J. SATO[a)], An Pang TSAI[a)], Osamu SHIMOMURA
a) National Research Institute for Metal

1. Introduction

In order to understand the origin of the structural stability of quasicrystalline systems, it is important to investigate the pressure dependence of their structure. So, we have performed powder x-ray diffraction experiments for icosahedral Zn-Mn-Dy quasicrystal under pressure using a diamond anvil cell at room temperature. This quasicrystalline system is considered to be suitable for observing lattice transformation under pressure, because the icosahedral Zn-Mn-rare-earth quasicrystals have simple structure in the sense that their structures do not have atomic clusters[1)].

2. Experiments

As for the experimental technique, it is important to make a good hydrostatic condition, because applying not well defined stress field leads poor results. So, we use He gas as a pressure medium which can generate quasi-hydrostatic condition up to 50 GPa[2)]. In addition to this, the powder sample was made to a pellet of 10 μm (t.), which is thin enough to avoid direct compression by anvils.

3. Results

The experimental results show no significant change of the x-ray diffraction profiles up to 42 GPa. With respect to the pressure dependence of the d-values, monotonic change was observed, and also no axis direction dependence was observed (Fig. 1a). However, gradual Bragg peak broadening was observed in the pressure region above 25 GPa (Fig. 1b). Summing up these results, we consider that icosahedral Zn-Mn-Dy quasicrystal is compressed isotropically under hydrostatic pressure up to 42 GPa, and the quasi-periodic lattice is conserved perfectly below 25 GPa, however, some imperfection such as local distortion is induced in the quasi-periodic lattice in the pressure region above 25 GPa.

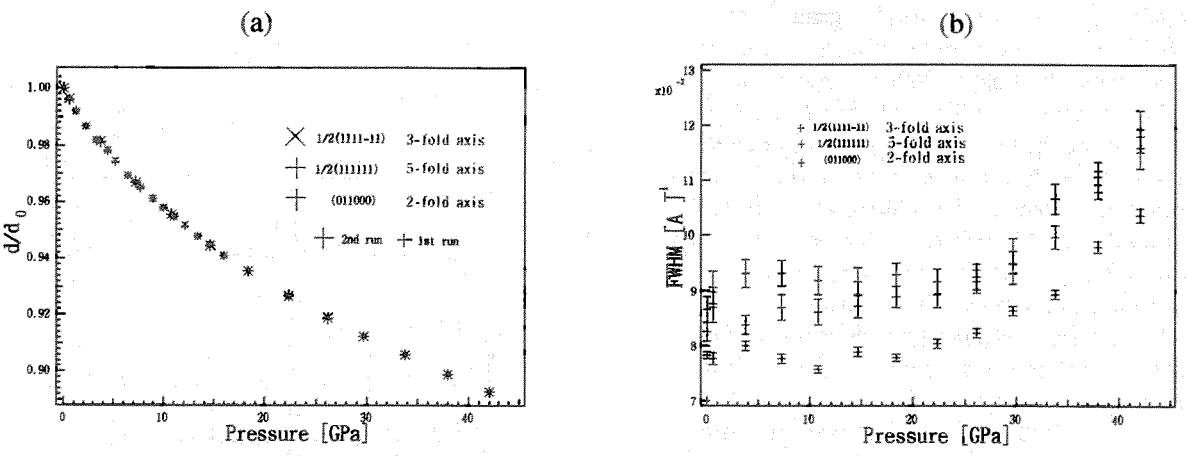

Fig. 1 Pressure dependence of the d-values of icosahedral Zn-Mg-Dy quasicrystal (a), and pressure dependence of the Bragg peak widths (b)

References

1) E.Abe *et al.*, Phys. Rev. Lett. **82**, 5269, 1999
2) K.Takemura, J. Appl. Phys. **89**, 662, 2001

5.3 Structual physics research

5.3.1 A UHV diffractometer for studies on semiconductor surfaces

Masamitu TAKAHASI, Yasuhiro YONEDA, Hirotane INOUE[a)], Naomasa YAMAMOTO[a)]
and Jun-ichiro MIZUKI
a) Himeji Institute for Technology

1. Introduction

Because of many technological applications to electronic and optoelectronic devices, molecular beam epitaxy (MBE) growth of III-V group semiconductors has received considerable attention for over three decades. Structural information on the growing surfaces is essential not only to improve the quality of the grown films but also to develop devices with novel functions. Recently, surface X-ray diffraction (SXD) using synchrotron radiation has been recognized as a powerful technique for studies on growth of semiconductors [1,2]. We report a new X-ray diffractometer directly connected with an MBE chamber. This instrument has been installed on a synchrotron experimental station, BL11XU at SPring-8.

2. Apparatus

The diffractometer is based on the (4+2) type and equipped with an axis for rotating the receiving slit about the normal of the slit plane. This additional axis is used to align the resolution of the receiving slit properly for the surface X-ray diffraction measurement. For the alignment of the sample and the whole setup with respect to the X-ray beam, an XYZ-stage and an adjustable base plate are furnished. X-rays enter and leave the chamber through two cylindrical Be windows welded onto the MBE chamber. A graphite sheet which can be heated up to 250 °C is placed along the inside of the Be windows to protect the Be windows from being coated with evaporated materials.

3. Results

To demonstrate the performance of our diffractometer, we present an example of static surface crystallography. Figure 1 shows a rocking curve of a SXD peak, (2,5/4,0.2), which comes from the four-fold symmetry of the surface reconstruction. The wavelength used was 1.24 Å. This peak was measured with an Al plate of 0.3 mm thickness in front of the NaI scintillation detector to avoid the pile-up effect. Taking into consideration the attenuation factor of the Al plate, the peak intensity is more than 200000 cps. The full width of half maximum (FWHM) of this peak was found to be 0.04 °, corresponding to a coherent domain size of about 1000 Å. Several observed structure factors were consistent with a first-principle calculation [3].

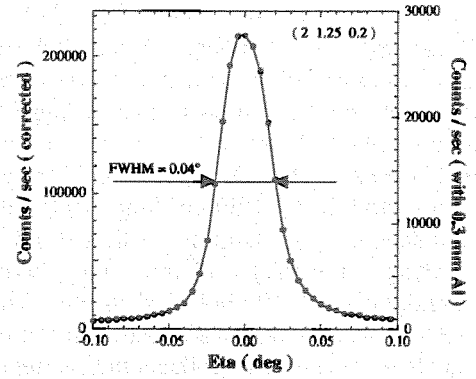

Fig. 1 A rocking curve of a surface diffraction peak

The combination of the growth chamber and the X-ray diffractometer provides an opportunity to the study of growth dynamics. X-ray diffraction oscillation allows a better understanding of the growth process than the RHEED oscillation [4] since the X-ray scattering can be interpreted in terms of the kinematic scattering theory. Figure 2 shows the evolution of the SXD intensity of (0,0,1) during the homoepitaxial growth of GaAs(001). The amplitude of the oscillation is gradually damped after opening the Ga shutter owing to increase of the surface roughness. Interruption of the growth induces recovering of the surface morphology.

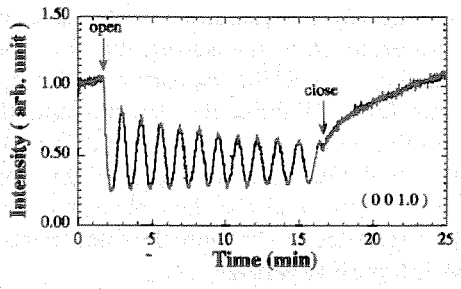

Fig. 2 The evolution of the diffracted intensity of X-rays during the homoepitaxial growth on GaAs(001)

References

1) Y. Garreau, M. Sauvage-Simkin, N. Jedrecy, R. Pinchaux and M. B. Veron, Phys. Rev. B 54, 17638, 1996
2) P. H. Fuoss, D. W. Kisker, G. Renaud, K. L. Tokuda, S. Brennan and J. L. Kahn, Phys. Rev. Lett. 63, 2791, 1992
3) W. G. Schmidt and F. Bechstedt, Surf. Sci. 360, L473, 1996
4) B. A. Joyce, J. Cryst. Growth 99, 9, 1990

5.3.2 An x-ray spectrometer for materials science on BL11XU at SPring-8

Toshiya INAMI, Tatsuo FUKUDA, Jun'ichiro MIZUKI, Takeshi MATSUMURA[a)], Hironori NAKAO[b)], Youichi MURAKAMI[a)], Kazuma HIROTA[a)], Yasuo ENDOH[c)]

a) Department of Physics, Tohoku University

b) Photon Factory, Institute of Materials Structure Science, High Energy Accelerator Research Organization

c) Institute for Materials Research, Tohoku University

The physics of strongly correlated transition metal oxides, including high-T_c cuprates and CMR manganites, is currently attracting enormous attention. In particular, measurements of the electronic structure and electronic excitation spectrum in these materials are important for understanding the electronic dynamics and thus the electronic properties. Inelastic x-ray scattering measurement is expected to be a powerful tool for investigating electronic structure of these materials, because x rays couple directly to electron charge and can promote excitations over a few eV such as an interband transition. Especially, resonant inelastic x-ray scattering (RIXS) in the hard x-ray regime has specific features suited for such experiments, *i.e.* bulk sensitivity, element selectivity and the ability to obtain momentum-dependent information.[1-3)]

We have recently constructed an x-ray spectrometer of moderate energy resolution (0.1 $\sim$ 1 eV) and energy transfer ($\sim$ 30 eV) at JAERI beamline BL11XU of SPring-8 for this purpose.[4)] The entire system is composed of a high resolution monochromator, a focusing mirror, a sample table, and a backscattering energy analyzer. (Fig. 1) The sample, the analyzer and the detector are placed approximately on a Rowland circle of about 2 m in diameter. Incident x-rays from a SPring-8 standard undulator are monochromatized down to about 0.5 eV band width by a diamond 111 pre-monochromator, and are monochromatized again by the high resolution monochromator (channel cut Si 333) in the experimental hutch to about 0.12 eV band width. The Pt-coated fused-quartz mirror of 50 cm long is placed after the monochromator and focuses the x-rays horizontally on the sample. The sample position is 1.5 m downstream from the mirror. The horizontal beam size at the sample is typically 0.12 mm. The photon flux at the sample measured by a PIN photo-diode is about 10^{11} photons/s at a 100 mA ring current. The sample table consists of ω and ϕ tables, in addition to the χ arc ($\pm 5°$). x and y tables are also attached on the top of the ϕ table. The analyzer mounted on the end of the analyzer arm of 2 m collects the scattered x-rays from the sample. The momentum transfer is selected by rotating the analyzer arm in the horizontal scattering plane. The energy analysis is done by a Johann-type (R = 2 m) spherically bent diced-Ge 531 analyzer of 76.2 mm in diameter. Perfect Ge single crystals, of which dimensions are 0.2(H) x 2(V) mm^2, are glued on a glass substrate. The calculated energy resolution of the analyzer is 85 meV. The detector is mounted on the end of the detector arm of 2 m. A slit is placed in front of the detector.

The total energy resolution of the spectrometer was evaluated from measuring the full width at half maximum (FWHM) of elastic scattering from a plastic film. Without the detector slit, the energy resolution was about 300 meV (FWHM). The energy resolution can be improved by applying the detector slit, and the data measured with the 200 μm(H) detector slit show the total energy resolution 130 meV (FWHM).

Finally, we are grateful to P. Abbamonte for making the diced Ge analyzer. We also thank to C.-C. Kao, H. Hayashi, E. E. Alp and T. Toellner for helpful discussions. This work was partly supported by Core Research for Evolutional Science and Technology, Japan Science and Technology Corporation.

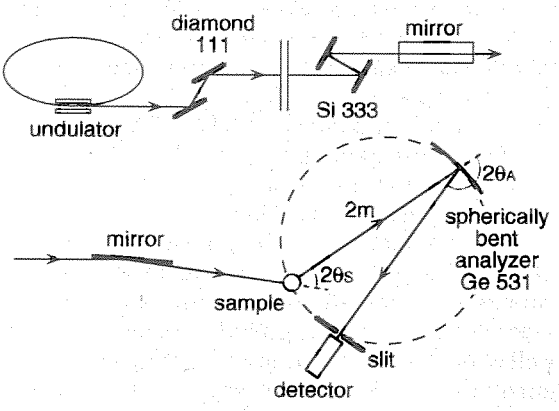

Fig. 1 Schematic layout of the spectrometer Side view to the mirror (above) and top view after the mirror (below)

References

1) J.P. Hill *et al.* Phys. Rev. Lett., **80**, 4967, 1998
2) P. Abbamonte *et al.*, Phys. Rev. Lett., **83**, 860, 1999
3) M.Z. Hasan *et al.* Science, **288**, 1811, 2000
4) T. Inami *et al*, Nucl. Instr. and Meth. A, **467-468**, 1081, 2001

5.3.3 Resonant inelastic x-ray scattering study on the orbital-ordered Mott insulator $LaMnO_3$

Toshiya INAMI, Tatsuo FUKUDA, Jun'ichiro MIZUKI, Youichi MURAKAMI[a], Sumio ISHIHARA[b], Kazuma HIROTA[a], Sadamichi MAEKAWA[c] and Yasuo ENDOH[c]

a) Department of Physics, Tohoku University
b) Department of Applied Physics, University of Tokyo
c) Institute for Materials Research, Tohoku University

1. Introduction

Recent intensive experimental and theoretical work on manganites has revealed that orbital degree of freedom (anisotropic shape of the electronic cloud) plays an important role in a various properties of the manganites, for example, transport properties, magnetic structures, spin dynamics, stability of charge-ordered phase and so on. Electronic structure and electron dynamics are thus also expected to reflect strong influence of the symmetry of orbitals. Resonant inelastic x-ray scattering (RIXS) in the hard x-ray regime is a powerful tool for investigating electron dynamics of condensed matter.[1] Advantages of this technique are ability of access to a wide kinematic range in energy and momentum space and direct coupling to electron charge. Recently we have constructed an x-ray spectrometer at JAERI beamline BL11XU of SPring-8 for this method.[2] Here we show the first experimental results on RIXS of the cubic manganite $LaMnO_3$, which shows $d_{3x^2-r^2}/d_{3y^2-r^2}$-type orbital-order below 780 K, using this spectrometer.

2. Results

The experiments were carried out with total energy resolution 0.5 eV using two $LaMnO_3$ single crystals at room temperature. We measured inelastic scattering for several incident energies and found that three inelastic peaks at 2.5, 8 and 11 eV appear only when the incident energy is tuned near the Mn K absorption edge. (Fig. 1) We then measured momentum dependence of these resonant peaks, which reveals that energy dispersion of the three peaks along $\vec{Q} = (h, h, 0)$ and $(h, 0, 0)$ is very weak. The 8 and 11 eV peaks are considered local charge-transfer-type excitations from the O $2p$ orbitals to the unoccupied Mn $3d$ orbitals and Mn $4s$ or $4p$ orbitals, respectively. These assignments are consistent with previous optical conductivity measurements. On the other hand, the 2.5 eV peak is attributed to a transition from effective lower Hubbard band (LHB) to upper Hubbard band (UHB). Theoretical calculations indicate that the observed weak dispersion of the 2.5 eV peak is caused by orbital order of $LaMnO_3$.[3] Due to orbital order of $LaMnO_3$, LHB has the $d_{3x^2-r^2}$ and $d_{3y^2-r^2}$ orbital characters and UHB has $d_{y^2-z^2}$ and $d_{z^2-x^2}$ ones. Because of the symmetry, hopping integral between the $d_{y^2-z^2}$ and $d_{z^2-x^2}$ orbitals in UHB is small, and this results in weak dispersion of UHB. Since RIXS spectra are approximately given by a convolution of UHB and LHB, q-independent RIXS spectra arise from this flat UHB dispersion. We also measured polarization dependence of the peaks. The intensity of the 2.5 eV peak was measured as a function of the azimuthal angle (sample rotation about the scattering vector) and shows characteristic two-fold oscillation. This result is in qualitative agreement with the theoretical prediction.[3] The theory also suggests that, as mentioned above, since the 2.5 eV excitation is a transition between the bands with different orbital characters from each other, it can be regarded as an "orbital excitation".[3]

This work was partly supported by Core Research for Evolutional Science and Technology, Japan Science and Technology Corporation.

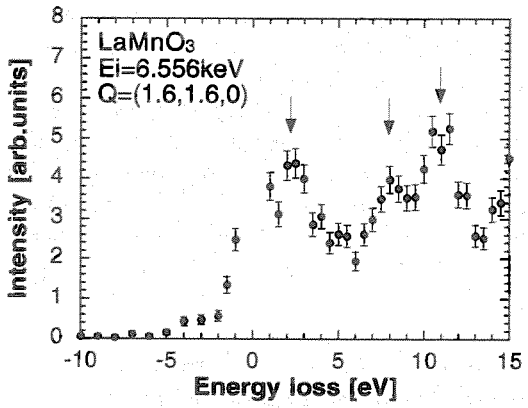

Fig. 1 Resonant inelastic x-ray scattering spectrum of $LaMnO_3$ at $\vec{Q}$=(1.6,1.6,0) Three features at 2.5 eV, 8 eV and 11 eV are shown by arrows.

References

1) M.Z. Hasan *et al.* Science, **288**, 1811, 2000
2) T. Inami *et al*, Nucl. Instr. and Meth. A, **467-468**, 1081, 2001
3) H. Kondo *et al*, Phy. Rev. B, **64**, 014414, 2001

5.3.4 Crystal structure of Pd-perovskite catalyst in redox fluctuating atmospheres II

Yasuo NISHIHATA, Jun'ichiro MIZUKI, Takahiro AKAO, Hirohisa TANAKA[a], Mari UENISHI[a], Mareo KIMURA[b], Tokuhiko OKAMOTO[b], Noriaki HAMADA[c]

a) Materials R&D Div., Technical Center, Daihatsu Motor Co., Ltd.

b) Materials Analysis & Evaluation Div., Toyota Central R&D Labs., Inc.

c) Faculty of Science and Technology, Science University of Tokyo

1. Introduction

A state-of-the-art automotive catalyst is stoutly desired to be immortal, because it is not replaced during the life cycle of a vehicle. Precious metals initially have nano-meter order dispersions as active species of the catalyst, but the catalytic activity deteriorates owing to the particle growth of precious metals during the vehicle usage. It is important to control the catalytic active site not only to achieve and maintain high efficiency, but also to economize on precious metals. Perovskite crystals including the precious metal such as palladium, $LaM_{1-x}Pd_xO_3$ (M = Fe, Co, $Fe_{0.6}Co_{0.4}$), are expected to realize a self-regeneration of the metals by making use of spontaneously occurring reduction-oxidation (redox) fluctuation in the real automotive exhaust gas without auxiliary treatment. The purpose of this study is to clarify the mechanism to maintain high catalytic activity and to suppress the particle growth of the precious metals.

2. Experiments

Pd-containing perovskite catalysts were prepared by the alkoxide method. The powdered catalyst, $LaFe_{0.57}Co_{0.38}Pd_{0.05}O_3$, was subjected to thermal ageings under oxidation, reduction, oxidation atmospheres in due order at 800 °C for 1 hour on each ageing stage. We have employed the x-ray anomalous diffraction (XAD) technique near the Pd K-edge (24.35 keV) in order to determine the distribution of Pd in the catalyst, using Si (311) double crystal monochromator and two mirrors for higher-order harmonics rejection at bending-magnet beamline BL14B1 at SPring-8.

3. Results

Figures 1(a) and 1(b) represent the energy dependence of x-ray intensity for (100) and (110) Bragg reflections from the oxidized catalyst. Two Bragg peaks from the perovskite catalyst were assigned as a pseudocubic cell of the perovskite structure ABO_3, where A and B cations are in twelve- and six-fold coordinations, respectively. The structure factors for the pseudocubic cell are expressed approximately in the form: $F(100) \propto |f_A - f_B - f_O|$ and $F(110) \propto |f_A + f_B - f_O|$, where f_A, f_B and f_O are atomic scattering factors for the A-site, B-site and oxygen atoms, respectively. The cusp of the intensity of these reflections at the Pd K-edge indicates that Pd definitely forms solid solution with the perovskite crystal. Especially, the increase of (100) reflection at the edge energy proves that Pd occupies the B-site without any uncertainty by considering the structure factors. On the other hand, the cusp of the intensity was not observed for the reduced catalyst. This implies that Pd is not involved in the diffraction from the perovskite crystals.

In conclusion, Pd occupies the B-site in the oxidation atmosphere. In consideration for the results of XAFS (data not shown here), Pd segregates out from the perovskite crystals and forms small metallic alloy particles with Co in the reduced atmosphere. This structure change repeats reversibly under the condition of the redox fluctuation atmospheres, so that the particle growth of precious metals can be suppressed.

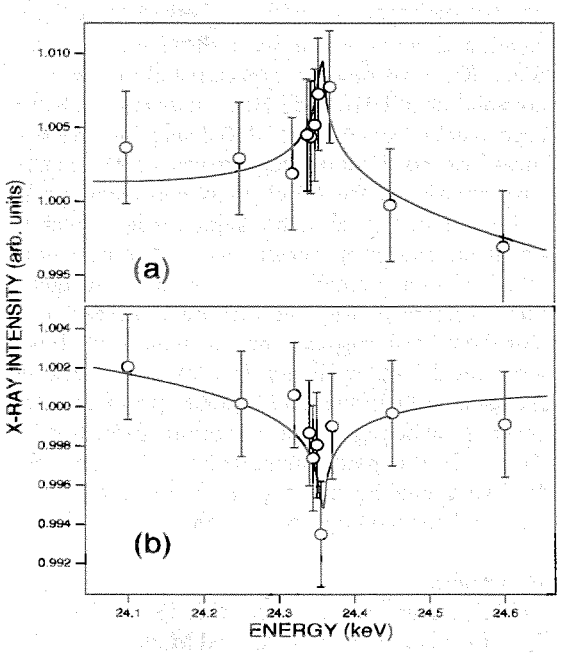

Fig. 1 Energy dependence of x-ray intensity for (a) (100) and (b) (110) Bragg reflections from the oxidized catalyst near the Pd K-edge

5.3.5 Reversal of magnetization in perovskite chromium oxides

Kenji YOSHII, Akio NAKAMURA [a], Hideki ABE [b],
Yutaka SHIMOJYO [c], Yoshinobu ISHII [c], Yukio MORII [c]
a) Department of Materials Science, Japan Atomic Energy Research Institute (JAERI), Tokai, Ibaraki 319-1195, Japan
b) National Institute for Materials Science (NIMS), Tsukuba, Ibaraki 305-0047, Japan
c) Advanced Science Research Center, Japan Atomic Energy Research Institute (JAERI), Tokai, Ibaraki 319-1195, Japan

Perovskite chromium oxides $LnCrO_3$ (*Ln*: lanthanides) have an orthorhombic crystal structure (space group *Pnma*) at room temperature. Due to the antisymmetric Dzyaloshinsky-Moriya interaction, these compounds exhibit so-called canted-antiferromagnetic order of the localized Cr^{3+} moments ($3d^3$) at Néel temperatures (T_N) of ~110-280 K. Here, we report a magnetization reversal effect found in both a solid solution series between $LaCrO_3$ (T_N~280 K) and $PrCrO_3$ (T_N~240 K), i.e., $La_{1-x}Pr_xCrO_3$, and $GdCrO_3$ [1-3].

Figure 1 shows the magnetization plotted against temperature for $La_{0.5}Pr_{0.5}CrO_3$ (x=0.5 for $La_{1-x}Pr_xCrO_3$) which was measured on cooling the sample with an applied field of 100 Oe [1]. Canted-antiferromagnetic order is observed below T_N~260 K, accompanied by the increase in magnetization. The magnetization decreases again below ~220 K and exhibits a negative polarity below ~160 K. Therefore, its direction is reverse to that of the applied field at low temperatures, which is not normal behavior of magnetic materials. The largest absolute value of the negative magnetization (at 2 K) is ~30–40 times as large as that of positive magnetization observed at ~220 K. The same qualitative behavior has been found for $0.2 \leq x \leq 0.8$ in $La_{1-x}Pr_xCrO_3$. The absolute value of the negative magnetization showed a tendency to increase with increasing x up to 0.8, suggesting a contribution of a Pr^{3+} ($4f^2$) localized moment to this phenomenon.

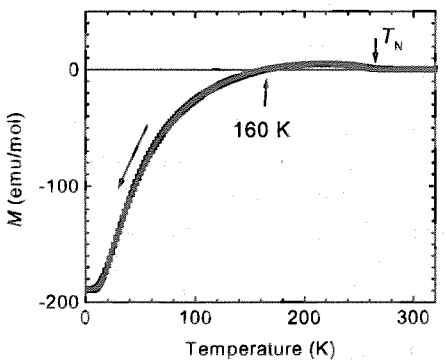

Fig. 1 Magnetization (*M*) plotted against temperature for $La_{0.5}Pr_{0.5}CrO_3$ measured on field-cooling with an applied field of 100 Oe

Similar magnetic properties have been obtained also for $GdCrO_3$ (T_N~170 K), where the lanthanide ion (Gd^{3+}; $4f^7$) has a localized moment [2]. Figure 2 shows the magnetization plotted as a function of time at 30 K for $GdCrO_3$, measured immediately after field-cooling with an field of 100 Oe down to 30 K. As the change of the magnetization is very small of ~0.4% during ~2×10^5 s (~2 days), the magnetic state exhibiting the negative magnetization is almost stable in this time scale.

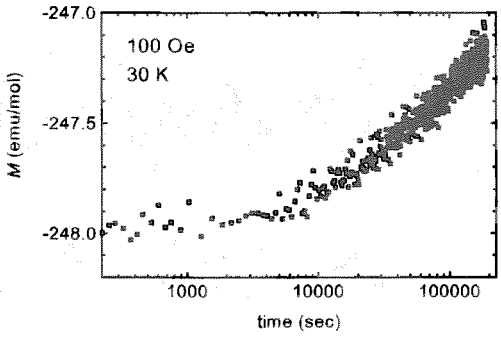

Fig. 2 Magnetization (*M*) plotted as a function of time for $GdCrO_3$ at 30 K, measured after field-cooling with an applied field of 100 Oe

Powder neutron diffraction measurements performed with a high resolution powder diffractometer (HRPD) provided the crystal structure of *Pnma* with an antiferromagnetically ordered Cr^{3+} moment of 2.50(5) μ_B/Cr^{3+} along the *b*-axis at 4 K [3]. A canted-antiferromagnetic component plausibly contributing the negative magnetization has not been clearly observed below T_N. Further studies are required to reveal the origin of the present characteristic magnetic behavior.

References

1) K. Yoshii and A. Nakamura, J. Solid State Chem., **155**, 447-450, 2000
2) K. Yoshii, J. Solid State Chem., **159**, 204-208, 2001
3) K. Yoshii *et al*, J. Solid State Chem. 2001, in press

5.3.6 PDF analysis of semiconductive CdTe-ZnTe alloys by high-energy x-ray diffraction

Yasuhiro YONEDA, Norimasa MATSUMOTO, Shinji KOHARA[a)] and Kentarou SUZUYA
a) Japan Synchrotron Radiation Research Institute (JASRI)

1. Introduction

The study of alloys is complicated by the fact that considerable local atomic strains are present due to the disordering effect of the alloying. This means that local bond-lengths can differ from those inferred from the average (crystallographic) structure by as much as 0.1 Å.

Both CdTe and ZnTe have the zinc-blende structure ($F\bar{4}3m$) where the Te atoms and Cd, Zn atoms occupy the two interpenetrating face-centered-cubic (fcc) lattices. In the alloys the lattice parameter of $Cd_{1-x}Zn_xTe$ interpolates linearly between the end member values consistent with Vegard's law. However, both XAFS experiments show that the atomic nearest neighbor (nn) distance deviate strongly from Vegard's law. Rather, they stay closer to their natural lengths found in the end-member compounds: $L^0_{Cd-Te} = 2.80$ Å and $L^0_{Zn-Te} = 2.64$ Å.[1-3)]

2. Experimental setup for PDF analysis

The High-energy X-ray diffraction experiments were carried out at a bending magnet beamline BL14B1 in SPring-8. The X-ray beam was monochromatized at 60 keV and horizontally focused on a sample 3 mm wide.[4)] Since the sample was investigated in transmission geometry, the diffraction data was obtained with very low systematic corrections, especially for very small absorption corrections for the sample.

3. Results

The resulting PDF obtained from the $Cd_{0.7}Zn_{0.3}Te$ and pure ZnTe samples is shown in Fig. 1.

The nearest neighbor peak is the only peak which is sharp in the experimental PDFs, as can be seen in Fig. 1. From the second-neighbor onwards the significant atomic displacements in the alloy samples result in broad atom-pair distributions without any resolvable splitting.

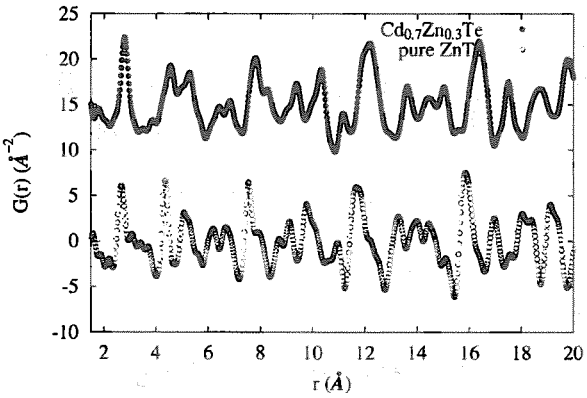

Fig. 1 $G(r)$ **for** $Cd_{0.7}Zn_{0.3}Te$ **and pure ZnTe**

References

1) R. Weil, R. Nkum, E. Muranevich and L. Benguigui, Phys. Rev. Lett. **62**, 2744, 1989
2) H. Terauchi, Y. Yoneda, H. Kasatani, K. Sakaue, T. Koshiba, S. Murakami, Y. Kuroiwa, Y. Noda, S. Sugai, S. Nakashima and H. Maeda, *Proc. of 7th Int. Conf. X-ray Absorption Fine Structure, Kobe, 1992*, Jpn. J. Appl. Phys. **32**, Suppl. 32-2, 728, 1993
3) Y. Yoneda, K. Sakaue, H. Terauchi, H. Kasatani, N. Kuroda, *Proc. of Advanced Materials '93*, Trans. Mat. Res. Soc. Jpn. **14B**, 1755, 1994
4) Y. Yoneda, N. Matsumoto, Y. Furukawa and T. Ishikawa, J. Synchrotron Rad. **8**, 18, 2001

5.3.7 Periodic hole structure in $Sr_{14}Cu_{24}O_{41}$

Tatsuo FUKUDA, Masaaki MATSUDA[a)], Jun'ichiro MIZUKI
a) Advanced Science Research Center, Japan Atomic Energy Research Institute (JAERI)

1. Introduction

$Sr_{14}Cu_{24}O_{41}$ consists of an alternating stack of the plane containing edge sharing CuO_2 chains, and the plane containing two-leg Cu_2O_3 ladders sandwiched by Sr layers. Stoichiometric $Sr_{14}Cu_{24}O_{41}$ already contains holes which exist mostly in the chain: The hole spins are believed to be localized at oxygen, and they couple with copper spins to become nonmagnetic due to the Zhang-Rice (ZR) singlet formation. Moreover, dimers are formed between Cu^{2+} ions that are separated by twice the distance between nearest-neighbor Cu ions along the chain direction ($//c$) at low temperature. The arrangement of the dimers in the chain was discussed mainly with two possible models. The first is that each dimer is separated by one ZR singlet (model I), in which a lattice distortion with *four* times the periodicity of the chain structure is required, while the second is that the dimers are separated by two ZR singlets (model II), in which a lattice distortion with *five* times the periodicity of the chain structure could be achieved. Model I was supported by the synchrotron x-ray study with 15.5 keV[1)], while model II is consistent with the results by neutron scattering study[2)]. In order to work out the discrepancy, high-energy synchrotron x-ray diffraction measurements were carried out, because we believe the difference of penetration depth between neutrons and 15.5 keV-x-rays causes the inconsistency.

2. Experimental

The sample we studied is a crystal of $Sr_{14}Cu_{24}O_{41}$, which was grown at RIKEN using the traveling-solvent floating-zone (TSFZ) method with radiation heating without crucible. This crystal is the same one used for previous studies[1,2)]. Synchrotron x-ray diffraction measurements were performed on beam line 14B1 of SPring-8. We used the incident x-ray energy of about 54 keV. By using this energy, penetration depth of $Sr_{14}Cu_{24}O_{41}$ becomes a few mm, which is about the same size of the sample crystal we studied.

3. Results

Figure 1 shows a typical result of the θ-2θ scan of $Sr_{14}Cu_{24}O_{41}$ along chain direction, that is, $Q = (0, 0, L_c)$ [$L_c \sim 2.2$]. It is expected that Bragg peaks of the chain appear at $L_c = 2n$ (n: integer), and that satellite peaks of lattice distortion exist at $L_c = 2n \pm 1/4$ for model I and at $L_c = 2n \pm 1/5$ for model II. It can be seen that a peak exists at $L_c = 2.2$ but not at $L_c = 2.25$, which reveals a lattice distortion of *five* times the periodicity of the chain structure (model II). Moreover, we found that the peak intensity is very sensitive to the surface state for lower-energy experiments, but that it changes little for high-energy studies. This may be the reasons that the results are different from the one previously reported[1)]. We also calculated intensity ratios of satellite peaks with dimer model II, and confirmed that the model is consistent with experimental results.

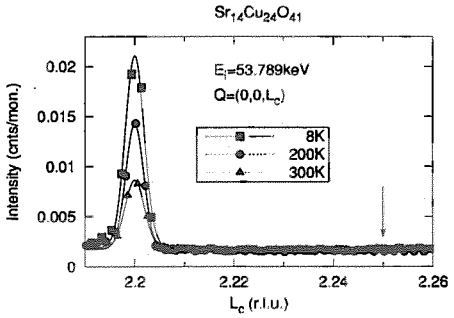

Fig. 1 θ-2θ scan spectrum of $Sr_{14}Cu_{24}O_{41}$ along $Q = (0, 0, L_c)$ [$L_c \sim 2.2$]

References

1) D.E. Cox, T. Iglesias, K. Hirota, G. Shirane, M. Matsuda, N. Motoyama, H. Eisaki, S. Uchida, Phys. Rev. **B57**, 10750, 1998
2) M. Matsuda, T. Yoshihama, K. Kakurai, G. Shirane, Phys. Rev. **B59**, 1060, 1999

5.3.8 Charge ordered state in single crystalline $CaFeO_3$ thin film studied by X-ray anomalous diffraction

Takahiro AKAO*, Yuichi AZUMA, Yasuo NISHIHATA, Jun'ichiro MIZUKI,
Noriaki HAMADA[a], Naoaki HAYASHI[b], Takahito TERASHIMA[b], Mikio TAKANO[b]

a) Faculty of Science and Technology, Science University of Tokyo

b) Institute for Chemical Research, Kyoto University

* present address: Faculty of Engineering Tottori Univ.

1. Introduction

Charge ordering (CO) in perovskite-type oxides has been intensively investigated in recent years.[1] $CaFeO_3$ shows the CO transition at 290 K [2]. The transition accompanies the metal-insulator transition like as other mixed valence materials. The crystal of $CaFeO_3$ has a distorted perovskite-type structure, where each FeO_6 octahedron is tilted about [001] and [110]. There having been those explicit works, however, what physical picture is appropriate for the CO in $CaFeO_3$ is still in controversy, because of lack of quantitative information on each electronic state of Fe(1) and Fe(2) separately. In this work, we have studied a quantitative electronic state difference between Fe(1) and Fe(2) in the CO state of $CaFeO_3$ by means of an X-ray anomalous diffraction technique. Furthermore, a subsequent electronic band structure calculation being compared with the experiment is performed to obtain the physical picture of the CO state in $CaFeO_3$.

2. Experiments

$CaFeO_3$ single crystalline thin films were fabricated by means of pulsed laser deposition technique with epitaxial growth [3]. X-ray anomalous diffraction (XAD) experiment for the $CaFeO_3$ thin films was carried out near Fe-K absorption edge ($E \approx 7112$ eV) in X-ray energy with the κ-type six-circle diffractometer installed on BL-14B1 beam line at SPring-8. The κ-type six-circle diffractometer was used in the four-circle geometry. The X-rays were monochromatized by a Si(111) double crystal system.

3. Results

The observed energy dependence of the anomalous scattering intensity of the $(0.5, 0.5, 0.5)_p$ reflection together with fitting result is shown in Fig. 1. The most suitable fitting leads the energy shifts, ΔE of 3.9(3) eV. This tells that the excitation energy from $1s$ to $4p$ state differs with 3.9 eV between Fe(1) and Fe(2) reflecting directly the electronic state difference between the two. This is the first observation regarding the electronic state-related information distinguished between Fe(1) and Fe(2).

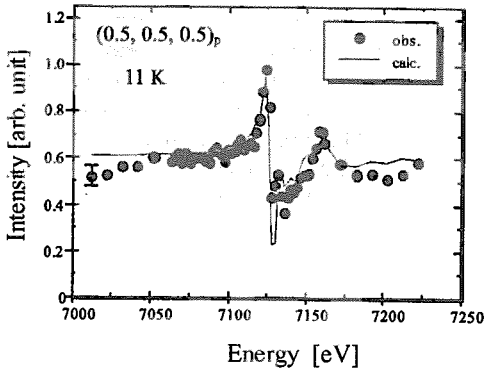

Fig. 1 Energy dependence of intensity of anomalous scattering for $(0.5, 0.5, 0.5)_p$ reflection at 11K

We have performed the first-principles electronic structure calculation (FLAPW) for antiferromagnetic $CaFeO_3$ in the low-temperature phase with using the reported crystal structure data[4]. It is expected that the hybridization of the Fe $4p$ orbital with the O $2p$ orbital in the CO state makes the $1s$ - $4p$ excitation energy become higher by 3.5 eV for Fe(1) atom than the Fe(2) atom. This agrees quantitatively with the result of 3.9 eV obtained by fitting for XAD of the $(0.5, 0.5, 0.5)_p$ reflection.

It can be concluded, therefore, by the XAD experiments together with the band structure calculation, that the electronic state of Fe(1) and Fe(2) in the CO state has been successfully revealed. The result strongly suggests that the holes are localized in the oxygen bonded to Fe(2) in the CO state.

References

1) *see* for example, J. B. Goodenough and J.–S. Zhou, Chem. Mater. **10**, 2980-2993, 1998
2) M. Takano, N. Nakanishi, Y. Takeda, S. Naka and T. Takada, Mat. Res. Bull. **12**, 923-928, 1977
3) T. Terashima, N. Hayashi and M. Takano, ICR Annual Report **6**, 21, 1999
4) P. M. Woodward, D. E. Cox, E. Moshopoulou, A. W. Sleight and S. Morimoto, Phys. Rev. **B 62**, 844-855, 2000

5.3.9 Local structure analysis by DAFS technique on spin-ladder system of $Ca_{14}Cu_{24}O_{41}$ thin film

Yusuke AZUMA[a)], Takahiro AKAO, Yasuo NISHIHATA, Jun'ichiro MIZUKI
a) Advanced Research Center of Science, Kwansei-Gakuin University

1. Introduction

Copper oxides with spin-1/2 Heisenberg ladders, where Cu spins interact with other Cu spins antiferromagnetically along rungs and legs, is called spin-ladder systems. $Sr_{14-x}Ca_xCu_{24}O_{41}$ contains Cu_2O_3 two-legged ladder, CuO_2 1D-chain and Sr/Ca layers alternately stacked along b-axis. Superconductivity in spin-ladder system $Sr_{14-x}Ca_xCu_{24}O_{41}$ has been observed only in a range of both high Ca content ($11<x<14$) and pressure ($1.5<P<8$ GPa). Although it is believed that an enhancement of the interaction between the ladder and chain with increasing Ca content causes the superconducting transition in consequence of the holes transferred from chain sites to the ladder[1)].

2. Experiment

In order to elucidate the local structure of Cu in the ladder site and the chain site separately, DAFS (Diffraction Anomalous Fine Structure) measurement on the Cu K-edge in $Ca_{14}Cu_{24}O_{41}$ thin film were carried out using a Si(111) double crystal monochromator at BL14B1 of SPring-8. The sample was used $Ca_{14}Cu_{24}O_{41}$ single crystal thin film.

3. Results

The DAFS spectra in ladder site were observed by taking integrated Bragg intensities with energies through Cu-K edge and the results were shown in Fig. 1. As it can be seen, DAFS oscillation was observed above the Cu-K edge. Figure 2 shows the radial structure function around Cu atom in ladder site which was given by DAFS analysis[3)].

Also DANES spectrum of the ladder site was found to be similar to the feature of the 5-coordination. This suggests that some of Cu atoms in ladder site are coordinated by five O atoms including an apical O atom belonging to the chain site.

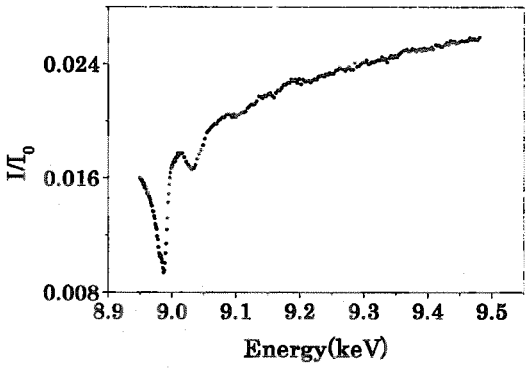

Fig. 1 DAFS spectra at ladder site

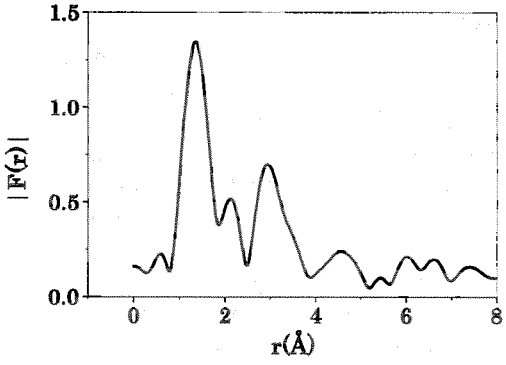

Fig. 2 Fourier transform

References

1) M.Isobe, *et al.*, Phys. Rev., **B. 57**, 613, 1998
2) Y.Frubayashi, *et al.*, Phys Rev., **B. 60**, R3720, 1999
3) J.Cross, Ph.D. thesis, University of Washington (1996)

5.3.10 Evidence for the diffusion of Au atoms into the Te UPD layer formed on a Au(111) substrate

Hiroyuki KAWAMURA, Masamitu TAKAHASI, Nobuhiko HOJO[a)], Masao MIYAKE[a)], Kuniaki MURASE[a)], Kazuhisa TAMURA[b)], Kohei UOSAKI[b)], Yasuhiro AWAKURA[a)], Jun-ichiro MIZUKI, Eiichiro MATSUBARA[c)]

a) Department of Material Science and Engineering, Kyoto University
b) Division of Chemistry, Graduate School of Science, Hokkaido University
c) Institute of Materials Research, Tohoku University

1. Introduction

A single atomic layer can be formed by the electrochemical processes using underpotential deposition (UPD), which is a surface-limited reaction to a sub-monolayer or monolayer coverage. In UPD, the electrochemical deposition of foreign metals onto substrate is performed at a positive potential relative to the reversible Nernst potential for bulk deposition. The method which alternates the UPD of two different elements to form a binary compound is referred to as the electrochemical atomic layer epitaxy (ECALE)[1]. Formation of cadmium chalcogenide layers such as CdTe on Au single crystal substrate using the ECALE technique has been investigated from the viewpoint of their applications to solar cells. The first step to the formation of CdTe films by ECALE is the reductive UPD of Te. The structure of Te UPD layer has been studied using STM and AFM[2-4], however, the structural analysis using STM and AFM is still limited to the two-dimensional surface structure. The structure normal to the substrate surface can be investigated by in-situ surface X-ray diffraction measurements.

2. Experimental

The in-situ surface X-ray diffraction measurements were carried out using a k-type multi-axis diffractometer installed on beamline 14B1 at SPring-8, Japan. The wavelength utilized was $\lambda = 1.10$ Å. The Te UPD layer was formed on a pre-treated Au(111) disk electrode in the electrolytic solution contained 0.1 mM TeO_2 and 10 mM H_2SO_4 as the supporting electrolyte. The potential for the Te UPD was applied to the Au(111) electrode during the X-ray diffraction measurements. The theoretical specular reflectivity for the electrode surface is given by the kinematical approximation. In the quantitative determination of the structure of the near-surface layers that include the surface adsorbate layers and the underlying Au layers, the parameters representing the electron density profiles are optimized so as to adequately describe the observed reflectivity.

3. Results

The measurements were carried out for a series of samples which were kept at UPD potential for 4 to 59 hours. Figure 1 shows the specular reflectivity measurement repeated on the same sample. The data collection in this case started 39 hours after the UPD potential was applied and lasted for 20 hours in total. The solid line is the calculated reflectivity profile based on the model where the first layer consists of 0.33 ML Te and 0.08 ML Au, while the second layer consists of 0.92 ML Au. The X-ray reflectivity measurement indicates that a portion of Au atoms migrate from the top layer of the Au(111) substrate to the top-most Te layer.

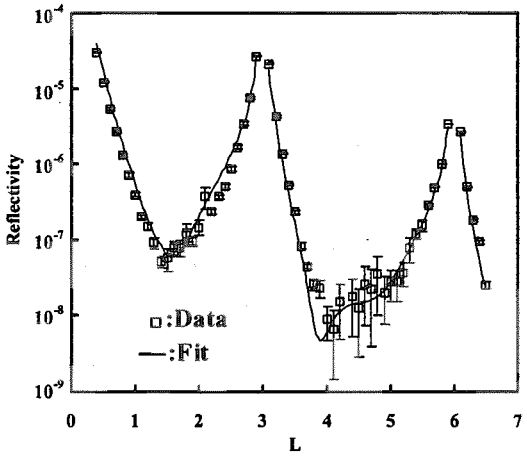

Fig. 1 Specular reflectivity for the Te UPD layer in 0.1 mM TeO_2 and 10 mM H_2SO_4

References

1) J. L. Stickney, 'Electrochemical Atomic Layer Epitaxy,' in Electroanalytical Chemistry, Vol. 21, A. J. Bard and I. Reubenstein, Editors, p.75, Marcel Dekker, New York, 1999, and referenced cited therein.
2) B. E. Hayden, I. S. Nandhakumar, J. Phys. Chem., **101**, 7751, 1997
3) D. W. Suggs, J. L. Stickney, J. Phys. Chem., **95**, 10056, 1991
4) N. Ikemiya, D. Iwai, K. Yamada, R. Vidu, S. Hara, Surf. Sci., **369**, 199, 1996

5.3.11 Effect of the UPD potential on the coverage of the Cd UPD layer formed on a Au(111) substrate

Hiroyuki KAWAMURA, Masamitu TAKAHASI and Jun-ichiro MIZUKI

1. Introduction

Formation of cadmium chalcogenide layers such as CdTe on Au single crystal substrate using the ECALE technique has been investigated from the view point of their application to solar cells. In the ECALE technique, the Cd layer is formed by the underpotential deposition (UPD) of Cd. The ordered adlattices of UPD Cd on a Au(111) surface in an 1 mM $CdSO_4$ + 100 mM H_2SO_4 solution were observed by STM[1], and the coverage change corresponding to the potential for the first and the second UPD was determined by potential-step chronocoulometric and QCM investigation[2]. It was reported that both sulfuric acid anions and Cd atoms adsorbed on the Au(111) substrate, and that the coverage of the first UPD layer was different from that of the second UPD layer. However, the surface-normal structure of the Cd UPD layer consisted of both sulfuric acid anions and Cd atoms, and the top layer structure of the Au(111) substrate under the Cd UPD layer are still unclear, because the structural analysis using STM is limited to the two-dimensional surface structure and is not able to directly understand the three-dimensional surface structure. Then, the Cd UPD layer structure normal to the substrate surface can be investigated by in-situ specular X-ray reflectivity measurements.

2. Experimental

The in-situ specular X-ray reflectivity measurements were carried out using a k-type multi-axis diffractometer installed on beamline 14B1 at SPring-8, Japan. The Cd UPD layer was formed on a pre-treated Au(111) disk electrode in the electrolytic solution contained 1 mM $CdSO_4$ and 100 mM H_2SO_4 as the supporting electrolyte. The potentials for the first and the second UPD were applied to the Au(111) electrode during the measurements. The theoretical specular reflectivity for the electrode surface is given by the kinematical approximation. In the quantitative determination of the structure of the near-surface layers that include the surface adsorbate layers and the underlying Au layer, the parameters representing the electron density profiles are optimized so as to adequately describe the observed reflectivity.

3. Results

Figure 1 shows the specular reflectivity for the Cd first (black triangle) and the second UPD layer (gray diamond), respectively. The black line is the calculated reflectivity profile for the first UPD layer based on the model where a 0.60 ML Cd atomic layer is on the reconstructed Au(111) surface and a 0.30 ML sulfuric acid anion layer is above the Cd atomic layer. The gray line is the calculated reflectivity profile for the second UPD layer which is based on the almost similar model to the first UPD layer.

The specular reflectivity measurement shows that the Cd UPD layer consists of both sulfuric acid anions and Cd atoms. However, the coverage of the Cd UPD layer changes little although the applied potential is different, which is contrary to that already reported[1,2]. Probably, the adsorption phase of the sulfuric acid anion in the Cd UPD layer changes when the applied UPD potential is changed, so that the different STM images might be obtained at the different UPD potential in the previous study[1,2].

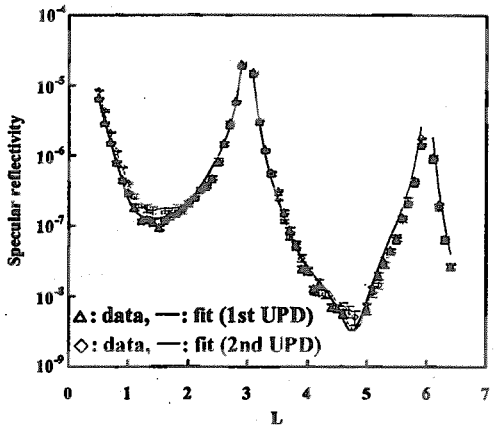

Fig. 1 Specular reflectivity for the Cd UPD layer on a Au(111) substrate in 1 mM $CdSO_4$ + 100 mM H_2SO_4

References

1) J. C. Bondos, A. A. Gewirth, R. G. Nuzzo, J. Phys. Chem., **100**, 8617, 1996
2) B. K. Niece, A. A. Gewirth, Langmuir, **13**, 6302, 1997

5.3.12 High-energy X-ray study of the structure of vitreous B_2O_3

Kentaro SUZUYA, Yasuhiro YONEDA, Norimasa MATSUMOTO[a)] and Shinji KOHARA[a)]
a) Japan Synchrotron Radiation Research Center

1. Introduction

High-energy X-ray ($E \geq 30$ keV) diffraction (HEXRD) at a synchrotron source provides the capability for studying the structure of encapsulated liquids and glasses in transmission geometry, with several advantages: higher resolution in real space due to the wide range of momentum transfer, $\hbar Q$, smaller correction terms, especially for absorption, reduction of truncation errors, the possibility of operating with extreme sample environments (high-temperature, high-pressure) and of direct comparison between X-ray and neutron diffraction data. The use of this technique, in conjunction with a neutron diffraction experiment on a diffractometer designed for disordered systems, is one of the best methods of investigating the structure of liquids and glasses, especially when combined with model calculations. We performed high-energy (40.9 keV) synchrotron X-ray diffraction experiments to obtain an accurate structure factor, $S(Q)$, for vitreous B_2O_3 up to high Q (~ 24 Å^{-1}), with low systematic corrections[1)]. The purpose of this study is to investigate the short- and intermediate-range structure of vitreous B_2O_3. We applied the reverse Monte Carlo (RMC) modelling technique to both the HEXRD and the published neutron diffraction data. On the basis of the RMC model, we discuss the validity of the boroxol ring (B_3O_6) model for vitreous B_2O_3.

2. Experiments

The X-ray diffraction measurements were carried out at the BL14B1 JAERI of SPring-8[2)]. RMC simulation was performed for a system containing 4000 atoms using the X-ray-weighted and neutron-weighted total structure factors $S(Q)$, simultaneously.

3. Results

The experimental X-ray and neutron structure factors, $S^X(Q)$ and $S^N(Q)$, are shown as dotted lines in Fig. 1. The results of the RMC simulation are plotted as solid lines in Fig. 1 for comparison. An excellent agreement is obtained for both the structure factors, apart from some small differences in $S^X(Q)$. The RMC model should be able to provide relatively detailed structural information, because of the contrast between the $S^X(Q)$ and $S^N(Q)$. The first sharp diffraction peak (FSDP) observed at $Q \sim 1.6$ Å^{-1} implies the presence of intermediate-range order due to the cages formed by the topological connection of BO_3 units in the network. Figure 2 represents a 5 Å thick section of the RMC configuration. The presence of the boroxol rings (B_3O_6) is clearly visible.

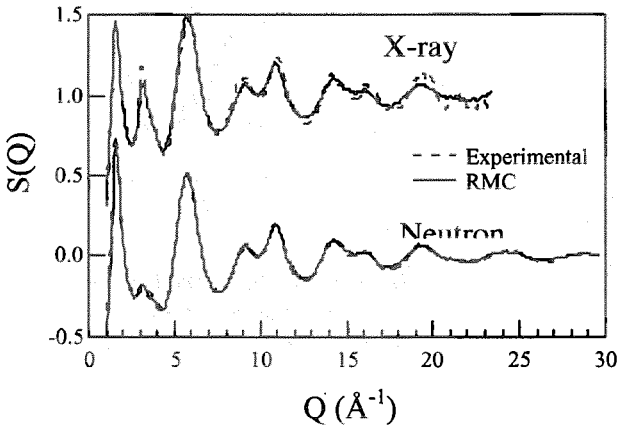

Fig. 1 S(Q) of vitreous B_2O_3

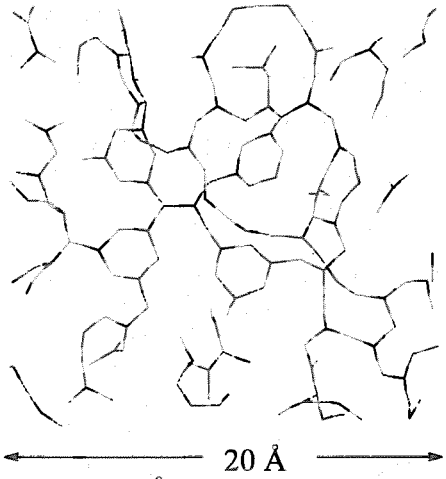

Fig. 2 A 5Å thick side of part of the largest RMC configuration for B-O network

References

1) K.Suzuya, S.Kohara, Y.Yoneda, N.Umesaki, Phys. Chem. Glasses **41**, 282, 2000
2) Y.Yoneda, N.Matsumoto, Y.Furukawa, T.Ishikawa, J. Synchrotron Rad., **8**, 18, 2001

5.4 Surface chemistry research

5.4.1 Photoemission spectroscopic study on initial oxidation of Si(001) surfaces induced by supersonic O_2 molecular beams

Yuden TERAOKA and Akitaka YOSHIGOE

1. Introduction

In the surface reaction dynamics study, the incident energy (E_t) of reactant molecules is an important parameter for induction of new surface reactions. From an application point of view, the precise control of Si oxidation is important for nano-fabrication of gate insulators used in Si-based LSI's. Although the incident energy of O_2 molecules has been known as an effective factor for initial oxidation of Si surfaces, the known data are not enough to obtain sufficient understanding of incident energy roles. Therefore, the incident energy dependence of O_2 dissociative chemisorption on Si(001) surfaces has been investigated in a wide range of incident energy.

2. Experimental

All experiments were performed at the surface reaction analysis apparatus (SUREAC2000) installed at the JAERI soft x-ray beamline, BL23SU, in the SPring-8. The base pressure of the analysis chamber is less than 3×10^{-8} Pa. An electron energy analyzer and a supersonic seed molecular beams (SSMB) generator are equipped with the chamber. The O_2 SSMB's are generated by the adiabatic expansion of O_2, He and/or Ar mixture. Owing to high nozzle temperature of 1400 K, the upper limit of O_2 incident energy is 3 eV. The O_2 flux density is typically 2×10^{14} molecules/cm^2/sec. Although the thermally-flashed Si(001) surface was clean, re-oxidation took place during cooling down and partially-oxidized surfaces were formed. The oxidation behavior of the partially-oxidized surface was firstly investigated using the SSMB technique and high-resolution photoemission spectroscopy with synchrotron radiation (SR).

3. Results

Two incident energy thresholds (1.0 eV and 2.6 eV) were found by O-1s photoemission measurements for oxygen saturated surfaces[1]. Referring to the prediction of first-principles calculation, the first energy was assigned to a potential energy barrier for direct O_2 dissociative chemisorption at Si dimer backbonds. The second energy was interpreted as that for direct oxidation at the second Si layer backbonds. In order to verify the interpretation, high-resolution Si-2p photoemission spectra were measured as a function of E_t [2]. The representative spectra are shown in Fig. 1. Since an Si^{1+} component was dominant as shown in Fig. 1(a), the topmost Si dimers were terminated as Si-H (denoted as C) and Si-OH. After 2 hours O_2 exposure, the spectra changed slightly as shown in Fig. 1(b). The increase of Si^{2+} and Si^{3+} components were attributed to the oxidation of residual Si dimer sites by the O_2 exposure. Almost all sites of Si-OH and Si-H were kept as they were against the O_2 exposure. Chemical bonding states shown in Fig. 1(b) were not changed up to E_t=1.0 eV. An Si^{4+} component and distorted interface Si (A and B) appeared above the first threshold energy of 1.0 eV as shown in Fig. 1(c) because direct O_2 dissociative chemisorption at dimer backbonds took place due to the action of incident energy. Above the second threshold of 2.6 eV, the intensity increase of Si^{4+} component is corresponding to direct oxidation of the second layer backbonds. Consequently, the incident energy induced oxidation has been verified experimentally for the first time.

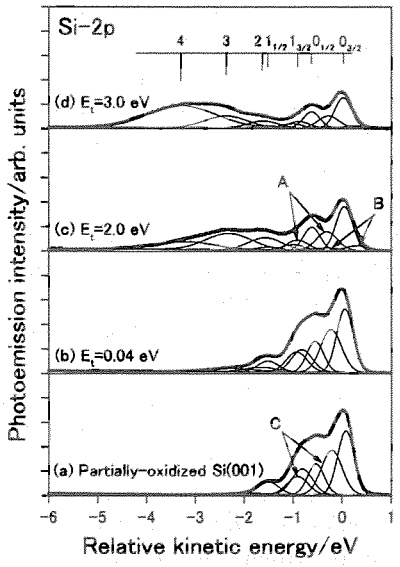

Fig. 1 Si-2p photoemission spectra for (a) partially-oxidized Si(001) surface, (b) oxygen saturated surface by O_2 gas exposure, (c) by O_2 SSMB irradiation with E_t=2.0 eV and (d) with E_t=3.0 eV

References

1)A. Yoshigoe, Y. Teraoka, Jpn. J. Appl. Phys. **39**, 7026, 2000
2) Y. Teraoka, A. Yoshigoe, M. Sano, Proc. 22nd Symposium on Dry Process, 85, 2000

5.4.2 Local structures of carbon nitride film

Iwao SHIMOYAMA, Tetsuhiro SEKIGUCHI, Yuji BABA, Guohua WU [a)]
a) University of Science and Technology of China

1. Introduction

Recently, carbon nitride (CN_x) has attracted much attention because of characteristic physical and electrical properties.[1, 2)] Up to now, many kinds of crystal phase of CN_x have been theoretically proposed.[3)] However, most of them have not been experimentally confirmed yet, because most of the CN_x films synthesized were amorphous in which long-range order lacks and variety of possible local structures are included. Near edge x-ray absorption fine structure (NEXAFS) is known as one of the superior methods to study such complex system due to the localization nature of core excitation. In order to clarify the local structures around nitrogen sites, we measured N 1s NEXAFS spectra of CN_x films.

2. Experimental

Experiments were performed at the BL-11A station of the Photon Factory in the High Energy Accelerator Research Organization (KEK-PF). CN_x thin films were synthesized *in situ* by nitrogen-ion implantation in Highly Oriented Pyrolitic Graphite (HOPG) to avoid the effect of contamination. Ion implantation was performed at room temperature and at 3.0 keV energy. The ion fluence was calibrated by a Faraday cup and determined to be 1.7×10^{15} ions/cm^2. After the procedure, thin films were annealed for 3 minutes. To study the structural change induced by annealing, polarization dependences of NEXAFS spectra were observed for the samples with different annealing temperatures (T = 840 and 1100 ℃). The nitrogen concentration was measured by x-ray photoelectron spectra and the [N]/[C] ratios were less than 0.05 for both samples.

3. Results and Discussion

Figure 1 shows the N 1s NEXAFS spectra of the CN_x film. In the figure, solid and broken curves show the results at grazing incidence (θ = 10°) and at normal incidence (θ = 90°), respectively. Upper and lower figures correspond to the results for annealing with T = 840 and 1100 ℃, respectively. In both figures, three discrete peaks **a**, **b**, **c** and a broad peak **d** are observed at the energies of 398.3, 399.5, 400.7, and 407 eV, respectively. Those show different polarization dependences. While the peaks **a** and **c** are enhanced at grazing incidence and suppressed at normal incidence, the peak **d** show opposite tendency. The polarization dependence of the peaks **a** and **c** is similar to that of the π^* resonance in C 1s NEXAFS spectra of HOPG[4)] and strongly supports that the peaks **a** and **c** are assigned to π^* resonances and the peak **d** is assigned to σ^* resonance. As shown in Fig. 1-(B), such polarization dependences are enhanced by the annealing at higher temperature. Furthermore, close inspection shows that the intensity of the peak **c** is especially enhanced as annealing temperature increases. On

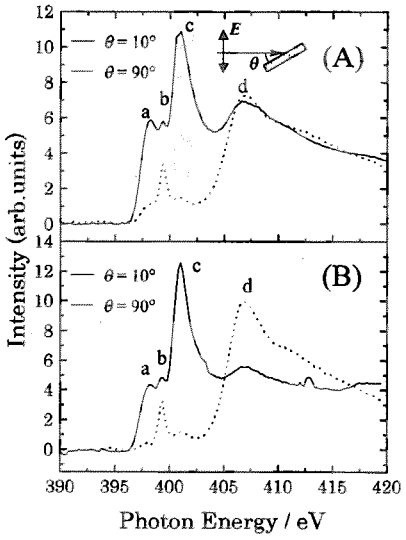

Fig. 1 N 1s NEXAFS spectra of the CN_x film synthesized by low ion implantation
(A) and (B) show the result for 840 and 1100 ℃ annealing. Solid and dotted lines show the results for grazing and normal incidence of x-ray. The incidence angle θ is defined as an angle between surface and x-ray beam.

the other hand, the peak **b** shows little polarization dependence. This means that the local structure corresponding to the peak **b** would have random orientation. Therefore, it is considered that the peaks **a**, **b**, and **c** originate from different local structures around nitrogen sites.

Nitrogen atom generally forms trivalence state. Considering the coordination number of carbon atoms, three kinds of local structures can be candidates for the origins of the N 1s→π* resonances. Namely, nitrogen atom is coordinated to one, two, and three carbon atoms, we can image cyanic structure, pyridine-like structure, and graphite-like structure, respectively. Schematic structural model is depicted in Fig. 2. Among them, pyridine-like and graphite-like structures can have graphitic orientation. This means that the peaks **a** and **c** which show graphite-like polarization dependence correspond to either pyridine-like or graphite-like structure. Furthermore, as mentioned above, the peak **c** is especially enhanced by annealing. We consider that is caused by structural change of graphite crystal. If the graphite crystal damaged by ion implantation is recovered by annealing, pyridine-like structures should change to graphite-like structures. This means that the graphite-like structures should increase by the annealing procedure. On the other hand, since cyanic group is bonded with graphite plane by single C-C bond, this structure is expected to have random orientation. Therefore, we concluded that the peak **a**, **b**, and **c** are assigned to pyridine-like, cyanic, and graphite-like structure, respectively.[5, 6] According to the static exchange approximation (STEX) calculation reported by Plashkevych *et al.*[7], the energy sequence of the π* resonances in N 1s NEXAFS spectra for pyridine-like, cyanic, and graphite-like structures agree with our assignment, hence their calculation supports our interpretation.

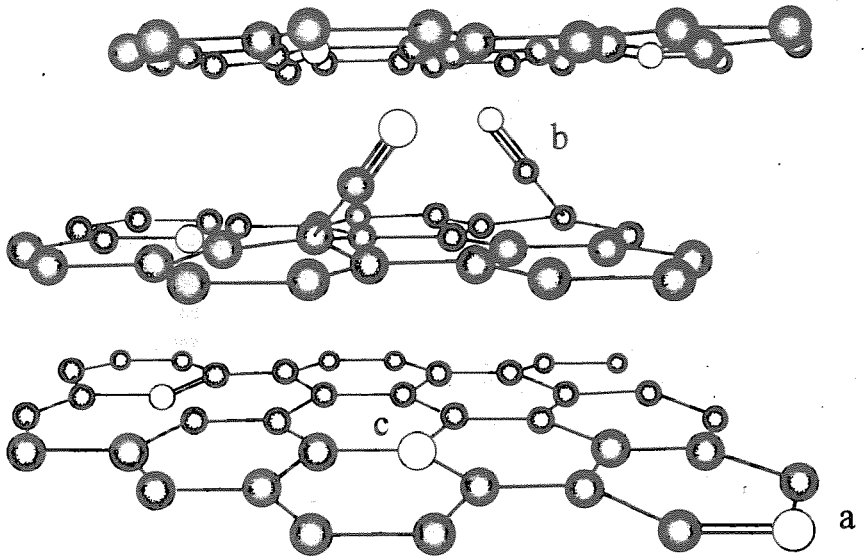

Fig. 2 Schematic diagrams of CN_x local structures in graphite matrix
Dark and white balls show graphite and nitrogen atoms, respectively. a: pyridinelike structure b: cyanic structure c: graphitelike structure

References

1) A. Y. Liu and M. L. Cohen, Science **245**, 841, 1989
2) A. Snis and S. F. Mater, Phys. Rev. B **60**, 10855, 1999
3) D. M. Teter and R. J. Hemley, Science **271**, 53, 1996
4) R. A. Rosenberg, P. J. Love, and V. Rehn, Phys. Rev. B **33**, 4034, 1986
5) I. Shimoyama, G. Wu, T. Sekiguchi, and Y. Baba, Phys. Rev. B **62**, R6053, 2000
6) I. Shimoyama, G. Wu, T. Sekiguchi, and Y. Baba, J. Elect. Spectrosc. Relat. Phenom. **114-116**, 841, 2001
7) O. Plashkevych, A. Snis, L. Yang, H. Ågren, and S. F. Mater, Phys. Scr. **63**, 70, 2001

5.4.3 Yields of DNA strand breaks and base damages induced in hydrated plasmid DNA film by γ-rays and α particles

Akinari YOKOYA, Siobhan CUNNIFFE[a)], David STEVENS[a)], Peter O'NEILL[a)]
a) Medical Research Council, U.K.

1. Introduction

Yields of strand breaks of DNA as well as base damages induced in solution have been studied by systematically changing the scavenger concentration[1)]. These studies showed that there are significant amounts of DNA damages that are not suppressed by even though a high radical scavenger concentration around cell mimetic condition. Direct energy deposition on DNA molecule, as well as interaction with diffusible water radicals, would significantly contribute to the yield of DNA-damage-induction in a living cell. To elucidate the mechanism of the direct type damage, we examined yields of chemically stable DNA damages as a function of hydration level during irradiation of low LET γ–rays and high LET α particles. The yields of single (ssb) and double strand break (dsb) are measured by gel electrophoresis method. Oxidative base damages, such as 8-oxo-G, are visualized by treatment with base excision repair enzymes (Nth and Fpg).

2. Experimental

Plasmid DNA (pUC18, 2686 base pairs) was obtained from an *E.Coli* HB101 host and the DNA was extracted using alkali-lysis followed by purification with banding twice on cesium-chloride-ethidium-bromide gradients. Following freeze-drying procedure, the samples on a polymer membrane were placed in a plastic chamber with a sodium hydroxide solution to maintain an appropriate humidity condition. Experiments are performed at γ- and α- irradiation facilities at Medical Research Council in U.K. The conformational change of the plasmid DNA after irradiation was quantified by an agarose gel electrophoresis method. All procedures were carried out at 5.7 ℃ except incubation with the repair enzymes, which convert base damages into detectable ssb (37 ℃).

3. Results and discussion

The yields of prompt ssb and dsb induced by both radiations only show a slight increase with increasing hydration level, from vacuum-dried up to 35 water molecules per nucleotide (Figure 1). This increase indicates that diffusible OH radicals, if produced in the hydrated layer, do not significantly contribute to the induction of strand breaks. The dsb yield for α-irradiation is about 2 times larger than that for γ-irradiation, though the ssb yields are similar for both radiations. The yield of enzymatically revealed ssb induced in γ-irradiated samples, increases with increasing level of hydration over the range studied. The yields of enzymatically revealed dsb for γ-irradiated samples also increase with increasing hydration. It is inferred that certain types of clustered DNA damage, e.g. a base damage and a ssb in close proximity on the opposite strand, are induced in hydrated DNA.

In contrast, for samples irradiated with α-particles, the yields of ssb and dsb do not significant increase after enzymatic treatment irrespective of the extent of hydration in the range studied. The efficiencies of the enzymes may be significantly reduced, since direct energy deposition in hydrated DNA by high-LET α-radiation probably induces more complex clustered DNA damages, such as 2 or more lesions located within a few base pairs, which are known to strongly inhibit the enzymes' activities[2)].

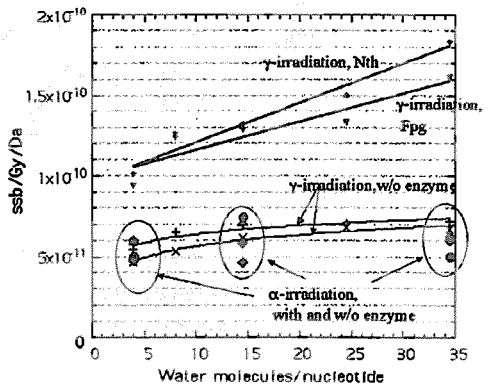

Fig. 1 Dependence of the yield of ssb induced by γ and α -irradiation on the level of hydration

References

1) J. Fulford, H. Nikjoo, D.T. Goodhead and P. O'Neill, *Int. J. Radiat. Biol.* in press, 2001
2) M-H. David-cordonnier, J. Laval and P. O'Neill, *J. Biol. Chem.* **275**, 11865, 2000

5.4.4 EPR Apparatus installed in soft X-ray beamline (BL23SU) at SPring-8 for biophysical studies

Ken AKAMATSU, Akinari YOKOYA

1. Introduction

Soft X-rays below 2 keV are an attractive light source for selecting K-shell photoabsorption on an element in biomaterials such as DNA. Though the molecular change of the biomolecules have been investigated intensively from the point of view of final photoporducts, there is little knowledge about intermediate radical process by the core level electron excitation because of the lack of an *in situ* EPR device combined with an intense soft X-ray synchrotron beamline. In this study, we measured EPR specra of the guanine pellet irradiated with soft X-rays with an energy of 1s → σ* resonance to elucidate the mechanism of guanine base damages in DNA, such as 8-oxo-G which induces a point mutation in a living cell.

2. Experimental

We have developed an EPR system (SLEEPRS; Synchrotron Light Exciting Electron Paramagnetic Resonance System) installed in a soft X-ray undulator beamline (BL23SU), SPring-8)[1]. The X-band EPR (TE300, JEOL, Japan) was connected with the high vacuum beamline transport channel (Figure 1). Pellet of guanine, which is one of the four DNA bases, was set on the top of Cu rod and the temperature was controlled at 77 K by a closed-cycle cryogenic system. Sample was irradiated with 539 eV soft X-rays and the EPR signal was measured during and after irradiation.

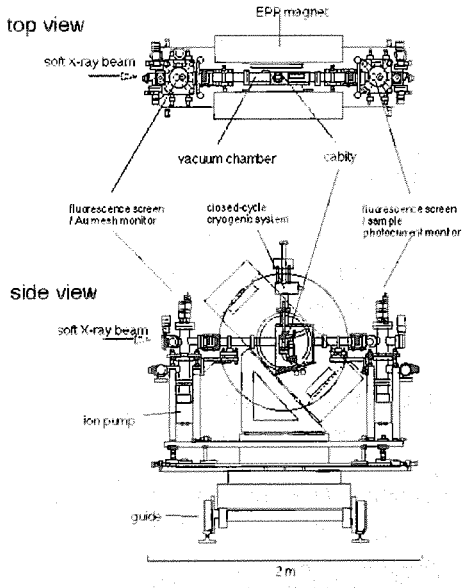

Fig. 1 Schematic illustration of SLEEPRS
The vacuum chamber is mounted in the magnet gap of about 150 mm (see top view). The chamber is connected to the beamline vacuum pipe at both the front- and back-end. These devices can be removed from the beamline along the guide for off-line experiments or maintenance.

3. Results and discussion

The obtained EPR signal is shown in Figure 2. The intensity of the strong two lines was proportional to the photon flux density and immediately disappeared by beam-off. A broad singlet signal, however, remained after the beam-off and grew larger by repetition of the irradiation. Hütterman and co-workers predicted that a radical cation or anion of guanine in DNA is induced by X-ray irradiaion[2]. However, there has not been obtained an evidence of these radicals yet. It is inferred that the two lines reported here were guanine radical cation and/or anion as the result of the core level excitation of a 1s electron of oxygen to an anti-bonding orbital (σ*) and following spectator Auger decay process in the molecule. These short-lived radicals would be instantly transformed to be a stable radical observed as the singlet. These results demonstrate that the *in situ* measurement of EPR combined with a brilliant soft X-ray source will provide a possibility for pursuing physicochemical investigation of DNA base damage induction.

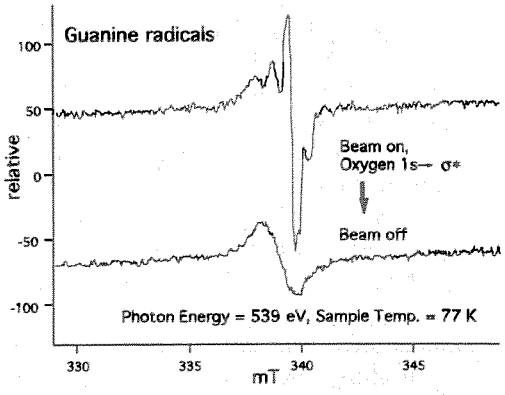

Fig.2 EPR spectra of guanine pellet irradiated with monochromatized soft X-rays at oxygen 1s →σ* energy

References

1) A. Yokoya and K. Akamatsu, *Nuclear Inst. Met A.* **467-468**, 1333, 2001
2) J. Hütterman, M. Röhrig and W. Köhnlein, *Int. J. Radiat. Biol.* **61**, 299, 1992

5.5 Heavy Atom Science

5.5.1 Circular dichroism measurements with periodic photon-helicity switching by a variably-polarizing undulator at BL23SU at SPring-8

Akane AGUI, Akitaka YOSHIGOE, Takeshi NAKATANI, Tomohiro MATSUSHITA[a], Yuji SAITOH, Akinari YOKOYA, Hitoshi TANAKA[a], Yoshikazu MIYAHARA[a], Taihei SHIMADA[b], Masao TAKEUCHI[a], Teruhiko BIZEN[a], Sigeki SASAKI[a], Hideki AOYAGI[a], Togo P. KUDO[a], Kazumichi SATO[a], Shukui WU[a], Yoichi HIRAMATSU[c], Masaichiro MIZUMAKI[a] and Haruo OHKUMA[a]

a) Japan Synchrotron Radiation Research Center
b) Neutron Research Center
c) Ishikawajima-Harima Heavy Industries (IHI) Co., Ltd.

1. Introduction

Light polarization has become increasingly important for such soft x-ray spectroscopic technique as circular dichroism (CD) measurements. Such experimental methods require good polarization quality and the fast switching of photon helicity. To promote high-sensitivity studies and to improve the signal-and-noise ratio for circular dichroism experiments, we have developed a *new* CD measurement system coupled with the right and left circular polarizations (RCP and LCP) switching[1].

2. Experimental system

BL23SU[2] is a beamline for soft X-ray spectroscopy studies in a wide variety of applications, such as surface chemistry, biology, and condensed matter physics. The light source (ID23) is an APPLE-2 type undulator. This undulator generates any kind of elliptical polarization of light by adjusting the relative position of pairs of magnet rows (phase shift) and changes the photon energy in the soft X-ray range changing the gap distance between the upper and lower jaws.

Experiments can be performed with a personal computer by using sophisticated application software. The beamline workstation is connected to the computer and controls the undulator and the monochromator [3], which establishes the selected monochromatized photon energy, maintaining robustness of the system.

3. Results

The magnetic CD sample current (I_I) and monitor current (I_0) were recorded by mean of total electron yield. During the MCD measurements, the undulator control, the monochromator control, and the data accumulation were synchronously operated. For instance, a measurement cycle proceeds as follows, (1) photon energy tuning → (2) ID23 phase shift to provide RCP X-rays → (3) simultaneous sampling of I_0 and I_I → (4) ID23 phase shift to provide LCP X-rays → and (5) sampling again I_0 and I_I. At this point the cycle returns back to (1) to be continued. Figure 1 shows the first result of MCD measurement of Fe2*p* absorption of Fe metal in the magnetic field of 0.4 T excited by RCP and LCP soft X-rays. We believe that the circular dichroism measurement system with periodic photon-helicity switching by an APPLE-2 type undulator provides great opportunities for the study of very weak circular dichroism signals in the soft X-ray region.

It should note that the closed orbit distortion of the storage ring caused by ID23 drive is minimized using the staring magnets installed in the upper and lower stream of the undulator.

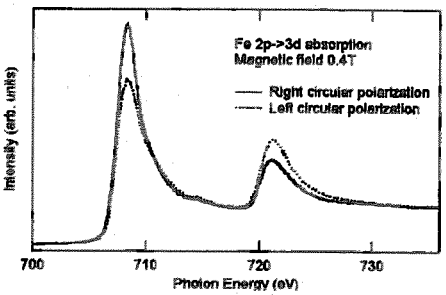

Fig. 1 Fe $L_{2,3}$ absorption spectra of Fe metal in a magnetic field 0.4 T excited by right and left polarized X-ray

References

1) A.Agui, A.Yoshigoe, T.Nakatani, T.Matsushita, Y.Saitoh, A.Yokoya, H.Tanaka, Y.Miyahara, T.Shimada, M.Takeuchi, T.Bizen, S.Sasaki, M.Takao, H.Aoyagi, T.P.Kudo, K.Satoh, S.Wu, Y.Hiramatsu, and H.Ohkuma, Rev. Sci. Inst., 72, 3191, 2001
2) A.Yokoya, T.Sekiguchi, Y.Saitoh, T.Okane, T.Nakatani, T.Shimada, H.Kobayashi, M.Takao, Y.Teraoka, Y.Yahashi, S.Sasaki, Y.Miyahara and T.A.Sasaki, J. Synchrotron Rad., 5, 10, 1998
3) Y.Saitoh, Y.Teraoka, A.Agui, A.Yoshigoe and A.Yokoya, Nucl. Instrum. Methods, 2001, to be published

5.5.2 First results from the actinide science beamline BL23SU at SPring-8

Yuji SAITOH, Takeshi NAKATANI[a)], Tomohiro MATSUSHITA[a)], Akane AGUI,
Akitaka YOSHIGOE, Yuden TERAOKA and Akinari YOKOYA
a) Japan Synchrotron Radiation Research Institute

1. Introduction

The "Actinide Science" beamline BL23SU at SPring-8 has been designed and constructed for various spectroscopic studies in the soft x-ray energy range[1,2]. The radiation source is a double-array undulator based on an APPLE-2 type[3]. The optical system consists of the prefocusing mirrors, a monochromator and the post-focusing mirrors. Varied-line-spacing plane gratings (VLSPG) are equipped with the monochromator.

Among the technical goals of this beamline was to realize the measurement of circular dichroism (CD) by switching the helicity of light with the APPLE-2 undulator itself. In the CD measurements, energy resolution much smaller than the natural width of the core-level excitations was required for high-precision site-selective investigation of magnetic materials and so on. In this paper, we report on results obtained in the first stage of the commissioning on this beamline[4].

2. Energy resolution

The energy resolution of this beamline was first tested by measuring the photoabsorption spectra of several gases. Among them, we show the $1s$-π^* photoabsorption spectrum of N_2 in Fig. 1. From the fitting analysis with 8 Voigt peaks, a resolving power of ~16,000 was deduced Similar results have been reported recently from Elettra and BESSY II.

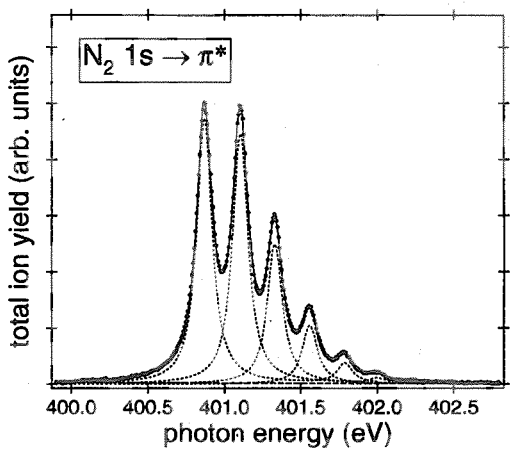

Fig. 1 Total ion yield spectrum of N_2 at the N $1s$-π^* resonance

3. Photon flux

The photon flux available on the sample is of fundamental importance for evaluating the feasibility of the various experiments. The photon flux at the first experimental station was measured with a Si photodiode (IRD AXUV-100) and an evaporated Au film for the first harmonic of the circular polarization mode. Figure 2 shows the results normalized to a stored electron current of 100 mA and a 0.02% bandwidth. In the energy range from 0.5 up to 1.8 keV, the photon flux in the region of 10^{11} photons/sec/100 mA/0.02% b.w. is realized.

Although the photon flux decreases with increasing photon energy, the energy region up to 2.1 keV can be available for the measurement such as the Si $1s$ photoabsortion spectrum[5]. It is also noteworthy that the photoabsorption experiment on multiply charged ions, for which high flux is essential, has successfully performed at this beamline[6].

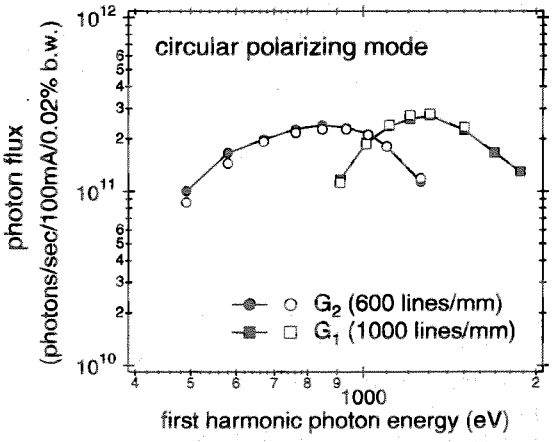

Fig. 2 Photon flux for the first harmonic in the circular polarizing mode of the APPLE-2 undulator at the first experimental station estimated with a photodiode (solid symbols and lines) and an evaporated Au film (open symbols)

References

1) A. Yokoya *et al.*, J. Synchrotron Rad., **5**,10, 1998
2) T. Nakatani *et al.*, J. Synchrotron Rad., **5**, 536, 1998
3) S. Sasaki, Nucl. Instrum. Methods, **A 347**, 83, 1994
4) Y. Saitoh *et al.*, Nucl. Instrum. Methods, A, in press
5) A. Yoshigoe *et al.*, J. Synchrotron Rad., **8**, 502, 2001
6) M. Ohura *et al.*, Phys. Rev., **A 63**, 014704, 2001

5.5.3 Experimental technique for radiative-process-resolved x-ray absorption spectroscopy at inner-shell excitation thresholds

Yasuji MURAMATSU and Rupert C. C. PERERA[a)]
a) Center for X-Ray Optics, Lawrence Berkeley National Laboratory

1. Introduction

X-ray absorption spectroscopy (XAS) at inner-shell excitation thresholds provides significant information about the electronic structures of molecules and materials. In fluorescence yield (FY) x-ray absorption measurements, detected x-rays are usually normal fluorescence. However, detected x-rays often include not only normal fluorescent x-rays, but also those emitted from other radiative processes such as resonant elastic/inelastic x-ray scattering at the thresholds. We could, therefore, obtain very detailed information about x-ray absorption followed by radiative-decay for inner-shell excitations if it were possible to measure the x-ray absorption spectra resolved for individual radiative processes. One simple technique for obtaining radiative-process-resolved (RPR) x-ray absorption measurements is to selectively determine the photon energy of emitted x-rays by optimizing the window widths of position sensitive detectors (PSD) in wavelength-dispersive x-ray spectrometers. In this paper, we demonstrate the RPR-XAS technique in an examination of graphite and diamond [1, 2].

2. Experimental

RPR x-ray absorption spectra can be obtained from partial fluorescence yield (PFY) x-ray absorption measurements. In PFY x-ray absorption measurements, x-ray emission signals are selectively extracted from specified radiative processes by optimizing the window width on a PSD. Spectroscopic measurements in this study were carried out using a grating x-ray spectrometer in the BL-8.0.1 beamline at the Advanced Light Source (ALS) facility.

3. Results and Discussion

Figure 1 shows the C *K* x-ray emission spectra and PFY/TEY absorption spectra of (a) graphite and (b) diamond. The width of the wide window in this PSD setup (denoted by A in the figure) was tuned over a range of 263 to 298 eV. The low-energy window (B) was adjusted from 263 to 284 eV, while that of the high-energy window (C) was tuned from 284 to 298 eV, as illustrated in the x-ray emission spectrum. We detected resonant inelastic x-ray scattering (RIXS) in the low-energy window (B), elastic x-ray scattering in the high-energy window (C), and both RIXS and elastic x-ray scattering in the wide window (A). Therefore, the energy-dependent spectra of elastic x-ray scattering can be obtained from the PFY-absorption spectra of (C) or from the spectra obtained after subtracting (B) from (A). In the high-energy-window PFY-absorption spectrum (C) and the subtracted spectrum (A) - (B) of graphite, a sharp peak was observed near 285 eV, followed by a slight plateau in the energy region from 285 to 292 eV. This sharp peak and the broad plateau correspond to the threshold unoccupied electronic structure, and can be identified as *participator* resonant elastic x-ray scattering (REXS) via π^* orbitals. On the other hand, no *participator* REXS is observed in the spectra of diamond.

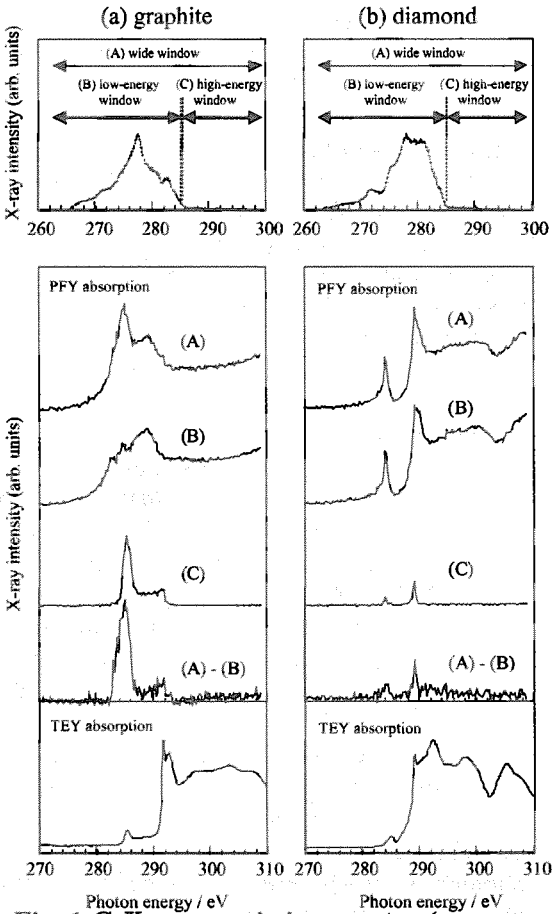

Fig. 1 C *K* x-ray emission spectra (upper panels) and PFY and total-electron-yield (TEY) absorption spectra (lower panels) of (a) graphite powder and (b) diamond
The PFY-absorption spectra were taken by monitoring the x-ray intensity measured by the PSD with (A) wide, (B) low-energy, and (C) high-energy windows. Spectra obtained after subtracting (B) from (A), denoted by (A) - (B), are also shown.

References

1) Y. Muramatsu *et al.*, Phys. Rev. **B 61**, R2393, 2000
2) Y. Muramatsu *et al.*, J. Synchrotron Rad., **8**, 369, 2001

5.5.4 Soft x-ray emission and absorption spectra in the C *K* region of sputtered amorphous carbon films

Yasuji MURAMATSU, Eric M. GULLIKSON[a)], Rupert C. C. PERERA[a)]
a) Center for X-Ray Optics, Lawrence Berkeley National Laboratory

1. Introduction

Amorphous carbon films are important materials of interest in both industrial application and material science. They are believed to consist of random structures of sp^2- and sp^3-hybridized carbon atoms. Furthermore, the structure and chemical bonding states of amorphous carbon films are thought to determine their mechanical and optical properties. Soft x-ray emission and absorption (SXEA) spectroscopy using synchrotron radiation has recently been utilized to characterize various carbon films. SXEA proved capable of obtaining electronic-structure information about both occupied and unoccupied orbitals. However, spectral features observed in the SXEA spectra of amorphous carbon films have not yet been clearly assigned. We have, therefore, measured the high-resolution soft x-ray emission and absorption spectra of amorphous carbon films systematically deposited by various sputtering methods under a variety of conditions to characterize these films from their electronic-structure[1)].

2. Experimental

Amorphous carbon films were deposited by RF, ion-beam, and electron-cyclotron-resonance (ECR) sputtering under various deposition conditions. For RF-sputtered carbon films, the pressure of the source gas was 5×10^{-2} (denoted by R1 in Fig. 1), 1×10^{-1} (R2), or 1×10^{-2} Torr (R3). For ion-beam-sputtered carbon films, the annealing temperature was as-dep. (I1), 400 °C (I2), or 700 °C (I3). For ECR-sputtered carbon films, an acceleration voltage of -20 (E1), -75 (E2), or -100 V (E3) was used. Spectroscopic measurements of SXEA in the C *K* region were made at the Advanced Light Source (ALS) facility. X-ray emission spectra were measured using a grating x-ray spectrometer installed in the beamline BL-8.0.1 while total-electron-yield (TEY) x-ray absorption spectra were measured in beamline BL-6.3.2.

3. Results and discussion

Figure 1 shows the TEY absorption spectra of amorphous carbon films and reference carbon materials at the C *K* threshold. Fine structure consisting of at least five peaks, observed at 285 eV (denoted by C in the figure), 286.5 eV (D), 287.5 eV (E), 288.5 eV (F), and 292.5 eV (G), was clearly observed among the amorphous carbon films. Although relative peak intensities among these five peaks were dependent on the deposition method and conditions, these peaks were observed at constant energy positions. In C *K* x-ray emission spectra, spectral features of these amorphous carbon films were essentially similar, consisting of a broad main peak around 279 eV and a high-energy shoulder peak near 283 eV. However, the peak-to-height ratio of the shoulder-peak to the main-peak depended on the deposition method and conditions. These spectral features suggest that local structures and chemical bonding states are essentially similar among the variously formed amorphous carbon films, however their ratio of sp^2- to sp^3-configured carbon atoms differs depending on the deposition method and conditions.

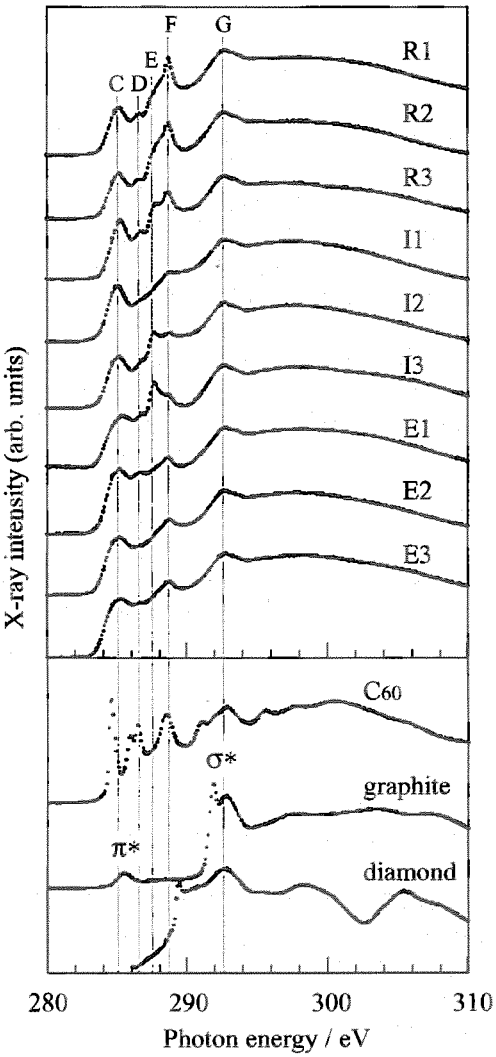

Fig. 1 TEY x-ray absorption spectra at the C *K* threshold of amorphous carbon films deposited by RF (R1-3), ion-beam (I1-3), and ECR sputtering (E1-3)
Spectra of C_{60}, graphite, and diamond are shown as references.

Reference

1) Y. Muramatsu *et al.*, Carbon, **39**, 1403-1407, 2001

5.5.5 Soft x-ray absorption spectra in the O *K* region of microporous carbon and reference aromatic compounds substituted with oxygenated functional groups

Yasuji MURAMATSU, Eric M. GULLIKSON[a)] and Rupert C. C. PERERA[a)]
a) Center for X-Ray Optics, Lawrence Berkeley National Laboratory

1. Introduction

Adsorption properties of microporous carbon are thought to be dependent on the oxidation state of graphitic surface within the micropores. In order to obtain information about the oxidation states of the inner graphitic surface in microporous carbon, soft x-ray emission and absorption spectra of microporous carbon using synchrotron radiation have been measured[1, 2]. In this paper, we describe the soft x-ray absorption spectra in the O *K* region of microporous carbon in addition to a number of reference aromatic compounds substituted with various functional groups, and discuss the chemical bonding states of oxygen in microporous carbon.

2. Experimental

Commercially obtained microporous carbon powder and reference aromatic compounds substituted with typical oxygenated functional groups such as hydroxy (-OH), carboxy (-COOH), carbonyl (>C=O), formyl (-CH=O), and epoxy (-O-) groups were used for spectroscopic measurements. The molecules examined were (A) phloroglucinol, (B) myo-inositol, (C) 1,1'-bi-2-naphthol, (D) 9-(hydroxymethyl) anthracene, (E) 1-naphthoic acid, (F) 9-anthracenecarboxylic acid, (G) 4-phenylbenzoic acid, (H) trimellitic acid, (I) bianthrone, (J) anthrone, (K) 9-anthraldehyde, (L) dibenzo-18-crown 6-ether, (M) 2-hydroxy-1-naphthoic acid, (N) 1-hydroxy-2-naphthoic acid, (O) quinizarin, (P) xanthone, and (Q) naphthalene-1,4,5,8-tetracarboxylic dianhydride. Total-electron-yield (TEY) x-ray absorption measurements were taken for these samples at beamline BL-6.3.2 in the Advanced Light Source (ALS) facility.

3. Results and discussion

Figure 1 shows the TEY x-ray absorption spectra of microporous carbon and the reference aromatic compounds. Spectral features of microporous carbon consist of threshold peaks near 530 eV (denoted by I and II), a plateau (III), and a high-energy broad peak (IV). In the reference aromatic compounds, spectral features are clearly dependent on the oxygenated function group. From comparison of spectral features between microporous carbon and reference aromatic compounds, the peak structure of microporous carbon can be approximated as the sum of the spectra from -COOH and >C=O. In this case, peak (I) results from the >C=O group, peak (II) from the –COOH group, peak (III) from the –COOH group, and peak (IV) from both the -COOH and >C=O groups. Spectral feature analysis using discrete variational (DV) -Xα molecular orbital calculations of the reference aromatic compounds revealed that the existence of measured low-energy peaks (I, II) can be explained by π* orbitals in -COOH and >C(H)=O while the plateau (III) and measured peak (IV) are determined to arise from π* orbitals in -COOH and from σ* orbitals in -COOH and >C(H)=O, respectively.

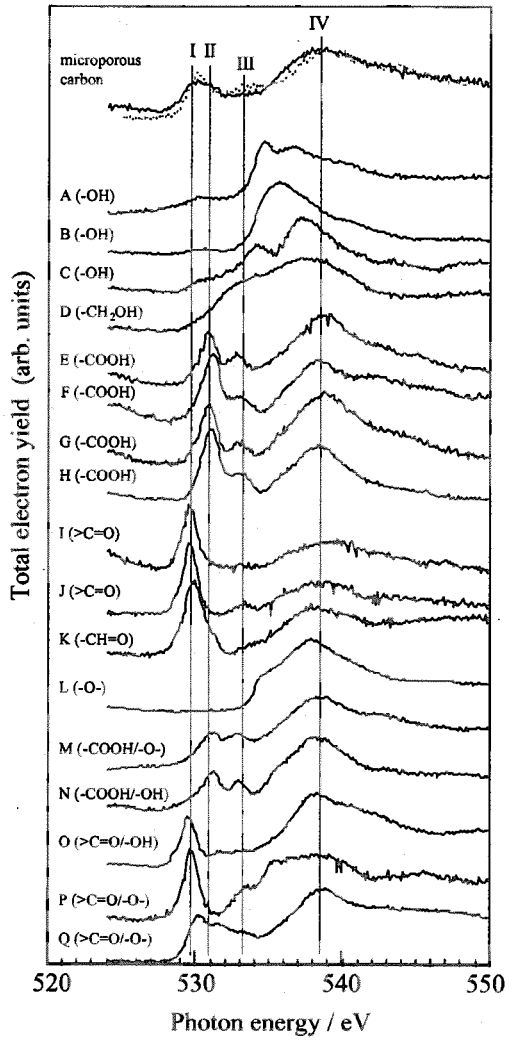

Fig. 1 TEY x-ray absorption spectra in the O *K* region of microporous carbon and reference aromatic compounds
Dotted line of the microporous carbon shows the fluorescence-yield x-ray absorption spectrum.

References

1) Y. Muramatsu *et al.*, J. Electron Spectrosc. and Relat. Phenom., **301**, 114-116, 2001
2) Y. Muramatsu *et al.*, Surf. Rev. Lett. (to be published)

5.6 Electronic Material Science

5.6.1 Nuclear resonant scattering of synchrotron radiation by ^{40}K

Makoto SETO[a)], Shinji KITAO[a)], Yasuhiro KOBAYASHI[a)], Rie HARUKI[a)],
Takaya MITSUI Yoshitaka YODA[b)], Xiao Wei ZHANG[c)] and Yutaka MAEDA[a)]
a) Res. Reactor Institute, Kyoto Univ., Kumatori, Sennan, Osaka 590-0494, Japan
b) Japan Synchrotron Radiation Research Institute, 1-1-1 Kouto, Mikazuki-cho, Sayo-gun, Hyogo 679-5198,Japan
c) KEK-PF, Tsukuba, Ibaraki 305-0801, Japan

1. Introduction

Potassium is one of the most important elements in material and biological sciences, and the extensive and detailed investigation on the local vibration and electronic states of the element will lead new developments of the areas of the researches. However, the resonance excitation of ^{40}K using SR has not been accomplished yet. Though the energy tunability of synchrotron radiation has a possibility to do nuclear resonant excitation experiments of various nuclides, the resonance excitation with synchrotron radiation has been observed only for few isotopes: ^{57}Fe, ^{169}Tm, ^{119}Sn, ^{83}Kr, ^{181}Ta, ^{151}Eu and ^{161}Dy. Therefore, the increase of the nuclide that can be excited with synchrotron radiation is highly important. Recently, we have succeeded in observing the nuclear resonance scattering by ^{40}K for the first time using high and high-brilliant synchrotron radiation of Spring-8[1)].

2. Experimental and results

The experiment was performed at BL11XU of the SPring-8. The storage ring was operated in a 116-bunch mode, giving a bunch distance of 41.3 ns. Experimental set-up is shown in Fig. 1. The 3rd harmonic of the undulator radiation was reduced to ~2 eV bandwidth at an energy of 29.83 KeV with a double crystal Si(333) monochromator. An Al plate of 2 mm thickness was placed in front of the slits to reduce the first harmonic radiation (9.94 KeV) passing through the monochromator. The sample was KCl powder purchased from Oak Ridge National Laboratories whose isotope ratio (^{39}K: ^{40}K: ^{41}K) was 90.42:4.03:5.55. It was measured as a tablet of 4 mm diameter and 3 mm thickness, held in a polyethylene sample holder at room temperature (298 K). The powder KCl sample was placed on the Be window of a Si-avalanche photo-diode detector. As ^{40}K is a radioactive nuclide decaying into ^{40}Ca(89.28 %, β decay) and into ^{40}Ar(10.72 %, electron-capture decay), the measured background contained the radioactive emission from ^{40}K. The signal due to the resonance excitation has a time structure depending on the incident pulse timing. Therefore, by limiting the measuring time window to an adequate duration in which the signal due to the resonance excitation can be observed, a good signal-to-noise ratio can be obtained. We have searched delayed counts in the time interval 5-15 ns after the prompt incident pulse. The result of the energy scan is shown in Fig. 2. Obviously, the nuclear resonant scattering by ^{40}K is observed.

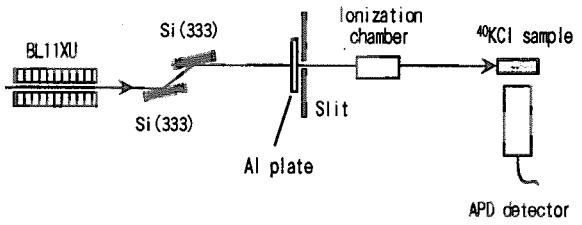

Fig. 1 Schematic view of experimental

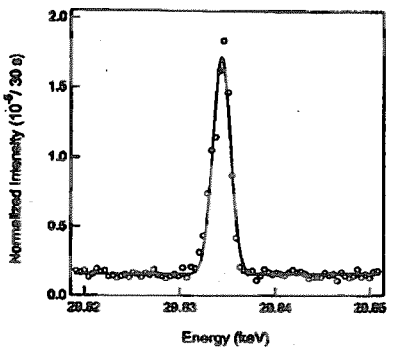

Fig. 2 Energy spectrum of delayed emission from ^{40}K in KCL

3. Summary

We should emphasize that we could measure the nuclear resonant scattering of synchrotron radiation by the radioactive ^{40}K nuclide in spite of the constant radioactive background, and this is the step for the future study using the radioactive nuclides. For example, ^{129}I, ^{133}Ba, and ^{238}U are the radioactive nuclide by which the nuclear resonant inelastic scattering is expected to be observed. Our observation of the nuclear resonant excitation of ^{40}K shows that the electric and vibrational studies on potassium can be possible. Therefore, the promising future of experimental studies on potassium in material and life sciences is opened.

Reference

1) M.Seto *et al.*, Phys. Rev. Lett., **84**, 566, 2000

5.6.2 Bragg angular dependence of the quantum beat of nuclear resonant scattering

Takaya MITSUI, Yasuhiro KOBAYASHI[a], Makoto SETO[a] and Xiao Wei ZHANG[b]
a) Research Reactor Institute, Kyoto Univ., Kumatori, Sennan, Osaka 590-0494, Japan
b) KEK-PF, Tsukuba, Ibaraki 305-0801, Japan

1. Introduction

$^{57}FeBO_3$ (Iron borate) single crystals offer the unique possibility to study nuclear Bragg diffraction of quite different character. Especially, the (h h h) reflections allow for h=2n+1 purely nuclear reflections. It is due to the antiferromagnetic structure of iron borate. In addition the reflections with h=4n+2 should be nearly pure nuclear because of accidental cancellation of electric scattering amplitude of the unit cell. In pure nuclear reflections, all hyperfine transitions can be observed by contrast to the antiferromagnetic superlattice reflections, so that the quantum beat of Mössbauer time spectra are constructed by only the $\Delta m=\pm1$ transitions. On the other hand, for the reflections with h=4n+2, time spectrum may show the strong Bragg angular dependence for the spin alignments parallel or perpendicular to the scattering plane. In order to demonstrate the angular dependence of the quantum beat of nuclear Bragg scattering experimentally, Mössbauer time spectra in the reflections (2 2 2) {θ_B=10.266°} and (10 10 10) {θ_B=63.014°} were measured under the two different conditions; ($H_{ex}\perp$ Scattering plane and H_{ex}// Scattering plane)[1].

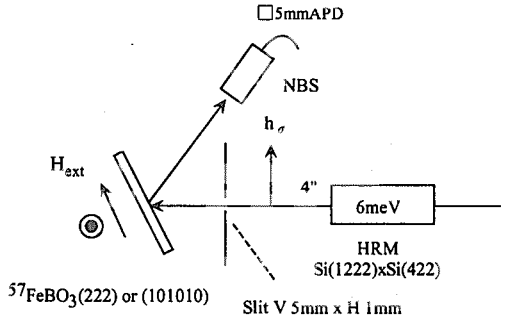

Fig. 1 Schematic view of experimental setup

2. Experimental

The experiments were performed at the NE3 undulator beam line of KEK. The experimental set-up is shown in Fig. 1. A 4-bounce precision monochromator produced the σ -polarized X-ray with the energy width of 6.4 meV at 14.4 keV nuclear resonance in ^{57}Fe. The static magnetic field (12 Oe) were applied parallel to $^{57}FeBO_3$ single crystal surface and parallel or perpendicular to the scattering plane. Mössbauer time spectra of (2 2 2) refection and (10 10 10) refrection were measured by fast detector (APD).

3. Results

The measured time spectra of reflections (10 10 10) and (2 2 2) are shown in Fig. 2 (a),(b) and Fig. 2 (c),(d) respectively; [(a),(c);$H_{ex}\perp$scattering plane, (b),(d);H_{ex} // scattering plane]. The time spectra of (2 2 2) reflection show the similar short periods of quantum beat patterns which are related to $\Delta m=\pm1$ transitions [See Fig. 2 (c),(d)]. On the contrary, the time spectra of (10 10 10) reflection show the obvious dependence for the external magnetic field conditions [See Fig. 2 (a),(b)]. Especially, in the case of $H_{ex}\perp$scattering plane, only $\Delta m=0$ transitions contribute to the quantum beat of the time spectrum [See Fig. 2 (a)]. It is due to the Bragg angle dependence of polarization factors of nuclear Bragg scattering amplitudes. {Theoretical detail is described in Ref. 2.} The time spectrum of the high angle Bragg diffraction will become the useful tool for the research of magnetic structure of magnetic crystals {spin- reorientation transition etc}.

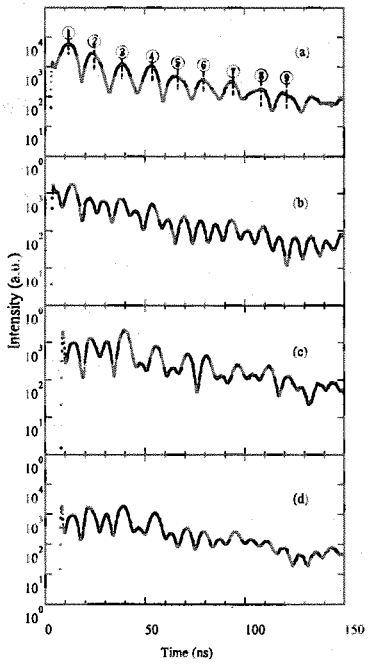

Fig. 2 Time spectra of nuclear Bragg scattering of $^{57}FeBO_3$ in (10 10 10) and (2 2 2) reflections [(a),(c);$H_{ex}\perp$ scattering plane, (b),(d);H_{ex} // scattering plane]

References

1) T.Mitsui *et al.*, PF Activity Report (2000) in press
2) U.V.Bürck *et al.*, J.Phys.C:Solid St.Phys.**13**, 4511, 1980

5.6.3 High-resolution photoemission spectroscopy of $Yb_2Co_3X_9$ (X = Ga and Al)

Tetsuo OKANE, Shin'ichi FUJIMORI, Akihiro INO, Atsushi FUJIMORI[a)],
S. K. DHAR[b)], C. MITRA[b)], P. MANFRINTTI[c)] and A. PALENZONA[c)]
a) University of Tokyo b) T.I.F.R. c) Universita di Genova

1. Introduction

The isostructural compounds $Yb_2Co_3X_9$ (X = Ga, Al), which crystallize in the orthorhombic $Y_2Co_3Ga_9$-type structure, show the typical properties of heavy-fermion antiferromagnets for X = Al, while they show mixed-valent behavior for X = Ga[1)]. On the other hand, for photoemission spectroscopy (PES) of Yb compounds, the single-impurity Anderson model (SIAM) predicts the presence of a sharp many-body resonance, so-called *Kondo peak* at the energy k_BT_K (T_K: Kondo temperature) below the Fermi level (E_F), which has a width of k_BT_K and loses its weight as the temperature rises[2)], We have performed the high-resolution PES study for $Yb_2Co_3X_9$ (X = Ga, Al) to investigate a difference of the electronic structures between the Kondo-lattice and the mixed-valent systems.

2. Experiment

The $Yb_2Co_3Ga_9$ and $Yb_2Co_3Al_9$ samples were polycrystalline samples prepared in an induction furnace. Photoemission spectra were measured with He I (21.2 eV) or He II (40.8 eV) radiation produced by a He discharge lamp. The overall instrumental resolution was ~ 5 meV.

3. Results and discussion

Figure 1 shows the valence-band PES spectra of $Yb_2Co_3Ga_9$ and $Yb_2Co_3Al_9$. One can see that only in the spectrum of $Yb_2Co_3Ga_9$ there are two spike-like sharp structures just below E_F and at 1.35 eV, which are interpreted as the signal of the Yb^{2+} $4f$ spin-orbit doublet of the $4f^{13}{}_{7/2}$ and $4f^{13}{}_{5/2}$ final states. In order to extract the line-shape of the Yb^{2+} $4f$ signal, the valence-band spectrum of $Lu_2Co_3Ga_9$, which is almost the same as that of $Yb_2Co_3Ga_9$ except for the $4f$ component, was subtracted from that of $Yb_2Co_3Ga_9$, as shown in Fig. 1. The difference spectrum is regarded as the pure Yb^{2+} $4f$ signal. Here the Yb^{2+} $4f$ signal can be decomposed into two sets of spin-orbit doublet, i.e., the surface and bulk components and the additional structures that are humps at 0.3 and 1.6 eV. The bulk Yb $4f^{13}{}_{7/2}$ peak, which lies just below E_F, has a peak position at the binding energy of 26 meV. This peak position is comparable to k_BT_K = 23 meV estimated from the Kondo temperature 260 K of the thermodynamic properties in $Yb_2Co_3Ga_9$[1)]. The result agrees with the prediction of SIAM.

On the other hand, we cannot observe the bulk component of the Yb^{2+} $4f$ signals in the spectrum of $Yb_2Co_3Al_9$ measured at T = 14 K. Thermodynamic measurements indicate that the Kondo temperature of $Yb_2Co_3Al_9$ is negligibly small compared to that in $Yb_2Co_3Ga_9$[1)]. Therefore, the result in Fig. 1 seems to reflect the difference in the Kondo temperatures of these compounds, and is consistent with SIAM. Meanwhile, the multiplet structure of the Yb^{3+} $4f$ component is observed in the binding-energy range from 5 to 11 eV, and the energy position of the multiplet structure is shifted by 0.4 eV towards E_F in going from $Yb_2Co_3Ga_9$ to $Yb_2Co_3Al_9$[3)]. This indicates the rise of the $4f$ energy level in going from $Yb_2Co_3Ga_9$ to $Yb_2Co_3Al_9$, which would stabilize the Yb^{3+} configuration in $Yb_2Co_3Al_9$ and make the Kondo temperature lower. The origin of the variation from the mixed-valent Ga-based compounds to the heavy fermion Al-based compounds is attributed to the rise of the $4f$ energy level and possible decrease in the $4f$-ligand hybridization strength.

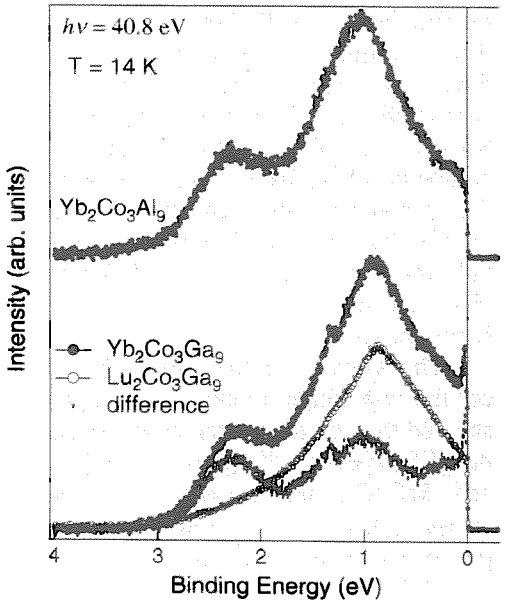

Fig. 1 valence band PES spectra of $Yb_2Co_3X_9$ (X = Ga, Al)

References

1) S.K.Dhar *et al.*, Physica B **259-261**,150,1999
2) N.E.Bickers *et al.*, Phys. Rev. B **36**, 2036, 1987
3) T.Okane *et al.*, in preparation

5.6.4 Photoemission study of quasi-one-dimensional halogen-bridged Ni compound $[Ni(chxn)_2Br]Br_2$

Shin-ichi FUJIMORI, Akihiro INO, Testuo OKANE, Atushi FUJIMORI, Kozo OKADA[a], Toshio MANABE[b], Masahiro YAMASHITA[b], Hideo KISHIDA[c] and Hiroshi OKAMOTO[c]

a) Department of Physics, Faculty of Science, Okayama University, Tsushima-naka, Okayama 700-8530, Japan
b) Department of Chemistry, Graduate School of Science, Tokyo Metropolitan University, Tokyo 192-0397, Japan
c) Department of Advanced Material Science, Graduate School of Frontier Science, University of Tokyo, Tokyo 113-8656, Japan

The one-dimensional (1D) halogen (*X*) bridged transition-metal (*M*) compounds (*MX*-chain compounds) have been attracting much attention as a good target material to investigate the properties of the 1D electronic state under the influence of strong electron-lattice interactions and electron-electron correlations. In particular, the complex with *X*=Br and *M*=Ni, $[Ni(chxn)_2Br]Br_2$ (chxn=1R, 2R-cyclohexanediamine) is known to show no lattice distortions related to Peierls or Spin-Pierls transition even at low temperatures. The magnetic susceptibility χ is described by Boner-Fisher formula with S=1/2 and J=3600K, and this material can be regarded as the 1D Heisenberg chain. In addition to these purely academic interests, it is recently recognized that these strongly-correlated 1D electron systems show strong non-linear optical effects[1]. These effects are indispensable for the opto-electronic switching or modulating devices, and it is hoped that these materials may become key materials for the future optical technology.

In the present study, the electronic structure of this compound is studied by angle-resolved photoelectron spectroscopy (ARPES). We have measured the ARPES spectra of $[Ni(chxn)_2Br]Br_2$ with parallel to the chain axis (not shown). To illustrate the peak structure of these spectra more clearly, we have derived experimental band dispersion by taking the second derivatives of the smoothed ARPES spectra. Figure 1 shows their gray-scale plot as a function of binding energy and momentum, where the dark part corresponds to peak positions. In the spectra, only one "band" having about 0.5e V energy dispersion, is found in the first half of the Brillouin zone. This result is qualitatively different from those of Cu-O based strongly-correlated 1D elecron system like $SrCuO_2$[2]. In these Cu-O based 1D compounds, two bands originated with the spinon and holon are observed in the first half of the Brillouin zone, and only one band originated with holon is observed in the second half of the Brillouin zone.

The analysis of the spectra based on the *d-p* chain model calculations showed that the model can describe the ARPES spectra of $[Ni(chxn)_2Br]Br_2$ and $SrCuO_2$, and suggests that the charge-transfer energy Δ is smaller in $[Ni(chxn)_2Br]Br_2$ compared with that of $SrCuO_2$[3].

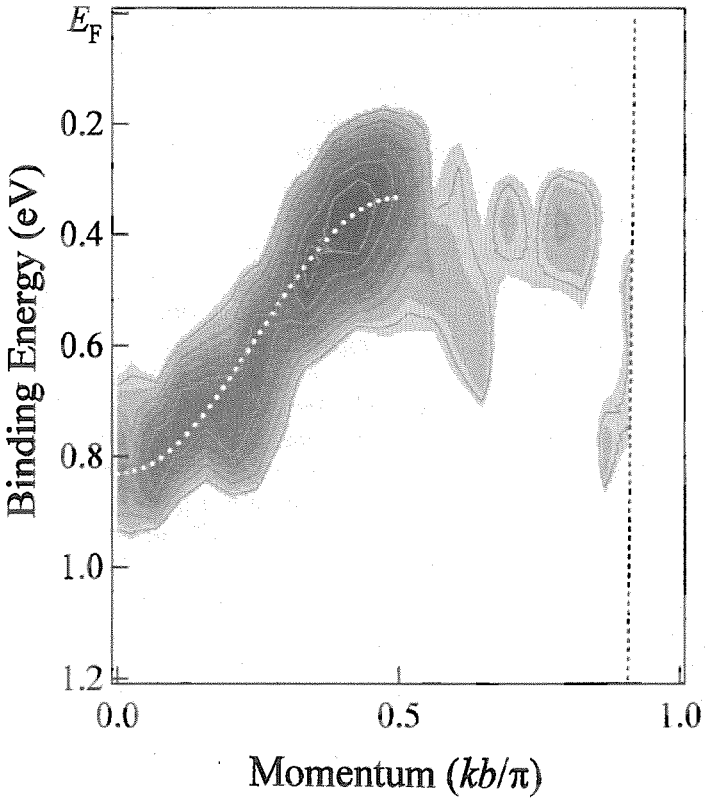

Fig. 1 "band dispersion" of $[Ni(chxn)_2Br]Br_2$

References

1) H. Kishida *et al.*, Nature **405**, 929, 2000
2) C. Kim *et al*, Phys. Rev. Lett., **77**, 4054, 1996
3) S.-i. Fujimori *et al.*, submitted

5.7 Experimental facilities development

5.7.1 Diamond double-crystal monochromator in Bragg geometry installed on BL11XU at SPring-8[1)]

Kazukiyo TOZAWA, Motoharu MARUSHITA [a)], Takaya MITSUI,
Tatsuo FUKUDA, Masamitu TAKAHASI, Toshiya INAMI,
Yoshinori KATAYAMA, Hideaki SHIWAKU, Jun'ichiro MIZUKI
a) Ishikawajima-Harima Heavy Industries Co., Ltd.

1. Introduction

It is well known that one of the major problems in X-ray optics for third-generation synchrotron facilities is the thermal deformation produced by the high heat load. Extremely high heat load from the SPring-8 standard in-vacuum undulator[2)] impinges on the beamline optics. The total radiation power and peak heat flux are calculated to be 13.7 kW and 525 kW/mrad^2, respectively, when the undulator gap is 8 mm and the storage current is 100 mA. Since diamond is known to have very attractive thermal properties and high quality single crystals are available, ESRF, ASP and SPring-8 have been using it as a monochromator crystal[3-5)].

2. Experimental

The present synthetic diamond (111) plates were manufactured by Sumitomo Electric Industries, Ltd.[6)]. The size of the diamond crystals used at BL-11XU is 8.6 mm (w) x 3.5 mm (l) x 0.35 mm (t) (first crystal) and 10 mm (w) x 4.7 mm (l) x 0.39 mm (t) (second crystal). The first diamond crystal is exposed to a maximum total power of 460 W when the undulator gap is 8 mm at 100 mA electron current. In the present design, the crystal is mounted across a 5 mm-wide groove on a copper support. Fig. 1 shows the water-cooled copper block. The incident X-rays pass through the groove. This design prevents the block from heating by the transmitted X-rays through the diamond. The thermal contact between the diamond and the copper was achieved by using a thin layer of Ga/In eutectic. The second crystal simply sits on a thin plate, see Fig. 2. The second crystal was exposed to X-rays from below.

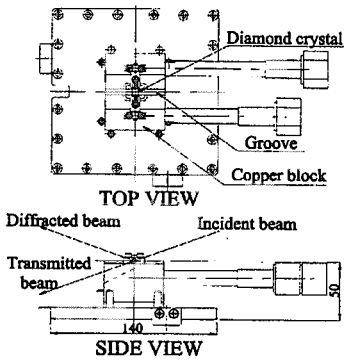

Fig. 1 Top view and side view of the copper block

The first crystal was located at 38.5 m from the undulator. The sequence of the optical elements from the undulator installed in the beamline before the monochromator was as follows:

Graphite filters (thickness: 0.3 mm) - XY-slits (aperture: 1 mm x 1 mm) at 29 m from the undulator - Be window (thickness: 0.5 mm).

The intensity of the higher-order reflection, mainly (333), was measured by a PIN photo-diode detector with a metal filter in front. The filter was 2 mm thick aluminum for X-ray energies of 6.6 keV and 10.2 keV, 0.5 mm stainless steel for 14.5 keV, 1 mm copper for 25.5 keV and 2 mm copper for 36.7 keV.

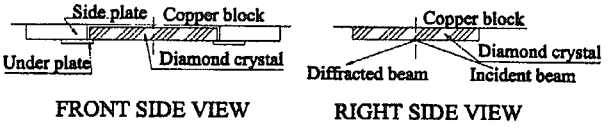

Fig. 2 Front side and right side view of the second diamond crystal mounting

3. Results

The rocking curve scanning was carried out at five different energies, 6.6, 10.2, 14.5, 25.5 and 36.7 keV, in order to estimate the deformation and thermal stress in the crystal which could be introduced by holding the crystal and by X-ray exposure. The deformation and thermal stress in the crystal would result in an increase of the full-width at half-maximum (FWHM) of the double-crystal rocking curve. Table 1 gives the incident and absorbed power to the first crystal. Figure 3 shows the FWHM and the peak intensity of the rocking curve as a function of storage ring currents at Bragg angles of 6.78 deg. (25.5 keV for (111) and 76.5 keV for (333)). The maximum absorbed power in the first diamond crystal was about 80 W, see Table 1. As seen in this figure, no thermal broadening of the rocking curve was observed. Figure 4 shows the FWHM of the double-crystal rocking curve as a function of energy for the (111) and (333) reflections, together with the calculated curves[3)]. The scatter in the data could be due to a difference of the X-ray beam

Table 1 Incident and absorbed power by the first diamond crystal as a function of the undulator gap and the photon energy[a]

Diamond (111) photon energy (keV)	6.6	10.2	14.5	25.5	36.7
Diamond (333) photon energy (keV)	19.9	30.5	43.4	76.5	110.2
Gap (mm)	11.2	15.25	21.65	13.1	17.2
Deflection parameter K	1.94	1.33	0.766	1.57	1.05
Incident power (W/mA)	3.3	1.9	0.84	2.4	1.4
Absorbed power (W/mA)	0.51	0.42	0.23	0.8	0.59

[a]**The incident flux and the absorbed power in the first crystal were calculated by employing the computer code SPECTRA[7] using the data of the photon cross sections.**

position on the diamond crystal. The discrepancy between the calculated and the observed results increased with energy. This was probably due to the increase of the footprint area of the X-rays on the mosaic crystal with energy. The mosaic width can be calculated by the following equation,

$$\text{Mosaic width}=\sqrt{(\text{observed}^2-\text{calculation}^2)}/\sqrt{2}$$

Using this equation, the mosaic width of each crystal was estimated to be 2-5 arcsec.

In order to estimate the stress introduced by holding the second crystal, the FWHM measurements by rocking the first ($\Delta\theta_1$) and the second crystal ($\Delta\theta_2$) were performed in a [+—] arrangement, with a silicon (333) crystal inserted downstream of the monochromator. Figure 5 shows the FWHM of the rocking curves at 14.5 keV. The calculated value was obtained by the DuMond diagram with the assumption that the diamond is a perfect crystal. It can be said by considering the way of holding the first crystal that no stress is introduced to the first crystal. Therefore, since almost no difference of the FWHM between the first and the second crystal scanning was observed within the experimental accuracy, it was concluded that no stress was introduced to the second crystal by the holding. The divergence after the diamond double-crystal monochromator was about 9 arcsec at 14.5 keV observed by rocking the Si (333) crystal.

4. Conclusions

Two diamond crystals in double-crystal monochromator in Bragg geometry was installed for the first time and tested at SPring-8. It was observed that the first crystal was not deformed by heat load up to 330 W total power. The second crystal was mounted without introducing significant stress.

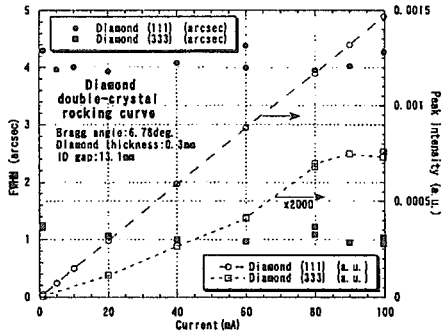

Fig. 3 FWHM and the peak intensity of the diamond double-crystal rocking curve at a Bragg angle of 6.78 deg

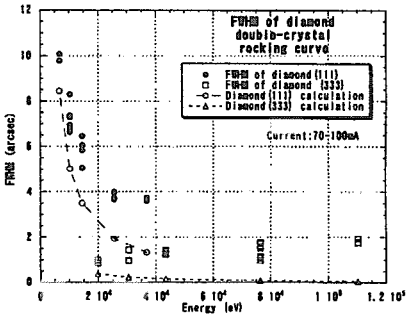

Fig. 4 Calculated and measured FWHM of the diamond double-crystal rocking curves

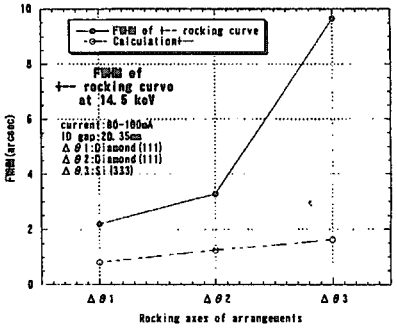

Fig. 5 FWHM of [+—] arrangement rocking curves at 14.5 keV

References

1) M.Marushita *et al.*, Nucl. Instr. and Meth. A **467-468**, 392, 2001
2) T.Hara *et al.*, J. Synchrotron Radiat., **5**, 403, 1998
3) A.K Freund, Opt. Eng., **34**, 432, 1995
4) P.B Fernandez *et al.*, Nucl. Instr. and Meth., A **400** , 476, 1997
5) J.Matsui *et al.*, SPring-8 Annual Report, p. 125, 1997
6) H Sumiya *et al.*, Rev. High Press. Sci. Technol., **7**, 960, 1998
7) H.Kitamura, T.Tanaka, SPECTRA Synchrotron Radiation Calculation Program. Ver.1.1., SPring-8, Japan.

5.7.2 Investigate of photoneutron spectrum due to gas bremsstrahlung at the insertion device beamline of SPring-8

Yoshihiro ASANO

1. Introduction

In order to investigate the radiation fields around synchrotron radiation beamlines, photo-neutron spectra due to the interactions of thick targets of lead and copper with gas bremsstrahlung which generated by the interaction of stored electrons with residual gas molecules in a storage ring vacuum chamber, were measured outside the hutch (an enclosure of the beam, optical elements or experimental instruments) of the insertion device beamline of SPring-8, BL11XU, by using high sensitive multi-moderated Bonner type ^{3}He counters[1]. The measurement data were unfolded and converted to the spectra and effective doses.

2. Experiments and calculations

The intensities of gas bremsstrahlung were measured by using PWO detector. The targets and the PWO detector were installed alternately on the photon beam axis upstream of the monochromator. The targets were employed for lead of 10 cm in thickness ($17.8X_0$, X_0: radiation length), and copper of 10 cm in thickness ($6.94X_0$). The helium-3 counters with moderators of various thickness were set outside the optics hutch. The distances from the center of the targets to the counters are 330.6 cm and 340.2 cm for upstream (No.1) and downstream sides (No.2), respectively.

The yields of photoneutron production and energy spectra due to gas bremsstrahlung were calculated by using EGS4 with cross section libraries of photoneutron production. The photoneutron transport calculation from the target to the estimated points and converted to the effective dose is performed by using MCNP4b with LANLHE library.

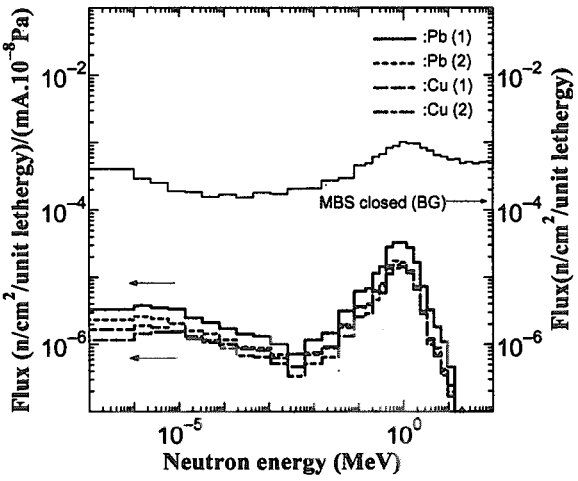

Fig. 1 Leakage photoneutron spectra at the position No.1 and No2 due to gas bremsstrahlung produced by the interaction of 8 GeV stored electron of 1 mA current with the residual gas molecules of 10 nPa vacuum pressure within the normal straight section of 16.54 m

The power of the gas bremsstrahlung is 25.8 nW/mA/10^{-8} Pa. The thin solid line indicates the background neutron spectrum due to cosmic ray. The solid and dotted lines indicate the spectra at position No.1 and No.2 due to the interaction of gas bremsstrahlung with lead target, respectively. The dashed and dot-dashed lines indicate the spectra at position No1 and No2 with copper target, respectively.

3. Results

The neutron spectra were unfolded with the SAND II code, shown in Fig. 1, and the effective dose rates were obtained on the bases of the measured data. As the results, the calculations on the assumption of isotropic emissions could be compared with the measurement data, showing good agreements within 20 % errors in upstream side of the target. On the other hand, the difference of about 70 % is recognized in downstream side of the lead target. In comparison with previous data, we obtained the agreements within the factor 2 for calculated data without considering the scattering neutrons, and within the factor 1.7 for measurement data by using Anderson Brawn type REM meter.

Reference

1) Y.Asano, Proc. of Int.Workshop on Radiation Safety at Synchrotron Radiation Sources at APS (2000)

6. List of publications

6.1 List of publications on Advanced Photon Research Center

High peak power laser development (Laser System Development Group)

1. Journal

1) Ultrafast, Ultrahigh-peak, and high-average power Ti:sapphire laser system and its applications, (Invited Paper)
   K. Yamakawa and C. P. J. Barty,
   IEEE J. Selected Topics in Quantum Electronics, Vol. 6, pp. 658-675, 2000
2) Wave-front measurements of terawatt-class ultrashort laser pulses by the Fresnel phase-retrieval method
   S. Matsuoka ,and K. Yamakawa
   Journal of the Optical Society of America, B, 17,663-667,2000
3) Contrast and phase characterization of a high-peak power 20-fs laser pulse
   M. Aoyama, A. Sagisaka, K. Yamakawa, et al.
   Appl. Phys., B70, S149-S153, 2000
4) Numerical analysis of type I third-harmonic generation through third-order and cascading second-order nonlinear optical processes
   T. Zhang, K. Yamakawa
   Japanese Journal of Applied Physics, vol. 39, pp. 91-95, 2000
5) Noncollinear Chirp-Compensated Second Harmonic Generation with Subpicosecond Laser Pulses
   T. Zhang, M. Aoyama, and K. Yamakawa
   Jpn. J. Appl. Phys. Vol.39 (2000) 1146
6) Noncollinear Second Harmonic Generation with Compensation of Phase Mismatch by Controlling Frequency Chirp and Tilted Pulse Fronts of Femtosecond Laser Pulses
   M. Aoyama, T. Zhang, M. Tsukakoshi, and K. Yamakawa
   Jpn. J. Appl. Phys. Vol.39 (2000) 3394
7) Efficient Noncollinear Second-Harmonic Generation with Proper Frequency Chirp and Tilted Pulse Fronts of Femtosecond Laser Pulses
   M. Aoyama, T. Zhang, M. Tsukakoshi, and K. Yamakawa
   Jpn. J. Appl. Phys. Vol.39 (2000) 2651
8) Vacuum ultraviolet Ar excimer emission initiated by high intensity laser produced electrons
   S. Kubodera, J. Kawanaka and W. Sasaki
   Opt. Comm., vol. 182, pp. 407-412, 2000
9) 134 nm vacuum ultraviolet emission using an Ar/Kr gas mixture excited by a quasi-continuous-wave gas jet discharge
   J. Kawanaka, S. Kubodera, and W. Sasaki
   Appl. Phys. B, vol. 72, pp. 179-182, 2001
10) Observation of vacuum ultraviolet Kr_2* laser oscillation pumped by a compact discharge device
    W. Sasaki, T. Shirai, S. Kubodera, J. Kawanaka and T. Igarashi
    Optics. Lett., vol. 26, pp. 503-505, 2001
11) Tunable continuous-wave Yb:YLF laser operation with a diode-pumped chirped-pulse amplification system
    J. Kawanaka, H. Nishioka, N. Inoue, and K. Ueda
    Appl. Opt., vol. 40, pp. 3542-3546, 2001
12) Quatrature frequency conversion scheme using $CsLiB_6O_{10}$ crystals for the efficient second-harmonic generation of high power Nd:YAG laser
    H. Kiriyama, S. Matuoka, F. Nakano, K. Yamakawa
    Optical Review, vol. 7, pp. 281-283, 2000
13) Highly efficient second-harmonic generation in novel four-pass quadrature frequency cpnversion
    H. Kiriyama, S. Matuoka, Y. Maruyama, T. Arisawa
    Nuclear Instruments & Methods in Physics Research, A 455, pp. 236-238, 2000

2. Proceedings

1) Discharge pumped vacuum ultraviolet Kr_2^* laser
T. Shirai, W. Sasaki, S. Kubodera, J. Kawanaka, and T. Igarashi
Proceedings of the XIII International Symposium on Gas Flow & Chemical Lasers and High Power Laser Conference (GCL/HPL, SPIE), pp. 334, 2000
2) Energy extraction performance for CPA system in Yb-doped materials at low temperature
J. Kawanaka, H. Nishioka and K. Ueda
Abstracts of the second symposium on advanced photon research, pp. 24, 2000
3) Improved saturation fluence for peta-watt CPA system in low temperature Yb-doped materials
J. Kawanaka, H. Nishioka and K. Ueda
Technical Digest of Conference on Lasers and Electro-Optics (CLEO) 2000 (OSA), pp. 250-251 (2000)
4) Energy extraction performance for a diode-pumped CPA system in Yb-doped materials at low temperature
J. Kawanaka, H. Nishioka, N. Inoue and K. Ueda
The XIII International Symposium on Gas Flow & Chemical Lasers and High Power Laser Conference(GCL/HPL, SPIE), pp. 141, 2000
5) Observation of vacuum ultraviolet Kr_2* laser oscillation pumped by a compact discharge device
S. Kubodera, T. Shirai, W. Sasaki, J. Kawanaka and T. Igarashi
Technical Digest of Conference on Lasers and Electro-Optics (CLEO) 2001 (OSA), pp. 461, 2001
6) Efficient second-harmonic generation of high power Nd:YAG laser in multi-pass quadrature frequency conversion scheme
H. Kiriyama, F. Nakano, K. Yamakawa
Technical Report of IEICE, vol.LQE2000-67, (2000-10), 2000
7) Highefficiency, high average power second-harmonic generation in a two-pass quadrature frequency cobversion scheme using $CsLiB_6O_{10}$ crystals
H. Kiriyama, S. Matuoka, F. Nakano, A. Sagisaka, K. Yamakawa
CLEO Europe '2000 Conference Digest CThB8, 285, 2000
8) Wave-front reconstruction of terawatt-class ultrashort laser pulses using Fresnel phase retrieval method
S. Matsuoka and K. Yamakawa
Technical Digest of Conference on Lasers and Electro-Optics (CLEO) 2000 (OSA), pp. 289-290 (2000)

3. Patents

1) Method for changing a wavelength of a laser light
H. Kiriyama, Y. Maruyama, T. Arisawa
Patent number: 09/640,747
2) Wavefront measurement method
S. Matsuoka, K. Yamakawa
Application number: 11-288301

X-ray laser development (X-ray Laser Research Group)

1. Journals

1) Observation of X-Ray Spectra from nitrogen clusters irradiated with high-intensity ultrashort laser pulses
Sagisaka, H. Honda, K. Kondo, H. Suzuki, K. Nagashima, T. Kawachi, A. Nagashima, Y. Kato, H. Takuma
Applied Physics B70 549-554 (2000)
2) Optical guidance of terrawatt laser pulses by the implosion phase of fast Z-pinch discharge in a gas-filled capillary
T. Hosokai, M. Kando, H. Dewa, H. Kotaki, S. Kondo, N. Hasegawa, K. Horioka and K. Nakajima
Optics Letters (Optical Society America) vol. 25, 10 (2000)
3) Fast Z-pinch optical guiding for laser wakefield acceleration

T.Hosokai, M.Kando, H.Dewa, H.Kotaki, S.Kondo, K.Horioka, K.Nakajima
Nuclear Instruments and Methodes in Physics Research A 455 (2000) 155-160

4) Fast Z-pinch optical guiding for X-ray generation and laser-plasma accelerators
T. Hosokai, M. Kando, H. Dewa, H. Kotaki, S. Kondo, N. Hasegawa,
K. Horioka and K. Nakajima
Nuclear Instruments and Methode B

5) Effect of multipulse waveform on Gains of Soft X-ray Lines of Lithium-like Aluminum in Recombining Plasmas
Kazunobu Okasaka, Tetsuya Kawachi, Hitoshi Oyama, Tamio Hara,
Naohiro Yamaguchi and Kozo Ando
Jpn. J. Appl. Phys. Vol. 39 (2000) pp. 70-81

6) Technical Information of X-ray Lasers
Yoshiaki Kato
Japanese Journal of Optics, vol.29, No.5, pp.279-285 (2000)

7) Research on Advanced Photon Science
Yoshiaki Kato
Gensiryoku EYE, vol.46, No.6, pp.55-57 (2000)

2. Proceedings

1) Development of table-top transient collisional excitation x-ray lasers
M. Kado, T. Kawachi, N. Hasegawa, M. Tanaka, K. Takahashi, K. Sukegawa, K. Nagashima, A. Nagashima, Y. Kato
Proc. SPIE Vol.3886, 278-284 (2000)

2) Study of TCE X-Ray Laser-Driven Innershell Photoionization Soft X-Ray Laser in Sodium Vapor
P. Lu, T. Kawachi, K. Moribayashi, M. Tanaka, M. Kado, N. Hasegawa, K. Sukegawa, S. Namba, K. Nagashima, A. Nagashima, Y. Kato
Proceedings of the Second Symposium on Advanced Photon Research

Free electron laser development (Free Electron Laser Research Group)

1. Journals

1) Recent Progresses of Free-Electron Lasers Driven by a Superconducting RF Linac
Eisuke Minehara
Genshiryoku eye, vol.46, No.6, p.66-67 (2000)

2) JAERI Design Options for Realizing a Compact and Stand-Alone Superconducting RF Linac-Based High Power Free-Electron Laser
Eisuke Minehara, Toshihiko Yamauchi, Masayoshi Sugimoto, Masaru Sawamura, Ryoichi Hajima, Ryoji Nagai, Nobuhiro Kikuzawa, Nobuyuki Nishimori, Toshiyuki Shizuma
Nuclear Instrument and Methods in Plysical Research, U.S.A., 2000, in press

3) Second Harmonic Generation in CdTe plate bg Free Electron Laser
Toshihiko Yamauchi, Nobuhiro Kikuzawa, Eisuke Minehara, Ryoji Nagai, Nobuyuki Nishimori, Masaru Sawamura, Ryoichi Hajima, Toshiyuki Shizuma, Takehito Hayakawa
Japanese Journal of Applied Physics, 39(10), p.5912-5913 (2000)

4) Decomposition Experiment of Dioxins by IR Laser Irradiation
Toshihiko Yamauchi, Eisuke Minehara, Nobuhiro Kikuzawa, Takehito Hayakawa, Masaru Sawamura, Ryoji Nagai, Nobuyuki Nishimori, Ryoichi Hajima, Toshiyuki Shizuma, Yasudaka Kamei, Shinichi Ito, Yukio Furukawa
Society of Environmental Science, Japan, 13(3), p.383-390(2000)

5) Simulated performance of energy-recovery transport system for the JAERI-FEL
Toshiyuki Shizuma, Ryoichi Hajima, Eisuke Minehara
Nuclear Instrument and Methods in Plysics Research, U.S.A., 2000,

6) High Power Lasing of the JAERI-FEL Driven by Superconducting RF Linac
Ryoji Nagai, Ryoichi Hajima, Nobuyuki Nishimori, Masaru Sawamura, Nobuhiro Kikuzawa, Toshiyuki Shizuma, Eisuke Minehara
Extended Abstracts (The 61st Autumn Meeting), Hokkaido, 2000, in press

7) 3rd-Harmonic Lasing at JAERI-FEL

Ryoichi Hajima, Ryoji Nagai, Nobuyuki Nishimori, Nobuhiro Kikuzawa, Eisuke Minehara
Nuclear Instrument and Methods in Plysical Research, U.S.A., 2000, in press

8) Analyses of superradiance and spiking-mode lading observed at JAERI-FEL
Ryoichi Hajima, Nobuyuki Nishimori, Ryoji Nagai, Eisuke Minehara
Nuclear Instrument and Methods in Plysical Research, U.S.A., 2000, in press

9) Development of an Optical Resonator with High-Efficient Output Coupler for the JAERI Far-Infrared Free-Electron Laser
Ryoji Nagai, Ryoichi Hajima, Nobuyuki Nishimori, Masaru Sawamura, Nobuhiro Kikuzawa, Toshiyuki Shizuma, Eisuke Minehara
Journal of Nuclear Science and Technology, 38(1), p.15-18 (2001)

10) Decomposition Experiment of Dioxins by IR Laser Irradiation
Toshihiko Yamauchi, Eisuke Minehara, Nobuhiro Kikuzawa, Takehito Hayakawa, Masaru Sawamura, Ryoji Nagai, Nobuyuki Nishimori, Ryoichi Hajima, Toshiyuki Shizuma, Yasutaka Kamei, Hisato Ikai, Shinichi Ito, Yukio Furukawa
22nd Inter. FEL Conf. And 7th FEL Users Workshop, U.S.A., 2000, in press

11) Decomposition Test of PCB by CO2 Laser Irradiation
Toshihiko Yamauchi, Yasutaka Kamei, Shinichi Ito, Yukio Furukawa, Eisuke Minehara
Society of Environmental Science, Japan, 14(1), p.73-76 (2001)

12) World-Strongest Lasing of Superconducting RF Linac Based Free-Electron Lasers and Their Industrial Applications and Academic Uses
Eisuke Minehara
Isotope News, No.559, pp.8-10 (2000)

13) Yrast bands in N=91 isotones
Takehito Hayakawa, Masumi Oshima, Yuichi Hatsukawa, Jyunichi Katakura, Hidenori Iimura, Makoto Matsuda, Nobuo Shinohara, Yousuke Tou, Shirou Mitarai*, Toshiyuki Shizuma, Masahiko Sugawara, Hideshige Kusakari
The European Physical Journal A, 9(2), p.153-156 (2001)

14) A Report of "Workshop on Physics of, and Science with, the X-ray Free-Electron Laser"
Ryoichi Hajima, Mitsuru Uesaka, Tadashi Matsushita
Journal of the Japanese Society for Synchrotron Radiation Research, 13(5), p.56-58 (2001)

15) JAERI superconducting rf linac based free electron laser facility
Eisuke Minehara, Toshihiko Yamauchi, Masayoshi Sugimoto, Masaru Sawamura, Ryoichi Hajima, Ryoji Nagai, Nobuhiro Kikuzawa, Nobuyuki Nishimori, Toshiyuki Shizuma
Nucl. Instrum. Methods Phys. Res., Sect. A445, p.183-186 (2000)

16) Design of energy recovery transport for the JAERI FEL driven by a superconducting linac
Ryoichi Hajima, Eisuke Minehara, Masaru Sawamura, Ryoji Nagai, Nobuhiro Kikuzawa, Nobuyuki Nishimori, Masayoshi Sugimoto, Toshiyuki Shizuma, N.A.Vimokurov
Nucl. Instrum. Methods Phys. Res., Sect. A445, p.384-388 (2000)

2. Proceedings

1) Design Consideration for the JAERI Industrial 1.3μm 40KW Highly Efficient FEL Driven by the Superconducting rf Linac
Eisuke Minehara, Masayoshi Sugimoto, Toshihiko Yamauchi, Masaru Sawamura, Ryoichi Hajima, Ryoji Nagai, Nobuhiro Kikuzawa, Takehito Hayakawa, Nobuyuki Nishimori, Toshiyuki Shizuma
Proceedings of 13th International Conference on High Power Panticle Beams(BEAMS2000), Nagaoka, 2000, p.236-239

2) The JAERI Superconducting rf Linac Driver for An Industrial 1.3μm 40KW Highly Efficient Free Electron Laser
Eisuke Minehara, Toshihiko Yamauchi, Masayoshi Sugimoto, Masaru Sawamura, Ryoichi Hajima, Ryoji Nagai, Nobuhiro Kikuzawa, Takehito Hayakawa, Nobuyuki Nishimori, Toshiyuki Shizuma
Proceedings of 7th European Particle Accelerator Conference, Australia, 2000, p.758-760

3) Injector Design for the JAERI-FEL energy-recovery transport
Toshiyuki Shizuma, Ryoichi Hajima, Masaru Sawamura, Ryoji Nagai, Nobuhiro Kikuzawa, Nobuyuki Nishimori, Eisuke Minehara

Proceedings of 7th European Particle Accelerator Conference, Australia, 2000, p.1033-1035
4) Study on emittance dilution in the JAERI-FEL energy-recovery transport
Ryoichi Hajima, Toshiyuki Shizuma, Eisuke Minehara
Proceedings of 7th European Particle Accelerator Conference, Australia, 2000, p.1074-1076
5) A thermionic electron gun system for the JAERI superconducting FEL
Nobuyuki Nishimori, Ryoji Nagai, Ryoichi Hajima, Toshiyuki Shizuma, Eisuke Minehara
Proceedings of 7th European Particle Accelerator Conference, Australia, 2000, p.1672-1674
6) Temperature Characteristics of RF Control System for the JAERI FEL
Masaru Sawamura, Ryoji Nagai, Nobuhiro Kikuzawa, Nobuyuki Nishimori, Ryoichi Hajima, Toshiyuki Shizuma, Toshihiko Yamauchi, Eisuke Minehara
Proceedings of the 25th Linear Accelerator Meeting in Japan, Himeji, 2000, p.201-203
7) Optimization of the Optical Resonator for JAERI Far-Infrared Free-Electron Laser
Ryoji Nagai, Ryoichi Hajima, Nobuyuki Nishimori, Masaru Sawamura, Nobuhiro Kikuzawa, Toshiyuki Shizuma, Eisuke Minehara
Proceedings of the 25th Linear Accelerator Meeting in Japan, Himeji, 2000, p.369-371
8) Performance of the thermionic electron gun at JAERI FEL
Nobuyuki Nishimori, Ryoji Nagai, Ryoichi Hajima, Toshiyuki Shizuma, Eisuke Minehara
Proceedings of the 25th Linear Accelerator Meeting in Japan, Himeji, 2000, p.71-73
9) Improvement and Performance of JAERI high power FEL
Nobuyuki Nishimori, Ryoji Nagai, Ryoichi Hajima, Eisuke Minehara
Proceedings of the 25th Linear Accelerator Meeting in Japan, Himeji, 2000, p.50-52
10) Comparison between JAERI and other high power FEL
Nobuyuki Nishimori, Ryoichi Hajima, Ryoji Nagai
Proceedings of the 25th Linear Accelerator Meeting in Japan, Himeji, 2000, p.374-376
11) Design of an Energy-Recovery Beam Line for the JAERI-FEL
Toshiyuki Shizuma, Ryoichi Hajima, Eisuke Minehara
Proceedings of the 25th Linear Accelerator Meeting in Japan, Himeji, 2000, p.53-55
12) The JAERI superconducting linac based FEL
Toshiyuki Shizuma, Eisuke Minehara, Masaru Sawamura, Ryoichi Hajima, Ryoji Nagai, Nobuhiro Kikuzawa, Nobuyuki Nishimori, Toshihiko Yamauchi
Proceedings of XX International Linac Conference, California, 2000, in press
13) A Proposal of R&D Program for Future X-ray FELs at JAERI
Ryoichi Hajima, Eisuke Minehara
Proceedings of the 25th Linear Accelerator Meeting in Japan, Himeji, 2000, p.47-49
14) Present Status and Future Directions of the JAERI Superconducting RF Linac-Based FEL
Eisuke Minehara, Toshihiko Yamauchi, Masayoshi Sugimoto, Masaru Sawamura, Ryoichi Hajima, Ryoji Nagai, Nobuhiro Kikuzawa, Nobuyuki Nishimori, Toshiyuki Shizuma
Proceedings of the 25th Linear Accelerator Meeting in Japan, Himeji, 2000, p.7-8
15) JAERI Superconducting RF Linac-Based FEL
Eisuke Minehara
Proceedings of the 3rd Superconducting Linear Accelerator Meeting in Japan, Tsukuba, 2000, p.14-15
16) Development of SHG Autocorrelation System for JAERI FEL
Nobuhiro Kikuzawa, Toshihiko Yamauchi, Ryoji Nagai, Nobuyuki Nishimori, Ryoichi Hajima, Toshiyuki Shizuma, Masaru Sawamura, Eisuke Minehara
Proceedings of the 25th Linear Accelerator Meeting in Japan, Himeji, 2000, p.366-368
17) High extraction efficiency observed at JAERI Free Electron Laser
Nobuyuki Nishimori, Ryoichi Hajima, Ryoji Nagai, Eisuke Minehara
Proceedings of The 22nd International Free-Electron Laser Conference, U.S.A, 2000, in press
18) An Optical Resonator with Scraper Output Coupler for the JAERI Far-Infrared Free-Electron Laser
Ryoji Nagai, Masaru Sawamura, Ryoichi Hajima, Nobuhiro Kikuzawa, Nobuyuki Nishimori, Toshiyuki Shizuma, Eisuke Minehara
Proceedings of The 22nd International Free-Electron Laser Conference, U.S.A., 2000, in press
19) Current Technological and Applicational Development of Free-Electron Lasers
Eisuke Minehara, Toshihiko Yamauchi, Masayoshi Sugimoto, Masaru Sawamura, Ryoichi Hajima, Ryoji Nagai, Nobuhiro Kikuzawa, Takehito Hayakawa, Nobuyuki Nishimori

Proceedings of the 10th Topical Meeting on Free Electron Laser and High Power Radiation, Funabashi, 2001, in press
20) Improved performance of the JAERI injection and free electron laser system
Nobuyuki Nishimori, Eisuke Minehara, Masaru Sawamura, Ryoji Nagai, Nobuhiro Kikuzawa, Masayoshi Sugimoto, Ryoichi Hajima, Toshiyuki Shizuma
Proceedings of 21th Int. Free Electron Laser Conf., Germany, 2000, p.432-436

Optics research and development (Novel Optics Research Group)

1. Journals

1) X-ray scattering study of interfacial roughness correlation in Mo/Si multilayers fabricated by ion beam sputtering
A. Ulyanenkov, R. Matsuo, K. Omote, K. Inaba, J. Harada, M. Ishino, M. Nishii, O. Yoda
J. Appl. Phys. 87, 7255-7260 (2000)
2) A spectroscopic comparison of samarium doped LiYF4 and KY3F10
P. R. Wells, A. Sugiyama, T. P. J. Han, H. G. Gallagher
J. of Luminescence 87-89, 1029-1031 (2000)
3) Varied-line-spacing laminar-type holographic grating for the standard soft X-ray flat-field spectrograph
M. Koike, T. Namioka, E. Gullikson, Y. Harada, S. Ishikawa, T. Imazono, S. Mrowka, N. Miyata, M. Yanagihara, J. H. Underwood, K. Sano, N. Ogiwara, O. Yoda, S. Nagai
Proc. SPIE, 4146, 163-170 (2000)
4) Feasibility study of a direct bonding technique for laser crystals
A. Sugiyama, H. Fukuyama, Y. Kataoka, A. Nishimura, Y. Okada
Proc. SPIE, 4231, 261-268 (2000)

2. Proceedings

1) Optics developments for CPA lasers in JAERI
A. Sugiyama, H. Fukuyama, M. Katsurayama, Y. Anzai,
IEEJ,OQD-00-50 (2000)
2) Density measurements of micro defects inside optical materials using a laser tomography method,
H. Fukuyama, A. Sugiyama
JAERI-Tech 2000-058, 1-33(2000)
3) Development of Evaluation System for Soft X-ray Optical Elements
M. Koike, O. Yoda, M. Ishino, K. Sano, Y. Harada, H. Sasai, N. Moriya, M. Jinno
JAERI-Conf 2001-011, 72-75 (2001)
4) Reduction in Thermal Lens Effects by Index-matching Fluid on the Hybrid Material of Yb:glass and Sapphire
A. Nishimura, T. Usami, A. Sugiyama, K. Ohara, A. Nagashima
JAERI-Conf 2001-011, 84-88 (2001)
5) Evaluation for the Bonded Region of a Direct Bonded Ti:sapphire Crystal
A. Sugiyama, H. Fukuyama, Y. Kataoka, Y. Okada
JAERI-Conf 2001-011, 216-220 (2001)
6) Measurement for Titanium Density Distribution on Ti:sapphire Rods for High Intensity Pump Source
T. Usami, A. Nishimura, A. Sugiyama
JAERI-Conf 2001-011, 221-224 (2001)
7) Boundary Structure of Mo/Si Multilayers for Soft X-ray Mirrors
M. Ishino, O. Yoda, Y. Haishi, F. Arimoto, M. Takeda, S. Watanabe, S. Ohnuki, H. Abe
JAERI-Conf 2001-011, 228-231 (2001)

3. Patents

1) Method to increase heat resistibility of Mo/Si multilayers
M. Ishino, O. Yoda
Application number: 2001-76031

Laser driven particle acceleration research (Laser Acceleration Research Group)

1. Journals

1) Compact X-ray sources by intense laser interactions with beams and plasmas
Hideyuki Kotaki, Masaki Kando, Hideki Dewa, Shuji Kondo, Takahiro Watanabe, Toru Ueda, Kenichi Kinoshita, Koji Yoshii, Mitsuru Uesaka, Kazuhisa Nakajima
Nucl. Inst. and Meth. A vol.455 (2000) pp.166-171
2) Generation Fast Z-pinch optical guiding for laser wakefield acceleration
M Tomonao Hosokai, Masaki Kando, Hideki Dewa, Hideyuki Kotaki, Shuji Kondo, Noboru Hasegawa, Kazuhiko Horiba, Kazuhisa Nakajima
Nucl. Inst. and Meth. A vol.455 (2000) pp.155-160
3) Generation and Application of Femtosecond X-ray Pulse
Mitsuru Uesaka, Hideyuki Kotaki, Kazuhisa Nakajima, Hideki Harano, Kenich Kinoshita, Takahiro Watanabe, Toru Ueda, Koji Yoshii, Masaki Kando, Hideki Dewa, Shuji Kondo, Fumio Sakai
Nuclear Instruments and Methode A , vol.455 (2000) pp.90-98
4) Experimental Verification of Laser Photocathode RF Gun as an Injector for a Laser Plasma Accelerator Production and utilization of synchronized femtosecond electron and laser single pulses
M. Uesaka, T. Watanabe, T. Ueda, M. Kando, K. Nakajima, H. Kotaki, A. Ogata
IEEE Trans. on Plasma Sci., vol.28, No.4, (2000) pp.1133-1142
5) Recent progress on laser acceleration
Kazuhisa Nakajima
Physics Research A 455, pp. 140-147 (2000)
6) Electron Acceleration by Laser Wakefield (in Japanese)
Kazuhisa Nakajima
Houshasen Kagaku, No.70, pp.43-70 (2000)
7) Fixed blueshift of high intensity short pulse lasers propagating in gas chambers
J. K. Koga, N. Naumova, M. kando, L.N. Tsintsadze, K. Nakajima, S. V. Bulanov, H. Dewa, H. Kotaki, T. Tajima
Physics of Plasmas, Vol. 7, pp. 5223-5231 (2000)
8) Particle acceleration by ultraintense laser interactions with beams and plasmas
Kazuhisa Nakajima
Laser and Particle Beams, 18, No.3, pp.1-10 (2000)

2. Proceedings

1) Relativistic Ion Acceleration by Ultraintense Laser Interactions
K. Nakajima, J. K. Koga and K. Nakagawa
The 9th Workshop on Advanced Accelerator Concepts, Santa Fe, June 10-16, 2000
2) GeV Laser Acceleration Research at JAERI-APR
K. Nakajima,T. Hosokai, S. Kanazawa, M. Kando, S. Kondoh, H. Kotaki, T. Yokoyama
The 9th Workshop on Advanced Accelerator Concepts, Santa Fe, June 10-16, 2000
3) Commissioning of Photocathode RF Gun Based Microtron at JAERI-Kansai (in Japanese)
M. Kando, H. Kotaki, S. Kondo, T. Hosokai, T. Yokoyama, S. Kanazawa, H. Dewa, K. Nakajima, F. Sakai, T. Ishizuka, T. Hori
Proceedings of The 25th Linear Accelerator Meeting in Japan, July 12-14, (2000) pp.9-11
4) Conditioning Photocathode RF-Gun in JAERI-Kansai (in Japanese)
H. Kotaki, M. Kando, S. Kondo, S. Kanazawa, T. Yokoyama, T. Hosokai and K. Nakajima
Proceedings of The 25th Linear Accelerator Meeting in Japan, July 12-14, (2000) pp.147-149
5) Design of W-band photoinjector
Xiongwei Zhu, Kazuhisa Nakajima
Proceedings of the 25th Linear Accelerator Meeting in Japan, pp. 180-182, Himeji, Jul. 12-14, 2000
6) Fast Z-pinch optical guiding for 1GeV laser-plasma acceleration
T.Hosokai, M.Kando, H.Dewa, H.Kotaki, S.Kondo, K.Horioka, K.Nakajima
13th International Conference on High Power Particle Beams (Nagaoka Japan Jun 2000),

Beams'2000 PROC (to be published)

7) High Energy Particle Acceleration by Super Strong Laser-Plasma Interactions
Kazuhisa Nakajima, James K. Koga, Igor V. Smetanin
International Conference on LASERS 2000, Albuquerque, Dec. 4-8, 2000

8) Photocathode Microtron for the Laser Acceleration Experiments (in Japanese)
M. Kando, H. Kotaki, S. Kondo, T. Hosokai, S. Kanazawa, T. Yokoyama, T. Matoba, K. Nakajima
The Second Symposium on Advanced Photon Research, Nov. 9-10, 2000

9) High Energy Gain Electron Beam Acceleration by 100 TW Laser (in Japanese)
H. Kotaki, M. Kando, S. Kondo, T. Hosokai, S. Kanazawa, T. Yokoyama, K. Nakajima
The Second Symposium on Advanced Photon Research, Nov. 9-10, 2000

10) High Energy Gain Electron Beam Acceleration by 100 TW Laser (in Japanese)
H. Kotaki, M. Kando, S. Kondo, T. Hosokai, S. Kanazawa, T. Yokoyama, T. Matoba, K. Nakajima
21st Annual Meeting of The Laser Society of Japan, Tokyo International Forum, Jan. 31, 2001

11) Plan of JAERI-Kansai Project (in Japanese)
H. Kotaki, M. Kando, S. Kondo, T. Hosokai, S. Kanazawa, T. Yokoyama, T. Matoba, K. Nakajima
Yayoi Kenkyu-kai, Hongo Campus, University of Tokyo, Mar. 6, 2001

12) High Energy Laser-Plasma Accelerator Developments at JAERI-APR
H. Kotaki, M. Kando, S. Kondo, S. Kanazawa, T. Yokoyama, T. Hosokai, T. Matoba, H. Nakanishi and K. Nakajima
The 18th International Conference on High Energy Accelerators, Epochal Tsukuba, Tsukuba, Japan, March 26 - 30, 2001

13) High Energy Laser-Plasma Accelerator Developments at JAERI-APR
K. Kinoshita, M. Uesaka, T. Watanabe, T. Ueda, K. Yoshii, H. Harano, F. Sakai, H. Kotaki, K. Nakajima, H. Nakanishi, A. Ogata
Proceedings of the 11th Symposium on Accelerator Science and Technology, Harima Science Garden City, October 22 1997, pp. 479-480

3. Patents

1) Method of electron beam monitoring in the microtron
T. Hori, F. Sakai, and M. Kando
Application number: 2000-206277

Advanced photon simulation research (Simulation Group for Advanced Photon Science)

1. Journals

1) Molecular dynamics simulation of laser shock phenomena
E. Ohmura, I. Fukumoto, I. Miyamoto
Journal of the Society for Precision Engineering, Vol. 66, No. 4, pp. 635-639 (2000)

2) Development of a collisional radiative model of x-ray lasers
A. Sasaki, T. Utsumi, K. Moribayashi, T. Tajima, H. Takuma
J. Quant. Spectrosc. Radiat. Transf., Vol. 65, No. 1-3, pp. 501-509 (2000)

3) Effect of field ionization on interaction of metallic foils with subpicosecond laser pulse
A. Zhidkov, A. Sasaki
Phys. Plasmas, Vol. 7, No. 5, pp. 1341-1344 (2000)

4) Photon gas in a relativistic magnetoplasma
N.L. Tsintsadze, H. Hakimi Pajouh, L.N. Tsintsadze, J.T. Mendonca, P.K. Shukla
Phys. Plasmas, Vol. 7, No. 6, pp. 2348-2353 (2000)

5) Generation of collimated beams of relativistic ions in laser-plasma interactions
S.V. Bulanov, T.Zh.Esirkepov, F. Califano, Y. Kato, T.V. Liseikina, K. Mima, N.M. Naumova, K. Nishihara, F. Pegoraro, H. Ruhl, Y. Sentoku, Y. Ueshima
JETP Lett., Vol. 71, No. 10, pp. 407-411 (2000)

6) Numerical analysis of 10's femtosecond relativistic electron beam generation using single 12TW50fs laser pulse

N. Hafz, M. Uesaka, J. Koga, K. Nakajima
Nucl. Instrum. Methods in Phys. Res. A, Vol. 455, pp. 148-154 (2000)

7) Proton and ion acceleration by an ultra-shortpulse sub Peta-watt laser in deformed double-layer thin foils
Y. Ueshima, Y. Sentoku, Y. Kishimoto
Nucl. Instrum. Methods in Phys. Res. A, Vol. 455, pp. 181-184 (2000)

8) Toward an ultimate goal for universal solution by the CIP method
T. Yabe, T. Utsumi
CFD Journal, Vol. 9, No. 3, pp. 185-193 (2000)

9) Prepulse effects on the interaction of intense femtosecond laser pulses with high-Z solids
A. Zhidkov, A. Sasaki, T. Utsumi, I. Fukumoto, T. Tajima, F. Saito, Y. Hironaka, K.G. Nakamura, K. Kondo, M. Yoshida
Phys. Rev., E, Vol. 62, No. 5, pp. 7232-7240 (2000)

10) High density collimated beams of relativistic ions produced by petawatt laser pulses in plasmas
Y. Sentoku, T.V. Liseikina, T.Zh. Esirkepov, F. Califano, N.M. Naumova, Y. Ueshima, V.A. Vshivkov, Y. Kato, K. Mima, K. Nishihara, F. Pegoraro, S.V. Bulanov
Phys. Rev., E, Vol. 62, No. 5, pp. 7271-7281 (2000)

11) Laser interaction with neutrons
T. Tajima, K. Soyama, J. Koga, H. Takuma
J. Phys. Soc. Japan, Vol. 69, No. 12, pp. 3840-3846 (2000)

12) Fixed blueshift of high intensity short pulse lasers propagating in gas chambers
J.K. Koga, N. Naumova, M. Kando, L.N. Tsintsadze, K. Nakajima, S.V. Bulanov, H. Dewa, H. Kotaki, T. Tajima
Phys. Plasmas, Vol. 7, No. 2, pp. 5223-5231 (2000)

13) Strong relativistic effects on dielectronic recombination of metastable Li^+ ions
Li-Bo Zhao, T. Shirai
Phys. Rev. A, Vol. 63, No 1. , pp. 010703-1-4 (2001)

14) Numerical simulation of the x-ray lasers
A. Sasaki
J. Plasma Fus. Sci., Vol. 77, No. 2, pp. 146-152 (2001)

2. Reports

1) Report on the international conferences on atomic processes in plasmas and atomic data
A. Sasaki, I. Murakami, H. Takabe
Rev. Laser Eng., Vol. 28, No. 7, pp. 446-449 (2000)

2) Application of x-ray emission from inner-shell excited states and hollow atoms produced by high intensity laser irradiation
K. Moribayashi, A. Sasaki, A. Zhidkov, Y. Ueshima, K. Suto, T. Kagawa
Atomic collision research in Japan (Progress Report, The Society for Atomic Collision Research), No. 26, pp. 111-113 (2000)

3) Molecular dynamics simulation of ablation process with ultrashort-pulse laser:
Focused on Laser Precision Microfabrication (LPM2000)
E. Ohmura, I. Fukumoto, I. Miyamoto
RIKEN Review, No. 32, pp. 19-22 (2001)

3. Proceedings

1) Simulations of the transient collisional X-ray lasers
A. Sasaki, T. Utsumi, K. Moribayashi, M. Kado, T. Kawachi
Proc. American Physical Society 12th Topical Conference on Atomic Processes in Plasmas (Reno, 2000.3), AIP Conference Proceedings, Vol. 547, pp. 133-144 (2000)

2) A self organized criticality model for the propagation of high intensity pulses in gases
J. Koga
Proceedings of the 2nd Symposium on Advanced Photon Research (Kyoto, 2000.11)
JAERI-Conf 2001-011, pp. 58-63 (2001)

3) JAERI-Kansai advanced photon simulation research
M. Yamagiwa, Simulation Group for Advanced Photon Science

Proceedings of the 2nd Symposium on Advanced Photon Research (Kyoto, 2000.11)
JAERI-Conf 2001-011, pp. 105-108 (2001)

4) Effect of the radiation damping on interaction of ultra-intense laser pulses with an overdense plasma
A. Zhidkov, J. Koga, A. Sasaki, Y. Ueshima
Proceedings of the 2nd Symposium on Advanced Photon Research (Kyoto, 2000.11)
JAERI-Conf 2001-011, pp. 109-112 (2001)

5) Analysis of the transient collisional x-ray lasers
A. Sasaki, T. Utsumi, K. Moribayashi, A. Zhidkov, T. Kawachi, M. Kado, M. Tanaka, N. Hasegawa, H. Daido
Proceedings of the 2nd Symposium on Advanced Photon Research (Kyoto, 2000.11)
JAERI-Conf 2001-011, pp. 134-137 (2001)

6) Numerical simulation of foils irradiated with high power ultrashort laser pulse
T. Utsumi, A. Sasaki, T. Kunugi, S. Fujii
Proceedings of the 2nd Symposium on Advanced Photon Research (Kyoto, 2000.11)
JAERI-Conf 2001-011, pp. 153-154 (2001)

7) X-ray emission simulation from hollow atoms produced by high intensity laser irradiation
K. Moribayashi, A. Sasaki, A. Zhidkov, K. Suto, T. Kagawa
Proceedings of the 2nd Symposium on Advanced Photon Research (Kyoto, 2000.11)
JAERI-Conf 2001-011, pp. 157-160 (2001)

8) Ultra-short pulse electron generation with gas plasma and thin foil
Y. Ueshima
Proceedings of the 2nd Symposium on Advanced Photon Research (Kyoto, 2000.11)
JAERI-Conf 2001-011, pp. 169-171 (2001)

9) Molecular dynamics simulation of laser shock phenomena
I. Fukumoto
Proceedings of the 2nd Symposium on Advanced Photon Research (Kyoto, 2000.11)
JAERI-Conf 2001-011, pp. 264-267 (2001)

Applied Photon Research (Applied Photon Research Group)

1. Journals

1) Ab Initio Molecular Orbital Study of the C2H4 + Cl2 → C2H4Cl2 Reaction
Y. Kurosaki
J. Mol. Struct. THEOCHEM 503, 231-240 (2000)

2) Ab Initio Molecular Orbital Study of Potential Energy Surface for the H2NO(2B1) → NO(2P) + H2 Reaction
Y. Kurosaki and T. Takayanagi
J. Mol. Struct. THEOCHEM 507, 119-126 (2000)

3) Three-Dimensional Quantum Reactive Scattering Calculations for the Nonadiabatic (D + H2)+ Reaction System
T. Takayanagi, Y. Kurosaki, and A. Ichihara
J. Chem. Phys. 112, 2615-2622 (2000)

4) Ab Initio Molecular Orbital Calculations of Potential Energy Surfaces for the N(4S, 2D, 2P) + H2 Reactions
T. Takayanagi, Y. Kurosaki, and K. Yokoyama
Chem. Phys. Lett. 321, 106-112 (2000)

5) Theoretical Study of Kinetic Isotope Effects on Rate Constants for the H2 + C2H → H + C2H2 Reaction and Its Isotopic Variants
Y. Kurosaki and T. Takayanagi
J. Chem. Phys. 113, 4060-4072 (2000)

6) Ab Initio Calculations for the N(2D) + CH4 Reaction; Does the N(2D) Atom Really Insert Into CH Bonds of Alkane Molecules?
T. Takayanagi, Y. Kurosaki, and K. Yokoyama
Int. J. Quantum Chem. 79, 190-197 (2000)

7) Quantum Scattering Calculations for the Electronically Nonadiabatic Br(2P1/2) + H2 → HBr + H Reaction

T. Takayanagi and Y. Kurosaki
J. Chem. Phys. 113, 7158-7164 (2000)

8) Potential Energy Surface for the C2H4 + Cl2 → C2H4Cl + Cl Reaction: Ab Initio Molecular Orbital Study
Y. Kurosaki
J. Mol. Struct. THEOCHEM 545, 225-232 (2001)

9) "Femtosecond time-resolved fluorescence spectra of a coumarin dye in glycerol"
Hiroshi Murakami
Journal of Molecular Liquids 89, p.33-45 (2000)

10) Characteristics of Plasma in Uranium Atomic Beam Produced by Electron-Beam Heating
Hironori Ohba, Akihiko Nishimura, Koichi Ogura, and Takemasa Shibata
JAERI-Research 2000-030 (2000.8)

11) Metastable States' Population of Uranium Atoms Produced by Electron-Beam Heating
Hironori Ohba, Akihiko Nishimura, Koichi Ogura, and Takemasa Shibata
JAERI-Research 2000-033 (2000.8)

12) Effect of Electron Beam on Velocities of Uranium Atomic Beams Produced by Electron Beam Heating
Hironori Ohba, Koichi Ogura, Akihiko Nishimura, Koji Tamura, and Takemasa Shibata
The Japan Society of Applied Physics Vol.39, pp;5347-5351 (2000)

6.2 List of publications on Synchrotron Radiation Research Center

Experimental facilities development (Experimental Facilities Development Group)

1. Journals

1) Performance of a PbWO4 Crystal Calorimeter for 0.2-1.0 GeV Electrons
H.Shimizu, Y.Sakamoto, T.hashimoto, K.Abe, Y.Asano, T.Kinashi, T.Matsumoto, T.Matsumura, H.Okuno, H.Y.Yoshida
Nucle. Inst. & Methods Physics Research A, 467-475, 2000
2) Measurement of Gas bremsstrahlung at the SPring-8 Insertion Device Beamline using PWO scintillator
Y.Asano, T.Matsumura, R.Chiba, T.Hashimoto, A.Miura, H.Shimizu, Y.Tajima, H.Y. Yoshida
Nucle. Inst. & Methods Physics Research A, 451, p685-696, 2000
3) Diamond Double-crystal Monochromator in Bragg Geometry Installed at BL-11XU in Spring-8
M.Marushita, T.Mitsui, T.Fukuda, M.Takahashi, I.Inami, Y.Katayama, J.Mizuki
Nucl. Instr. & Meth. A, 467-468, 392, 2001

2. Proceedings

1) Estimation of Synchrotron Radiation Dose Outside the Hutch of SPring-8 Beamline
Yoshihiro Asano
10th Int. Conf. on Radiation Protection, Hiroshima, May 14-19, 2000
2) Simulation of Angular Distribution of Gas Bremsstrahlung Depending on the Residual Gas Pressure of Storage Ring
Yoshihiro Asano
Proc. of the 2nd International Workshop on EGS, p.286-292, KEK Proceedings 2000-20 Tukuba, Aug. 8-10th, 2000
3) Demagnetization of undulator magnets irradiated with electron beam
T.Bizen, T.Tanaka, Y.Asano, D.E.Kim, J.S.Bak, H.S.Lee, H.Kitamura
SRI'2000, Berlin, Aug. 2000

3. Reports

1) A study on radiation shielding and safety analysis for synchrotron radiation beamline
Yoshihiro Asano
JAERI-Research 2001-006, 146p, 2001

High pressure science (High Pressure Science Group)

1. Journals

1) Single crystal growth of the high pressure phase of $(VO)_2P_2O_7$ at 3GPa
T. Saito, T. Terashima, M. Azuma, M. Takano, T. Goto, H. Ohta, W. Utsumi, P. Bordet, D. C. Johnston
J. Solid State Chem., 153, 124-131, 2000
2) Formation of metastable assemblages and reduction of the grain size in the postspinel transformation of Mg_2SiO_4
T. Kubo, E. Ohtani, T. Kato, S. Urakawa, A. Suzuki, Y. Kanbe, K. Funakoshi, W. Utsumi, K. Fujino
Geophys. Res. Lett., 27, 807-813, 2000
3) Determination of the phase boundary between ilmenite and perovskite in $MgSiO_3$ by in situ x-ray diffraction and quench experiments
K. Kuroda, T. Irifune, N. Nishiyama, M. Miyashita, K. Funakoshi, W. Utsumi
Phys. Chem. Minerals, 27, 523-532, 2000
4) High-pressure phase transformation in $CaMgSi_2O_6$ and implications for origin of ultra-deep diamond inclusions
T. Irifune, M. Miyashita, T. Inoue, J. Ando, K. Funakoshi, W. Utsumi
Geophys. Res. Lett., 27, 3541-3544, 2000
5) Melting of portlandite up to 6 GPa

H. Fukui, O. Ohtaka, T. Nagai, T. Katsura, K. Funakoshi, W. Utsumi
Phys. Chem. Minerals, 27, 367-370, 2000

6) Thermoelastic properties of the high-pressure phase of SnO_2 determined by in situ x-ray observations up to 30GPa and 1400K
S. Ono, E. Ito, T. Katsura, A. Yoneda, M. J. Walter, S. Urakawa, W. Utsumi, K. Funakoshi
Phys. Chem Minerals, 27, 618-622, 2000

7) Phase relations and equations of state of ZrO_2 under high-temperature and high-pressure
O. Ohtaka, H. Fukui, T. Fujisawa, K. Funakoshi, W. Utsumi, T. Irifune, K. Kuroda, T. Kikegawa
Phys. Rev. B, 63, 174108-1-8, 2001

8) In situ observation of ilmenite-perovskite phase transition in $MgSiO_3$ using synchrotron radiation
S. Ono, T. Katsura, E. Ito, M. Kanzaki, A. Yoneda, M. J. Walter, S. Urakawa, W. Utsumi, K. Funakoshi
Geophys. Res. Lett., 28, 835-838, 2001

9) Phase Relations and Volume Change of Hafnia under High-Pressure and High-Temperature
O. Ohtaka, H. Fukui, T. Kunisada, T. Fujisawa, K. Funakoshi, W. Utsumi, T. Irifune, K. Kuroda, T. Kikegawa
J. Am. Ceram. Soc., 84, 1369-73, 2001

10) High pressure high temperature experiments using multi-anvil device -Method and Facility-
W. Utsumi, K. Funakoshi, N. Yagi, S. Urakawa, O. Ohtaka, T. Katsura, T. Irifune, T. Inoue, T. Uchida
Jpn. Mag. Mineral. Petrol. Sci., 30, 100-101, 2001, in Japanese

11) High pressure high temperature experiments using multi-anvil device -Method and Facility-
K. Funakoshi, W. Utsumi, O. Ohtaka, T. Irifune, T. Inoue, E. Ito, T. Katsura, A. Kubo, K. Hirose, J. Ando, A. Suzuki, T. Kubo, H. Terasaki
Jpn. Mag. Mineral. Petrol. Sci., 30, 102-103, 2001, in Japanese

12) Crystal structure of NiO under high pressure
T. Eto, S. Endo, M. Imai, Y. Katayama, T. Kikegawa
Phys. Rev. B, 61, 14984-14988, 2000

13) A first-order phase transition in liquid phosphorus
Y. Katayama
Rev. High Pressure Sci. Tech., 10, 221-227, 2000, in Japanese

14) High Pressure XAFS
Y. Katayama
Jpn. Soc. Synchrotron Rad. Res., 13, 385-387, 2000, in Japanese

15) Anharmonic Effective Pair Potentials of gamma- and alpha-CuBr at High Pressure
A. Yoshiasa, M. Okube, O. Ohtaka, O. Kamishima, Y. Katayama
Jpn. J. Appl. Phys., 39, 6747-6751, 2000

16) X-ray diffraction study on structural change in liquid selenium under high pressure
Y. Katayama, T. Mizutani, W. Utsumi, O. Shimomura, K. Tsuji
Phys. stat. sol., (b) 223, 401-404, 2001

17) XAFS study on liquid selenium under high pressure
Y.Katayama
J. Synchrotron Rad. Res., 8, 182-185, 2001

18) Structural changes of quartz-type crystalline and vitreous GeO_2 under pressure
O. Ohtaka, A. Yoshiasa, H. Fukui, K. Murai, M. Okabe, Y. Katayama, W. Utsumi, Y. Nishihata
J. Synchrotron Rad. Res., 8, 791-793, 2001

19) Phase transitions of LnAs(Ln=Pr, Nd, Sm, Gd, Dy and Ho) with NaCl-type structure at high pressures
I. Shirotani, K. Yamanashi, J. Hayashi, Y. Tanaka, N. Ishimatsu, O. Shirotani, T. Kikegawa
J. Phys.: Condens. Matter, 13, 1939-1946, 2001

20) Construction of laser-heated diamond anvil cell system for in situ x-ray diffraction study at SPring-8
T. Watanuki, O. Shimomura, T. Yagi, T. Kondo, M. Isshiki
Rev. Sci. Instrum., 72, 1289-1292, 2001

21) Laser heated diamond anvil apparatus at the Photon Factory and SPring-8: Problems and improvements
T. Yagi, T. Kondo, T. Watanuki, O. Shimomura, T. Kikegawa
Rev. Sci. Instrum., 72, 1293-1297, 2001

22) X-ray induced photoemission of a localized electron and its application to site-selective x-ray absorption fine structure measurement
M. Ishii, Y. Yoshino, K. Takarabe, O. Shimomura
J. Appl. Phys., 88, 3962-3967, 2000
23) Phase transitions of MnO to 137 GPa
T. Kondo, T. Yagi, Y. Syono, Y. Noguchi, T. Atou, Y Kikegawa, O. Shimomura
J. Appl. Phys., 87, 4153-4159, 2000
24) Pressure-Induced Metallization and Structural Transition of Orthorhombic Se
K. Nakano, Y. Akahama, H. Kawamura, M. Takumi, K. Nagata
Phys. stat. sol., (b) 223, 397-400, 2001
25) Synchrotron radiation X-ray powder diffractometer with a cylindrical imaging plate
A.Fujiwara, K. Ishii, T. Watanuki, H. Suematsu, H. Nakao, K. Ohwada, Y. Fujii, Y. Murakami, T. Kikegawa, O. Shimomura, T. Matsubara, S. Daicho, S. Kitamura, C. Katayama
J. Appl. Cryst., 33, 1241-1245, 2000
26) Structural Phase Transitions of Endohedral Metallofullerene La@C_{82} Studied by Single Crystal X-ray Diffraction
T. Watanuki, A. Fujiwara, K. Ishii, Y. Matsuoka, H. Suematsu, K. Ohwada, H. Nakao, Y. Fujii, T. Kodama, K. Kikuchi, Y. Achiba,
Mol. Cryst. and Liq. Cryst., 340, 639-642, 2000
27) Structural Phase Transition in $(NH_3)K_3C_{60}$
K. Ishii, T. Watanuki, A. Fujiwara, H. Suematsu, Y. Iwasa, H. Shimoda, T. Takenobu, T. Mitani
Mol. Cryst. and Liq. Cryst., 340, 571-576, 2000
28) Crystal structure of Europium C60 Compounds
H. Ootoshi, K. Ishii, A. Fujiwara, T. Watanuki, Y. Matsuoka, H. Suematsu
Mol. Cryst. And Liq.Cryst., 340, 565-570, 2000

2. Proceedings

1) In situ x-ray observation of cubic BC_2N formation under high pressures and temperatures
W. Utsumi, T. Okada, K. Funakoshi, O. Shimomura
Proc. of the 8th NIRIM International Symposium on Advanced Materials (ISAM2001), 39-40, 2001
2) Structural studies on liquids under high pressure using synchrotron radiation
Y. Katayama
Proc. of the 8th NIRIM International Symposium on Advanced Materials (ISAM2001), 39-40, 2001
3) Structural Transitions in Phosphorus to 280 GPa
Y. Akahama, H. Kawamura, S. Carlson, T. Le Bihan, D. Hausermann, O. Shimomura
Science and Technology of High Pressure, Proc. of AIRAPT-17, (Universities Press, Hyderabad, India, 463-466, 2000
4) Crystal structure of NiO under high pressure
T. Eto, S. Endo, M. Imai, Y. Katayama, T. Kikegawa
Science and Technology of High Pressure, Proc. of AIRAPT-17, (Universities Press, Hyderabad, India, 487-490, 2000
5) Anomaly in the melting curve of black phosphorus associated with a liquid-liquid transition
T. Mizutani, Y. Katayama, W. Utsumi, K. Funakoshi, M. Yamakata, O. Shimomura
Science and Technology of High Pressure, Proc. of AIRAPT-17, (Universities Press, Hyderabad, India, 525-528, 2000
6) Phase relations of $Ca(OH)_2$ under high-pressure and high-temperature conditions
H. Fukui, O. Ohtaka, T. Katsura, T. Nagai, K. Funakoshi, W. Utsumi, T. Kikegawa
Science and Technology of High Pressure, Proc. of AIRAPT-17, (Universities Press, Hyderabad, India, 554-557, 2000
7) Laser heating systems at the Photon Factoryand SPring-8,
T. Yagi, T. Kondo, T. Kikegawa, T. Watanuki, Y. Katayama, O. Shimomura:
Science and Technology of High Pressure, Proc. of AIRAPT-17, (Universities Press, Hyderabad, India, 1027-1030, 2000
8) Ruby scale at low temperatures calibrated by the NaCl gauge

K. Nakano, N. Matsui, I. Nakahata, Y. Akahama, Y. Ohishi, H. Kawamura
Science and Technology of High Pressure, Proc. of AIRAPT-17, (Universities Press, Hyderabad, India, 1081-1084, 2000

9) A new cubic anvil press with radial slit system at the SPring-8
M. Yamakata, T. Mizutani, W. Utsumi, Y. Katayama, O. Shimomura
Science and Technology of High Pressure, Proc. of AIRAPT-17, (Universities Press, Hyderabad, India, 1109-1112, 2000

Structural physics research (Structural Physics Research Group)

1. Journals

1) Magnetic ordering in the kagome lattice antiferromagnet $KCr_3(OH)_6(SO4)_2$
T. Inami, T. Morimoto, M. Nishiyama, S. Maegawa, Y. Oka, H. Okumura
Phys. Rev. B, 64, 054421, 2001
2) An inelastic X-ray scattering spectrometer for materials science on BL11XU at SPring-8
T. Inami, T. Fukuda, J. Mizuki, H. Nakao, T. Matsumura, Y. Murakami, K. Hirota, Y. Endoh
Nucl. Instr. & Meth. A, 467-468, 1081, 2001
3) Fixed-height exit bender of synchrotron X-rays above 40 keV"
Y. Yoneda, N. Matsumoto, Y. Furukawa, T. Ishikawa,
J. Synchrotron Rad., 8, 18-21, 2001
4) High-energy X-ray focusing with fixed exit bender
Y. Yoneda, N. Matsumoto, Y. Furukawa, T. Ishikawa
Nucl. Instrum. Methods A, 467-468, 370-372, 2001
5) 31P NMR Study of Magnesium Phosphate Glasses
F. Fayon, D. Massiot, K. Suzuya, D.L. Price
Journal of Non-Crystalline Solids 283, 88-94, 2001
6) A horizontal teo-axis diffractometer for high-Energy X-ray diffraction using synchrotron radiation on bending magnet beamline BL04B2 at SPring-8
S. Kohara, K. Suzuya, Y. Kashihara, N. Matsumoto, N. Umesaki, I. Sakai
Nuclear Instruments and Methods in Physics Research A, 467-468, 1031-1034, 2001
7) Neutron Inelastic Scattering of Densified GeO2 Glass
K. Suzuya, K. Shibata, N. Umesaki, N. Kitamura, S. Kohara
Journal of the Physical Society of Japan, 70, Supplement A, 256-258, 2001
8) High-Energy X-ray Diffraction Studies of Non-Crystalline Materials
H. Ohno, S. Kohara, N. Umesaki, K. Suzuya
Journal of Non-Crystalline Solids, 2001, in press
9) Evidence for the Diffusion of Au Atoms into the Te upd layer Formed on a Au(111) Substrate
H. Kawamura, M. Takahasi, N. Hojo, M. Miyake, K. Murase, k. Tamura, K. Uosaki, Y. Awakura, J. Mizuki, E. Matsubara
J. Electrochem. Soc., 2001, in press
10) Effect of surface structure on crystal-truncation-rod scattering under the Bragg condition
T. Takahashi, W. Yashiro, M. Takahasi, S. Kusano, X. W. Zhang, M. Ando
Phys. Rev. B, 62, 3630, 2000
11) EXAFS spectra above Pb and Pt K edges observed at low temperature
Y. Nishihata, J. Mizuki, S. Emura, T. Uruga
J. Synchrotron Rad., 8, 294-296, 2001
12) Structural changes of quartz-type crystalline and vitreous GeO2 under pressure
O. Ohtaka, A. Yoshiasa, H. Fukui, K. Murai, M. Okube, Y. Katayama, W. Utsumi, Y. Nishihata
J. Synchrotron Rad., 8, 791-793, 2001
13) An intelligent catalyst
H. Tanaka, M. Uenishi, I. Tan, M. Kimura, J. Mizuki, Y. Nishihata
SAE Paper 2001-01-1301, 2001
14) Structural Analysis of Corrosion Product of Fe-Cr Alloy Film Using Synchrotron Radiation
M. Yamashita, H. Konishi, M. Takahasi, J. Mizuki, H. Uchida
Materials Science Res. Int., Special Technical Publication – 1, 398, 2001
15) Magnetic and electrical resistivity studies of $Pr_{1-x}TiO_3$

K. Yoshii, A. Nakamura, H. Abe
Jpn. J. Appl. Phys. Suppl., 39-1, 484-487, 2000

16) Reversal of magnetization in $La_{0.5}Pr_{0.5}CrO_3$
K. Yoshii, A. Nakamura
J. Solid State Chem. 155, 447-450, 2000

17) Magnetism and transport of $Ln_{0.5}Sr_{0.5}Fe_{0.5}Co_{0.5}O_3$ (*Ln*=La and Pr)
K. Yoshii, H. Abe
Transactions of the Materials Research Society of Japan, 26[1], 75-78, 2001

18) Magnetic properties of $LnTi_{0.5}V_{0.5}O_3$ (*Ln*=Ce and Pr)
K. Yoshii, H. Abe
J. Solid State Chem., 156, 452-457, 2001

19) Magnetism and transport of $Ln_{0.5}Sr_{0.5}CoO_3$ (*Ln*=Pr, Nd, Sm and Eu)
K. Yoshii, H. Abe, A. Nakamura
Mater. Res. Bull., 36, 1447-1454, 2001

20) Magnetic properties of perovskite $GdCrO_3$,
K. Yoshii
J. Solid State Chem., 159, 204-208, 2001

21) XAS and MCD studies in $Eu_{0.6}Sr_{0.4}MnO_3$
M. Mizumaki, Y. Saitoh, A. Agui, K. Yoshii, A. Fujimori, S. Nakamura,
J. Synchrotron Rad., 8, 440-442, 2001

22) Structure, magnetism and transport of $Ln_{1-x}TiO_3$ (Ln=Ce and Pr)
K. Yoshii, H. Abe, S. Tsutsui, A. Nakamura
J. Magn. Magn. Mater., 226-230, 900-901, 2001

23) Magnetic and structural properties of $Pr_{1-x}A_xCoO_3$ (A=Sr and Ba)
K. Yoshii, S. Tsutsui, A. Nakamura
J. Magn. Magn. Mater., 226-230, 829-830, 2001

24) Antiferromagnetic-ferromagnetic crossover in UO_2-TiO_x multi-phase systems
A. Nakamura, S. Tsutsui, K. Yoshii
J. Magn. Magn. Mater., 226-230, 876-878, 2001

25) Ferromagnetism in $ErTi_2Ga_4$
H. Abe, K. Yoshii, H. Kitazawa
J. Phys. Soc. Jpn., 70, 3042-3045, 2001

26) High-energy X-ray Diffraction of disorderd materials in high-energy X-ray diffraction beamline BL04B2 at SPring-8
S. Kohara, K. Suzuya
Journal of the Japanese society for synchrotron radiation research, 14,2001, in press

27) Electrochemical growth of Pd on Au(111) and Au(001) studied by surface X-ray diffraction
M. Takahasi, J. Mizuki, K. Tamura, T. Kondo, K. Uosaki
Journal of the vacuum society of Japan, 44, 375, 2001

2. Proceedings

1) A Highly Conductive RTMS; Alkylimidazolium Fluorohydrogenates
Proceedings of 6th International Conference of Molten Salt Chemistry
R. Hagiwara, K. Matsumoto, T. Tsuda, Y. Ito, S. Kohara, K. Suzuya
Technology, China, Shanghai, P. 136 - 139

2) Magnetic and transport studies of $LaFe_{1-x}Ni_xTiO_3$
K. Yoshii, H. Abe, N. M. Masaki, A. Nakamura
Ferrites: Proceedings of the eighth international conference on ferrites, 2000 (ICF8), 278-280, 2001

Surface chemistry research (Surface Chemistry Research Group)

1. Journals

1) Kinetic energy effects of oxygen molecular beams in initial oxidation of silicon surfaces
Y. Teraoka, A. Yoshigoe, M. Sano
J. Vac. Soc. Jpn., 43, 412, 2000, in Japanese

2) Influence of translational energy for surface reaction of silicon with oxygen molecules
Y. Teraoka, A. Yoshigoe, M. Sano
J. Surf. Sci. Soc. Jpn., 21, 444-447, 2000, in Japanese
3) X-ray photoelectron spectroscopic observation on the formation of carbon nitride thin films produced by low-energy nitrogen ion implantation
I. Shimoyama, T. Sekiguchi, Y. Baba
Jpn. J. Appl. Phys., 39, Pt.1, 4540-4544, 2000
4) Site-specific fragmentation of acetone adsorbed on Si(100) in the carbon 1s adsorption
T. Sekiguchi, H.I. Sekiguchi, Y. Baba
Surf. Sci., 454-456, 363-368, 2000
5) Evidence for the existence of nitrogen-substituted graphite structure by polarization dependence of near edge X-ray absorption fine structure
I. Shimoyama, G. Wu, T. Sekiguchi, Y. Baba
Phys. Rev. B, 62, R6053-R6056, 2000
6) The oxidation behaviors of Fe, Cr and Ni in O_2^+-ion implanted SUS304 stainless steel by in situ SR-XPS I. Oxidation behaviors
Y. Li, Y. Baba, T. Sekiguchi
J. Chinese Society for Corrosion and Protection, 20, 321-330, 2000, in Chinese
7) The oxidation behaviors of Fe, Cr and Ni in O_2^+-ion implanted SUS304 stainless steel by in situ SR-XPS II. Chemical state of oxygen
Y. Li, Y. Baba, T. Sekiguchi
J. Chinese Society for Corrosion and Protection, 20, 331-337, 2000 in Chinese
8) Site-specific desorption from condensed C- and N-deuterated formamide near the carbon and nitrogen K-edge
H.I. Sekiguchi, T. Sekiguchi, M. Imamura, N. Matsubayashi, H. Shimada, Y. Baba
Surf. Sci., 454-456, 407-411, 2000
9) Non-destructive depth profile analysis by high-energy synchrotron-radiation XPS
H. Yamamoto, Y. Baba
J. Korean Vacuum Soc., 9, No. S2, 84-88, 2000
10) Chemical states of oxygen implanted in SUS 304 stainless steel and pure metals studied by in situ XPS using synchrotron radiation
Y. Li, Y. Baba, T. Sekiguchi
J. Materials Science, 35, 6123-6130, 2000
11) Photon-stimulated ion desorption from molybdenum oxides following Mo $2p_{3/2}$ excitation
G. Wu, Y. Baba, T. Sekiguchi, I. Shimoyama
J. Synchrotron Rad., 8, Part2, 469-471, 2001
12) Orientation-selective excitation and dissociation in multilayered benzene
T. Sekiguchi, Y. Baba, H.I. Sekiguchi, M. Imamura, N. Matsubayashi, H. Shimada
Appl. Surf. Sci., 169-170, 287-291, 2001
13) Study of electronic structure of graphite-like carbon nitride
I. Shimoyama, G. Wu, T. Sekiguchi, Y. Baba
J. Electron Spectrosc. Relat. Phenom., 114-116, 841-848, 2001
14) Fragmentation and charge neutralization pathways depending on molecular orientation at surfaces
T. Sekiguchi, H.I. Sekiguchi, M. Imamura, N. Matsubayashi, H. Shimada, Y. Baba
Surf. Sci., 482-485, 279-284, 2001
15) Study on the oxidation behavior of Fe, Cr and Ni in O_2^+-ion implanted SUS304 stainless steel by in situ SR-XPS and ex situ scanning tunnelling microscope
Y. Li, Y. Baba, T. Sekiguchi
Corrosion Sci., 43, 903-917, 2001
16) Local electronic structures in solid carbon nitride
I. Shimoyama, T. Sekiguchi, Y. Baba, G. Wu
Photon Factory News, 18, 17-22, 2001, in Japanese
17) Commissioning of surface chemistry end-station in BL23SU of SPring-8
Y. Teraoka, A. Yoshigoe
Appl. Surf. Sci., 169-170, 738-741, 2001
18) Initial oxidation of Si(001) induced by translational kinetic energy of O_2 supersonic molecular beams

A. Yoshigoe, M. Sano, Y. Teraoka
Jpn. J. Appl. Phys., 39, 7026-7030, 2001

19) "In-situ" observation using synchrotron radiation photoemission spectroscopy on initial Si(001) oxidation caused by translational kinetic energy of O_2
A. Yoshigoe, Y. Teraoka
J. Vac. Soc. Jpn., 44, 195-198, 2001, in Japanese

20) In-situ Si-2p core-level spectroscopy using synchrotron radiation for initial oxidation on Si(001) surfaces induced by translational kinetic energy of O_2 molecules
A. Yoshigoe, Y. Teraoka
Transactions of the Materials Research Society of Japan, 26, 755-758, 2001

21) Initial stages of oxygen chemisorption on Si(001) surfaces induced by translational kinetic energy of O_2 at room temperature
A. Yoshigoe, Y. Teraoka
Surf. Sci., 482-485, 189-195, 2001

22) A grating monochromator of BL23SU at SPring-8 covering silicon and oxygen K-edges
A. Yoshigoe, A. Agui, T. Nakatani, T. Matsusita, Y. Saitoh, A. Yokoya
J. Synchrotron Rad., 8, 502-504, 2001

23) Oxygen K-edge X-ray absorption near edge structures (XANES) of sublimated films of amino acids
M. Tanaka, T. Koketsu, K. Nakagawa, A. Agui, A. Yokoya
J. Synchrotron Radiat., 8, 1009-1011, 2001

24) Photoabsorption spectum of DNA and related compounds
K. Akamatsu, A. Yokoya
J. Synchrotron Radiat., 8, 1001-1002, 2001

25) EPR spectrometer installed in a soft X-ray beamline at SPring-8 for biophysical studies
A. Yokoya, K. Akamatsu
Nuclear Instruments and Methods, Section A, 1333-1337, 2001

26) Synchronous Beam Diagnostic System using Cordless Telephones at SPring-8
T. P. Kudo, H. Aoyagi, K. Sato, S. Wu, H. Tanaka, S. Sasaki, T. Nakatani, M. Takeuchi, T. Shimada, Y. Hiramatsu, A. Yokoya, A. Agui, A. Yoshigoe, H. Ohkuma, Y. Miyahara, T. Ishikawa, H. Kitamura
Nuclear Instruments and Methods, Phys. Res. A, 239-243, 2001

27) Photoionizaation of Ne^{3+} ions in the region of 1s->2p autoionizing resonance
M. Ohura, H. Yamaoka, K. Kawatsura, J. Kimata, T. Hayaishi, T. Takahashi, T. Koizumi, T. Sekioka, M. Terasawa, Y. Ito, Y. Awaya, A. Yokoya, A. Agui, A. Yoshigoe, Y Saitoh
Phys. Rev. A, 63, 014704- 1-4, 2001

28) X-ray absorption near edge structures (XANES) of DNA or its components around oxygen *K*-edge and the application for radiation biology
K. Akamatsu, A. Yokoya
Radiat. Res., 155, 449-452, 2001

29) A grating monochromator of BL23SU at SPring-8 covering silicon and oxygen K-edges
A. Yoshigoe, A. Agui, T. Nakatani, T. Matsusita, Y. Saitoh, A. Yokoya
J. Synchrotron Rad., 8, 502-504, 2001

30) Verification of NEXAFS assignments by a comparison of fragmentation between gaseous and condensed methyl formate
Hiromi Ikeura-Sekiguchi, Tetsuhiro Sekiguchi, Norio Saito, Isao H. Suzuki
J. Synchrotron Rad., 8, 548-550, 2001

31) Inner Shell Excitation and Dissociation of Condensed Formamide
Hiromi Ikeura-Sekiguchi, Tetsuhiro Sekiguchi, Yoshinori Kitajima, Yuji Baba
Applied Surface Science 169-170, 281-285, 2001

2. Proceedings

1) Modeling of Production Process of DNA Damage by Irradiation with Monochromatic X-rays around K-edge of Phosphorus
R. Watanabe, A. Yokoya, K. Saito
Proceedings of IRPA10, Hiroshima (2000) CD-ROM

2) Initial Oxidation of Si(001) Surfaces Induced by Translational Energy of O_2 Molecules

Y. Teraoka, A. Yoshigoe, M. Sano
Proceedings of the 22nd Dry Process Symposium, 85-90, 2000

3) The role of translational kinetic energy of O_2 molecules for initial oxidation processes on Si(001) surfaces
A. Yoshigoe, Y. Teraoka
Proceedings of the 4th Japan-Russia Seminar on Semiconductor Surfaces, 135-137, 2000

4) Photoemission spectroscopy of Si(001) surfaces oxidized by hyperthermal O_2 molecular beams
Y. Teraoka, A. Yoshigoe
Proceedings of 25th International Conference on the Physics of Semiconductors Part I, 321-322, 2000

5) Photoemission and Molecular Scattering Study on Initial Oxidation of Si(001) Surfaces Induced by O_2 Translational Energy
Y. Teraoka, A. Yoshigoe, M. Sano
Proceedings of Symposium on Surface Science, 86-89, 2001

3. Reports

1) Influence of incident O_2 translational energy to initial oxidation of Si(001) surface
Y. Teraoka, A. Yoshigoe and M. Sano
Atomic Collision Research in Japan, 26, 114-116, 2000

2) Manufacture of surface reaction analysis apparatus and its application to analysis of initial oxidation processes on Si(001) surfaces
Y. Teraoka, A. Yoshigoe, M. Sano
JAERI-Tech 2000-080, 2000

3) Absolute measurement of photon-flux using a multi-electrode ion chamber
M. Sano, A. Yoshigoe, Y. Teraoka, N. Saito, I. Suzuki
JAERI-Tech 2000-081, 2000

4) Specifications for gas treatment apparatus
Y. Teraoka, A. Yoshigoe
JAERI-Tech 2001-005, 2001

5) Specifications for surface reaction analysis apparatus
Y. Teraoka, A. Yoshigoe
JAERI-Tech 2001-006, 2001

6) Design and manufacture of apparatus for analysis of atomic process on solid surfaces
A. Yoshigoe, Y. Teraoka
JAERI-Tech 2001-009, 2001

7) Design and manufacture of multi-electrode ion chamber for absolute photon-flux measurements of soft x-rays
A. Yoshigoe, Y. Teraoka
JAERI-Tech 2001-026, 2001

8) Construction of surface reaction analysis apparatus and its application to initial oxidation of silicon surfaces
Y. Teraoka and A. Yoshigoe
JAERI-Review 2001-003, 104, 2001

Heavy atom science (Heavy Atom Science Research Group)

1. Journals

1) Bulk 4f Electronic States of Ce-Based Heavy Fermion System Probed by High-Re solution Resonance Photoemission
A.Sekiyama, K. Kadono, K. Matsuda, T. Iwasaki, S. Ueda, S. Imada, S. Suga, R. Settai, H. Azuma,
Y. Onuki, Y. Saitoh
J. Phys. Soc. Jpn., 69, 2771, 2000

2) Probing bulk states of correlated electron systems by high-resolution reson ance photoemission
A.Sekiyama, T. Iwasaki, K. Matsuda, Y. Saitoh, Y. Onuki, S. Suga

Nature, 403, 396, 2000
3) Bulk and surface electronic structures of CePdX (X=As, Sb) studied by 3d-4f resonance photoemission
T. Iwasaki, S. Suga, S. Imada, A. Sekiyama, K. Matsuda, M. Kotsugi, K.-S. An, T. Muro, S. Ueda, T. Matsushita, Y. Saitoh, T. Nakatani, H. Ishii, O. Sakai, R. Takayama, T. Suzuki, T. Oguchi, K. Kato, A. Ochiai
Phys. Rev. B, 61, 4621, 2000
4) High-resolution Ce 3d-edge resonant photoemission study of CeNi2
See-Hun Yang, S.-J. Oh, Hyeong-Do Kim,Ran-Ju Jung, A. Sekiyama, T. Iwasaki, S. Suga, Y. Saitoh, E.-J. Cho, J.-G Park
Phys. Rev. B, 61, 13329, 2000
5) Performance of a very high resolution soft x-ray beamline BL25SU with a twin-helical undulator at SPring-8
Y. Saitoh, H. Kimura, Y. Suzuki, T. Nakatani, T. Matsushita, T. Muro, T. Miyahara, M. Fujisawa, K. Soda, S. Ueda, H. Harada, M. Kotsugi, A. Sekiyama, S. Suga
Rev. Sci. Instrum., 71, 3254, 2000
6) High-resolution resonant photoemission study of CeRu2
K. Matsuda, A. Sekiyama, S. Suga, S. Imada, Y. Saitoh, T. Matsushita, S. Ueda, H.Harada, T. Iwasaki, M. Kotsugi, M. Hedo, Y. Onuki, E. Yamamoto, Y. Haga, R. Takayama, O. Sakai
Physica B, 281&282, 729, 2000
7) Resonance photoemission study of CePtP
T. Iwasaki, A. Sekiyama, S. Ueda, K. Matsuda, M. Kotsugi, S. Imada, S. Suga, Y. Saitoh, T. Matsushita, T. Nakatani, R. Takayama, O. Sakai, H. Osaka, M. K asaya, K. Takegahara, H. Harima
Physica B, 281&282, 105, 2000
8) Local magnetic states in La1-xSrxMnO3 and Nd1-xSrxMnO3
S. Imada, S. Suga, T. Muro, S. Ueda, R. -J. Jung, M. Kotsugi, Y. Saitoh, T. Matsushita, H. Kuwahara, H. Morimoto, Y. Tokura
Physica B, 281&282, 498, 2000
9) Metastable Domain Structures of Ferromagnetic Microstructures Observed by Soft X-Ray Magnetic Circular Dichroism Microscopy
S. Imada, S. Ueda, R. -J. Jung, Y. Saitoh, M. Kotsugi, W. Kuch, J. Gilles, S. Kang, F. Offi, J. Kirshner, H. Daimon, T. Kimura, J. Yanagisawa, K. Gamo, S. Suga
Jpn. J. Appl. Phys., 39, L585, 2000
10) Soft x-ray emission and absorption spectra in the O K region of oxygen Incorporated in microporous carbon
Y. Muramatsu, Y. Ueno, Y. Ishiwata, R. Eguchi, M. Watanabe, S. Shin, R. C. C. Perera
Carbon, 39, 1399-1402, 2001
11) Soft x-ray emission and absorption spectra in the C K region of sputtered amorphous carbon films
Y. Muramatsu, S. Hirono, S. Umemura, Y. Ueno, T. Hayashi, M. M. Grush, E. M. Gullikson, R. C. C. Perera
Carbon, 39, 1403-1407, 2001
12) First operation of circular dichroism measurements with periodic photon-helicity switching by a variably polarizing undulator at BL23SU at SPring-8
A.Agui, A. Yoshigoe, T. Nakatani, T. Matsushita, Y. Saitoh , A.Yokoya, H. Tanaka, Y. Miyahara, T. Shimada, M. Takeuchi, T. Bizen, S. Sasaki, M. Takao, H. Aoyagi, T. P. Kudo, K. Satoh, S. Wu, Y. Hiramats, H. Ohkuma,
Rev. Sci. Inst., 72, 3191, 2001
13) Resonat O Ka Emission of CuGeO3 Single-Crystal
A. Agui, J.-H. Guo, C. Sathe, J. Nordgren, M. Hidaka, I. Yamada
Solid State Communication, 118 (12), 619-622, 2001
14) Valence excitations observed in resonat soft X-ray emission spectra of K2Ni(CN)4.H2O at the Ni 2p edge
Y. Takata, T. Hatsui,N. Kosugi, A. Agui, M. Magnuson, C. Sathe, J.-E. Rubensson, J. Nardgren
J. Elec. Spec. & Related Phen., 114-116, 909-913, 2001
15) Experimental technique for radiative-process-resolved x-ray absorption spectroscopy at the inner-shell excitation thresholds

Y. Muramatsu, Y. Ueno, T. A. Sasaki, E. M. Gullikson, R. C. C. Perera
J. Synchrotron Radiation, 8, 369, 2001
16) XAS and MCD studies in Eu0.6Sr0.4MnO3
M. Mizumaki, Y. Saitoh, A. Agui, K. Yoshii, A. Fujimori, S. Nakamura
J. Synchrotron Rad., 8, 440-442, 2001
17) Soft X-ray absorption spectra of ilmenite family
A. Agui, M. Mizumaki, Y. Saitoh, T. Matsushita, T. Nakatani, A. Fukaya, E. Torikai
J. Synchrotron Rad., 8, 907-909, 2001
18) Oxygen K-edge X-ray absorption near edge structures (XANES) of sublimated films of amino acids
M. Tanaka, K. Nakagawa, T. Koketsu, A. Agui, A. Yokoya
J. Synchrotron Rad., 8, 1009-1011, 2001
19) First operation of circular dichroism measurements with periodic photon-hericity switching by a variably-polarizing undulator at BL23SU at the SPring-8
A. Agui, A. Yoshigoe, A. Yokoya, Y. Saitoh, T. Shimada, T. Nakatani, T. Matsushita, Y. Miyahara, H. Tanaka, M. Takeuchi, T. Bizen, S. Sasaki, M. Takao, K. Saotome, H. Aoyagi, T. Kudo, S. Wu, K. Satoh, H. Ohkuma
Rev. Sci. Inst., 72, 3191-3197, 2001
20) Experimental technique for radiation-process-resolved fluorescence-yield X-ray absorption spectroscopy
Y. Muramatsu
Advances in X-ray Chemical Analysis, Japan, 32, 147, 2001

2. Proceedings

1) Soft x-ray emission spectra in the OK region of oxygen incorporated in microporous carbon
Y. Muramatsu, M. Watanabe, Y. Ueno, S. Shin, R. C. C. Perera,
Proceedings of ICESS8/J. Electron Spectrosc. and Relat. Phenom., 114-116, 301-305, 2001

3. Reports

1) MCD measurement with periodic photon helisity switching
A. Agui, T. Nakatani, T. Matsushita
SPring-8 Research Frontiers 1999/2000, 79-81, 2001
2) Highlights of SPring-8 BL23SU in 2000
A. Agui, A. Yoshigoe, T. Nakatani, Y. Saitoh, Y. Teraoka, M. Yokoya
JAERI-Tech 2001-043, 2001
3) Soft X-ray beamline -BL23SU- at SPring-8
A. Agui, A. Yoshigoe, Y. Saitoh, Y. Teraoka, A. Yokoya
JAERI-Review 2001-003, 87, 2001
4) High lights of SPring-8 BL23SU in 2000
A. Agui, A. Yoshigoe, Y. Saitoh, K. Nakatani, A. Yokoya
JAERI-Tech 2001-043

Electric material science (Electronic Material Science Group)

1. Journals

1) Theoretical and experimental study of resonant 3d X-ray photoemission and resonant L3M4,5 M4,5 Auger transition of PdO
T.Uozumi, T.Okane, K.Yoshii., T.A.Sasaki, A.Kotani
J. Phys. Soc. Jpn., 69, 1226-1233, 2000
2) Dynamics of Fe Cations in Nafion Membranes Studied by Nuclear Resonant Quasielastic Scattering of Synchrotron Radiation
R. Haruki, M. Seto, S. Kitao, Y. Yoda, Yu. Maeda
J. Phys. Soc. Jpn., Vol.69, No.12, 4049-4054, 2000
3) Nuclear Resonant Quasielastic Scattering Fe Cations in Nafion Membranes Effect of Dynamics in a Short Time Range
R. Haruki, M. Seto, S. Kitao, Y. Kobayashi, Y. Yoda, T. Mitsui, Yu. Maeda
J. Phys. Soc. Jpn., Vol. 70, No.2, 445-448, 2001

4) Nuclear Resonant Scattering Beamline at Spring-8
Y. Yoda, M. Yabashi, K. Izumi, X. W. Zhang, S. Kisimoto, S. Kitao, M. Seto, T. Mitsui,T. Harami, Y. Imai, S. Kikuta
Nucl. Instr. & Meth A, 467-468, 715, 2001

5) The Experimental Apparatus for Synchrotron Radiation Mossbauer Spectroscopy of BL11 in Spring-8
T. Mitsui, S. Kitao, X. W. Zhang, M. Marushita, M. Seto
Nucl. Instr. & Meth. A, 467-468, 1105, 2001

Appendix A Activities of the Research Committee

A research committee was organized in FY1996 to promote activities on advanced photon and synchrotron radiation research in Kansai Research Establishment, JAERI. There are three technical subcommittees for Laser System, Laser Utilization and Synchrotron Radiation Utilization, under the committee.

Committee for Advanced Photon and Synchrotron Radiation Research

First meeting	March 21	1997	Tokyo
Second meeting	February 3	1998	Tokyo
Third meeting	March 9	1999	Tokyo
Fourth meeting	February 10	2000	Tokyo
Fifth meeting	March 2	2001	Kashiwa

Technical Subcommittee for Laser System

First meeting	December 8	1997	Tokyo
Second meeting	July 30	1998	Tokyo
Third meeting	December 13	1999	Tokyo
Fourth meeting	February 1	2001	Tokyo

Technical Subcommittee for Laser Utilization

First meeting	December 10	1997	Tokyo
Second meeting	December 3	1998	Tokyo
Third meeting	December 24	1999	Tokyo
Fourth meeting	February 15	2001	Kizu

Technical Subcommittee for Synchrotron Radiation Utilization

First meeting	December 9	1997	Tokyo
Second meeting	November 27	1998	Harima (SPring-8)
Third meeting	February 8	2000	Harima (SPring-8)
Fourth meeting	February 28	2001	Harima (SPring-8)

Member of Committee

Committee for Advanced Photon and Synchrotron Radiation Research (FY2000)

Chairman	Chiyoe	YAMANAKA	Director General, Institute for Laser Technology
Vice-Chairman	Susumu	NAMBA	Professor, Technical Research Center, Nagasaki Institute of Applied Science
	Shuntaro	WATANABE	Professor, Institute for Solid State Physics, The University of Tokyo
	Seishi	KIKUTA	Executive Director, Deputy Director General, Japan Synchrotron Radiation Research Institute
	Katsunobu	AOYAGI	Professor, Interdisciplinary Graduate School of Science and Engineering, Tokyo Institute of Technology
	Fumio	INABA	Professor Emeritus, Tohoku University
	Nobutsugu	IMANISHI	Professor, Graduate School of Engineering, Kyoto University
	Yoshitaka	KIMURA	Director, Institute of Materials Structure Science, High Energy Accelerator Research Organization
	Hiroshi	TAKATA	Director, Harima Research Laboratory, Sumitomo Electric Industries, Ltd.
	Kohei	TAMAO	Director, Institute of Chemistry, Kyoto University
	Michitaka	TERASAWA	Professor, Department of Engineering, Himeji Institute of Technology
	Yasuki	NAGAI	Director, Research Center for Nuclear Physics, Osaka University
	Takeshi	NAMIOKA	Professor Emeritus, Tohoku University
	Tatsuhiko	YAMANAKA	Director, Institute of Laser Engineering, Osaka University
	Hiroyoshi	LANG	Professor, Faculty of Technology, Tokyo University of Agriculture and Technology
	Yukio	SUDO	Director, Office of Planning, JAERI
	Hideo	OHNO	Director General, Kansai Research Establishment, JAERI
Subcommittee	Yoshiaki	KATO	Director, Advanced Photon Research Center, JAERI
	Osamu	SHIMOMURA	Director, Synchrotron Radiation Research Center, JAERI
Secretary	Toyoaki	KIMURA	Senior Staff, Office of Planning, JAERI
	Takashi	ARISAWA	Prime Scientist, Advanced Photon Research Center, JAERI
	Siro	NAGAI	Deputy Director, Advanced Photon Research Center, JAERI
	Junichiro	MIZUKI	Deputy Director, Synchrotron Radiation Research Center, JAERI
	Noboru	TSUCHIDA	Deputy General Manager, Kansai Research Establishment, JAERI

Technical Subcommittee for Laser System (FY2000)

Chief	Shuntaro	WATANABE	Professor, Institute for Solid State Physics, The University of Tokyo
	Shinichiro	AOSHIMA	Central Research Laboratory, Mahatmas Photonics K.K.
	Ichita	ENDO	Professor, Graduate School of Advanced Sciences of Matter, Hiroshima University
	Ichiro	KATAYAMA	Professor, Institute of Particle and Nuclear Studies, High Energy Accelerator Research Organization
	Hiroo	KINOSHITA	Professor, Laboratory of Advanced Science and Technology for Industry, Himeji Institute of Technology
	Takatomo	SASAKI	Professor, Faculty of Engineering, Osaka University
	Toshihisa	TOMIE	Principal Scientist, Electro technical Laboratory
	Masahiro	NAKATSUKA	Professor, Institute of Laser Engineering, Osaka University
	Takashi	FUJIMOTO	Professor, Graduate School of Engineering, Kyoto University
	Kenzo	MIYAZAKI	Professor, Institute of Advanced Energy Laboratory, Kyoto University
	Tetsuo	YAMAZAKI	Professor, Institute of Advanced Energy Laboratory, Kyoto University
	Kuniyoshi	YOKOO	Professor, Research Institute of Electrical Communication, Tohoku University
	Yoshiaki	KATO	Director, Advanced Photon Research Center, JAERI
Secretary	Noboru	TSUCHIDA	Deputy General Manager, Kansai Research Establishment, JAERI
	Akihiko	NISHIMURA	Senior Scientist, Advanced Photon Research Center, JAERI

Technical Subcommittee for Applied Photon Research (FY2000)

Chief	Susumu	NAMBA	Professor, Technical Research Center, Nagasaki Institute of Applied Science
	Atsushi	OGATA	Professor, Graduate School of Advanced Sciences of Matter, Hiroshima University
	Yoneyoshi	KITAKAWA	Assistant Professor, Institute of Laser Engineering, Osaka University
	Nobuhiro	GEMMA	Research & Development Center, Toshiba Corporation
	Takayoshi	KOBAYASHI	Professor, Faculty of Science, The University of Tokyo
	Naoki	SATO	Professor, Institute for Chemical Research, Kyoto University
	Seiichi	TAGAWA	Professor, Institute of Scientific and Industrial Research, Osaka University
	Yasushi	NISHIDA	Professor, Faculty of Engineering, Utsunomiya University
	Takayasu	MOCHIDUKI	Professor, Laboratory of Advanced Science and Technology for Industry, Himeji Institute of Technology
	Kazuhisa	NAKAJIMA	Invited Researcher, Advanced Photon Research Center, JAERI Assistant Professor, Accelerator Laboratory, High Energy Accelerator Research Organization
	Hiroyuki	DAIDO	Head, Advanced Photon Research Center, JAERI
Secretary	Noboru	TSUCHIDA	Deputy General Manager, Kansai Research Establishment, JAERI
	Norio	OGIWARA	Deputy Head, Advanced Photon Research Center, JAERI

Technical Subcommittee for Synchrotron Radiation (FY2000)

Chief	Seishi	KIKUTA	Executive Director, Deputy Director General, Japan Synchrotron Radiation Research Institute
	Tatsuo	UEKI	Director, Japan Synchrotron Radiation Research Institute
	Yoshichika	OHNUKI	Professor, Faculty of Science, Osaka University
	Shigi	SHIN	Assistant Professor, Institute for Solid State Physics, The University of Tokyo
	Toshio	TAKAHASHI	Assistant Professor, Institute for Solid State Physics, The University of Tokyo
	Kenichiro	TANAKA	Professor, Faculty of Science, Hiroshima University
	Kazuhiko	TSUJI	Professor, Faculty of Science and Technology, Keio University
	Saburo	NASU	Professor, Faculty of Engineering Science
	Kotaro	HIEDA	Professor, Faculty of Science, Rikkyo University
	Yoichi	MURAKAMI	Assistant Professor, Institute of Materials Structure Science, High Energy Accelerator Research Organization
	Osamu	SHIMOMURA	Director, Synchrotron Radiation Research Center, JAERI
Secretary	Siro	NAGAI	Deputy Director, Advanced Photon Research Center, JAERI
	Hironobu	OGAWA	Deputy General Manager, Synchrotron Radiation Research Center, JAERI

Appendix B Organization of Kansai Research Establishment
(April 1, 2000～March 31, 2001)

- **Kansai Research Establishment** (Director General: **H.OHNO**)
  - **Department of Administrative Services** (Director: **A.KOMAKI**)
    - Administrative Services Division (G. M.: **M.NISHINOYA**(until September) **H.YOSHIDA**(from October))
    - Accounts Division (G. M.: **Y.YAMAMOTO**)
    - Research Planning Division (G. M.: **S.NAGAI**)
    - Utilities and Maintenance Division (G. M.: **S.SUGAI**)
    - Safety Division (G. M.: **T.MATSUI**)
    - Neyagawa Office (G. M.: **H.IHARA**)
  - **Advanced Photon Research Center** (Director: **Y.KATO**)
    - Laser System Development Group (G. L.: **T.ARISAWA**)
    - X-ray Laser Research Group (G. L.: **A.NAGASHIMA**(until September) **Y.KATO**(from October))
    - Novel Optics Research Group (G. L.: **M.KOIKE**)
    - Laser Acceleration Research Group (G. L.: **K.NAKAJIMA**)
    - Simulation Group for Advanced Photon Science (G. L.: **T.TAJIMA**)
    - Free Electron Laser Research Group (G. L.: **E.MINEHARA**)
    - Applied Photon Research Group (G. L.: **Y.KATO**(until September) **H.DAIDO**(from October))
  - **Synchrotron Radiation Research Center** (Director: **O.SHIMOMURA**)
    - Synchrotron Radiation Administration Division (G. M.: **K.NAKAAKI**)
    - Experimental Facilities Development Group (G. L.: **J.MIZUKI**(until September) **T.HARAMI**(from October))
    - High Pressure Science Group (G. L.: **O.SHIMOMURA**)
    - Structural Physics Research Group (G. L.: **J.MIZUKI**)
    - Surface Chemistry Research Group (G. L.: **Y.BABA**)
    - Heavy Atom Science Group (G. L.: **T.SASAKI** (until September) **Y.BABA**(from October))
    - Electronic Material Science Group (G. L.: **A.FUJIMORI**)

G. M.: General Manager G. L.: Group Leader

Appendix C Personnel

(April 1, 2000～March 31, 2001)

Personnel at Advanced Photon Research Center

Yoshiaki KATO
Siro NAGAI
Takashi ARISAWA
Tohru MATOBA
Osamu YAMASHITA
Tsutomu WATANABE
Kazunori KIKUCHI
Naohiko KAYORA
Jun NAKAJIMA
Kiyomi ENDOH
Masako SHIGENARI

Laser System Development Group
Takashi ARISAWA
Koichi YAMAKAWA
Akihiko NISHIMURA
Akira OZU
Junji KAWANAKA
Hiromitsu KIRIYAMA
Yutaka AKAHANE
Kyoichi DEKI
Fumiaki MATSUOKA
Tsutomu USAMI
Fumihiko NAKANO
Makoto AOYAMA
Yuji FUKUDA

X-ray Laser Research Group
Yoshiaki KATO(from October)
Akira NAGASHIMA(until September)
Keisuke NAGASHIMA
Yoji SUZUKI
Masataka KADO
Tetsuya KAWACHI
Noboru HASEGAWA
Momoko TANAKA
Kouta SUKEGAWA
Kenjiro TAKAHASHI
Sin-ichi NANBA
Peixiang LU

Novel Optics Research Group
Masato KOIKE
Osamu YODA
Akira SUGIYAMA
Masahiko ISHINO
Hiroyasu FUKUYAMA

Laser Acceleration Research Group
Kazuhisa NAKAJIMA
Shuhei KANAZAWA
Hideyuki KOTAKI
Shuji KONDO
Takashi YOKOYAMA
Shin-ichi MASUDA

Simulation Group for Advanced Photon Science
Toshiki TAJIMA
Mitsuru YAMAGIWA
Toshizo SHIRAI
Akira SASAKI
James KOGA
Kengo MORIBAYASHI
Yutaka UESHIMA
Takayuki UTSUMI
Takuya ARAKAWA
Keisuke NAKAGAWA
Ichirou FUKUMOTO
Keiko SUTO
Hiroo TOTSUJI
Shingo SUZUKI

Free Electron Laser Research Group
Eisuke MINEHARA
Toshihiko YAMAUCHI
Masaru SAWAMURA
Ryoichi HAJIMA
Ryoji NAGAI
Nobuhiro KIKUZAWA
Takehito HAYAKAWA
Nobuyuki NISHIMORI
Toshiyuki SHIZUMA

Applied Photon Research Group
Hiroyuki DAIDO(from October)
Yoshiaki KATO(until September)
Norio OGIWARA
Yuichi SHIMIZU
Kazuaki SUGANUMA
Koichi OGURA
Yuzuru KUROSAKI
Hiroshi MURAKAMI
Akito SAGISAKA
Satoshi ORIMO
Yukio HAYASHI
Junkei KOU

(April 1, 2000～March 31, 2001)

Personnel at Synchrotron Radiation Research Center

Osamu SHIMOMURA
Fujiyasu NOMURA
Teikichi SASAKI
Jun-ichiro MIZUKI

Experimental Facilities Development Group
Jun-ichiro MIZUKI (until September)
Taikan HARAMI (from October)
Hiroyuki KONISHI
Yoshihiro ASANO
Hideaki SHIWAKU
Motoharu MARUSHITA
Yukio HAYASHI

High Pressure Science Group
Osamu SHIMOMURA
Nozomu HAMAYA
Wataru UTSUMI
Yoshinori KATAYAMA
Tetsu WATANUKI
Naoki ISHIMATSU
Taku OKADA
Takahiro AKAO

Structural Physics Research Group
Jun'ichiro MIZUKI
Yasuo NISHIHATA
Kentaro SUZUYA
Norimasa MATSUMOTO
Kenji YOSHII
Masamitu TAKAHASI
Toshiya INAMI
Yasuhiro YONEDA
Tatsuo FUKUDA

Surface Chemistry Research Group
Yuji BABA
Tetsuhiro SEKIGUCHI
Yuden TERAOKA
Akinari YOKOYA
Akitaka YOSHIGOE
Ken AKAMATSU
Iwao SHIMOYAMA

Heavy Atom Science Group
Teikichi SASAKI (until September)
Yuji BABA (from October)
Yasuji MURAMATSU
Yuji SAITOH
Akane AGUI

Electronic Material Science Group
Atsushi FUJIMORI
Makoto SETO
Tetsuo OKANE
Takaya MITUI
Shin'ichi FUJIMORI
Akihiro INO
Hiroyuki KAWAMURA

Synchrotron Radiation Administration Division
Katsuhiko NAKAAKI
Hironobu OGAWA
Shoichi ONO
Satoshi FURUTA (until September)
Kensin DOI

(April 1, 2000～March 31, 2001)

Personnel at Department of Administrative Services

Akira KOMAKI
Tetsuo KANAZAWA

Administrative Services Division
Yoshinori NISHINOYA(until September)
Hiroshi YOSHIDA(from October)
Hisayoshi KUROHA
Yoshimi KURATA
Ken SASAKI
Fumiyuki SAIZEN
Masako TANAKA(until September)
Yuko HASEGAWA(from October)
Shinji KOMATA
Michiyo YABUTA

Accounts Division
Yoshio YAMAMOTO
Saburo YAMAGISHI
Masahiko MATSUMOTO
Hiroyuki YAMANO
Taiki IKEJIMA
Kazumi TAKEDA
Susumu KAWASAKI
Norito HIRAMATSU

Research Planning Division
Siro NAGAI
Noboru TSUCHIDA
Sayaka HARAYAMA
Shuichi FUJITA
Noriko UEHARA

Utilities and Maintenance Division
Seiji SUGAI
Tadashi HANAWA
Jun MATSUMOTO
Taketomo ABE
Tsutomu TOMIYA
Kotomi WAKI

Safety Division
Tomoaki MATSUI
Yaichi FUKUSHIMA
Masayuki UENO
Masayuki KABUTOU
Yuko HASEGAWA(until September)
Izumi TAMURA(from October)

Neyagawa Office
Hitoshi IHARA
Atsuko HAYASHI

Appendix D Symposia

(1) The first JAERI-Kansai International Workshop on Ultrashort-pulse Ultrahigh-power Lasers and Simulation for Laser-plasma Interactions (held as "Joint ICFA/JAERI-Kansai International Workshop '97", organized by International Committee for Future Accelerators, hosted by Japan Atomic Energy Research Institute and High Energy Accelerator Research Organization)
July 14-18, **1997**, Kyoto, Japan
JAERI-Conf 98-004, "Proceedings of The first JAERI-Kansai International Workshop on Ultrashort-pulse Ultrahigh-power Lasers and Simulation for Laser-plasma Interactions July 14-18, 1997, Kyoto Research Park, Kyoto, Japan", March 1998.

(2) The 6th International Conference on Synchrotron Radiation Instrumentation (cosponsored by Japan Atomic Energy Research Institute, Japanese Society for Synchrotron Radiation Research, RIKEN and Japan Synchrotron Radiation Research Institute)
August 4－8, **1997**, Himeji, Japan
J. Synchrotron Radiation, 5 part 3, "SRI'97 Proceedings", May 1998.

(3) 6th International Conference on X-Ray Lasers (cosponsored by Japan Atomic Energy Research Institute and Osaka University)
August 31-September 4, **1998**, Kyoto, Japan
Institute of Physics Conference Series Number 159, "Proceedings of the 6th International Conference on X-Ray Lasers held in Kyoto, Japan, August 31-September 4, 1998"

(4) The Second International Conference on Synchrotron Radiation in Materials Science (cosponsored by Japan Atomic Energy Research Institute, RIKEN and Japan Synchrotron Radiation Research Institute)
October 31－November 3, **1998**, Kobe, Japan
Jpn. J. Appl. Phys. Suppl., 38-1, "Proceedings of the SRMS－2", June 1999.

(5) The First Symposium on Advanced Photon Research
November 8-9, **1999**, Kyoto, Japan
JAERI-Conf 2000-006, "Proceedings of The First Symposium on Advanced Photon Research November 8-9, 1999, Keihanna Plaza/Advanced Photon Research Center, Kyoto, Japan", March 2000.

(6) Workshop on Surface and Interface Using Synchrotron Radiation
March 16-17, **2000**, SPring-8, Japan.

(7) The Second Symposium on Advanced Photon Research
November 9-10, **2000**, Kyoto, Japan
JAERI-Conf 2001-011, "Proceedings of The Second Symposium on Advanced Photon Research November 9-10, 2000, Advanced Photon Research Center, Kyoto, Japan", July 2001.

(8) 2nd UK-Japan International Seminar of Application Radiation to Studies of Nano-structured Materials
(cosponsored by institute of Molecular Science, Japan Atomic Energy research Institute, RIKEN and JASRI)
July 9-10, **2000**, SPring-8, Japan

(9) International Workshop on "Crystallography at High Pressure and High Temperature using X-ray and Neutrons"
(cosponsored by Synchrotron Radiation Research Center of JAERI, JASRI and International Union of Crystallography Commission on High Pressure)
September 30-October 3, **2000**, SPring-8, Japan

国際単位系（SI）と換算表

表1　SI基本単位および補助単位

量	名称	記号
長さ	メートル	m
質量	キログラム	kg
時間	秒	s
電流	アンペア	A
熱力学温度	ケルビン	K
物質量	モル	mol
光度	カンデラ	cd
平面角	ラジアン	rad
立体角	ステラジアン	sr

表2　SIと併用される単位

名称	記号
分，時，日	min，h，d
度，分，秒	°，′，″
リットル	l，L
トン	t
電子ボルト	eV
原子質量単位	u

1 eV=1.60218×10^{-19}J

1 u=1.66054×10^{-27}kg

表3　固有の名称をもつSI組立単位

量	名称	記号	他のSI単位による表現
周波数	ヘルツ	Hz	s^{-1}
力	ニュートン	N	$m\cdot kg/s^2$
圧力，応力	パスカル	Pa	N/m^2
エネルギー，仕事，熱量	ジュール	J	N·m
工率，放射束	ワット	W	J/s
電気量，電荷	クーロン	C	A·s
電位，電圧，起電力	ボルト	V	W/A
静電容量	ファラド	F	C/V
電気抵抗	オーム	Ω	V/A
コンダクタンス	ジーメンス	S	A/V
磁束	ウェーバ	Wb	V·s
磁束密度	テスラ	T	Wb/m^2
インダクタンス	ヘンリー	H	Wb/A
セルシウス温度	セルシウス度	℃	
光束	ルーメン	lm	cd·sr
照度	ルクス	lx	lm/m^2
放射能	ベクレル	Bq	s^{-1}
吸収線量	グレイ	Gy	J/kg
線量等量	シーベルト	Sv	J/kg

表4　SIと共に暫定的に維持される単位

名称	記号
オングストローム	Å
バーン	b
バール	bar
ガル	Gal
キュリー	Ci
レントゲン	R
ラド	rad
レム	rem

1 Å=0.1nm=10^{-10}m

1 b=100fm^2=10^{-28}m^2

1 bar=0.1MPa=10^{5}Pa

1 Gal=1cm/s^2=10^{-2}m/s^2

1 Ci=3.7×10^{10}Bq

1 R=2.58×10^{-4}C/kg

1 rad=1cGy=10^{-2}Gy

1 rem=1cSv=10^{-2}Sv

表5　SI接頭語

倍数	接頭語	記号
10^{18}	エクサ	E
10^{15}	ペタ	P
10^{12}	テラ	T
10^{9}	ギガ	G
10^{6}	メガ	M
10^{3}	キロ	k
10^{2}	ヘクト	h
10^{1}	デカ	da
10^{-1}	デシ	d
10^{-2}	センチ	c
10^{-3}	ミリ	m
10^{-6}	マイクロ	μ
10^{-9}	ナノ	n
10^{-12}	ピコ	p
10^{-15}	フェムト	f
10^{-18}	アト	a

（注）

1．表1－5は「国際単位系」第5版，国際度量衡局1985年刊行による。ただし，1 eVおよび1 uの値はCODATAの1986年推奨値によった。

2．表4には海里，ノット，アール，ヘクタールも含まれているが日常の単位なのでここでは省略した。

3．barは，JISでは流体の圧力を表わす場合に限り表2のカテゴリーに分類されている。

4．EC閣僚理事会指令ではbar，barnおよび「血圧の単位」mmHgを表2のカテゴリーに入れている。

換　算　表

力	N(=10^{5}dyn)	kgf	lbf
	1	0.101972	0.224809
	9.80665	1	2.20462
	4.44822	0.453592	1

粘度　1 Pa·s(N·s/m^2)=10 P(ポアズ)(g/(cm·s))

動粘度　1m^2/s=10^{4}St(ストークス)(cm^2/s)

圧力	MPa(=10bar)	kgf/cm^2	atm	mmHg(Torr)	lbf/in^2(psi)
	1	10.1972	9.86923	7.50062×10^3	145.038
	0.0980665	1	0.967841	735.559	14.2233
	0.101325	1.03323	1	760	14.6959
	1.33322×10^{-4}	1.35951×10^{-3}	1.31579×10^{-3}	1	1.93368×10^{-2}
	6.89476×10^{-3}	7.03070×10^{-2}	6.80460×10^{-2}	51.7149	1

エネルギー・仕事・熱量	J(=10^7 erg)	kgf·m	kW·h	cal(計量法)	Btu	ft·lbf	eV
	1	0.101972	2.77778×10^{-7}	0.238889	9.47813×10^{-4}	0.737562	6.24150×10^{18}
	9.80665	1	2.72407×10^{-6}	2.34270	9.29487×10^{-3}	7.23301	6.12082×10^{19}
	3.6×10^6	3.67098×10^5	1	8.59999×10^5	3412.13	2.65522×10^6	2.24694×10^{25}
	4.18605	0.426858	1.16279×10^{-6}	1	3.96759×10^{-3}	3.08747	2.61272×10^{19}
	1055.06	107.586	2.93072×10^{-4}	252.042	1	778.172	6.58515×10^{21}
	1.35582	0.138255	3.76616×10^{-7}	0.323890	1.28506×10^{-3}	1	8.46233×10^{18}
	1.60218×10^{-19}	1.63377×10^{-20}	4.45050×10^{-26}	3.82743×10^{-20}	1.51857×10^{-22}	1.18171×10^{-19}	1

1 cal= 4.18605J（計量法）

= 4.184J（熱化学）

= 4.1855J（15℃）

= 4.1868J（国際蒸気表）

仕事率　1 PS(仏馬力)

= 75 kgf·m/s

= 735.499W

放射能	Bq	Ci
	1	2.70270×10^{-11}
	3.7×10^{10}	1

吸収線量	Gy	rad
	1	100
	0.01	1

照射線量	C/kg	R
	1	3876
	2.58×10^{-4}	1

線量当量	Sv	rem
	1	100
	0.01	1

（86年12月26日現在）

Annual Report of Kansai Research Establishment 2000 April 1, 2000 — March 31, 2001